Photoacoustic Doppler velocity measurements using time-domain cross-correlation

Joanna Brunker

Thesis submitted for the degree of
Doctor of Philosophy

29 November 2013
Final version, following minor corrections:
11 March 2014

Biomedical Optics Research Laboratory
Department of Medical Physics and Bioengineering
University College London

Declaration

I, Joanna Brunker, confirm that the work presented in this thesis is my own. Where information has been derived from other sources, I confirm that this has been indicated in the thesis.

11th March 2014

Abstract

The feasibility of making spatially resolved measurements of blood velocity using a pulsed photoacoustic Doppler technique has been investigated. Doppler time shifts were quantified via cross-correlation of photoacoustic waveform pairs. The waveforms were generated within a blood-simulating phantom using pairs of light pulses and detected using an ultrasound transducer. Two types of blood-simulating phantom were investigated. The first was a rotating wheel phantom consisting of micron-scale absorbers imprinted on an acetate sheet and moved at known velocities; this simulated plug flow. A time-correlation data processing scheme was used to quantify velocities in the range 0.15 to 1.5 m/s with accuracies as low as 1% and a measurement resolution <4%. The transducer beam width determines a maximum measurable velocity $|V_{\max}|$ beyond which correlation is lost due to absorbers moving out of the focal beam between the two laser pulses. Resolution and $|V_{\max}|$ can be scaled to much lower velocities such as those encountered in microvasculature (< 50 mm/s). Velocities in this range were investigated for the second type of phantom comprising absorbers, such as red blood cells or microspheres, flowing in a suspension within a transparent tube; this demonstrated non-plug flow. The absorber-filled tube could also be manually shifted for direct comparison between the plug and non-plug flow cases. Laminar flow gave rise to under-reading of the known velocities, which was exacerbated by increasing absorber concentrations and tube diameters, presumably due to inadequate light penetration into the tube. A novel signal processing scheme ("waveform segmentation") was developed to surmount this difficulty, and also adds the potential for mapping out the flow velocity profile across the tube. The results show that the absorber spatial heterogeneity can be resolved even using a relatively low frequency detector, and thus pave the way for applying the cross-correlation technique to make blood velocity measurements *in vivo*.

Acknowledgements

Above all, I would like to thank my supervisor, Prof. Paul Beard, for his continual help, guidance and encouragement in every aspect of the project; our meetings always gave me renewed energy and determination. I am also grateful to my second supervisor, Prof. Barbara Pedley, for her support, interest and enthusiasm, and for helping me to keep in mind the long-term goal of the project – to apply my flowmetry method to tumour blood flow.

In addition, my appreciation extends to many members of the Photoacoustic Imaging and Biomedical Optics groups who have contributed to making this work possible: in particular, to Dr. Terence Leung for his assistance with the signal processing, to Dr. Edward Zhang and Dr. Thomas Allen for their contributions to the experimental arrangements, to Dr. Jan Laufer for answering various experimental and theoretical queries, to Dr. Bradley Treeby for help with data processing issues such as signal filtering, and to Dr. Ollie Ogunlade and Teedah Saratoon for willingly donating their blood. I am also grateful to various individuals and departments throughout UCL for offering their time and facilities, especially the UCLH Blood Transfusion Unit for their blood samples and UCLH Haematology for the use of their microscopes and blood analysers, Prof. Nader Saffari (UCL Mechanical Engineering department) for generously lending various ultrasound transducers, Dr. Sandra Bond for the use of the microscopes in the Archaeology Department and her help with obtaining high magnification photographs of the microspheres, Dr. Andrew Davies (Neuroinflammation department) for the opportunity to observe flow real-time using confocal microscopy, and Dr. Timm Kruger (UCL Computational Chemistry department) for his helpful discussions regarding red blood cell motion. In addition, this work could not have been achieved without the generous use of lasers from Keith Oakes (Elforlight) and Gary Newham (Litron).

Prof. Jem Hebden, head of the UCL Department of Medical Physics and Bioengineering, deserves a special mention because without his inspiring encouragement I may never have had the courage to start a PhD. The project I undertook with him in the summer of 2007 was my first introduction to experimental research and I have been hooked ever since. For the final stages of my PhD, I am grateful once more to my supervisor Prof. Paul Beard for his repeated and detailed proof-reading, and to my examiners, Prof. Weindelt Steenbergen from the University of Twente (Netherlands) and Dr. Jean-Martial Mari from UCL, for the time and effort they dedicated to reading my final thesis and conducting my oral examination.

Not least, I owe many thanks to my friends and family for their time and encouragement, especially to my parents, for their loving interest in the project, their patient tolerance of my unsociable working hours, and their never-ending moral, material and financial support.

My appreciation also extends to those in the Engineering and Physical Sciences Research Council (EPSRC) responsible for funding this project.

Contents

List of Figures

List of Tables

List of Abbreviations

Below is a list of the most relevant abbreviations used in this thesis.

AIA	anti-angiogenic (or angiogenesis-inhibiting) agent
AR	acoustic resolution
CW	continuous-wave
FWHM	full width half maximum
Ht	haematocrit, or volume fraction of RBCs (≈ 0.45 for whole blood). In this thesis, concentrations are expressed relative to Ht = 0.45; for example, a volume fraction of 0.225 would be 50% Ht
OD	optical density = $\log_{10} = A/A_0$, where A_0 is the incident light intensity, and A is the light intensity after passing through an attenuating medium
OR	optical resolution
PA	photoacoustic
PAM	photoacoustic microscopy
PAI	photoacoustic imaging
PBS	phosphate buffered saline
PIV	particle image velocimetry
PRF	pulse repetition frequency
PVDF	polyvinyl difluoride
PZT	lead zirconate titanate
RBC	red blood cell
SNR	signal-to-noise ratio
US	ultrasound
VDA	vascular disrupting agent

List of Symbols

On the following page is a list of symbols used most frequently in this thesis. Typical units are given in brackets where relevant.

$C'(t)$	Mean of cross-correlation functions calculated for entire waveforms
$C'_s(t)$	Mean of cross-correlation functions for waveform segments
c	Speed of sound (m/s): approximately 1500 m/s in soft tissue; typically 1476 m/s in phantom experiments in this thesis
$\pm\Delta t'_s/2$	Measured time shift resolution (ns)
$\pm\Delta V'/2$	Measured velocity resolution (mm/s)
$\pm\delta t_s/2$	Known time shift resolution (ns)
$\pm\delta V/2$	Known velocity resolution (mm/s)
$\delta\bar{v}$	Average laminar flow velocity for a waveform segment (mm/s)
d_{D}	De-correlation distance (mm)
M	Number of data points in a waveform segment
$mean(V')_N$	Mean of N velocity measurements (mm/s)
μ_a	Absorption coefficient (mm^{-1})
m	Number of data points in the cross-correlation peak lobe
$p_1(t)$	First PA waveform in a pair
$p_1(t)$	Second PA waveform in a pair
Q	Flow rate (ml/hr)
R	Tube radius (μm)
Re	Reynolds number
R_{w}	Radial distance from the axle of the wheel phantom to the centre of the focal region of the transducer
$\pm std(V')_N$	Standard deviation of N velocity measurements i.e. velocity resolution (mm/s)
θ	Angle between transducer axis and flow direction (degrees)
T	Time separation between laser pulses (ms)
t_{P}	Time point at which a waveform segment appears in a PA signal (ns)
t_s	Known time shift (ns)
t'_s	Measured time shift (ns)
$\left\|t_{s,\max}\right\|$	Maximum measurable time shift (μs)
$\left\|t_{s,\max}\right\|_{\mathrm{obs}}$	Observed maximum measurable time shift (μs)
V	Known velocity (mm/s)
V'	Measured velocity (mm/s)
$\lvert V_{\max}\rvert$	Maximum measurable velocity (mm/s)
$\lvert V_{\max}\rvert_{\mathrm{obs}}$	Observed maximum measurable velocity (mm/s)
V'_n	The velocity measurement for a small waveform segment (mm/s)
$\bar{v}$	Average laminar flow velocity (mm/s)
$\hat{v}$	Maximum laminar flow velocity (mm/s)

Part I

Introduction

1

Introduction

This thesis was written to fulfil the requirements of the degree of Doctor of Philosophy at University College London. It was submitted to Prof. Wiendelt Steenbergen (University of Twente, Netherlands) and Dr. Jean-Martial Mari (UCL) who examined the author orally on Friday 20 December 2013. The examiners suggested minor corrections, which have been incorporated into this final version of the thesis.

The thesis presents work carried out in the Department of Medical Physics and Bioengineering at University College London (UCL) between September 2009 and November 2013. Unless otherwise stated, the work described is the author's own and is not the result of collaboration. The project was funded by the Engineering and Physical Sciences Research Council (EPSRC) through a four-year MRes/PhD doctoral training programme run between the UCL Centres for Medical Imaging Computing (CMIC) and Advanced Biomedical Imaging (CABI). The project supervisors were Prof. Paul Beard (UCL Department of Medical Physics and Bioengineering) and Prof. Barbara Pedley (UCL Cancer Institute).

The purpose of this opening chapter is to briefly introduce the motivation behind the project, to outline the principal goals, and then to detail the structure of the rest of the thesis.

1.1 Motivation

The long-term vision of this work is to develop a new blood flow method that can be applied *in vivo* at clinically useful depths in tissue. Such a method would, in particular, assist the diagnosis, understanding and treatment of different tumours. It would also be broadly applicable to many other clinical conditions, for example the detection and monitoring of circulation abnormalities resulting from Reynaud's syndrome, diabetes, atherosclerosis, and other vascular diseases, and the assessment of blood perfusion following skin grafts or burn treatment.

Measurement of blood flow in tumours is of significant interest since it will aid the development and refinement of new cancer therapies such as those based on Vascular Disrupting Agents (VDAs). VDAs work by inhibiting tumour blood flow, destroying the tumour blood vessels and creating regions of oxygen deficiency. Non-invasively monitoring these effects *in vivo* over time via measurements of tumour blood flow would elucidate how the therapies work, highlight the optimum treatment parameters, and inform the development of new treatments, whose efficacy can also be assessed.

There is currently no non-invasive flowmetry method ideally suited to studying blood flow in tumours. Doppler ultrasound is a well-established technique for measuring blood velocity, but it is limited to large vessels several millimetres in diameter; however tumour vessels have diameters ranging from 5-100 μm. Optical methods, such as Doppler optical coherence tomography, are more sensitive to small vessels since the contrast arises from haemoglobin in red blood cells. However, in most optical techniques the poor penetration of light in tissue limits the measurements to vessels less than approximately 1 mm below the skin surface.

Photoacoustic imaging is a new biomedical imaging technique that exploits laser-generated ultrasound waves, and thus combines the advantages of pure optical and pure ultrasound imaging modalities [15]. It derives optical contrast from haemoglobin, and enables 3D visualisation of blood vessels several centimetres deep into tissue on account of the relatively weak scattering of ultrasound compared to light. This makes the method well suited to imaging the tumour blood vessel structure, which aids tumour diagnosis, since the arrangement of blood vessels is characteristic of the

type of the tumour [69, 112] In addition, it has the potential to measure blood velocity using Doppler flowmetry techniques. This would be useful in its own right, for example to study the effect of VDAs as described above. However, there is also the potential to make measurements of blood oxygen saturation by varying the excitation laser wavelength and exploiting the known spectral differences between oxy- and deoxy-haemoglobin. Simultaneous measurement of blood flow and oxygen saturation would indicate which areas of the tumour are well-perfused with oxygen and nutrients; it would thus provide information relating to metabolism – a capability that no other modality can provide non-invasively without the use of contrast agents. The tumour metabolism is related to its aggressiveness, which frequently affects the choice of treatment. Repeated images and functional measurements would allow the effectiveness of the treatment to be monitored over time.

Several methods have been developed to measure the speed of blood flow using photoacoustics [90, 110, 118]. Essentially they all involve detecting the movement of red blood cells (RBCs) from the changes (such as time or frequency shifts) in the photoacoustic waves they emit. However, *in vivo* velocity measurements have so far only been achieved by focussing the laser light (the "optical resolution" mode); this achieves a penetration depth of less than approximately 1 mm, which strictly limits the pre-clinical and clinical utility. In contrast, measurements in the "acoustic resolution" mode have the potential to penetrate several centimetres into tissue, but *in vivo* flow measurements have not yet been achieved.

1.2 Aims of the project

The aim of the project was to explore a new photoacoustic Doppler method for measuring blood flow speed in the "acoustic resolution" mode. The method entails tracking the movement of red blood cells from the time shift in the photoacoustic signals they generate when illuminated with pulses of un-focussed laser light, and this is described in detail in Chapter 4. The idea was initially in the very early stages of development, and so the emphasis of the project was necessarily on developing the physics of the technique, and demonstrating its feasibility using laboratory experiments. The work culminating in this thesis entailed the fulfilment of the following key objectives:

(1) To identify and develop the most appropriate methods for signal excitation, data acquisition and signal processing;

(2) To identify, develop and evaluate the optimum experimental arrangement for practical implementation of the above methods;

(3) To develop tissue phantoms for experimental validation of the flowmetry method;

(4) To rigorously analyse the accuracy and resolution of velocity measurements made with tissue phantoms;

(5) To identify technical and methodological challenges that need to be addressed in order to apply the flowmetry technique *in vivo*.

This thesis makes some allusion to the work involved in meeting objectives (1)-(3), but the primary emphasis is on the work carried out to meet objectives (4) and (5).

1.3 Thesis structure

The thesis is divided into four parts.

The first part provides introductory material, and sets the project in context. Chapter 2 describes the nature of blood flow in vessels, and indicates its importance in cancer therapy. In Chapter 3, a comparison is made between existing methods for measuring blood flow speeds, and the need for a new flowmetry method is highlighted.

Part II of the thesis describes the methods used to experimentally validate the new, pulsed photoacoustic Doppler flowmetry method, and therefore relates to objectives (1)-(3). The principles of the flowmetry method are explained in Chapter 4, and Chapter 5 describes the experimental apparatus used, including the various tissue phantoms. The signal processing method is presented in Chapter 6.

The third and largest part of the thesis presents and analyses the results from the tissue phantom experiments and thus addresses objectives (4) and (5). The results in Chapter 7 are for idealised flow conditions achieved with a "wheel phantom", which permitted preliminary experimental validation of the flowmetry technique. Chapter 8 then describes measurements made with various fluid phantoms comprising absorbers flowing in a tube, which are more representative of flow in a blood vessel. Two main effects are observed, and these relate to the concentration of the flowing absorbers and to the diameter of the tube. The explanation for these effects necessitated an investigation into the fluid mechanics, and how the flow of absorbers translates into a measured velocity, and this is presented in Chapter 9: the theory is first explained by means of simplified simulations, and then a description is given of a new signal processing ("segmentation") method, which was subsequently applied to the velocity measurements. Potential limitations of the flowmetry technique are discussed in Chapter 10,

with particular reference to the transducers, laser(s) and oscilloscope used in the experimental setup. The benefits of filtering, interpolating and averaging the data are described.

The conclusions form the fourth part of the thesis. Summaries are given of the work involved in developing the methods in Part II and of the findings in Part III, which have so far resulted in four publications. Various suggestions are made for continuing with the work, and for applying the flowmetry technique *in vivo*, thereby addressing objective (5).

Finally, the thesis is appended with descriptions of methods used to characterise various ultrasound transducers in Appendix A, of different filter types in Appendix B, and of various relevant statistical measures in Appendix C. The bibliography beginning on page 238 is a full list of sources consulted and referred to in this work.

2

Background

2.1 Blood flow in microvasculature

Photoacoustic Doppler is envisaged primarily for the measurement of the low flow velocities in the microvasculature, not fast moving blood in the major arteries which is currently well served by alternative methods such as conventional pulsed wave Doppler ultrasound (see Chapter 3). The definition of vessels included in the microcirculation is somewhat arbitrary but generally includes arterioles, capillaries and venules, which have diameters less than 50 μm and mean flow velocities less than 50 mm/s. These values are several orders of magnitude smaller than the corresponding values for arteries and veins as shown in Table 2.1. In addition, the nature of flow varies from strongly pulsatile flow (for example, in the aorta and arteries) to almost stationary in the capillaries. This variation can be characterised using two dimensionless quantities – the Reynolds number Re, and the Womersley number α, which are defined by

$$\mathrm{Re} = \frac{D\bar{v}\rho}{\mu}, \tag{2.1}$$

and

$$\alpha = d\sqrt{\frac{2\pi f \rho}{\mu}}, \tag{2.2}$$

where D is the vessel diameter; $\bar{v}$, the mean flow velocity; ρ, the blood density; μ, the dynamic viscosity; and f is the frequency of pulsations. Reynolds numbers less than 2000 correspond to laminar flow, which exists in all but the very largest vessels. For $\alpha < 1$, the frequency of pulsations is sufficiently low for a parabolic (laminar) velocity profile to develop during each cycle, whereas for $\alpha > 10$, the velocity profile is relatively flat (plug-like flow). Therefore both the Reynolds numbers and the Womersley numbers indicate that the flow in the microcirculation is laminar and almost non-pulsatile.

This thesis initially presents velocity measurements made in plug flow conditions using a rotating wheel phantom, but the main results are for particles flowing in a laminar regime with low Reynolds numbers (see Section 8.5). The flow is also assumed to be non-pulsatile although the Womersley number is not considered explicitly.

Vessel	d (mm)	$\bar{v}$ (mm/s)	Re	α
Aorta	25	400	2500	260
Artery	4	450	450	40
Arteriole	0.05	50	0.5	0.5
Capillary	0.008	1	0.002	0.1
Venule	0.02	2	0.01	0.2
Vein	5	100	125	50
Vena cava	30	380	2800	310

Table 2.1: Reference values for mean velocity ($\bar{v}$), vessel diameter d, Reynolds number (Re) and Womersley number (α); adapted from [28, 103].

Red blood cells (RBCs) make an important contribution to the flow patterns in blood vessels. They have an average diameter of 7.5 μm [14] and form the main constituent of blood, with between 3.9×10^9 and 6.1×10^9 particles per millilitre [10, 11], which comprise approximately 45% of the total blood volume. In small arterioles and venules (10 to 25 μm in diameter) they flow in multi-file, migrating towards the vessel axis to leave a cell-free plasma layer that may skim off at branching points; in narrow capillaries (5 to 10 μm in diameter) the RBCs flow in single-file and may have to undergo deformation to squeeze through [74]. These effects are illustrated in Figure 2.1.

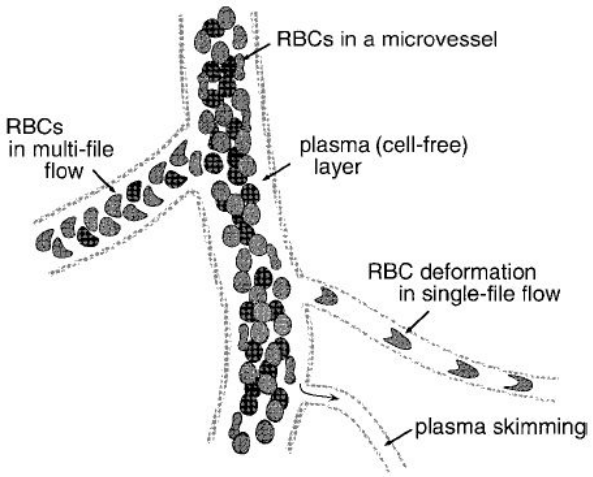

Figure 2.1: Blood flow structure in a microvascular region. (Taken from ref. [78]. Copyright The Physiological Society of Japan. Reproduced with permission.)

2.1.1 Blood flow in tumour vasculature

Accurate modelling of blood flow in microvessels is challenging, and even more so in tumour vasculature [65], which is typically tortuous and irregular, leading to chaotic and variable blood flow. In many tumours, the large inter-vascular distances and irregular vascular geometries lead to inadequate perfusion, and therefore regions of poor tissue oxygenation or *hypoxia*, which is illustrated in Figure 2.2. Hypoxia can increase the resistance of the tumour to therapy and can also cause alterations in gene expression of tumours, such as up-regulation of pro-angiogenic growth factors. Measurements of blood flow would provide an estimate for the amount of oxygen delivered to the tissue, and by simultaneously measuring oxygen uptake (perhaps in the form of tissue oxygen saturation, SO_2), measurements of metabolism could be obtained, serving as a marker of hypoxia.

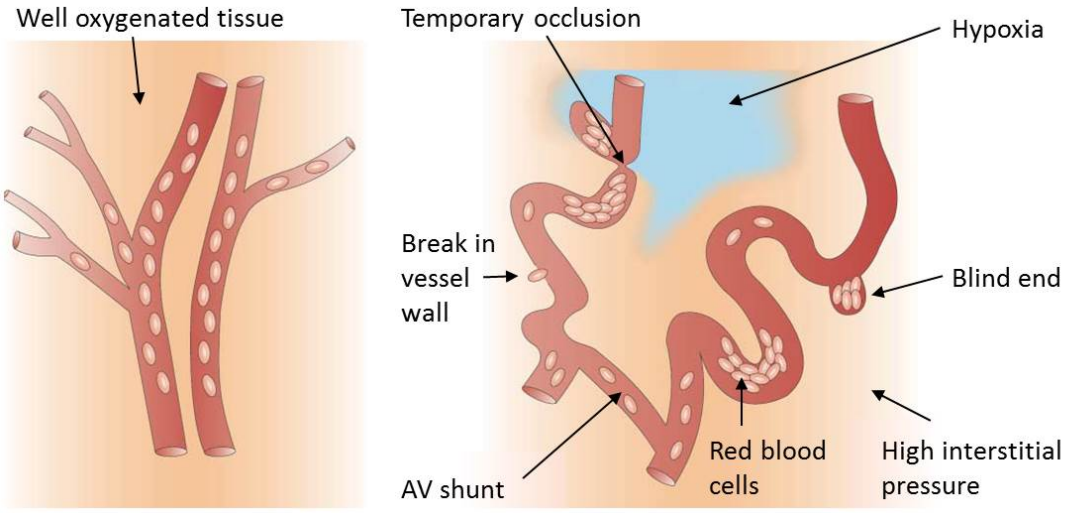

Figure 2.2: The vascular network of normal tissue (left) versus tumour tissue (right). The normal, regular vessel network results in well oxygenated tissue, whereas the irregularities in the tumour vasculature and flow create regions of hypoxia. (Adapted from ref. [21]. Copyright Nature Publishing Group. Reproduced with permission.)

2.2 Blood flow and cancer therapy

The spatial and temporal heterogeneity of tumour blood flow contributes directly to suboptimal drug distribution and therapy-resistant regions of tumour hypoxia; these effects are discussed briefly in the following sub-section. Sub-section 2.2.2 describes methods of vascular targeting and therapeutic modification of blood flow. These methods provide promising approaches towards inducing tumour cell death, particularly when combined with other more conventional cancer treatments.

2.2.1 Relevance of blood flow to anti-cancer therapies

Apart from surgery, which is the means of cure in about 50% of cured cancer cases [75], the most common forms of cancer treatment are radiotherapy and chemotherapy. Inadequate tumour perfusion can reduce the effectiveness of radiation therapy and chemotherapy, and this is partly explained by hypoxia-induced cell cycle arrest, among many other factors. In addition, chemotherapeutic and other drugs are dependent on tumour blood flow for efficient delivery. A technique that can interact synergistically with radiation or cytotoxic drugs is thermal therapy, or hyperthermia treatment, which is described in the final paragraph of this sub-section.

Radiotherapy

About 50-60% of cancer patients receive radiotherapy at some point during the course of their treatment, either alone or in combination with other treatment modalities [8, 43]. Radiotherapy uses high-energy radiation, such as x-rays, gamma-rays and charged particles, to induce irreparable DNA damage, which often leads to cell death. Cancer cells are principally affected due to their rapid proliferation, but in the absence of oxygen cells may temporarily cease to proliferate, and then rapidly re-grow during or after therapy once the micro-environmental conditions have improved. Therefore inadequate perfusion, resulting in large areas of hypoxic tissue, can increase radioresistance three-fold in comparison with cells which are well oxygenated at the time of irradiation [53, 56].

Chemotherapy

Chemotherapy uses drugs administered by various means including injecting, swallowing and rubbing into the skin; many drugs are designed to kill rapidly dividing cells, or cells with specific biomarkers relating to genetic alterations or defects of the patient's tumour. Certain chemotherapy agents may be more toxic to hypoxic cells, including bioreductive drugs, such as tirapazamine [79]; others, such as cisplatin, may only affect aerobic (oxygenated) cells. Any drug delivered intravenously must follow a multi-path route to reach the cancer cells, and this presents a number of physiological barriers [58] including the heterogeneous vessel network and blood flow.

Hyperthermia

In hyperthermia cancer treatments (also called "thermal therapy") a region affected by cancer is raised to temperatures around 40-45 °C (104-113 °F) [7, 85, 109]. The temperature increase is achieved by various methods [109] and is usually applied in conjunction with other treatments such as radiotherapy or chemotherapy. Even temperatures below 41 °C (106 °F) lead to thermosensitisation, whereby there is enhanced destruction of cells stressed by suboptimal metabolic environments (such as hypoxia) or in the process of repairing DNA damage.

In normal tissue the heat is dissipated by vasodilation, which can cause the blood flow to increase by as much as a factor of twenty. Tumour vessels are unable to consistently increase the blood flow in response to the temperature rise, which results in a perfusion and temperature difference between the normal and cancerous tissue. One problem with reduced tumour perfusion is that it can inhibit drug delivery and lead to an increase in hypoxia, which reduces the effectiveness of radiotherapy, although it

may benefit hypoxia targeted drugs. Upon initial heating there appears to be a transient increase in tumour blood flow, which could enhance drug delivery or radiation effects if administered at the appropriate time. It follows that effective hyperthermia treatment requires reliable measurements of flow and temperature, as well as a uniform heating method. In current practice, the temperature is monitored by means of probes inserted under CT (computerized tomography) guidance in the region of interest.

2.2.2 Therapeutic targeting of tumour vasculature

The concept of therapeutic targeting of tumour angiogenesis was first proposed by Judah Folkman in 1971 [45] but it was not until 1983 that Denekamp described tumour eradication by interruption of blood flow [34]. Vascular attack emerged as an anti-cancer therapy in 1990 [33] and there are currently many vascular-targeting molecules in clinical trials (see ref. [6] for a full list). They are usually used in combination with conventional therapies such as radiotherapy and chemotherapy.

Agents that target tumour vasculature can be divided into three classes based on their action:

- Anti-angiogenic molecules that inhibit tumour growth and "normalise" the blood vessels;
- Vascular disrupting agents that occlude blood vessels and inhibit flow resulting in tumour cell necrosis;
- Vasoactive agents that "hyper-abnormalise" the tumour vasculature.

Each of these classes are discussed respectively in the following three paragraphs.

Anti-angiogenic agents

Anti-angiogenic or angiogenesis-inhibiting agents (AIAs) are the most widely used strategies for tumour vasculature targeting. The aim is to alter the balance between stimulators and inhibitors of angiogenesis in favour of the latter, and thereby restore normal features in tumour vessels and inhibit the growth of new vessels, and subsequently the tumour [59]. This does not necessarily bring about tumour regression or necrosis [95], but it does improve blood circulation, leading to a temporary increase in oxygen and nutrient delivery and thereby making the cells more susceptible to therapeutic attack by radiation and/or drugs.

Vascular disrupting agents

Vascular disrupting agents cause blood vessel congestion and destruction, leading to extensive central tumour necrosis, an approach that contrasts the normalisation strategy employed by AIAs. Key differences between VDAs and AIAs are illustrated in Figure 2.3. The practical distinction is in the dosing strategy employed: AIAs are administered chronically (small doses over a long period) and VDAs acutely (often a single dose). However, individual agents may have both anti-angiogenic and anti-vascular effects.

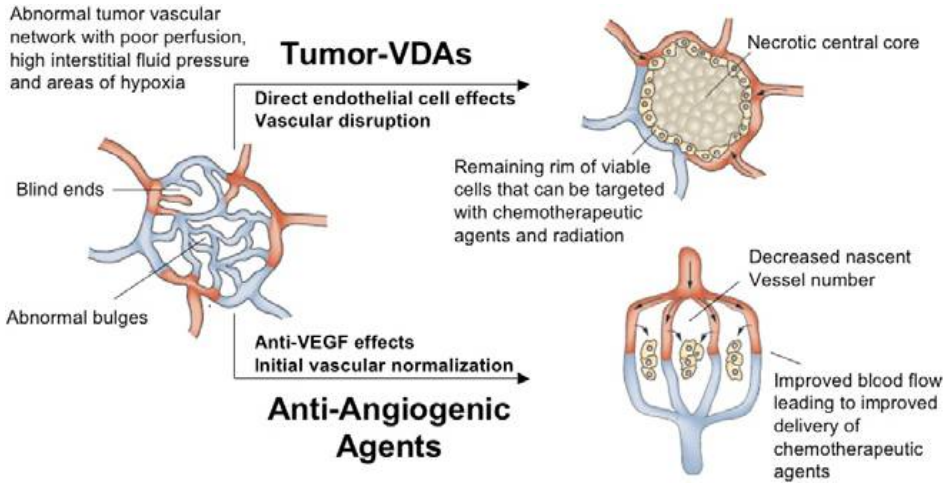

Figure 2.3: Illustration of the different pre-clinical effects of vascular disrupting agents and anti-angiogenic agents. (Taken from ref. [95]. Copyright Elsevier. Reproduced with permission.)

VDAs can cause an almost instant drop in tumour blood flow [102], and several possible mechanisms contributing to this flow shut-down are illustrated in Figure 2.4. The immature pericyte-defective nature of tumour vessels makes them particularly susceptible to attack by VDAs. Action of the drugs on the endothelial cell cytoskeleton can cause the cells to change in shape and "bleb" (bulge out of their membrane), which would increase vascular resistance and thereby reduce blood flow. Observations of fluid loss (*oedema*) and haemorrhage resulting from VDA treatment suggest that there is an increase in vascular permeability, leading to leakage of proteins out of the vessels, which increases the external pressure (the "interstitial fluid pressure", IFP) and also reduces blood flow. The slow flow resulting from the increased vascular resistance and increased IFP encourages RBC stacking (formation of rouleaux), which increases blood viscosity and further reduces flow. In tumour vessels, where flow is already heterogeneous and erratic, even a small flow reduction is likely to have a profound impact in terms of oxygen and nutrient delivery to cells already existing in

sub-optimal conditions. The effect on normal vessels, where the blood flow is regular and controllable, is likely to be much smaller.

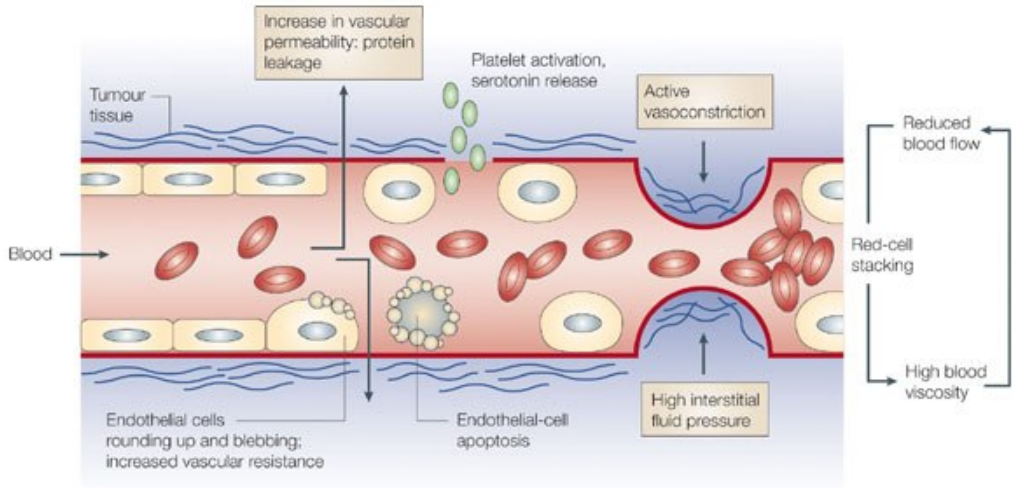

Figure 2.4: Possible mechanisms for rapid tumour vessel shut-down following treatment with Vascular Disrupting Agents. (Taken from ref. [101]. Copyright Nature Publishing Group. Reproduced with permission.)

VDAs are effective for killing about 90% of the tumour mass [44]. However, there typically remains a thin layer of viable tumour cells around the rim. This could be explained by better perfusion at the tumour periphery compared to the core, and close proximity to normal tissue where functioning vessels may be able to supply oxygen and nutrients via diffusion. The viable rim can lead to tumour re-growth, and so VDAs are only successful in halting tumour progression when used with conventional treatments. The blood flow reduction caused by VDAs can actually enhance the effect of drugs delivered intravenously by trapping them inside the tumour tissue: combretastatin A-4 phosphate (CA-4-P), a leading VDA, can improve the retention of targeted therapies (such as ^{131}Iodine-labelled antibodies) by over 70% [68], and administration of VDAs alongside chemotherapeutic agents such as cisplatin, paclitaxel and carboplatin can improve the dose by a factor more than thirteen [95] compared to administration of chemotherapy alone. VDAs can also be combined with bioreductive drugs [101] that are activated in the absence of oxygen. However, there still remains the risk of hypoxia-induced angiogenesis following VDA therapy. An additional concern is cardiotoxicity [44], which greatly limits the maximum safe dose.

Vasoactive agents

Vasoactive agents induce "hyper-abnormalisation" by causing vessel constriction or dilation, and vessel hyper-permeability. This strategy does not kill tumour cells and

therefore must be used in combination with cytotoxic therapies, for example doxorubican and melphalen (chemotherapeutics). In fact, the main purpose of the vasoactive agents is to assist drug delivery. A decrease in blood flow (vasoconstriction) increases tumour hypoxia in order to enhance the effect of anti-cancer agents targeting hypoxia; an increase in blood flow (vasodilation) reduces hypoxia and so enhances radiotherapy [85].

Vasoactive agents are very toxic when delivered systemically at effective doses. This necessitates the use of local administration or isolated limb perfusion, a technique in which the flow of blood to and from the limb is temporarily stopped with a tourniquet, and the drugs injected directly into the blood of the limb. An additional caveat is that tumour vessels often lack a contractile smooth muscle lining, which therefore renders vasoactive agents ineffective.

2.3 Further applications for blood flowmetry

The previous section discussed the role of blood flow in cancer therapy, which is of particular interest due to the prevalence of cancer in many different forms and the need to develop more effective treatments. However, it is worth noting that blood flow plays a critical role in the health of an individual in a wider sense, determining the onset and progression of a myriad of other clinical conditions. For example, degeneration of arterial walls leading to atherosclerosis commonly manifests as disruption of localised flow patterns [73], and blood flow abnormalities are also observed in diabetic patients due to increases in red blood cell aggregation and resistance to deformation [80]. Assessment of vascular and blood diseases requires blood flowmetry in localised tissue regions, but measurements of blood perfusion on a more global scale are also valuable, for example for the diagnosis and assessment of conditions such as Reynaud's syndrome [54] and for monitoring the success of skin grafts or burn treatment [96].

The following chapter describes current methods for measuring blood flow, with a particular emphasis on those involving ultrasound since, unlike other standard techniques such as MRI and CT, ultrasound and photoacoustic Doppler flowmetry do not involve the injection of contrast agents. Whilst Doppler ultrasound is only sensitive to flow in large blood vessels, photoacoustic Doppler methods have proved successful for measuring blood flow in microvessels using the so-called "optical resolution" mode. However, the limited penetration depth of less than 1 mm drives the development of the "acoustic resolution" mode of photoacoustic Doppler, which has the potential to penetrate several centimetres into tissue. The current spatial resolution of photoacoustic imaging tomography makes detection of flow in the smallest microves-

sels impractical in the acoustic resolution mode; however, it is envisaged that blood flow measurements could be made in vessels in the order of 100 μm. At the time of writing this thesis, the *in vivo* application of acoustic resolution photoacoustic Doppler flowmetry remains an aspiration, but has nonetheless formed the motivational force behind this work involving development of the method and demonstration of its feasibility.

3

Methods for measuring blood flow

Figure 3.1 illustrates the relative domains occupied by various imaging modalities in terms of resolution and sampling depth.

Magnetic resonance imaging (MRI), computerized tomography (CT) and ultrasound (US) imaging systems are already in widespread clinical use for relatively deep tissue imaging, and each have velocity measurement capabilities as additional features. MR-based flow methods [76] include phase contrast velocity MRI, time-of-flight MR angiography and contrast-enhanced MR-angiography, but these are currently expensive research tools with time-consuming image reconstruction that makes real-time flowmetry impractical. CT provides high-resolution anatomical images, but functional information is typically obtained by using CT in combination with positron emission tomography (PET) [27]: PET enables functional processes, including blood flow, to be monitored via injected radioactive tracers, but with only poor spatial resolution (several millimetres). The resolution and sampling depth of ultrasound imaging depends on the transducer operating frequency, with higher frequency ultrasound waves enabling improved image resolution at the expense of imaging depth. Doppler ultrasound is a well-documented technique that is used routinely in clinical practice [37]

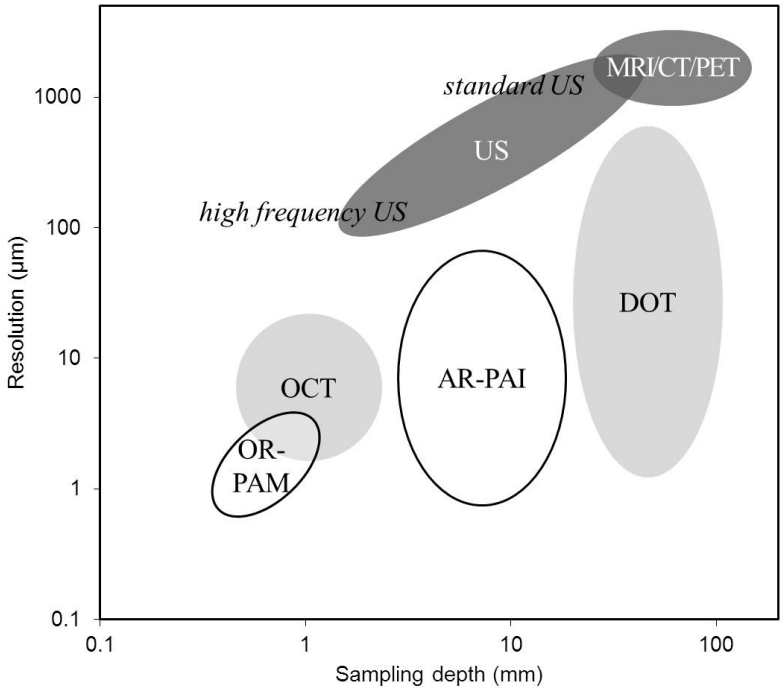

Figure 3.1: Illustration of the relative domains occupied by various imaging modalities in terms of resolution and sampling depth. AR-PAI: Acoustic Resolution Photoacoustic Imaging; CT: Computerized Tomography; DOT: Diffuse Optical Tomography; MRI: Magnetic Resonance Imaging; OCT: Optical Coherence Tomography; OR-PAM: Optical Resolution Photoacoustic Microscopy; PET: Positron Emission Tomography; US: Ultrasound. (Adapted from ref. [32]. Copyright Wiley-VCH Verlag GmbH & Co. KGaA. Reproduced with permission.)

and is discussed further below and in section 3.1.

Optical imaging modalities can provide spatial resolution values of a few micrometres, but they are limited by the light penetration depth in tissue. In methods such as confocal microscopy, two-photon microscopy and optical coherence tomography (OCT), where light photons undergo few scattering events, the penetration is limited to depths less than approximately 1 mm [107]. Diffuse optical tomography (DOT) is based on multiple-scattered photons and can provide functional and molecular imaging at depths of several centimetres but the spatial resolution and signal-to-noise ratio (SNR) are poor due to the strong optical scattering coefficient in tissue.

Photoacoustic imaging employs laser generated ultrasound – the Photoacoustic Effect [17] – to produce optical absorption based images of soft tissues [15]. As with pure optical imaging methods, it provides endogenous image contrast due to the strong optical absorption of haemoglobin at visible and near-infrared wavelengths, and this makes photoacoustic imaging well suited to providing images of vascular anatomy [69, 115, 116, 117]. Photacoustic imaging can be employed in the so-called optical resolution microscopy mode (OR-PAM), which achieves penetration depths comparable to pure optical imaging modalities. However, the so-called acoustic resolution (AR) mode is of greater clinical interest since the spatial resolution is enhanced at significantly greater penetration depths on account of the weaker ultrasonic scattering compared to optical scattering in tissue.

Photoacoustic flow measurements can be made in a manner analogous to conventional pulse-echo Doppler ultrasound – that is to say by recovering the Doppler frequency, phase or time shift encoded on to photoacoustic waves emitted by moving red blood cells. Unlike Doppler ultrasound, however, the detected acoustic signal is emitted by the blood cells as opposed to being weakly reflected from them. This offers significant SNR advantages especially when measuring flow in microvessels as these exhibit low echogenicity. Furthermore, Doppler ultrasound measurements of the relatively low flow velocity (< 50 mm/s) in microvessels can be corrupted by the much larger backscattered signal from the surrounding tissue which can move at comparable speeds due to respiratory or cardiac motion. In photoacoustic Doppler flowmetry this is likely to be less problematic due to the strong optical absorption of blood compared to that of the vessel wall and surrounding tissue. For these reasons, photoacoustic Doppler is envisaged primarily for the measurement of slow blood flow in microvasculature, not fast moving blood in the major arteries, which is currently well served by conventional Doppler ultrasound.

3.1 Doppler ultrasound

In Doppler ultrasound [37], the velocity of blood flow v is derived from the Doppler frequency shift Δf in ultrasound waves that are scattered from moving red blood cells:

$$v = \frac{\Delta f\, c}{2 f \cos\theta}, \tag{3.1}$$

where f is the transmitted frequency, c is the speed of sound, and θ is the angle between the axis of beam propagation and the direction of flow. In continuous-wave (CW) Doppler systems the transmitted ultrasound wave is narrowband enabling accurate measurement of small Doppler shifts, which typically occur at frequencies on the order of kHz, which are less than 0.1% of the transmitted frequencies (MHz). The received signal has a frequency $f + \Delta f$, and Δf is extracted using one of several possible demodulation methods: the simplest of these involves multiplying and filtering the transmitted and received signals, which determines the magnitude of Δf; to also discriminate flow direction, either heterodyne demodulation or quadrature-phase demodulation are used. Continuous-wave Doppler ultrasound does not suffer from an upper velocity limit, but seeing as ultrasound is transmitted continuously, it does not provide depth resolution.

When studying flow in deep-lying vessels, it is common to employ pulse-echo Doppler ultrasound, which entails transmission of short ultrasound pulses (pulse repetition frequency, PRF) and discrete sampling of the Doppler signal at intervals $T = 1/\mathrm{PRF}$. This enables velocity measurements at different depths, and the received signal can be time-gated to select the depth range of interest. The frequency of the received signal is shifted by Δf as in CW Doppler ultrasound, but this shift is measured indirectly via the time rate of change of phase. The choice of PRF is a compromise between the maximum measurable velocity $v_{\max}$ and the maximum acquisition depth $D_{\max}$:

$$v_{\max} = \frac{c\,\mathrm{PRF}}{4f}; \tag{3.2}$$

$$D_{\max} < \frac{c}{2\,\mathrm{PRF}}. \tag{3.3}$$

3.2 Photoacoustic flowmetry methods

The basic principles of photoacoustic Doppler flowmetry were first outlined over a decade ago [16]. Subsequently, photoacoustic measurements of flow in a tissue mimicking phantom were obtained by recovering Doppler frequency shifts using CW excitation [40, 41, 42]. However, in common with CW Doppler ultrasound, this approach cannot readily provide depth-resolved measurements. The use of pulsed excitation

overcomes this limitation and with this in mind a number of signal processing schemes have now been demonstrated as described in sub-sections 3.2.1 to 3.2.3 [15, 25]. Subsection 3.2.4 describes a newly-developed method whereby flow is measured indirectly via thermal diffusion.

3.2.1 Tone-burst excitation and spectral analysis

Sheinfeld et al. [90, 91, 92] describe a frequency-domain method that employs narrowband tone-burst excitation and a spectral analysis of the resulting photoacoustic waves in order to recover the Doppler frequency shifts. As with most spatially resolved Doppler flowmetry schemes, there is inevitably a velocity-spatial resolution compromise: a long-duration tone burst provides high spectral and therefore velocity resolution but at the cost of spatial resolution. For example, in one study [91], a tone burst duration of 3 μs was used providing a velocity resolution of 1.5 mm/s but a relatively low depth resolution of 4.5 mm. Moreover, although this study used a laser source emitting over a wavelength range of 1530 nm - 1565 nm to demonstrate the concept in a phantom, the limited availability of quasi-CW-modulated laser sources with sufficient output power at wavelengths that provide adequate penetration depth in tissue (i.e., wavelengths <900 nm) may present a practical limitation.

3.2.2 Bandwidth broadening

Yao et al. [110, 113] describe a pulsed time-domain approach for estimating the acoustic bandwidth broadening arising from the frequency difference between the extremities of a wavefront emitted by a target moving orthogonal to the axis of a focused transducer. This approach relies upon delivering a number of laser pulses to the tissue and recording the motion-induced fluctuations in the magnitude of the corresponding photoacoustic waveforms at a specific point in their time records. This discretely sampled time varying signal can then be used to estimate the velocity by computing its autocorrelation function in a manner analogous to autocorrelation based velocity estimation methods employed in colour flow ultrasound imaging [39, 60, 61]. This approach has successfully been used to measure blood flow with sub-mm/s velocity resolution in the microvasculature *in vivo* and also combined with measurements of other physiological parameters (including oxygen saturation) to give an estimate of the rate of oxygen consumption [104, 111], which is an impressive feat. However, it was achieved by deploying the "optical resolution" mode of photoacoustic sensing, and is therefore limited to a maximum penetration depth of approximately 1 mm due to the resolution degrading effects of the strong optical scattering exhibited by tissue. The method has yet to be demonstrated using the more general mode of photoacoustic

sensing in which localization is acoustically defined and which provides much greater penetration depths.

3.2.3 Time correlation methods

A variant of the above method, so-called photoacoustic correlation spectroscopy, has also been demonstrated in phantoms [29] and *in vivo* [30], again in optical resolution mode. This approach exploits the velocity dependent decay in photoacoustic signal amplitude that occurs as a group of absorbers moves across the field-of-view of the ultrasound receiver.

Another correlation-based flowmetry method makes use of a digital micromirror device (DMD) to illuminate the target with two light beams separated in both space and time. A number of laser pulses are delivered to the target and photoacoustic profiles obtained at the two illumination positions. These profiles are found from the motion-induced magnitude variations of the corresponding photoacoustic waveforms at a specific point in their time records, as in the bandwidth broadening method (subsection 3.2.2), and are cross-correlated in order to obtain time shift measurements from which the flow velocity of the absorbers is calculated. The minimum measurable velocity (resolution) is limited by the spatial separation d between the illuminations [71]. Using $d = 5$ μm, a resolution of 0.11 mm/s was obtained for superficial vessels *in vivo* [118], but is unlikely to be achieved for deeper vessels where multiple light scattering would make it difficult to resolve the closely-spaced illumination beams. Thus, again, this method is more suitable for implementation in the microscopy mode of photoacoustic imaging [72].

This thesis describes a different Doppler flowmetry approach based upon time correlation signal processing. This method is inspired by time correlation ultrasound flowmetry [20, 51, 52] and relies upon measuring the change in the time-of-arrival of successive photoacoustic waves emitted by a moving cluster of red blood cells under pulsed excitation using the cross-correlation function. It has the advantage that, by using short (nanosecond) laser pulses, it offers depth-resolved measurements with high spatial resolution and can employ the type of readily available pulsed Q-switched lasers used routinely in photoacoustic tissue imaging. It is also an inherently flexible approach. Velocity range and resolution are scalable with excitation pulse separation allowing it to be optimized for a wide range of physiologically realistic flow velocities. It also lends itself to both the acoustic and optical resolution modes of photoacoustic sensing enabling measurements to be made over the spatial scales of both modes.

Absorber heterogeneity

It is widely considered that the challenge in making acoustic resolution velocity measurements in blood relates to its optical heterogeneity and the ability to resolve this using a finite detector bandwidth. This is not a problem in the optical resolution mode, since the excitation spot is only a few micrometres in diameter and is therefore comparable to that of a single RBC, allowing the spatial heterogeneity in the optical absorption of blood to be resolved directly. However, in the acoustic resolution mode, where localization is achieved using the ultrasound transducer focus rather than the laser excitation beam, it is supposed that the spatial resolution is limited by the minimum detectable acoustic wavelength. Spatial separations of the order of 7.5 μm (a typical RBC diameter) correspond to ultrasound frequencies of 200 MHz (sound speed in tissue $\approx$ 1500 m/s), and therefore blood may appear spatially homogeneous using standard PZT ultrasound detectors, which typically have bandwidths of a few tens of MHz centred at frequencies less than 50 MHz. This may compromise the ability of time correlation methods to make blood velocity measurements.

The frequency content of PA signals depends on the size of the absorbers [35], and this is one reason why the heterogeneity limitation to acoustic resolution flowmetry is widely accepted. However, there are several long-standing experimental anomalies that leave the issue open to speculation. Prime examples are the successes of pulsed wave Doppler ultrasound [37] and cross-correlation pulse-echo ultrasound measurements of blood flow [52], although it is arguable that ultrasound scattering methods are assisted by the presence of speckle, which is not visible in photoacoustic imaging. However, studies of RBC aggregation have shown that, whilst changes in PA signals due to the spatial organisation of the cells are most significant for frequencies greater than 100 MHz [98], there are also detectable changes at frequencies less than 20 MHz [47, 55]. The results presented in this thesis add further weight to the evidence that spatial heterogeneity is *not* such a stringent limitation to acoustic resolution flowmetry as is commonly supposed, and this is a novel contribution to the field.

3.2.4 Thermal diffusion flowmetry

Recently, Sheinfeld and Eyal introduced so-called photoacoustic thermal diffusion flowmetry [88], which entails measuring flow speed from the temperature-dependent decay of PA signal amplitude due to thermal transfer. The method was demonstrated in phantoms using two 830 nm laser diodes, one inducing photothermal heating and the other tone-burst PA excitation [89]. A variant of this method employs high-intensity focussed ultrasound (HIFU) heating, which enables better confinement of the heated volume compared to the photothermal method, and has also been demonstrated in

phantoms at depths of several millimetres [105, 106].

Thermal diffusion flowmetry, regardless of the heating method, does not require optical heterogeneity of the absorbers since the contrast is derived from temperature-induced changes in the photoacoustic signals, rather than variation due to optical absorption. However, since the flow is measured indirectly via thermal transfer, calibration is required for absolute velocity measurements.

3.3 Other correlation-based techniques

This section briefly highlights some instances where time-domain cross-correlation methods are applied in flowmetry techniques other than those employing the Photoacoustic Effect.

The "gold standard" for capillary imaging involves video-monitoring systems comprising a video camera attached to an optical microscope. The transit time for individual red blood cells moving from one point to another can be measured from the cross-correlation of optical signals acquired at each point [32, 99]. This enables measurement of RBC velocity but is limited to only very superficial penetration depths.

Particle image velocimetry (PIV) is a method that involves visualising flow via the random pattern of tracer particles in consecutive digital images. The particle displacements are calculated by means of a two-dimensional cross-correlation [62]. This method has been applied to optical images with a spatial resolution in the order of 1 μm, and to ultrasound images with a resolution of approximately 100 μm, but is associated with certain limitations such as directional ambiguity [32, 103].

Scanning laser imaging correlation (SLIC) involves tracing a laser beam along or across the flow direction rapidly with respect to the particle motion and detecting fluctuations in the reflected light. The particle velocities are extracted from cross-correlations calculated for multiple pairs of signals acquired at different spatial locations [84]. SLIC has been used to obtain information about the direction and pattern of flow in vasculature in zebra fish embryos, but is impractical for deep tissue imaging.

3.4 A note on the use of the term "Doppler"

The Doppler effect, named after the Austrian physicist Christian Johann Doppler, is the apparent change in the observed frequency of a wave due to relative motion between the source and the observer. The time-domain cross-correlation technique

described in this thesis does not strictly measure a Doppler frequency shift, but, in common with other authors [91, 97, 113] in the field, the term "Doppler" is applied in a more generic sense.

The term "Doppler" is used equally loosely in ultrasound flowmetry as it is in photoacoustics; it is true that CW Doppler ultrasound involves measurement of a frequency shift, but in pulse-echo Doppler ultrasound the frequency shift is usually measured indirectly from the rate of change of phase in the received signal. This phase change arises from progressive time shifts of the received signal with respect to the transmitted pulse, and therefore is arguably not a "Doppler" effect at all [38] – despite the fact that the recovered frequency shift is almost identical to the "classical" Doppler shift detected in a CW system.

In the method described in this thesis, it would be possible to construe the measured time shift in terms of the time-varying amplitude, or the rate of change of phase, as in pulse-echo Doppler ultrasound. Therefore, the photoacoustic method is equally deserving of the term "Doppler", which is moreover clarified by the phrase "time-domain", as in the title of this thesis. In fact, the work is closely parallel to that described in one of the original publications [20] involving time-domain cross-correlation of pulse-echo Doppler ultrasound signals, referred to by the authors as a "time-domain formulation of pulse-Doppler ultrasound... by cross-correlation".

The following part of the thesis describes, in Chapter 4, the principles of the new photoacoustic Doppler flowmetry approach that was outlined briefly in sub-section 3.2.3, and then the experimental methods (Chapter 5) and signal processing protocols (Chapter 6) used to validate this method. In the first instance, the experiments were designed to demonstrate the idea that the velocity of moving absorbers can be measured from the time shifts in the photoacoustic waves they emit. This provides a basis for further, more tissue-realistic studies, and eventually *in vivo* applications to the medical cases described in Chapter 2.

Part II

Experimental methods

4

Principles of pulsed photoacoustic Doppler flowmetry

This chapter describes the theory of the pulsed photoacoustic Doppler flowmetry technique, which is implemented using time correlation signal processing as described in Chapter 6.

Figure 4.1 shows a schematic that illustrates the concept. A sample of tissue is irradiated with a wide field pulsed laser beam. Photoacoustic waves are emitted predominantly by the red blood cells (RBCs) within a subsurface blood vessel and detected by a directional ultrasound detector located on the tissue surface. Since an extended region of the tissue is illuminated due to the diffuse nature of light transport in tissue, the dimensions of the focal beam of the detector, rather than the illuminated volume, define the region over which the signals are collected and hence the lateral spatial resolution – the so-called acoustic resolution mode of photoacoustics. This is in contrast to previous flowmetry methods [30, 87, 110], which employ the optical resolution mode of photoacoustic microscopy and are thereby limited to sub-millimetre penetration depths.

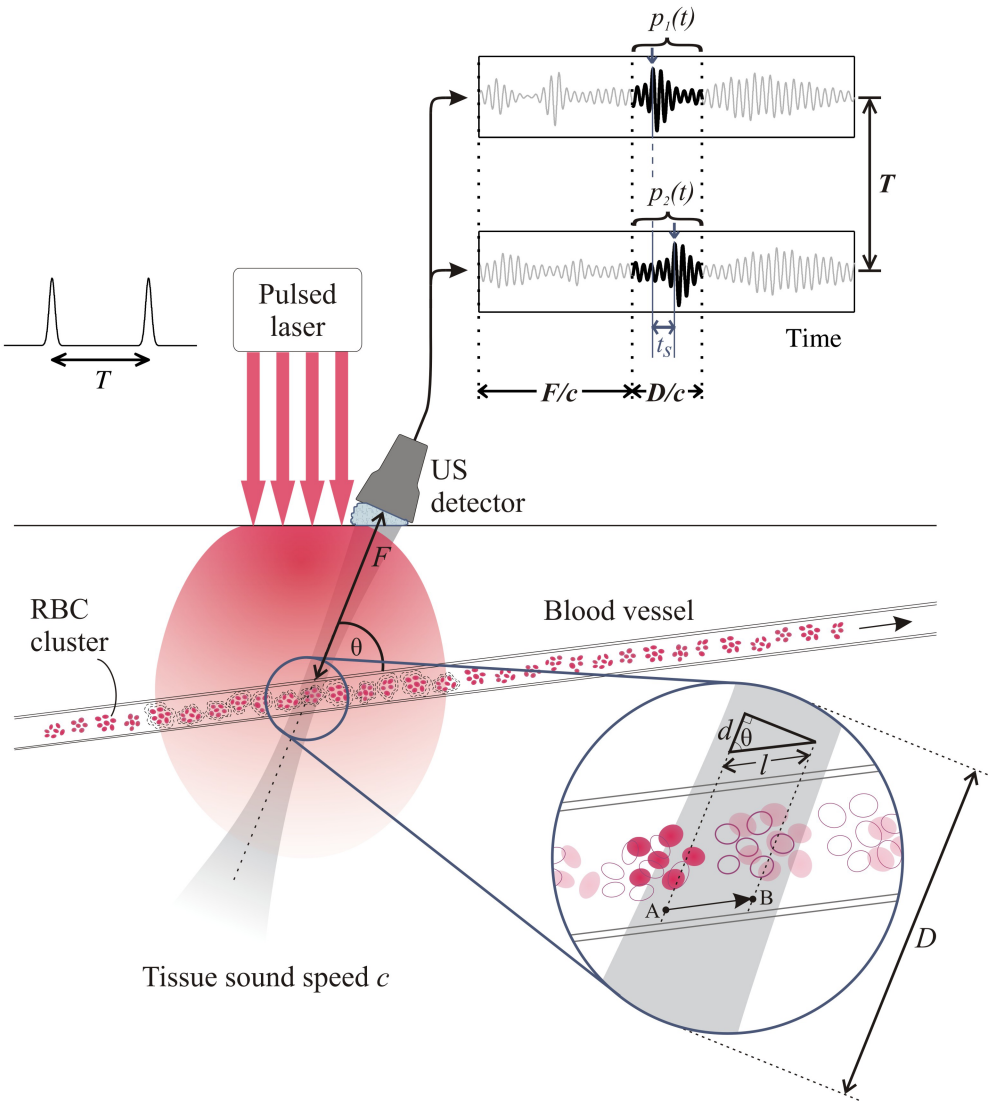

Figure 4.1: Schematic showing the detection of time-shifted photoacoustic signals. The two signals are generated from clusters of moving red blood cells (RBCs) when illuminated by a pair of laser pulses separated by a time T. The inset shows the distribution of RBCs (represented by solid ellipses) when the first laser pulse is fired, and the new positions (unfilled ellipses) coincident with the firing of the second laser pulse a time T later. Between the two pulses the cells have moved from A to B, a distance l along the blood vessel. The waveforms show segments of the two photoacoustic signals $p_1(t)$ and $p_2(t)$ that correspond to the location of the blood vessel and illustrate the time shift t_s between the two due to the motion of the RBCs.

In order to measure the flow of blood within a vessel as depicted in Figure 4.1, two assumptions about the spatial heterogeneity of blood are made. First, that it is composed of an ensemble of randomly distributed clusters of RBCs and second, that the density and orientation of RBCs within each cluster is also random. Thus, when irradiated with a laser pulse, a given cluster will emit a unique photoacoustic signature. By delivering a train of laser pulses and recording this signature over time, the motion of the cluster can be tracked at discrete time intervals as it progresses along the vessel. In its simplest form, this requires using two laser pulses, separated by a time T, to acquire a pair of photoacoustic waveforms that are identical in shape but shifted in time with respect to each other due to the motion of the RBC cluster. By cross-correlating these waveforms, the time shift between them can be obtained in order to estimate the velocity. In practice, this is achieved by delivering the first laser pulse, recording the resulting photoacoustic waveform and selecting a short time segment $p_1(t)$ that corresponds to the depth at which the blood vessel lies. The length of the time segment is proportional to the length D – the range gate – which determines the axial spatial resolution. The second laser pulse is emitted at a time T later during which the RBC cluster will have moved along the vessel thus altering the distance the photoacoustic waves will have travelled to the detector. The detected signal $p_2(t)$ due to the second laser pulse will therefore be a time-shifted replica of the first, assuming that during time T the RBC cluster has neither completely moved out of the focal beam of the detector nor undergone significant changes in its geometry or density which would alter its photoacoustic signature. In other words, the two signals must not have become completely decorrelated over time T. The velocity is then obtained from the time shift t_s between $p_1(t)$ and $p_2(t)$ as follows:

$$t_s = \frac{d}{c}, \tag{4.1}$$

where $d = l\cos\theta$ is the distance the RBC cluster has moved in the direction of a vector connecting the sample volume to the receiver, c is the speed of sound in the medium and θ is the angle between the direction of motion and the axis of the transducer receive beam. The velocity V of the RBC cluster is given by

$$V = \frac{l}{T}, \tag{4.2}$$

which, using Equation 4.1, can then be written

$$V = \frac{ct_s}{T\cos\theta}. \tag{4.3}$$

This is analogous to the classical Doppler frequency equation (3.1) derived for a moving sound source except that the velocity is now proportional to a fractional time shift rather than a fractional frequency shift.

The cross-correlation function can be used to determine the time shift t_s between the two photoacoustic waveforms $p_1(t)$ and $p_2(t)$. For continuous functions the cross-correlation is defined as:

$$(p_1 \star p_2)(t) = \int_{-\infty}^{\infty} p_1^* p_2(t+\tau) d\tau \tag{4.4}$$

where p_1^* is the complex conjugate of p_1.

Discretely sampled signals $\mathbf{p_1}_n$ and $\mathbf{p_2}_n$ are related to their continuous counterparts as follows:

$$\mathbf{p_1}_n \equiv p_1(t)|_{t=n\Delta t} \tag{4.5}$$

$$\mathbf{p_2}_n \equiv p_2(t)|_{t=n\Delta t} \tag{4.6}$$

for sample spacing Δt, and where $n = 0,\ldots,N-1$. For these discrete N-length vectors, an estimate of the cross-correlation function is given by

$$\hat{R}_{\mathbf{p_1}\mathbf{p_2}}(m) = \begin{cases} \frac{1}{N-|m|} \sum_{n=0}^{N-m-1} \mathbf{p_1}_{(n+m)} \mathbf{p}^*_{2n} & m \geq 0 \\ \hat{R}^*_{\mathbf{p_2}\mathbf{p_1}}(-m) & m < 0. \end{cases} \tag{4.7}$$

The normalisation factor $1/(N-|m|)$ produces an output vector $c(m) = \hat{R}(m-N), m = 1,\ldots,2N-1$, that is unbiased, avoiding the zero bias inherent in the standard cross-correlation function [4].

Although for illustrative purposes, only a single blood vessel is shown in Figure 4.1, in reality, there will be a number of vessels at different depths within the detector field-of-view. The blood flow in each of these can be ascertained by advancing the range gate along the time records of the two photoacoustic waveforms, computing the cross-correlation at each temporal position to obtain the time shift and using Equation 4.3 to obtain V. In this way a depth profile of velocity along the transducer line-of-sight can be obtained revealing flow wherever it is present. Ultimately it would be possible to acquire velocity depth profiles at different lateral positions, for example by scanning the transducer along and/or across the tissue surface, and thus form two-, three- and even four-dimensional images of blood flow. However, the experimental setups described in the following chapter were designed purely to demonstrate the principles of pulsed photoacoustic Doppler flowmetry in the first instance, and to identify any methodological challenges that would need to be addressed before the method could be applied *in vivo*.

5

Experimental designs

In order to demonstrate the pulsed photoacoustic Doppler flowmetry technique, a phantom comprising micron-scale absorbers was used to simulate the motion of red blood cells. A region of the phantom was excited with pairs of laser pulses separated by a time T. Light absorbing particles within the target area emitted a photoacoustic wave each time they were illuminated and these waves were detected using an ultrasound transducer and acquired using an oscilloscope.

Figure 5.1 shows the three principal experimental setups used to demonstrate the technique. The initial studies used a rotating wheel phantom in a setup illustrated in Figure 5.1(a). The wheel provided simple, linear motion ("plug flow") of absorbing clusters and therefore enabled the photoacoustic correlation method to be tested in the most straightforward case. In subsequent studies, the wheel phantom was replaced with a fluid phantom, as illustrated in Figure 5.1(b), which provided non-plug flow with low Reynolds numbers (see Equation 2.1, page 43). The de-correlation observed in the results (see Section 8.1) was attributed to differences in the beam profiles produced by two different lasers, and therefore further experiments used a single laser instead: this setup is illustrated in Figure 5.1(c), but apart from the illumina-

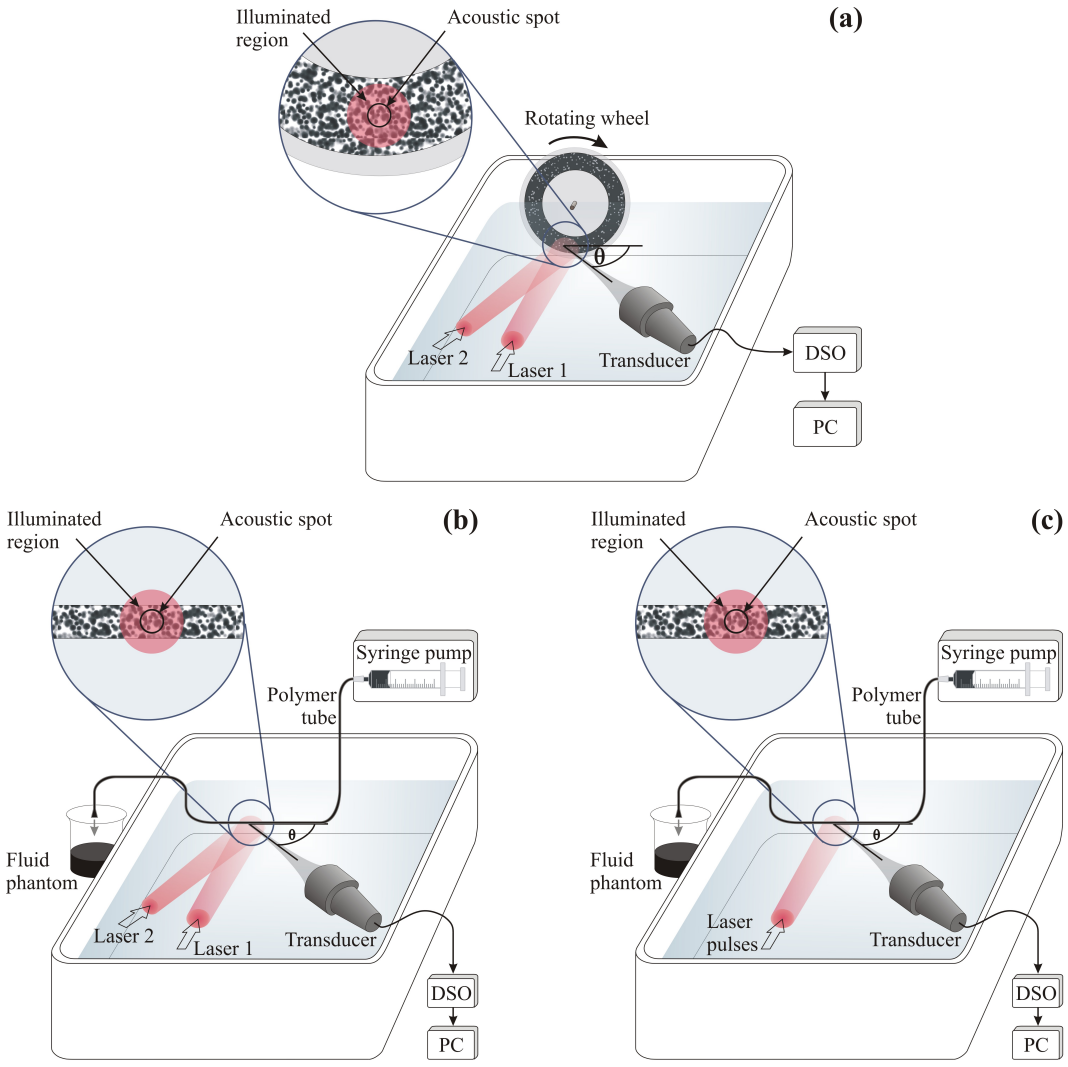

Figure 5.1: Experimental setups for pulsed photoacoustic Doppler flow measurement where the motion of micron-scale absorbers is used to represent blood flow. (a) Absorbers imprinted on to the rim of a rotating wheel; (b,c) Absorbers in a fluid suspension moving through an optically transparent polymer tube. In each case the phantoms are illuminated with pairs of laser pulses. In (a) and (b) the first pulse in each pair is emitted by laser 1 and the second by laser 2; in (c) both pulses arrive from the same laser source. The laser pulses are used to generate a pair of acoustic waveforms which are detected by an ultrasound receiver. The insets show typical distributions of the micron-scale absorbers. A large area (at least 2 cm diameter) of the absorbers is illuminated, but photoacoustic signals are only collected from the smaller region defined by the transducer focal spot. The signals were captured by an oscilloscope (DSO) and downloaded to a PC.

tion scheme it is identical to that in Figure 5.1(b). Further details of the phantoms, the lasers and the ultrasound transducers are discussed in Sections 5.1, 5.2 and 5.3 respectively.

5.1 Phantoms

The two types of blood-simulating phantom were the rotating wheel [Figure 5.1(a)] and the various different fluids used in the setups in Figure 5.1(b) and Figure 5.1(c). Optical microscopy images of the absorbers in each phantom are shown in Figure 5.2. The scale bars are only approximate, but it is clear that, for the phantoms shown in (a), (c), (d) and (e), the "particle" diameters are comparable to those of red blood cells (g), which *in vivo* are on average 7.5 μm [14]. The largest carbon microspheres (b) are about three times larger than RBCs, whereas the smaller polystyrene microspheres (f) are about three times smaller. The range of diameters within each sample of the carbon microspheres (b)-(d) is evidently much greater than that for the polystyrene microspheres (e) and (f) for which the coefficients of variation are specified to be $\leq 10\%$ and $\leq 1\%$ respectively. The bar graph below the photographs in Figure 5.2 shows that the concentrations of the suspensions were all less than a physiologically realistic RBC count. For a normal blood sample, such as that shown in Figure 5.2(g), there are between 3.9×10^9 and 6.1×10^9 particles per millilitre [10, 11], which typically account for a haematocrit of approximately 0.45 (volume of RBCs relative to the total blood volume).

5.1.1 Rotating wheel phantom

The wheel phantom comprises a Perspex disc mounted on the axle of a DC electric motor the speed of which was continuously adjustable. The disc is overlaid with a sheet of acetate imprinted around its rim with a non-uniform, random pattern of light-absorbing micron-scale dots, as shown in Figure 5.1(a) and Figure 5.2. Illumination of a region (about 2 cm in diameter) near the edge of the disc allowed the rotary motion of the dots ("particles") to be approximated over short distances to linear flow.

Figure 5.3 illustrates further details of the experimental setup in Figure 5.1(a). The angular velocity ω of the wheel phantom was measured by using the spokes of a wheel (thirty spokes in total) mounted behind the Perspex disc to form a chopper that periodically intercepted a beam of light between an LED and a photodiode (P2):

$$\omega = \frac{2\pi}{30 \times P}, \tag{5.1}$$

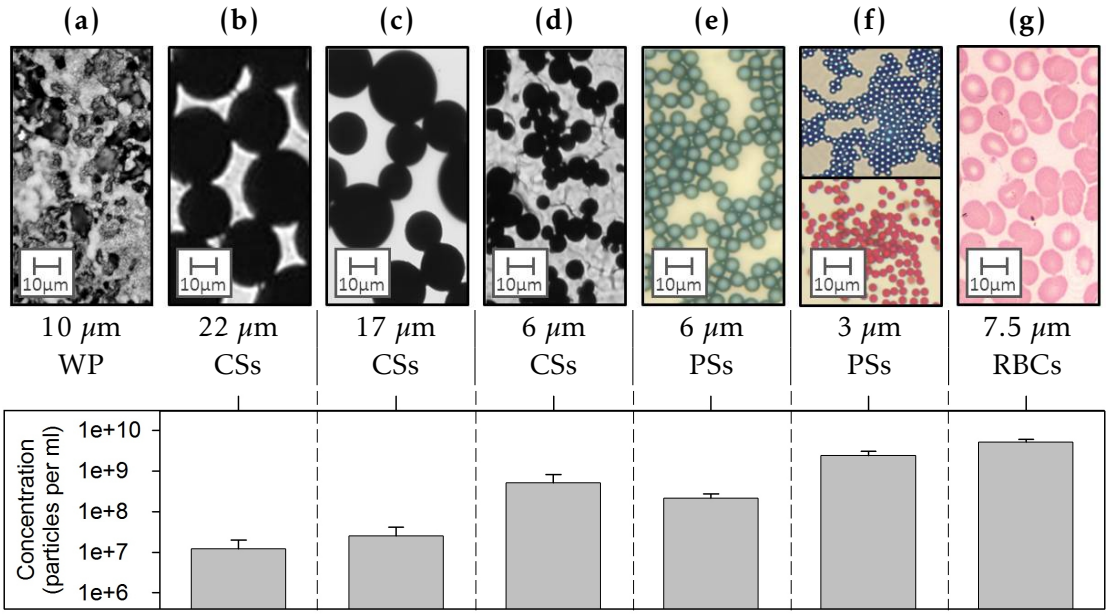

Figure 5.2: Comparison of optical microscopy images showing sizes of absorbers in the various phantoms. The average particle diameter is given under each image, and the bar graph below indicates approximate values for the concentration of particles in each of the fluids. (a) Wheel phantom (WP): micron-scale dots printed onto an acetate sheet; (b) Carbon microspheres (CSs), 22 μm; (c) Carbon microspheres (CSs), 17 μm; (d) Carbon microspheres (CSs), 6 μm; (e) Black polystyrene microspheres (PSs), 6 μm; (f) Blue (top) and red (bottom) polystyrene microspheres (PSs), 3 μm; (g) Red blood cells (RBCs) [9]. A few experiments, such as that in sub-section 10.3.1, used carbon microspheres larger than those in (b), but these are not shown.

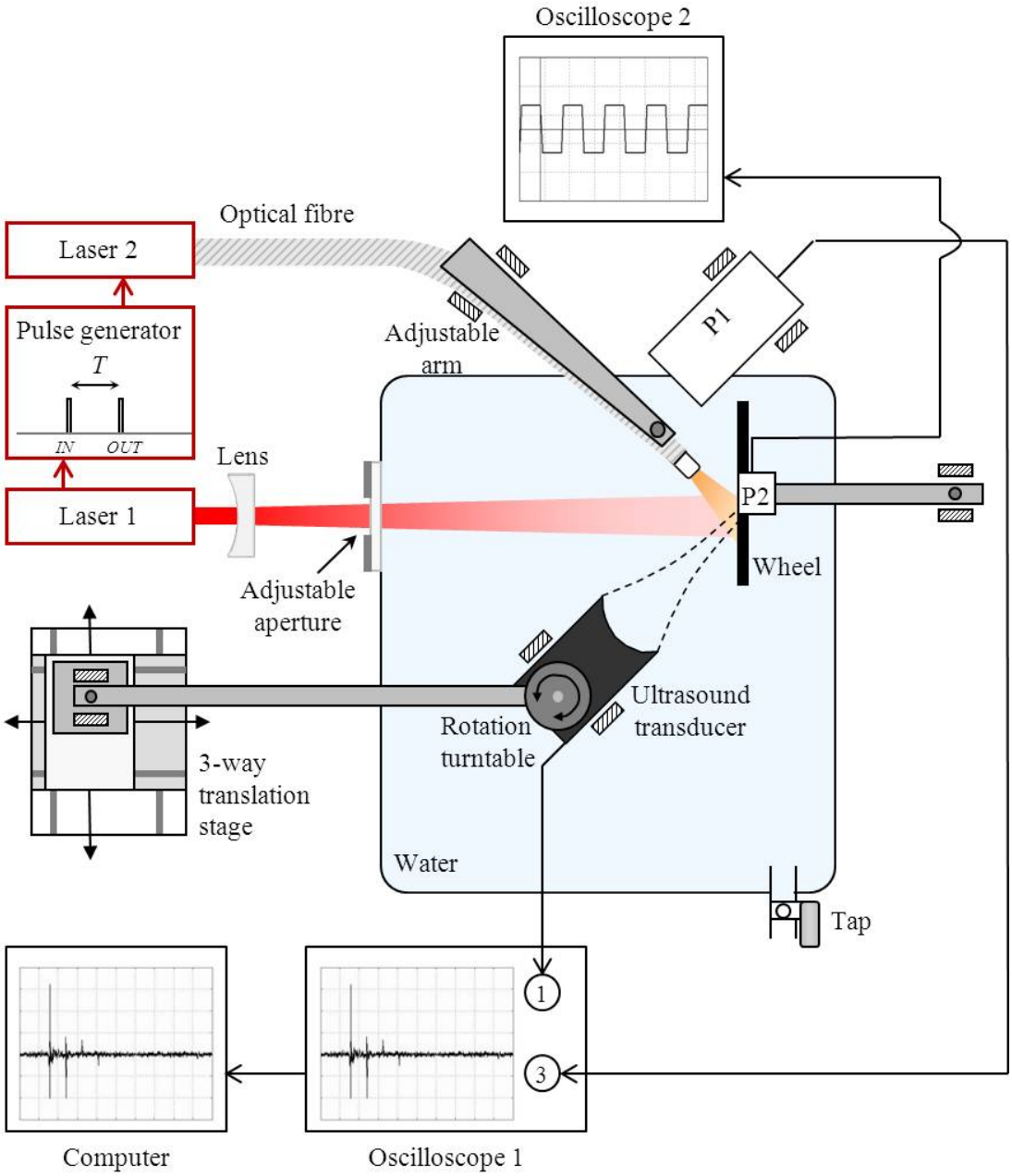

Figure 5.3: Details of the experimental setup shown in Fig. 5.1(a). Two laser pulses (one emitted by Laser 1 and the other by Laser 2) separated by a time T are used to generate a pair of photoacoustic waveforms. Each laser pulse triggers Oscilloscope 1 via Photodiode P1; the photoacoustic signal received by the ultrasound transducer is acquired on a separate channel, and then downloaded to the computer for processing. The spokes of the wheel block the light reaching Photodiode P2 and the resulting square wave output viewed on Oscilloscope 2 allows estimation of wheel rotation speed. All the apparatus is depicted from an aerial viewpoint, except the computer and the two oscilloscopes for which an *en face* view is adopted.

where P is the mean period of the square waveform acquired on Oscilloscope 2. Figure 5.4(a) illustrates the variation in the angular velocity measured by the chopper over a single revolution. The maximum and minimum periods, $P_{\max}$ and $P_{\min}$, were used to calculate a mean period P and an uncertainty $\delta P/2$:

$$P = \frac{1}{2}(P_{\max} + P_{\min}); \tag{5.2}$$

$$\frac{\delta P}{2} = \frac{1}{2}(P_{\max} - P_{\min}). \tag{5.3}$$

Calculation of the linear velocity from the angular velocity required measurement of R_{w}, which is the radial distance from the wheel axle to the centre of the focal region of the transducer, as shown in Figure 5.4(b). This measurement was carried out during the initial alignment of Laser 1, when no water was in the tank and a 1 OD filter was in place; the radial distance R_{w} (in mm) of the centre of the illuminated region was noted, then the tank was filled and the filter removed. The transducer was then positioned to give a maximum photoacoustic signal, which was assumed to emanate from $R_{\mathrm{w}} \pm \delta R_{\mathrm{w}}/2$, with uncertainty $\delta R_{\mathrm{w}}/2 = 1$ mm.

Uncertainties $\delta V/2$ in the linear velocity V were then estimated from the uncertainties in P and R_{w}:

$$V = R_{\mathrm{w}} \times \frac{2\pi}{30 \times P}; \tag{5.4}$$

$$\frac{\delta V}{2} = \frac{V}{2}\sqrt{\left(\frac{\delta R_{\mathrm{w}}}{R_{\mathrm{w}}}\right)^2 + \left(\frac{\delta P}{P}\right)^2}. \tag{5.5}$$

Measurements of velocity $V' \pm \Delta V'/2$ were made for speeds in the range 0.15 m/s to 1.5 m/s. Below 0.15 m/s the speed of the wheel motor was non-uniform, and above 1.5 m/s the wheel created turbulence in the water bath, which distorted the measured signal.

5.1.2 Fluid phantoms

Fluid flow was generated using a syringe pump (B. Braun Space®) with a 60 ml syringe (BD Plastipak™) and an optically transparent polymer tube. Table 5.1 details the sizes and materials of the tubes used variously in the experiments. The tolerances for the inner diameters (I.D.) and outer diameters (O.D.) are typically specified to be 5-10% for the entire production length of tubing (several metres). However, the experiments used lengths of approximately 50 cm, and flow was only measured in a region less than 1 cm. In these small sections the tube diameter is likely to deviate only slightly from the nominal value. The tolerances quoted in Table 5.1 are those used to calculate uncertainties in the "known" velocities V; they are all 5% of the diameters, except for the 800 μm tubing, for which a slightly smaller value is given based on the variation

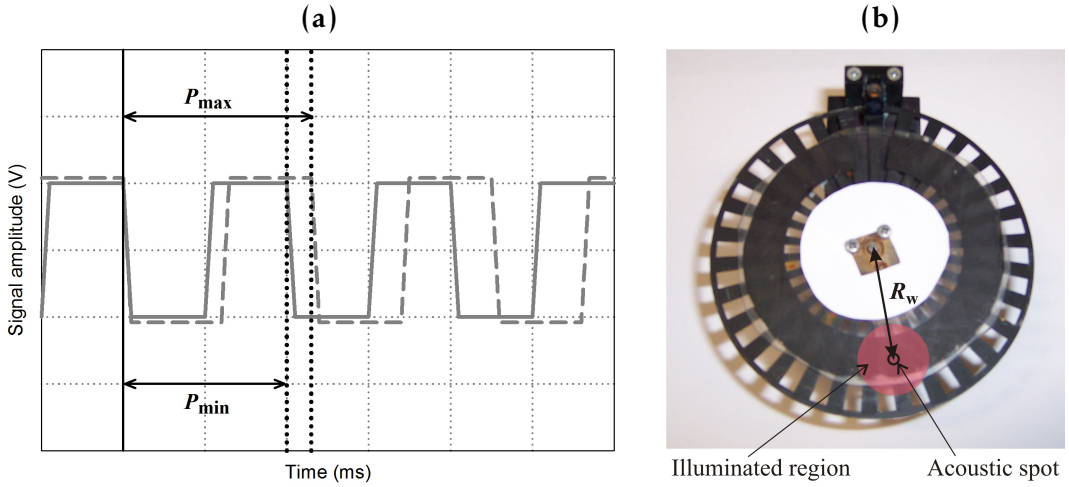

Figure 5.4: Determination of P and R_w for the calculation of the "known" velocity V. (a) Measurement of the maximum and minimum period values, P_{max} and P_{min}, from the waveform received from the chopper via Photodiode P2 and Oscilloscope 2 (Fig. 5.3). (b) R_w is the radial distance from the wheel axle to the centre of the transducer focal region.

Reference code	Material	I.D. (µm)		O.D. (µm)		Wall thickness	
		Nom. value	Tol.	Nom. value	Tol.	(mm)	(%)
MORCAP 81	THV-500	167	± 8	200	± 10	33	17%
MORCAP 20	PMMA (acrylic)	250	± 13	500	± 25	250	50%
MORCAP 82	THV-500	390	± 20	465	± 23	75	16%
MORCAP 3	PMMA (acrylic)	460	± 23	610	± 31	150	25%
MORCAP 14E	THV-2030G	583	± 29	680	± 34	97	14%
MORCAP 65, CT600-800-5	PMMA (acrylic)	600	± 30	800	± 40	200	25%
MORCAP 14F	THV-2030G	800	± 37.5	935	± 38	135	14%
MORCAP 55	PMMA (acrylic)	1400	± 70	1867	± 93	467	25%

Table 5.1: Characteristics of polymer tubes (Paradigm Optics) used to contain the fluid phantoms. The tolerances (tol.) for the inner diameters (I.D.) and outer diameters (O.D.) are typically 5% - 10% as specified for the entire production length of tubing; small sections are likely to deviate only slightly from the nominal (nom.) values.

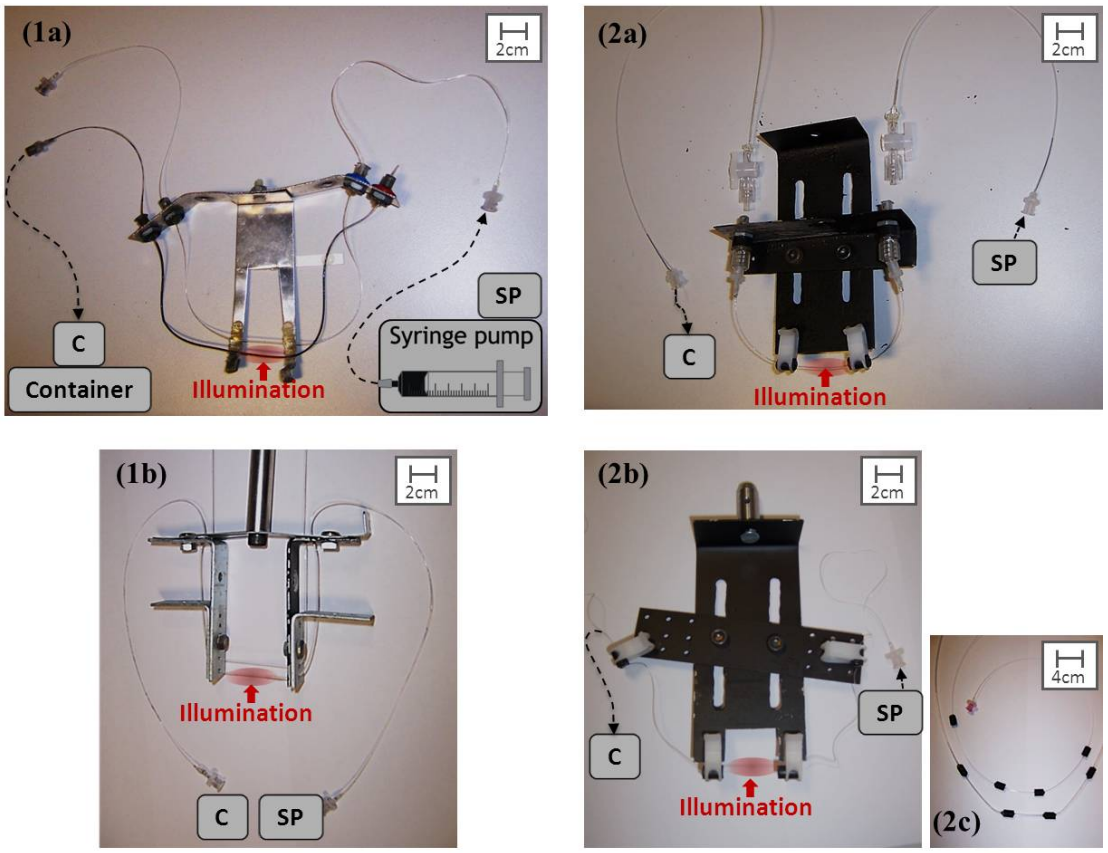

Figure 5.5: Four different designs of frames made for mounting the tubes in the setup shown in Fig. 5.1(b) and (c). Each figure is annotated with the illuminated region and the points at which fluid is injected from the syringe pump (SP) and emptied into the container (C). For the frames shown in (1a) and (1b) the tubes are glued semi-permanently in position. The designs shown in (2a) and (2b) are modular allowing different tubes to be clipped in and out of the frames. (2c) shows two lengths of tubing (diameters 1400 μm and 250 μm) fed through rubber supports that fit into the frames.

quoted on the reel. The tubes were known to have excellent optical clarity, which is essential to avoid generation of photoacoustic signals in the tube walls. The acoustic properties were not specified, but it is thought that THV is preferable to PMMA due to its more rubbery nature and consequently its closer acoustic impedance match to water. The flexibility of the THV tubing was also a practical advantage over the PMMA, since the latter required heating to bend it into a desired configuration and also had a tendency to snap.

Figure 5.5 shows four different designs of frames that were developed for mounting the tubes in the water-filled tank shown in Figure 5.1(b) and (c). The initial apparatus in Figure 5.5(1a) proved impractical for investigating different tubes since each tube was semi-permanently glued in position (using Norland 68 Optical Adhesive), and the

limited rigid support made the tubes susceptible to kinking. The more sturdy apparatus in (1b) maintained the tubes in the desired position, but still only allowed one or two tubes to be readily investigated. In the modular design in (2a), Luer connections were glued to both ends of short lengths of tubing (approximately 15 cm) which could then be clipped in and out of the frame, and screwed to matching Luer connections on the ends of lengths of polythene tubing that fed from the syringe pump and emptied into the container. This design allowed different tubes to be easily exchanged, but the multiple Luer connections were prone to blockage with absorbers (microspheres or RBCs). Therefore a modified design was developed which incorporated single, longer lengths of the tube under investigation and therefore only one connection (with the syringe in the pump) was required. This proved a successful means for generating consistent flow and for investigating many different tubes. Figure (2c) shows the small lengths of solid black rubber tubing through which the tubes were fed, enabling them to be mounted in the clips on the frame.

The flow rate Q (ml/hr) set on the syringe pump was used to determine the volume of fluid passing through the tubing, and from this and the tube diameter $2r$ (cm) the corresponding velocity V (mm/s) was calculated:

$$V = 10 \times \frac{Q}{3600 \times \pi \times R^2}. \tag{5.6}$$

The syringe pump could be programmed to deliver rates up to 200 ml/hr in steps of 0.01 ml/hr, and this range was adequate for each of the tube diameters, as illustrated in Figure 5.6: for the smallest tube diameter (167 μm) the average flow velocity could be calculated with a resolution of ± 0.06 mm/s, and for the largest tube diameter (1400 μm) the maximum flow speed $|V| = 36$ mm/s was still comparable to physiologically realistic velocities (up to 50 mm/s for flow in microvasculature).

A few experiments used a minimum flow rate of 0.25 ml/hr, giving a maximum fractional uncertainty $\delta Q/Q$ of 2%. However, flow rates were usually greater than 1 ml/hr, and typically tens of ml/hr, giving a fractional uncertainty approximately two orders of magnitude smaller than the uncertainties in the tube diameters ($\delta R/2 \approx 5\%$, as shown in Table 5.1). The uncertainty δV in the known velocity was therefore based solely on the tolerance δR in the radius of the tubing:

$$\frac{\delta V}{2} = \frac{V}{2}\sqrt{\left(\frac{\delta Q}{Q}\right)^2 + \left(2\frac{\delta R}{R}\right)^2} \tag{5.7}$$

$$\approx 2V\frac{\delta R}{2R}. \tag{5.8}$$

Flowing microspheres

The microspheres differed in material (carbon or polystyrene), size and colour.

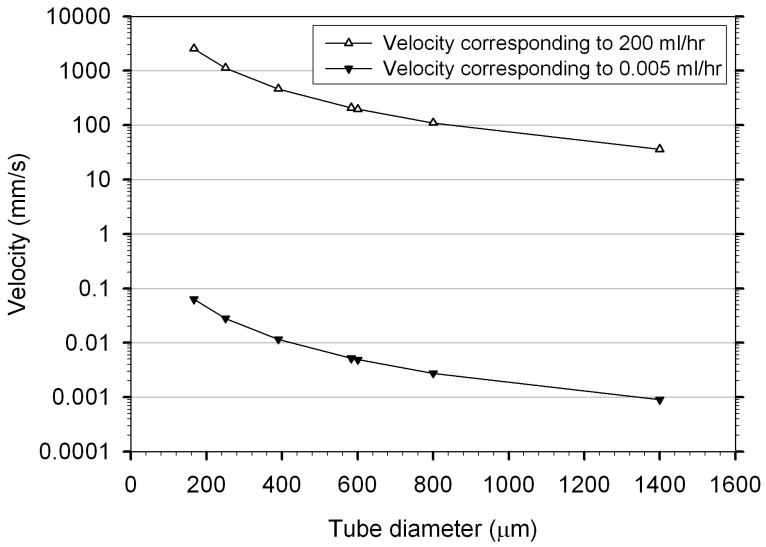

Figure 5.6: Ranges of speeds possible with different tube diameters based on the maximum flow rate of 200 ml/hr and the syringe pump resolution of ±0.005 ml/hr.

The carbon microspheres (BRACE GmbH) were supplied as dry samples. The solutions for suspending the microspheres were made by dissolving an appropriate mass of solid sodium polytungstate (71913, Sigma-Aldrich) into distilled water so that the mass density of the solution matched that of the microspheres. Particle aggregation was reduced by adding a 1% volume of TWEEN®20 (P1379, Sigma-Aldrich). Results are presented for three different sizes of microspheres, with mean particle diameters of 22 μm (GC-025), 17 μm (ACC-020) and 6 μm (GC-010), and suspended in solutions with the approximate concentrations given in Figure 5.2; different particle concentrations were not investigated.

The black-dyed polystyrene microspheres (24293-5, Polysciences) were supplied in a suspension of de-ionized water and had a mean particle diameter of $\phi = 6\mu$m. They were only used in their concentrated form ($W = 2.5\%$ w/v, or 0.025g of microspheres per ml of water), which, using the density of polystyrene ($\rho = 1.05$ g/ml), is calculated to be approximately $N = 2.1 \times 10^8$ particles/ml:

$$N = \frac{6W \times 10^{12}}{\rho \times \pi \times \phi^3}. \tag{5.9}$$

The 3 μm diameter polystyrene microspheres were obtained in dark red (42922-5ML-F, Sigma-Aldrich) and dark blue (68553-5ML-F, Sigma-Aldrich), both in a suspension of de-ionized water (5% w/v, equivalent to approximately 2.3×10^9 particles/ml). The red spheres were investigated in a range of different concentrations, prepared by diluting the original sample with distilled water. Unlike the carbon microspheres,

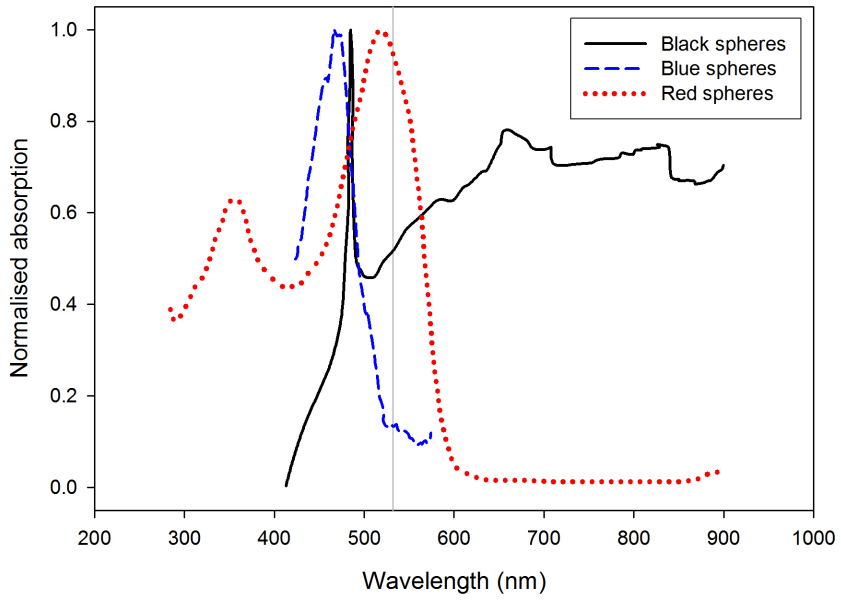

Figure 5.7: Absorption spectra supplied by Polysciences (reproduced with permission) for their black, blue and red polystyrene microspheres. Only the black spheres were used in the experiments, but the other two spectra are included for comparison. A vertical line marks 532 nm, which was the visible wavelength used to illuminate the spheres and generate photoacoustic signals.

density matching was not necessary since the density of the polystyrene particles (1.51 g/ml) was approximately equal to that of water.

Different colours of microspheres were also available from Polysciences, but those from Sigma-Aldrich were preferable since the concentration was closer to that of RBCs *in vivo* (between 3.9×10^9 and 6.1×10^9 particles per millilitre [10, 11]): the effect of concentration was found to be more important than the particle size. Polysciences provided absorption spectra for their black, blue and red microspheres, as shown in Figure 5.7. Unfortunately this information was not available for the spheres used from Sigma-Aldrich, but it may still be assumed that the dark red spheres are more strongly absorbing that the dark blue spheres at the operating wavelength of 532 nm. This was verified by measuring the absorption coefficients from the exponential fit to photoacoustic waveforms detected from each absorbing suspension in a cuvette [70]. Figure 5.8 shows measurements of absorption coefficients for wavelengths between 500 nm and 550 nm.

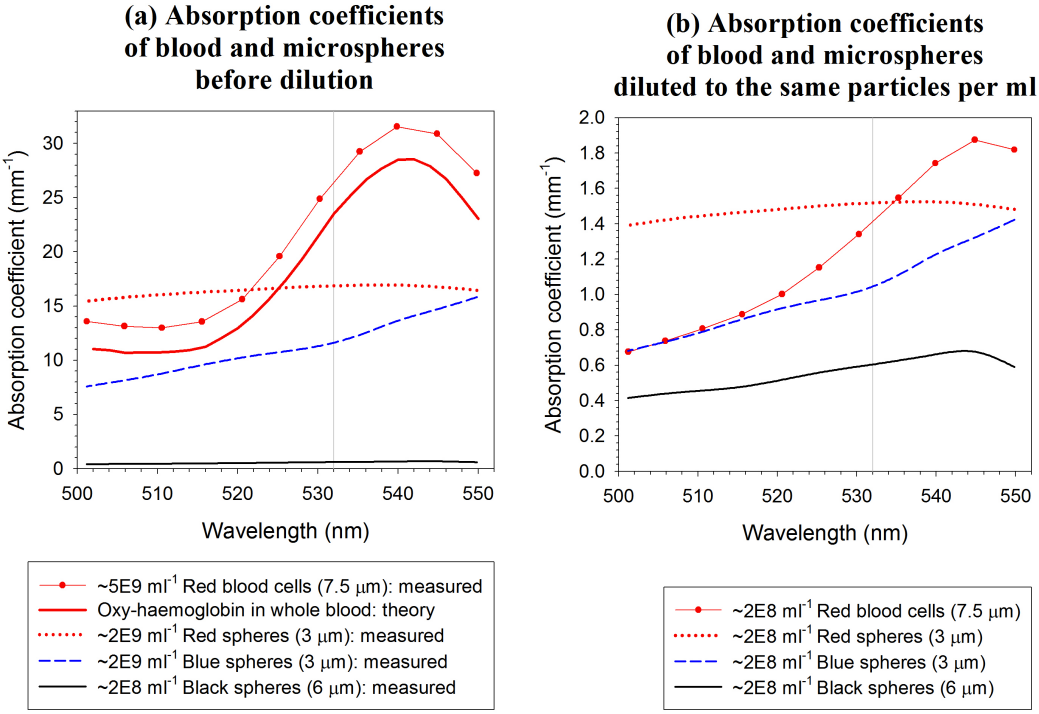

Figure 5.8: Absorption coefficient spectra for red blood cells, and red (42922-5ML-F, Sigma-Aldrich), blue (68553-5ML-F, Sigma-Aldrich) and black (24293-5, Polysciences) polystyrene microspheres. The absorption coefficient for each suspension was obtained by fitting an exponential function to the detected photoacoustic waveform [70]. The measurements in (a) are for the suspensions in their original particle concentrations (ml^{-1}); the red blood cells were in whole blood and give an absorption spectrum similar to that for oxy-haemoglobin [12]. In (b) the particle concentrations (ml^{-1}) were reduced to that of the black microspheres ($\sim 2 \times 10^8$ ml^{-1}). In both (a) and (b), a vertical line marks 532 nm, which was the visible laser wavelength used in the flowmetry experiments.

Flowing blood

Erythrocytes (red blood cells, RBCs) were obtained from the UCLH Blood Transfusion Unit in additive solution, with the leucocytes (white blood cells) depleted, giving a total pack volume of about 300 ml. The haematocrit (red blood cell count) in each pack was typically about 130% of a normal physiological haematocrit. Lower red blood cell concentrations were obtained by suspending the red blood cells in phosphate buffered saline, made by dissolving one tablet (P4417-100TAB, Sigma-Aldrich) in 200 ml of deionized water. The haematocrits of each of the resulting suspensions were measured using the blood analysers in UCLH Haematology.

5.1.3 "Manual shifting" experiments

The rotating wheel phantom simulates idealised motion of particles moving with a single velocity in one direction; this makes velocity measurements relatively straightforward. In the fluid phantoms, the absorbers are likely to move with a range of velocities around the "known" (average) value, and therefore accurate measurement of a mean velocity is more challenging. In order to verify the cross-correlation method for the fluid phantoms, a simpler experiment was designed whereby the absorber-filled tube was manually shifted on a translation stage by a known distance l (see Equation 4.2). The measured time shift t_s' was then compared with the known time shift t_s associated with l:

$$l = \frac{ct_s}{\cos\theta}. \tag{5.10}$$

The time separation T between the laser pulses is irrelevant in this case, but can be set to an arbitrary value in order to determine the corresponding velocity V (Equation 4.2). The relative uncertainty $\delta V/V$ is then equal to the relative uncertainty in the distance moved:

$$\delta V = V\frac{\delta l}{l}, \tag{5.11}$$

where the uncertainty $\delta l = \pm 2.5$ μm was determined by the ability to visually interpolate the 10 μm divisions on the translation stage.

5.2 Lasers

In the initial experiments, two Q-switched Nd:YAG lasers ("Ultra", Big Sky Laser Technologies, and "Minilite", Continuum) emitting at 1064 nm were used to produce the pulse pairs. In the first instance, one laser was operated at 20 Hz, and the second laser was triggered off the first after a time delay T that was pre-selected using a pulse

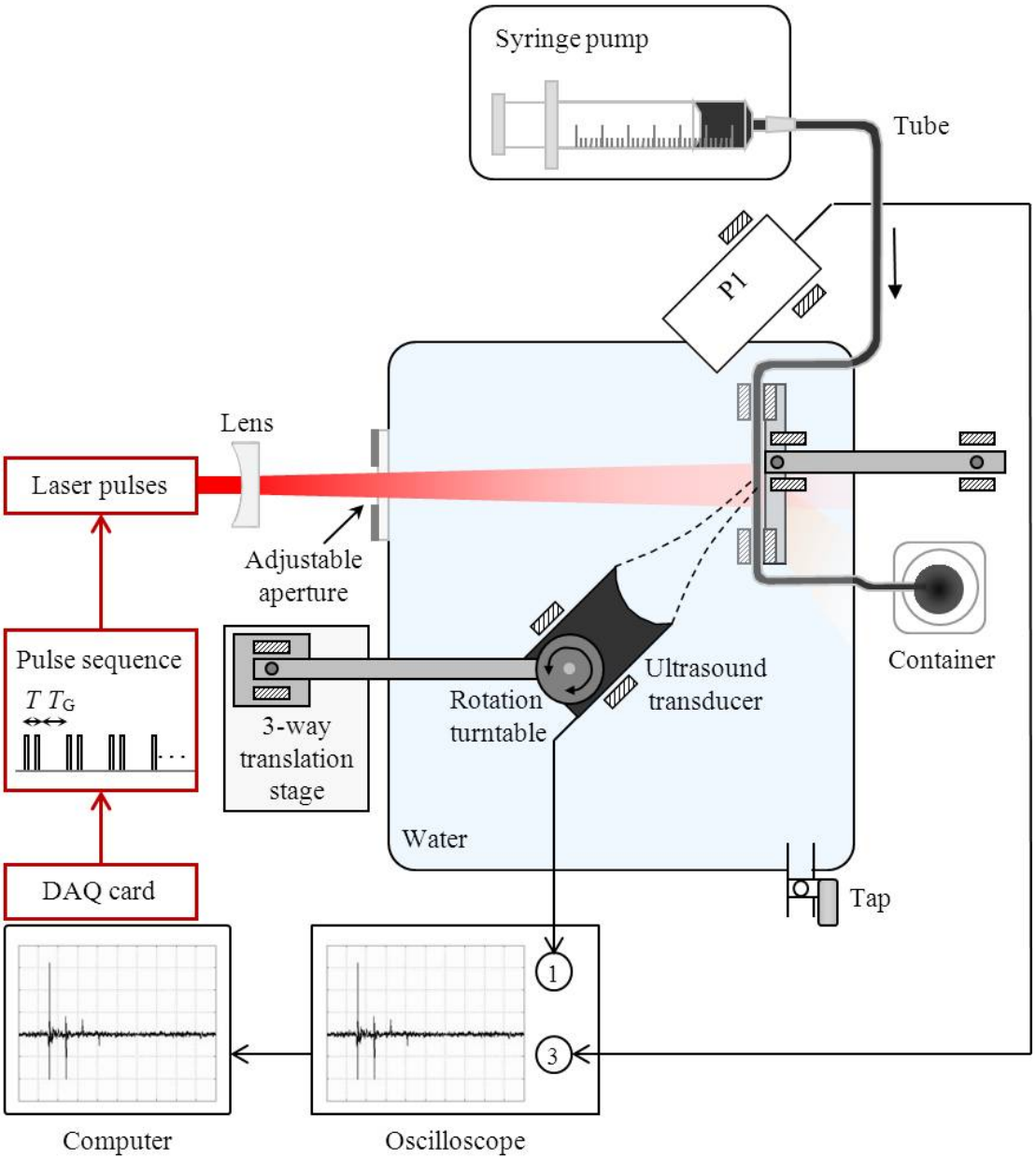

Figure 5.9: Details of the experimental setup shown in Fig. 5.1(b) and (c) for the fluid phantoms. Laser pulses are produced using a computer-controlled DAQ card which triggers the laser(s) with a sequence of pulses separated alternately by times T and T_G as defined in the text. Each laser pulse generates a signal in the photodiode P1 which triggers the oscilloscope at channel 3, and the photoacoustic signal received by the ultrasound transducer is viewed on channel 1. All the apparatus is depicted from an aerial viewpoint, except the computer and the oscilloscope for which an *en face* view is adopted.

generator, as illustrated in Figure 5.3 for the wheel phantom. In subsequent developments, the lasers were triggered using a counter/timer programmed with a DAQ card (NI PCI-6024E), as illustrated in Figure 5.9 for the fluid phantoms. In the case of the two Nd:YAG lasers, which both had a PRF of 20 Hz, the pulse sequence consisted of a train of pulses separated alternately by T and $T_G = (50 - T)$ ms. Figure 5.9 only shows one laser beam, since the triggering sequence was also applied to generate laser pulses from a single source, as described below. For the experiments involving two lasers, the beams emitted by each laser were adjusted to be of the same diameter and aligned so that they irradiated exactly the same region of the phantom.

Subsequent experiments employed a single high-repetition-rate laser ("FQ laser", Elforlight). This has the advantage of producing a series of near-identical laser pulses separated by fractions of a millisecond. Thus, there was no need to pre-select the time delay, and no triggering was required: instead, a range of pulse separations can be investigated from a single acquisition. For example, if the laser is pulsing at 1 kHz, cross-correlation of adjacent PA waveforms will give $T = 1$ ms, alternate waveforms will give $T = 2$ ms, and so on for pulse separations increasing in intervals of 1 ms.

A signal processing scheme was implemented in LabVIEW enabling a chosen range of pulse separations to be evaluated with a single mouse-click immediately after the PA waveforms were downloaded to the PC. Figure 5.10(b) illustrates the data processing possible in a short train of only five PA waveforms: four cross-correlation pairs can be evaluated for $T = 1$ ms, three pairs for $T = 2$ ms, two pairs for $T = 3$ ms, and also one pair for $T = 4$ ms (not shown), all from a single acquisition of 4.002 ms (assuming a signal length of 2 μs). A typical pulse train comprises 50 PA waveforms, enabling cross-correlation of many more waveform pairs, and investigation of pulse separations up to $T = 49$ ms: in general, for a train of N waveforms, $N - 1$ different pulse separations T_n can be investigated, with $N_P = N - T_n/T_{\mathrm{PRF}}$ cross-correlation pairs at each T_n, assuming that T_n (ms) is an integer multiple of the laser pulse repetition time $T_{\mathrm{PRF}} = 1000/\mathrm{PRF}$ (pulse repetition frequency, PRF, in Hz). The data processing can be performed immediately after the acquisition (total acquisition time $T_{\mathrm{acq}} = (N - 1)T_{\mathrm{PRF}}$), with the possibility of further post-processing. In contrast, the use of two separate low-repetition-rate lasers (for example, the "Ultra" and "Minilite") only allows a single pulse separation T to be evaluated for each acquisition. Figure 5.10(a) illustrates the data acquisition and processing required to evaluate two cross-correlation pairs at $T = 1$ ms, $T = 2$ ms and $T = 3$ ms. The total acquisition time is 156.006 ms. In general, to evaluate N_P cross-correlation pairs, $2N$ waveforms are required, and the total acquisition time is the sum of time taken to acquire data at each of the chosen pulse separations T_n: $T_{\mathrm{acq}} = \sum_n [T_n + (N - 1)T_{\mathrm{PRF}}]$. This is considerably

less efficient than the single-laser scheme illustrated in Figure 5.10(b); moreover, the different spatial profiles of the beams from the separate lasers may affect the degree of correlation between the signals, as discussed further in Section 8.1.

The high repetition rate of the FQ laser comes at the expense of pulse energy, and so the signals were passed from the ultrasound transducers through a 60 dB amplifier in order to obtain sufficient SNR. However, for blood, which has a lower absorption coefficient than the black microspheres at a wavelength of 1064 nm, even 100 dB amplification (a 60 dB and a 40 dB amplifier used in series) was insufficient. Frequency doubling to 532 nm where blood has a higher absorption coefficient may have been beneficial, but the crystal employed for this purpose provided a conversion efficiency of only a few percent.

Instead of the FQ laser, the blood experiments made use of a higher energy "PIV laser" (Litron Lasers), which incorporates a pair of identical lasers aligned so that they emit through a single aperture. Both lasers pulse at 15 Hz, and therefore they must be synchronised via a counter/timer to produce pulse pairs, as with the two separate "Ultra" and "Minilite" lasers, but with $T_G = (66.67 - T)$ ms (see Figure 5.9). However, the beams produced by the lasers in the PIV system are single-mode (TEM00), which should ensure the beam profiles are virtually identical. Moreover, the higher pulse energy compared to the FQ laser facilitates better signal-to-noise ratios in the photoacoustic signals generated. The greater SNR was significant for the microsphere phantoms, but the 60 dB amplifier was still required in order to obtain sufficient signal amplitude from blood.

The beam characteristics of each of the four lasers are listed in Table 5.2. The larger beam diameters for the Minilite and the Ultra are because these lasers were fibre-coupled. The free-space beams from the FQ and PIV lasers were expanded through a diverging lens so that the beam diameters incident on the phantom were approximately 5 mm and 10 mm respectively. This ensured that, in each case, the diameter of the illuminated region was significantly larger than the diameter of the detector focal beam in order to be representative of the acoustic resolution mode of photoacoustic detection. Beam expansion also ensured that the energy fluence values were of the same order of magnitude as the values specified by guidelines for maximum permissible exposure (MPE) to the skin (200 J/m^2 for a single pulse).

Name (Manufacturer)	**Part number**	**Wavelength (nm)**	**PRF (Hz)**	**Energy (mJ per pulse)**	**Beam diameter (mm)**	**Fluence (J/m^2)**
Minilite (Continuum)	996-0201	1064	20	~7.5	~10	95
Ultra (Big Sky Laser Technologies)	UL127511	1064	20	~9.5	~7	247
FQ laser (Elforlight)	FQ-800-5-Y-1064	1064	Up to 2500	~1.0	~2	318
PIV laser (Litron Lasers)	Nano-L-200-15 PIV	532	2x 15	~12	~2	3820

Table 5.2: Beam characteristics of four different lasers used to generate pairs of light pulses for illuminating the light-absorbing phantoms.

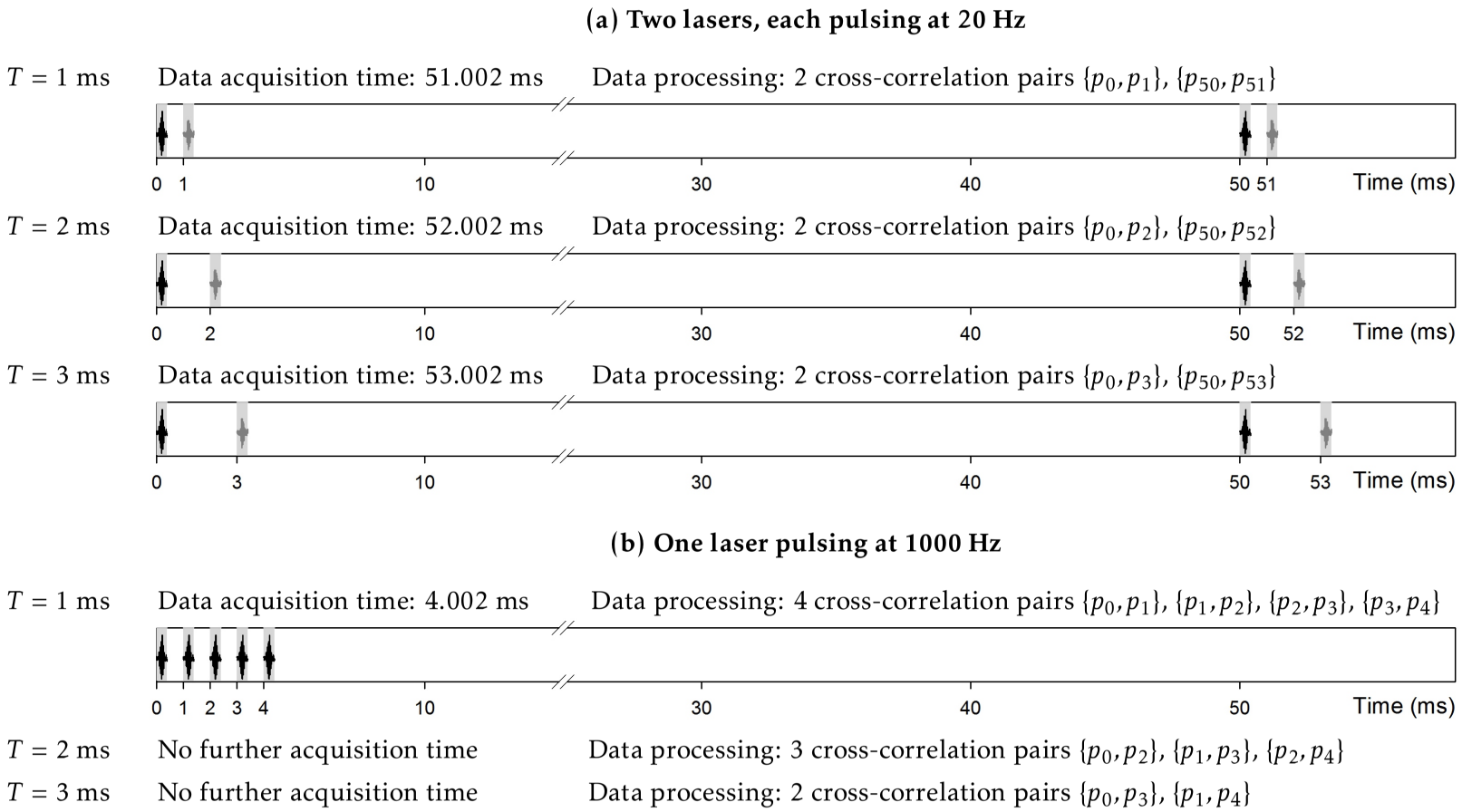

Figure 5.10: Illustration of the data acquisition and processing required for two different illumination schemes: (a) two lasers, each pulsing at 20 Hz and (b) a single laser pulsing at 1000 Hz.The length of each photoacoustic (PA) waveform is assumed to be 2 μs, although the figure does not show this to scale.

5.3 Transducers

(a) PZT transducers

Centre frequency (MHz)	-6dB Bandwidth (MHz)	Focus	Focal length (mm)	FWHM beam width (mm)
3.5	3	Cylindrical	32	1.98
5	2	Spherical	63	0.97
15	8	Spherical	19	0.15
20	8	Planar		1.28
20	10	Spherical	19	0.33
30	24	Spherical	19	0.35
50	33	Spherical	51	0.24

(b) PVDF transducers

Centre frequency (MHz)	-6dB Bandwidth (MHz)	Focus	Focal length (mm)	FWHM beam width (mm)
25	Unknown	Spherical	24	0.24
80	Unknown	Spherical	12	0.075

Table 5.3: Transducers used variously to detect photoacoustic signals generated in the light-absorbing phantoms. Table (a) lists the transducers fabricated from PZT, and (b) lists those fabricated from PVDF. Further details are given in Appendix A, page 218.

The photoacoustic signals were detected using a PZT or a PVDF transducer. Several different transducers were used variously in the experiments; the characteristics of each are given in Table 5.3, with further details in Appendix A. The experimental setup (Figure 5.1) was adapted to enable up to three transducers to acquire data simultaneously for comparison purposes. Each transducer position and angle θ were adjusted to give the maximum photoacoustic signal; for the focussed transducers this involved setting the distance from the illuminated region of the phantom to be approximately equal to the transducer focal length. The angle θ was measured to the nearest degree using a turntable with angular markings at 1° intervals.

Signal amplification was achieved using a low-noise 60 dB amplifier (322-8-B-50, Analog Modules). Two further amplifiers are listed in Table 5.4 but, after some investigation, the 60 dB was concluded to be the best choice in terms of the gain, bandwidth and input impedance. Further details are given in Appendix B.1.

Type (Manufacturer)	Model (serial number)	Gain	Bandwidth	Input impedance
Pulser-receiver (Panametrics)	5072PR (130138801)	59 dB	1 kHz - 35 MHz	500 Ω
Low noise amplifier (Analog Modules)	322-8-B-50 (93121303)	60 dB	45 MHz	50 Ω
Low noise amplifier (Analog Modules)	352A-1-B-1M (90022811)	40 dB	100 MHz	1 MΩ

Table 5.4: Details of three alternative amplifiers used in conjunction with the transducers listed in Table 5.3. Only the 60 dB amplifier was used to obtain the results in Chapter 8.

6

Measured velocities: signal acquisition and processing

The previous chapter described the experimental apparatus used to demonstrate the pulsed photoacoustic Doppler flowmetry technique. Several different laser illumination schemes were used to generate photoacoustic signals in various blood-simulating phantoms, and the signals were detected using one or more from a range of ultrasound transducers. This chapter details the time-domain cross-correlation methods used to process the photoacoustic signals in order to calculate the velocity of the moving absorbers in the phantoms.

6.1 Signal acquisition

To obtain a single velocity estimate V', the phantom was irradiated by a train of laser pulse pairs. The pulses within each pair were separated by a time T which was typically between 0.1 ms and 10 ms depending on the velocity range being measured. Each pulse pair was separated by a time T_{PRF} limited by the maximum PRF of the lasers

used (see Section 5.2); a high PRF permits much faster acquisition, with the minimum pulse pair separation ultimately limited by the acoustic transit time from the maximum depth of interest to the detector (which for cm depths is of the order of tens of microseconds). The corresponding photoacoustic waveform pairs produced by the laser pulse train were captured using the FastFrame™ Segmented Memory feature of the oscilloscope (DSO-Tektronix TDS784D). This enabled all the photoacoustic waveform pairs to be acquired in real time, concatenated in a single record and downloaded to a PC. The maximum memory capacity of the oscilloscope was 50,000 points, and so a typical FastFrame record comprised 25 waveform pairs, each waveform consisting of 1000 points. For a time sampling interval of 0.5 ns, this corresponds to a distance of $l = 1.06$ mm along a vessel at 45° to the ultrasound transducer axis (see Figure 4.1).

For the rotating wheel phantom and the flowing fluid phantoms, a velocity estimate could be made from a single FastFrame record. However, the "manual shifting" method required a slightly different approach: the tube was illuminated to generate a FastFrame set of photoacoustic signals in the initial position, and then manually shifted on a translation stage, before illuminating the tube a second time to generate a second set of photoacoustic signals. The first and second FastFrame records were then interleaved to produce a train of time-shifted waveform pairs similar to those for the freely moving phantoms.

6.2 Time shift measurement using cross-correlation

Figure 6.1(a) shows an example of a FastFrame record and Figure 6.1(b) shows a single waveform pair extracted from this record – these data were obtained with the rotating wheel phantom moving at a velocity of 0.13 ± 0.02 m/s, with $T = 1$ms and using the 5 MHz focused transducer. Figure 6.1(c) shows normalized versions of the two waveforms superimposed on the same graph in order to illustrate the time shift t_s between them. The discrete unbiased cross-correlation function (Equation 4.7, page 66) was then evaluated as illustrated in Figure 6.1(d). The time shift t_s between the waveform pair is then given by the horizontal position of the peak value of the cross-correlation function.

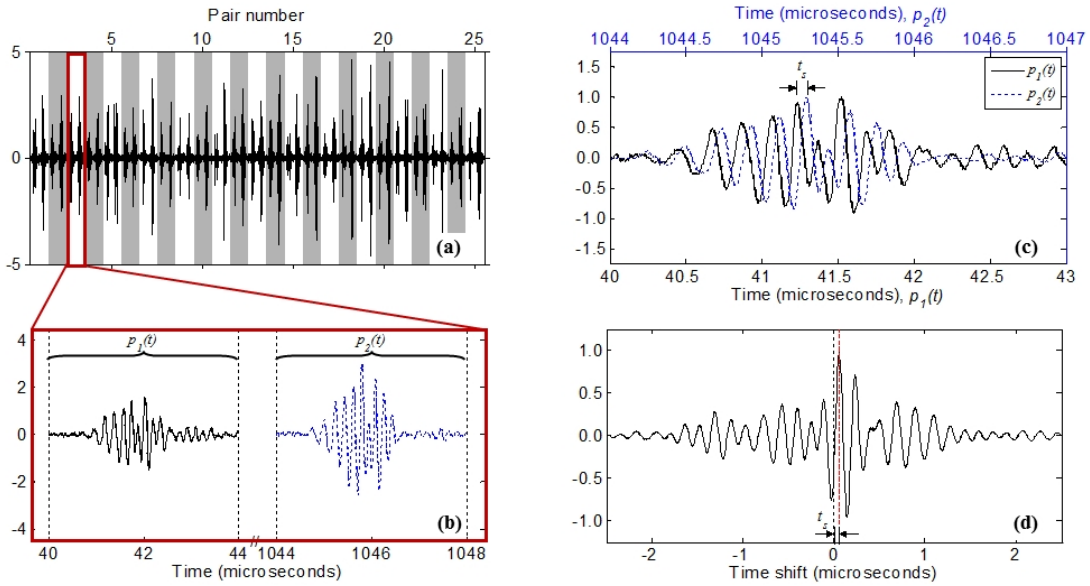

Figure 6.1: Signal processing scheme used to estimate time shift. (a) A FastFrame record consisting of 25 waveform pairs. Each pair of photoacoustic waveforms was acquired using a 5 MHz focused transducer following double pulse illumination ($T = 1$ ms) of the rotating wheel phantom. One such pair is enlarged in (b) where the first waveform $p_1(t)$ and second waveform $p_2(t)$ in the pair are shown in solid and dashed lines, respectively. The two waveforms are overlaid and normalized in (c) in order to illustrate the time shift t_s between them. The lower plot in (d) shows the cross-correlation function corresponding to the waveform pair. The position of the peak is marked with a dashed line and corresponds to the time shift t_s.

6.3 Mean cross-correlation function

Figure 6.2(a) and (b) illustrate the cross-correlation functions computed for all 25 waveform pairs in two separate data sets: in (a) the wheel phantom was rotating at a linear velocity $V = 0.210 \pm 0.009$ m/s ($t_s = 0.088 \pm 0.004$ μs) and in (b) the linear velocity was $V = 1.302 \pm 0.038$ m/s ($t_s = 0.544 \pm 0.016$ μs). Both data sets were obtained with $T = 1$ ms and using the 20 MHz planar transducer. The normalised amplitude of each cross-correlation function is displayed at each time shift value as an intensity-scaled pixel; the horizontal axes represent the time shift and the vertical axes represent the index of the waveform pair for which the cross-correlation is performed. This type of two-dimensional plot can aptly be described as a "carpet" [84].

A carpet plot is useful for data visualisation. In Figure 6.2(a) the waveform pairs are well correlated and there is a vertical red band at about 0.083 μs which represents the time shift measurement (i.e. the time shift at the maximum cross-correlation amplitude) in all but one of the pairs: for pair 3 the maximum amplitude occurs at -0.388 μs, as shown in Figure 6.2(c), which is a plot of the time shift measurements for each of the 25 cross-correlation functions. In Figure 6.2(b) the waveforms are poorly correlated due to the faster velocity of the phantom. A dark red vertical band is just visible at a time shift of about 0.5 μs, which represents the time shift measurement for only about six of the waveform pairs, as illustrated in Figure 6.2(d).

The mean of all the 25 time shift measurements for each data set is shown by the solid vertical lines in Figures 6.2(c) and (d), and takes values of 0.064 μs and 0.225 μs for (c) and (d) respectively. It is clear that these values are unrepresentative of the entire data sets: in particular, the mean of the data in Figure 6.2(c) is biased by the outlying measurement for pair 3, so it takes a value that is smaller than all the other 24 time shift measurements. Various methods for excluding the outliers have been described in detail in a previous report [22]; however, it is difficult to develop an objective method for data rejection that can be consistently applied to different data sets.

A more representative evaluation of the data entails calculating the average of all the 25 individual normalised cross-correlation functions. The mean cross-correlation functions $C(t)$ are shown in Figures 6.2(e) and (f) for the relevant data sets, and take maximum amplitude values at time shifts of 0.084 μs and 0.500 μs respectively. These time shift measurements match well with the visually apparent vertical bands in Figures 6.2(a) and (b) and are also in good agreement with the known values of 0.088 μs and 0.544 μs.

The reason for the under-reading in (f) is subject to speculation. One explanation involves consideration of the cross-correlation between two "random" photoacoustic

signals acquired using the same ultrasound transducer. The signals are random in the sense that the absorber distributions are unrelated, but the two signals will still bear some similarity due to the detector characteristics such as band limiting, and therefore the maximum amplitude cross-correlation peak will appear at a zero time shift. This stationary correlation will also exist in "non-random" photoacoustic waveform pairs, which are acquired from time-shifted absorbers. If the match between the absorber distributions is weak, for example at high speeds where the majority of absorbers have moved out of the detector focus by the time of the second laser illumination, the cross-correlation peak at the time shift that corresponds to the absorber velocity will have a small amplitude and may be biased towards lower time shifts by the dominance of the inherent peak at a zero time shift.

Figure 6.3(a) shows the mean cross-correlation function $C(t)$ corresponding to the data in Figure 6.1: the cross-correlation functions of all 25 waveform pairs in Figure 6.1(a) were computed and normalized to their maximum amplitudes. The standard deviation δy_i, which represents the uncertainty in the magnitude of each data point in Figure 6.3(a), was also calculated although it is not shown in the figure. The central lobe of $C(t)$ was then extracted (the m data points between the vertical dotted lines in Figure 6.3(a)) and a continuous function $g(t)$ fitted to it: in this example $g(t)$ is a Gaussian as shown in Figure 6.3(b). The horizontal position of the peak value of the fit was taken to be the time shift t_s' from which the velocity value V' was calculated using Equation 4.3, page 65.

The uncertainty $\Delta t_s'$ in the measured time shift t_s' is given by the uncertainty in the location of the peak value of $C(t)$. This was estimated from the standard deviation values (the y axis error bars δy_i) of the data points associated with the central lobe as follows. At each of the time shift data points t_i a sensitivity value s_i was calculated by numerical differentiation of the fitted curve:

$$s_i = \left| \frac{dg_i}{dt_i} \right|. \tag{6.1}$$

Time shift (x axis) errors δt_i for each point were then obtained from δy_i as follows:

$$\delta t_i = \frac{\delta y_i}{s_i}. \tag{6.2}$$

$\Delta t_s'$ was then taken as the mean of the x axis errors δt_i, weighted according to the sensitivities s_i:

$$\frac{\Delta t_s'}{2} = \frac{\sum_{i=1}^{m} (s_i \cdot \delta t_i)}{\sum_{i=1}^{m} s_i}. \tag{6.3}$$

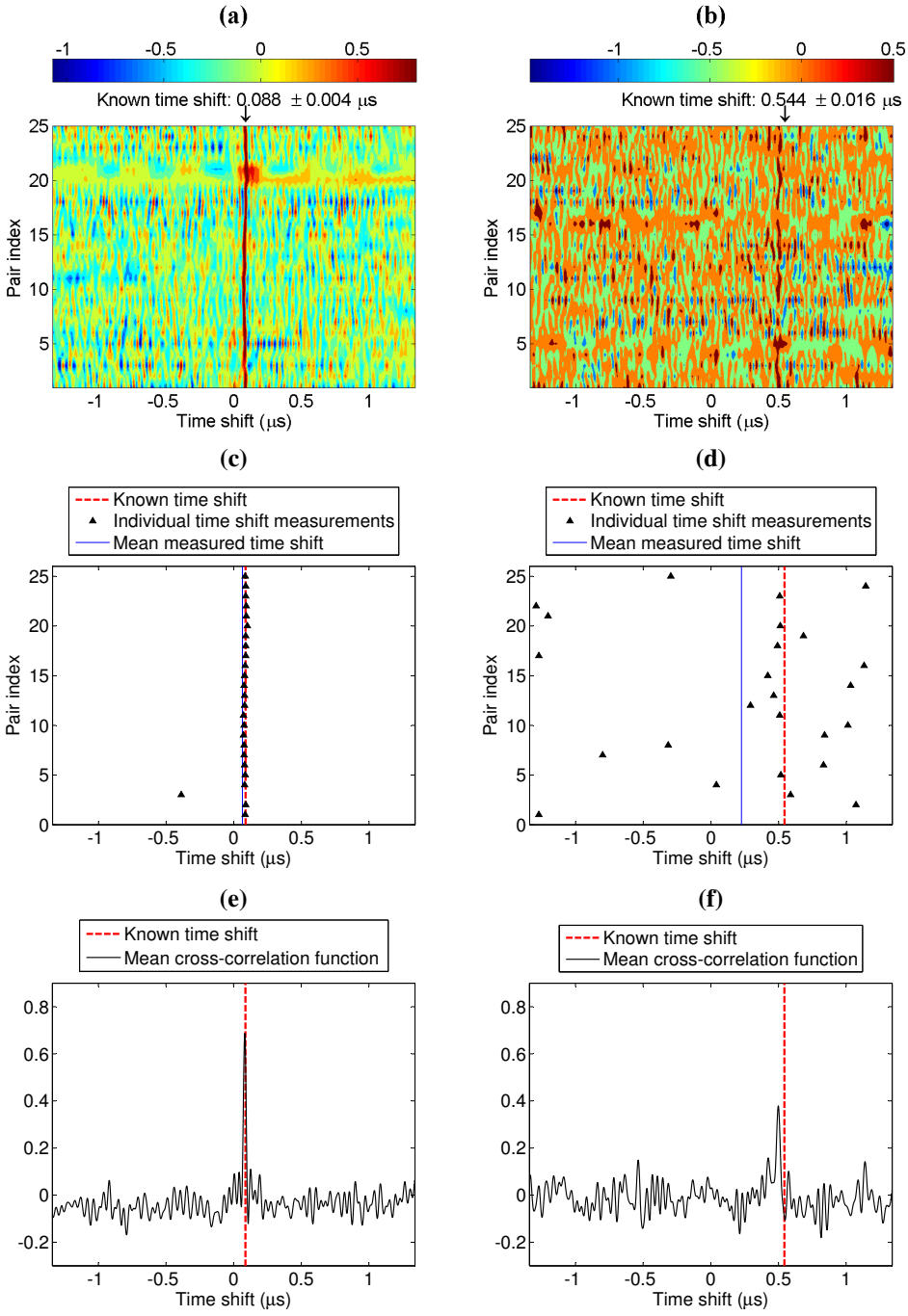

Figure 6.2: Analysis of cross-correlation functions calculated from pairs of photoacoustic waveforms acquired using a 20 MHz planar transducer following double pulse illumination (T = 1 ms) of the rotating wheel phantom. The linear velocity corresponds to a "known" time shift of 0.088 ± 0.004 μs for the data in the left column of plots, and to a time shift of 0.544 ± 0.016 μs for the right column of plots. (a) and (b) are "carpet plots" showing cross-correlation functions computed for the 25 waveform pairs in the two data sets. The normalised amplitude at each time shift value is displayed as an intensity-scaled pixel. Time shift measurements at the maximum cross-correlation amplitudes are plotted in (c) and (d). Mean functions $C(t)$ of the 25 cross-correlation functions in each data set are plotted in (e) and (f).

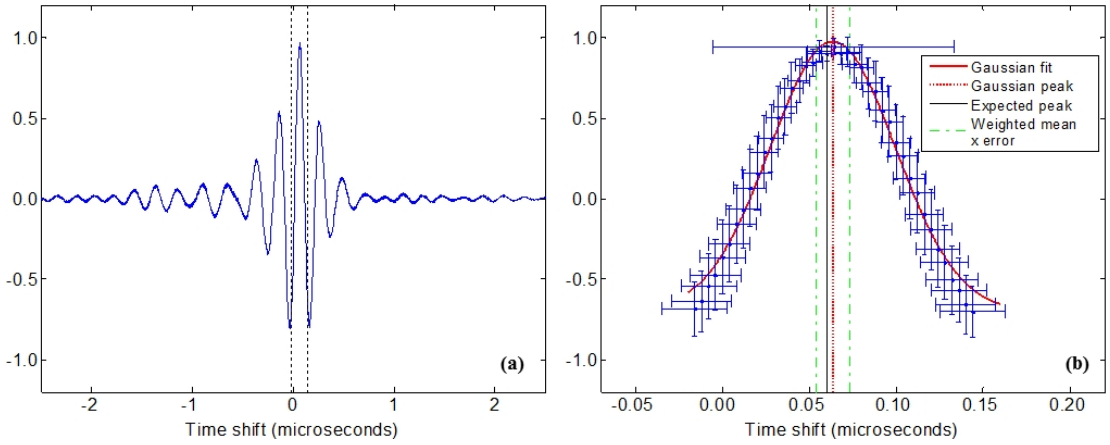

Figure 6.3: (a) Mean cross-correlation function $C(t)$ of the 25 photoacoustic waveform pairs shown in Fig. 6.1(a). (b) Expanded view of data between the vertical dotted lines in (a). For each data point, the y axis error bars correspond to the standard deviation of the 25 cross-correlation functions, and, using the Gaussian fit (solid curve), these errors are propagated to time shift (x axis) errors. The weighted mean time shift error is calculated using Equation 6.3 and indicated by the dashed vertical lines on either side of the peak of the Gaussian fit (vertical dotted line). The solid vertical line marks the position of the peak corresponding to the known velocity V.

The corresponding uncertainty $\pm\Delta V'/2$ in the velocity V' was then calculated using Equation 4.3:

$$\frac{\Delta V'}{2} = \frac{c}{T\cos\theta}\frac{\Delta t_s'}{2}. \tag{6.4}$$

The full expression for $\pm\Delta V'/2$ is given by Equation 6.5:

$$\frac{\Delta V'}{2} = \frac{V'}{2}\sqrt{\left(\frac{\Delta c}{c}\right)^2 + \left(\frac{\Delta t_s'}{t_s'}\right)^2 + \left(\frac{\Delta T}{T}\right)^2 + \left(\frac{\Delta\cos\theta}{\cos\theta}\right)^2}. \tag{6.5}$$

However, based on temperature variations of ±2.5°C (resulting in $\Delta c \approx 8$ m/s), a timing jitter of $\Delta T \approx 1.5$ ms, and a ±0.5° uncertainty in θ, the squared relative uncertainties for c, T and $\cos\theta$ are less than that for t_s' by three, five and two orders of magnitude respectively, and can therefore be neglected, and Equation 6.5 reduces to Equation 6.4. For the data shown in Figure 6.3(b) the peak of the Gaussian fit and the error calculated (using Equation 6.4) gives a measured velocity of 0.14 ± 0.01 m/s, which is in good agreement with the known value (0.13 ± 0.02 m/s) within the experimental uncertainty.

Initially, the data were acquired from the oscilloscope via LabVIEW and then post-processed in MATLAB. Subsequent developments entailed translation of the MATLAB code into LabVIEW, using a combination of LabVIEW code (VIs and sub-VIs) and embedded MATLAB code (MathScripts), which enabled all parameter selection, data ac-

quisition and signal processing to be carried out following a single mouse click. Figure 6.4 shows a screen shot of the main LabVIEW computer interface and an example of one page of the underlying code.

6.4 Summary

The sample data presented in this chapter demonstrate the principles of the signal processing methods used to measure time shifts between two photoacoustic waveforms. Within a train a photoacoustic waveform pairs, there are usually instances of pairs that are poorly correlated, and these anomalous time shift measurements can distort the final result derived from a statistical evaluation of the time shifts. However, this issue was addressed by taking the mean of all the cross-correlation functions to give a single time shift measurement from the set of individual correlation functions. The distinct advantage of this approach over statistical evaluation methods is that it removes the need for subjective and arbitrary exclusion of spurious cross-correlation maxima.

The mean cross-correlation method was used to calculate the time shifts of absorbers moving at different speeds in various phantoms and under a range experimental conditions. The resulting velocity measurements are presented and analysed in the following part of this thesis.

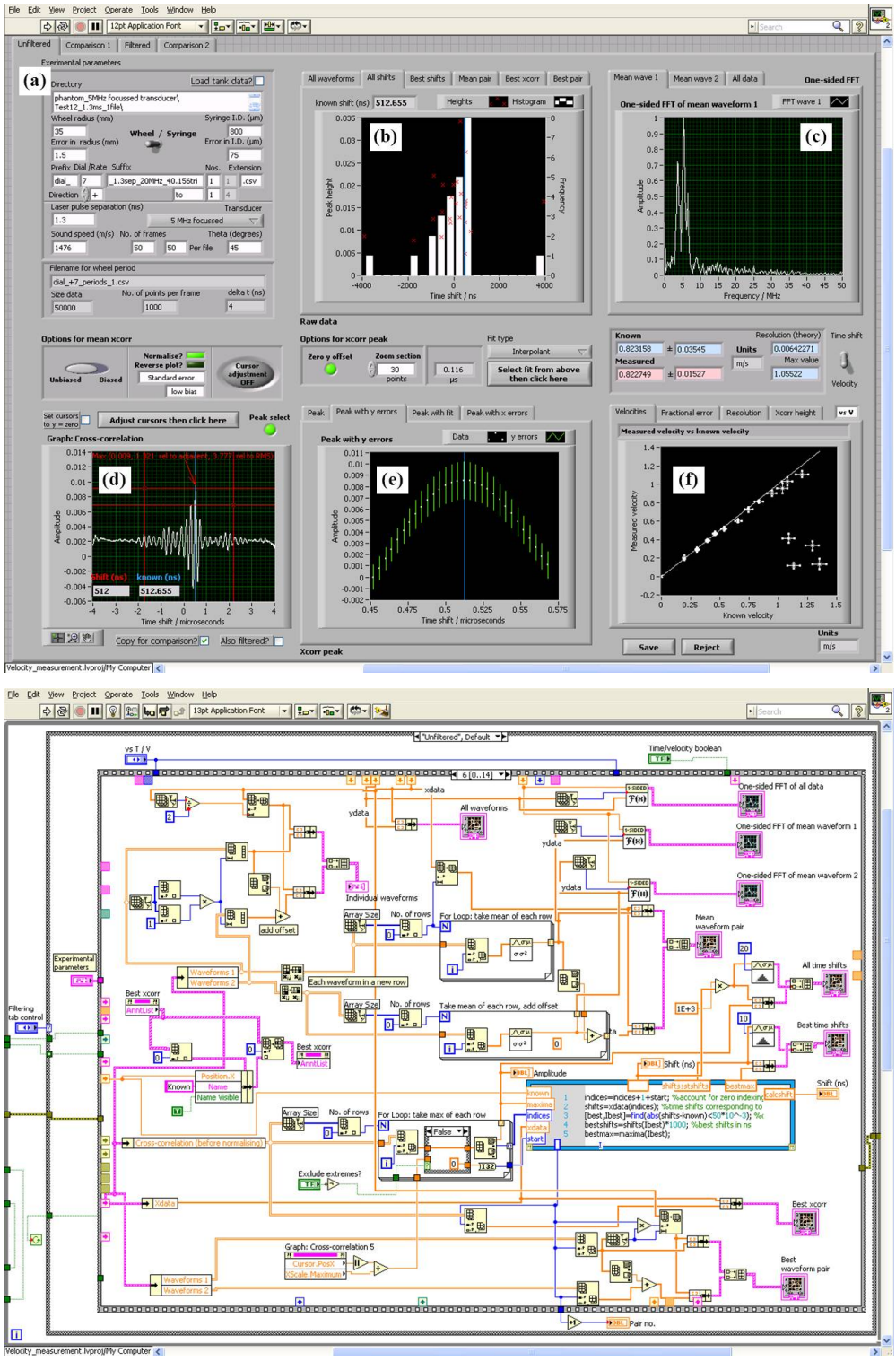

Figure 6.4: LabVIEW user interface (top) and a sample page of the underlying code (bottom) used to perform all the parameter selection, data acquisition and signal processing for the photoacoustic velocity measurements. (a) Table for user to enter experimental parameters such as time separation T; (b) histogram of time shift measurements for individual cross-correlation pairs; (c) mean FFT of the waveform pairs; (d) mean cross-correlation function; (e) peak of mean cross-correlation function, with y axis error bars (standard deviations); (f) measured velocities compared with known velocity values.

Part III

Results and discussion

7

Results: wheel phantom

To initially demonstrate the concept described in Chapter 4, a simple experiment was designed in which a two-dimensional distribution of absorbers was moved in a regular fashion, generating a single, uniform time shift. This was achieved using the rotating wheel phantom. Time shift measurements were made as described previously in Chapter 6, for the wheel moving at linear velocities in the range $|V| = 0.15 - 1.5$ m/s, and using three different transducers: 20 MHz planar, 5 MHz spherical focused and 3.5 MHz cylindrical focused.

The results in Figure 7.1 demonstrate that the majority of the photoacoustically measured velocities are in close agreement with the known values, the former increasing linearly with the latter. Although a detailed error analysis is provided in the following sub-sections, a cursory inspection of Figure 7.1 permits several observations in relation to the accuracy and resolution of the measurements to be made. Consider the results in Figure 7.1(a) acquired using the 20 MHz planar transducer. In the range $|V| = 0.15 - 1.0$ m/s, the measurements are consistently accurate to within 3% of the known velocities. The measurement resolution (vertical error bars) is on average about 6% of the measured velocity over the same velocity range, but approaches 10% for ve-

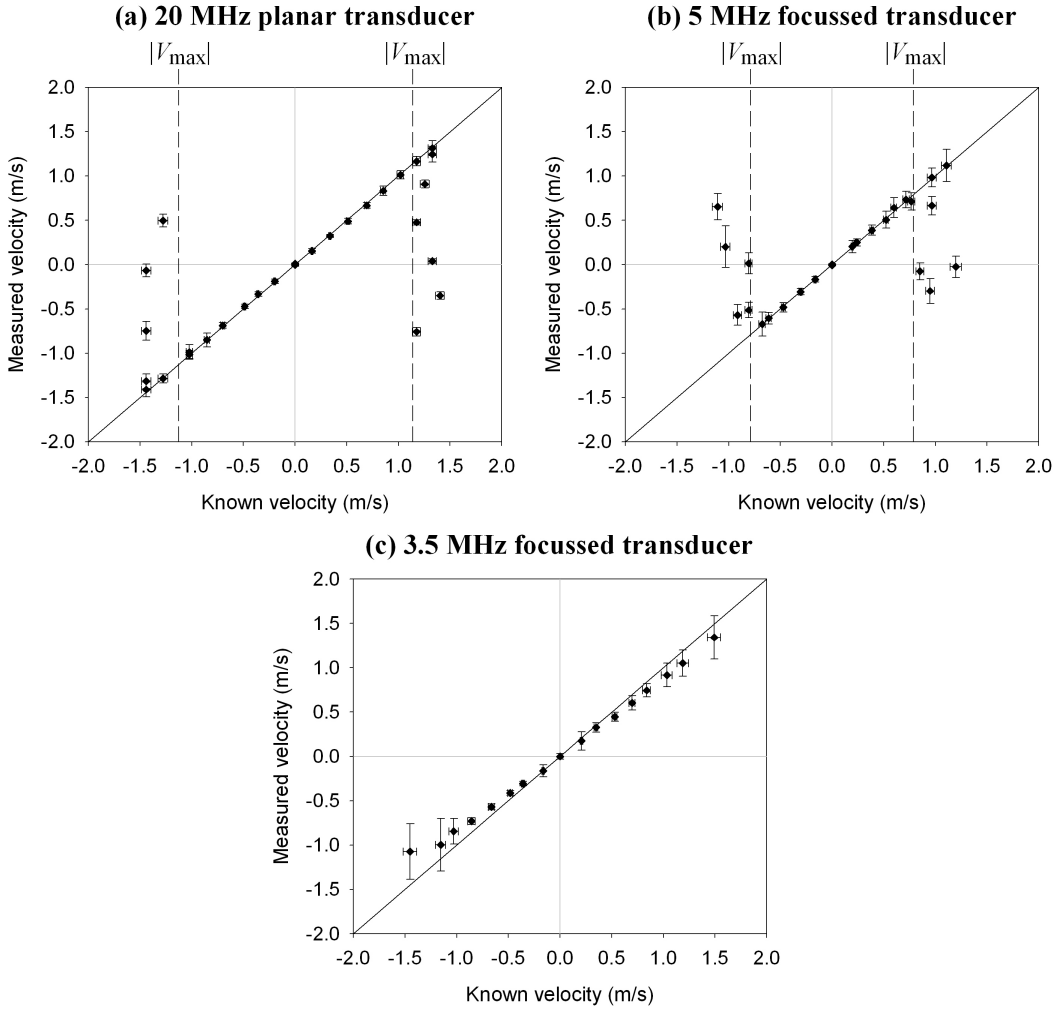

Figure 7.1: Comparison of velocity values V' calculated from the time-shifted photoacoustic waveform pairs with the known velocities V of the absorbers in the rotating wheel phantom. The time separation between the laser pulses was 1.5 ms. The data in (a) were acquired using a 20 MHz planar transducer with $\theta = 48°$, in (b) using a 5 MHz focused transducer with $\theta = 45°$, and in (c) using a 3.5 MHz cylindrically focused transducer with $\theta = 48°$. Correlation is lost for velocities beyond that marked by the dashed lines. The solid lines are lines of unity.

locities approaching $|V| = 1.1$ m/s. This is due to a reduction in correlation between the measured waveforms pairs as the distance the absorbers travel between successive laser pulses approaches that of the transducer focal beam width. At even higher velocities the absorbers move completely out of the transducer field-of-view between the two laser pulses resulting in near-complete loss of correlation and nonsensical velocity estimates – this defines the maximum measurable velocity, $|V_{\max}|$. Similar behaviour is observed for the measurements made using the 5 MHz focused transducer [Figure 7.1(b)], although $|V_{\max}|$ is lower because of the smaller transducer focal spot size. For the 3.5 MHz cylindrically focused transducer [Figure 7.1(c)] the measurements do not reach a limiting value within the range of velocities investigated due to the larger transducer beam width. Since all three data sets were recorded under identical experimental conditions, the differences in maximum measurable velocity, accuracy and resolution are due to the individual transducer characteristics.

The following three sub-sections discuss in more detail the factors that influence (a) the maximum measurable velocity, (b) the accuracy, and (c) the resolution of the measurements. The fourth sub-section describes how the results can be scaled to estimate the measurement resolution and the upper velocity limit for different velocity ranges. The final sub-section discusses how the velocity resolution is affected by the axial spatial resolution.

7.1 Upper velocity limits

The results in Figure 7.1(a) and 7.1(b) show that there are threshold velocities $|V_{\max}| \cong 1.1$ m/s and $|V_{\max}| \cong 0.8$ m/s, respectively beyond which the estimated velocity drops off very rapidly and bears little relation to the true velocity. This occurs because the irradiated absorbers have been swept entirely out of the transducer focal beam by the time the second laser pulse is emitted. As a consequence, there is almost a complete loss of correlation between the two waveforms within each pair. This effect is not observed in Figure 7.1(c) due to the larger beam width of the 3.5 MHz cylindrically focused transducer; this increases $|V_{\max}|$ to over 1.8 m/s, which is beyond the range of measured velocities. The results in Figure 7.1(a) and Figure 7.1(b) also show instances of accurate velocity measurements beyond $|V_{\max}|$ and this is discussed further on page 102.

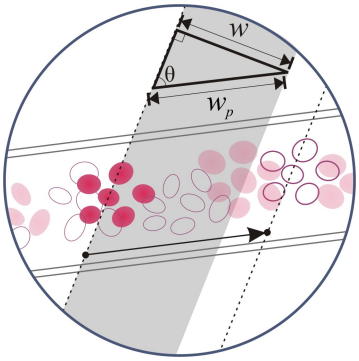

Figure 7.2: Demonstration of de-correlation due to the finite transducer beam width. If a cluster of RBCs (represented by solid ellipses) moves out of the transducer focal beam (grey shading) in the time between the two laser pulses the velocity is greater than Vmax and there is no correlation.

A theoretical value for the threshold or limiting speed $|V_{\max}|$ (meters per second) can be calculated from the focal beam diameter w and the pulse separation T:

$$|V_{\max}| = \frac{w_p}{T} = \frac{w}{T\,|\sin\theta|}, \tag{7.1}$$

where w is defined as the FWHM beam width at the focal length of the transducer. The geometrical relationship between w and w_p is illustrated in Figure 7.2.

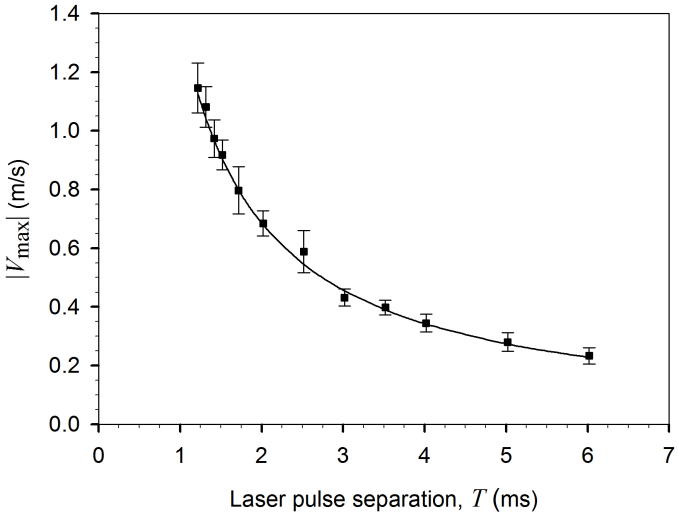

Figure 7.3: Values of maximum measurable velocity $V_{\max}$ observed using different laser pulse separations T between 1.2 ms and 6.0 ms. The data were acquired using the 5 MHz focused transducer with $\theta = 45°$. The solid line shows the theoretical values of $V_{\max}$ calculated using Equation 7.1 and the known beam width $w = 0:97$ mm.

From Equation 7.1 it can be seen that $|V_{\max}|$ depends on the pulse separation T as well as the beam width w. This behaviour is shown in Figure 7.3. Measurements in the range 0 – 1.5 m/s were made using the 5 MHz focused transducer and laser pulse separations between 1.2 ms and 6 ms, and the observed cut-off velocity is plotted as a function of time separation between the laser pulses. The maximum measurable velocity varies inversely with the pulse separation, and the data agree almost exactly with the theoretical values (solid line) calculated from Equation 7.1; the known beam width w of the transducer was 0.97 mm as determined by mapping the beam profile of the transducer when operating it as a transmitter (see Appendix A).

A large transducer beam width and a short laser pulse separation both conspire to increase $|V_{\max}|$. Selection of appropriate w_p and T therefore allows control over the maximum measurable velocity. Similarly, for measurement of a particular velocity V there exists a maximum pulse separation $T_{\max}$ beyond which V can no longer be accurately measured. Thus, for a specific velocity V and beam diameter w Equation 7.1 can be re-expressed:

$$T_{\max} = \frac{w_p}{|V|} = \frac{w}{|V \sin\theta|}. \tag{7.2}$$

Since the time shift t_s is proportional to both the speed $|V|$ and the pulse separation T, a maximum measurable time shift $\left|t_{s,\max}\right|$ can be found by rearranging Equation 7.1 or Equation 7.2 and substituting Equation 4.3:

$$t_{s,\max} = \frac{w}{c|\tan\theta|}. \tag{7.3}$$

7.2 Velocity accuracy

The accuracy of the velocity measurements is described by the fractional difference between the known velocity (V) and measured value (V'):

$$\text{Fractional error} = \frac{V - V'}{V} \quad (V \neq 0). \tag{7.4}$$

Figure 7.4 illustrates the accuracy of the measurements made using the 3.5 MHz, 5 MHz, and 20 MHz transducers. The x axis data have been re-scaled to give the velocity as a proportion of the $|V_{\max}|$ values calculated for the three transducers so that the limiting velocities of each can be directly compared.

In general, there is a small and relatively consistent fractional error for measurements made at velocities $|V/V_{\max}| < 1.0$: the fractional error averages 3% for the 20 MHz transducer, -1% for the 5 MHz transducer and 13% for the 3.5 MHz transducer. The relatively large under-reading (positive error) for the 3.5 MHz transducer is likely

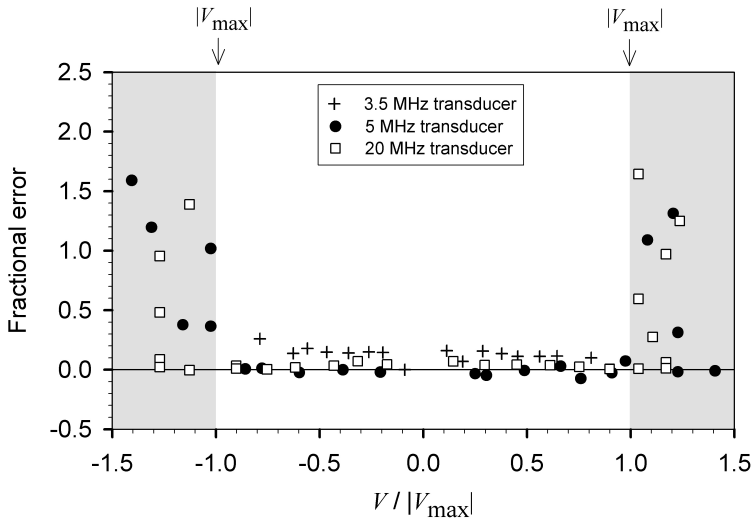

Figure 7.4: Accuracy of the data shown in Figs. 7.1(a) - 7.1(c). For the data acquired using the 5 MHz and 20 MHz transducers, correlation is lost when $V/V_{\max} > 1$, giving rise to poor accuracy (large fractional errors, shaded region). The measured range of velocities did not extend beyond $V_{\max}$ for the 3.5 MHz transducer.

to be due to an overestimate of R_w, the radial distance between the region of focus and the wheel axle.

The regime where $|V/V_{\max}| > 1.0$ is only pertinent to the 5 MHz and 20 MHz transducers, for which the fractional errors average 72% and 55%, respectively. $|V_{\max}|$ indicates a limit beyond which there is near-complete de-correlation between the two waveforms as a consequence of the absorbers being swept out of the detector field-of-view between successive laser pulses, as discussed in the previous subsection. It might be expected that de-correlation would give rise to a random distribution of velocity measurements; whilst Figure 7.1 and Figure 7.4 suggest that this is the case to some extent, it is also evident that beyond $|V_{\max}|$ the measurements consistently under-read the known velocity values with a tendency towards zero velocities. This is likely to be due to the limited transducer bandwidth, which gives rise to time-shift-independent signal features and therefore an apparent zero time shift between two de-correlated waveforms.

Figure 7.4 also shows instances of good correlation (fractional error close to zero) still occurring at velocities greater than $|V_{\max}|$; this reflects the fact that the transducer beam profile is not a top-hat function, and therefore there is still some possibility that correlation will occur even once the absorbers have moved out of the immediate field-of-view defined by the FWHM. The larger beam width of the 3.5 MHz transducer, when used with the same pulse separation ($T = 1.5$ ms), means that $|V_{\max}|$ was beyond

the range of measured velocities, and so no large changes are observed in the fractional error.

7.3 Velocity resolution

The measurement resolution describes the minimum measurable velocity under the experimental conditions described. For fixed values of c, θ and T, the fundamental velocity resolution limit $\pm\delta V/2$ is related to the smallest detectable time shift $\pm\delta t_s/2$ according to Equation 4.3:

$$\frac{\delta V}{2} = \frac{c}{T\cos\theta}\frac{\delta t_s}{2}. \tag{7.5}$$

The resolution may also be expressed as a percentage relative to the known velocity V:

$$\frac{\delta V/2}{V} \times 100 = \frac{\delta t_s/2}{t_s} \times 100. \tag{7.6}$$

In this section the minimum measurable time shift δt_s is taken to be equal to the oscilloscope sampling interval; in practice this is not a fundamental limitation (see Section 10.3), but it serves as a convenient and intuitive reference value.

The resolution of the experimentally measured time shifts and velocities are $\pm\Delta t_s'/2$ and $\pm\Delta V'/2$ respectively, and these can also be expressed as percentages relative to the measured time shifts t_s' (Equation 6.3) and the measured velocities V' (Equation 6.4).

In order to verify the influence of pulse separation on measurement resolution, a series of measurements was made using signals sampled with $\delta t_s = 4$ ns under experimental conditions where $c = 1476$ m/s and $\theta = 45°$. The pulse separation was varied in the range 0.1 to 45 ms, and the theoretical measurement resolution $\pm\delta t_s/2$ was compared with the experimentally determined measurement resolution $\pm\Delta t_s'/2$ (Equation 6.3). The results are shown in Figure 7.5 and illustrate three scenarios: $V = 0.00$ m/s, $V = 0.30$ m/s and $V = 0.77$ m/s. In the case of zero velocity, as $T/T_{\max}$ is increased there is no correlation loss due to movement of absorbers out of the transducer focal beam, and therefore these measurements serve as control data. Figure 7.5(a) shows the absolute resolution values, Figure 7.5(b) shows the percentage resolution values and Figure 7.5(c) shows the cross-correlation amplitude – the maximum amplitude of the mean cross-correlation functions $C(t)$ (see Section 6.3). The cross-correlation amplitude provides an approximate measure for the degree of correlation. Note that the x axis data for the moving phantoms have been re-scaled to give the T as a proportion of the $T_{\max}$ values calculated for each velocity (Equation 7.2) so that the results can be compared directly.

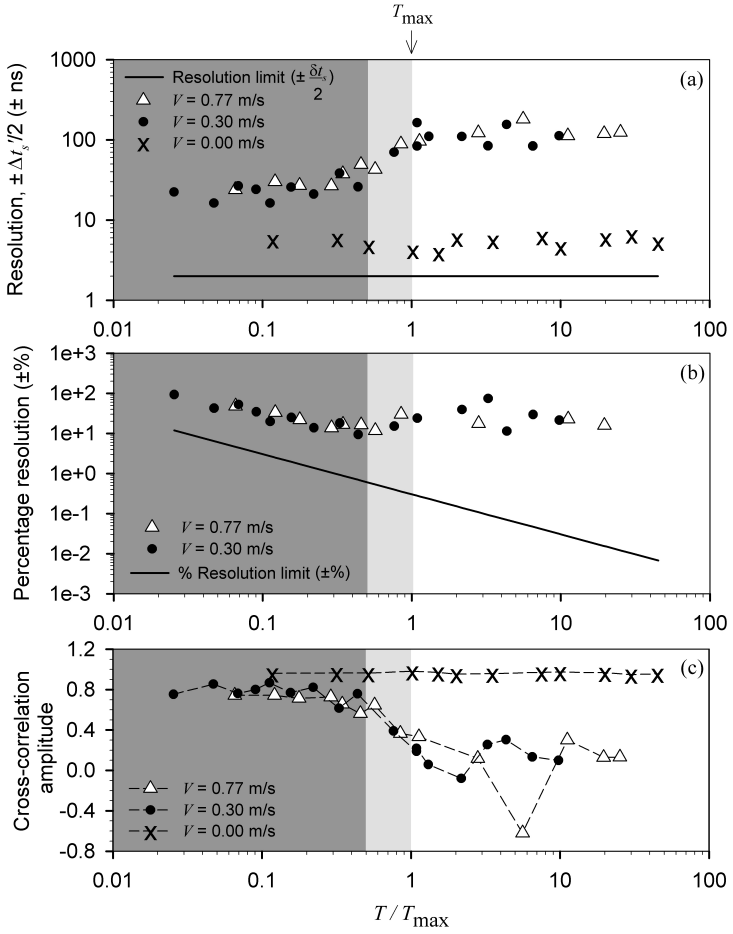

Figure 7.5: Resolution and cross-correlation amplitude measured using the 5 MHz focused transducer as a function of relative pulse separation $T = T_{max}$. (a) Resolution values. The solid line shows the fundamental resolution $\pm\delta t_s/2$ of the system limited by a temporal sampling interval $\delta t_s = 4$ ns. The symbols show the experimentally determined resolution values $\pm\Delta t_s'/2$ (Equation 6.3 for two different velocities; resolution values at zero velocity (invariant with T) are also shown for comparison, arbitrarily setting $T_{max} = 1$ ms. (b) Percentage resolution values for the non-stationary data shown in (a) and for the theoretical limit; percentage resolution for $V = 0.00$ m/s is undefined (division by zero). (c) Cross-correlation amplitudes for the velocities shown in (a), again setting $T_{max} = 1$ ms for $V = 0.00$ m/s.

In the case where the phantom was held stationary, changes in the measurement resolution are due solely to changes in pulse separation: there is no change in the degree of correlation as evidenced by Figure 7.5(c) which shows that the cross-correlation amplitude remains close to unity across the range of pulse separations. Figure 7.5(a) shows that, for $V = 0.00$ m/s, the measurement resolution is independent of T, as expected, but is up to three times the fundamental limit at each pulse separation value. This deviation from the ideal may be due to factors such as fluctuations in laser pulse energy, timing jitter in the synchronization of the two lasers and spurious absorbers moving in the water.

When the phantom is moving, the measurement resolution depends not only on the laser pulse separation, but also on the velocity, and therefore the degree of correlation. Figures 7.5(a) and 7.5(b) show that, at low pulse separations $T = T_{\max} < 0.5$ (indicated with the darkest shading), the absolute resolution is again fairly consistent, but poorer than for the stationary phantom due to reduced correlation, which is exacerbated by irregularity in the wheel rotation since this produces non-uniform absorber motion. The percentage resolution increases in proportion to $1/T$ as the time shift becomes larger compared to the time sampling interval δt_s, as expected. There is a consistently high degree of correlation over this range of pulse separations ($T = T_{\max} < 0.5$), as illustrated in Figure 7.5(c), although it is evident that even for these small time shifts there is a reduction in the crosscorrelation amplitude compared to the stationary case. As the pulse separation is increased further ($0.5 < T = T_{\max} < 1$, lighter shading) both the measurement resolution and the cross-correlation amplitude deteriorate due to de-correlation between waveforms in each pair. This de-correlation marks the approach towards the limiting pulse separation $T_{\max}$ (Equation 7.2), during which there is a progressive increase in the fraction of illuminated absorbers that move out of the transducer focal beam between the two laser pulses. For measurements exceeding $T_{\max}$, the near-total de-correlation of the waveform pairs means that measurement resolution is no longer dependent on velocity, or indeed pulse separation.

The results in Figure 7.5 have been used to demonstrate the effects of increasing pulse separation on the experimentally determined resolution of measurements made at fixed velocities. Since the measured time shift is proportional to V as well as T, the general trends observed in Figure 7.5 may also be expected in the variation of measurement resolution with increasing velocity (at fixed pulse separation).

Figure 7.6 illustrates the trends in resolution for the data shown in Figure 7.1, where the pulse separation is fixed ($T = 1.5$ ms), and the velocity is varied: the resolution values of the measurements made using the 3.5 MHz, 5 MHz, and 20 MHz transducers

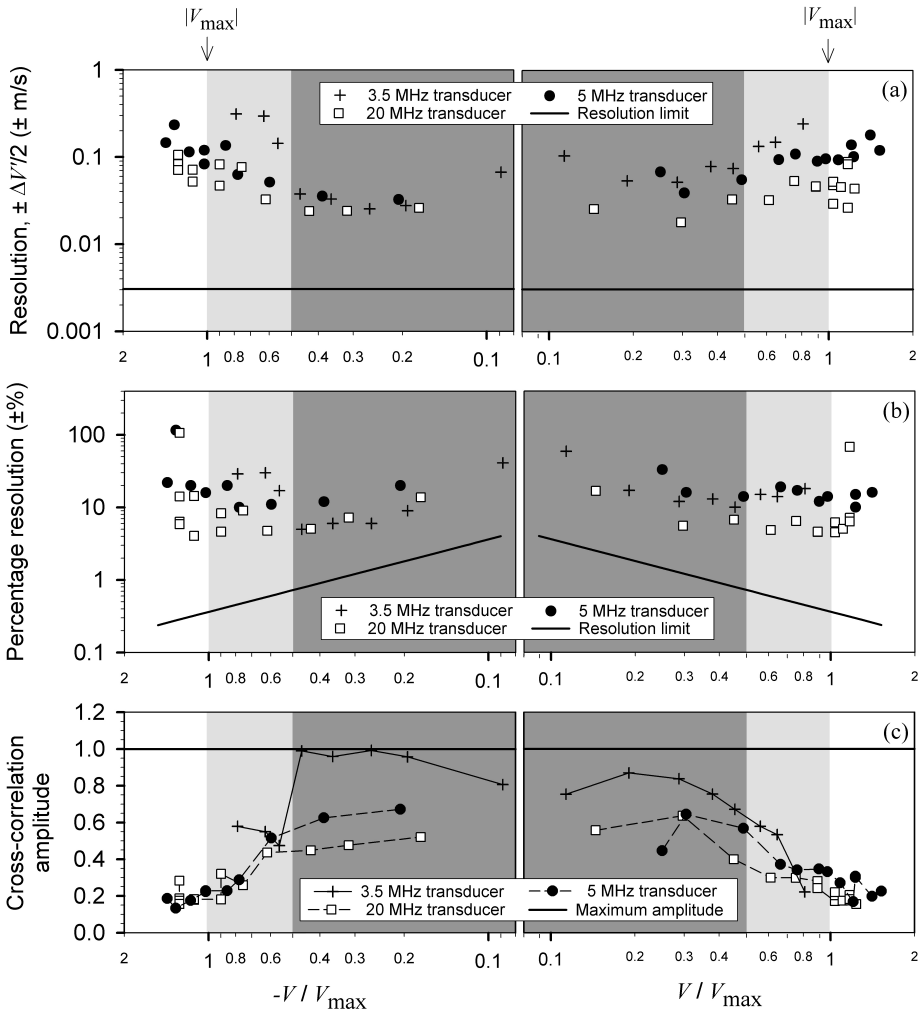

Figure 7.6: Resolution and cross-correlation amplitude as a function of $V/V_{\max}$ for the data shown in Fig. 7.1. (a) Resolution values. The solid line shows the fundamental resolution $\pm\delta V/2$ of the system limited by a temporal sampling interval $\delta t_s = 4$ ns. (b) Percentage resolution values. (c) Cross-correlation amplitudes for the data shown in (a) and (b).

are shown for the different values of $|V/V_{max}|$. Figure 7.6(a) shows the absolute resolution values and in Figure 7.6(b) the percentage resolution is shown, relative to the measured velocity values V' (Equation 7.6). Comparison of the resolution at different velocities with the cross-correlation amplitudes shown in Figure 7.6(c) indicates how the resolution is affected by the degree of correlation between waveform pairs. As in Figure 7.4, the x axis data have been rescaled to give the velocity as a proportion of the $|V_{max}|$ values.

For $0 \leq |V/V_{max}| < 0.5$ (dark grey shading) the measurement resolution [Figure 7.6(a)] appears to be approximately consistent (average ±0.02 m/s for the 20 MHz transducer, ±0.05 m/s for the 5 MHz transducer and ±0.05 m/s for the 3.5 MHz transducer), as expected from Equation 7.5. The consistency in the absolute resolution means that the percentage resolution improves inversely with increasing velocity, as illustrated in Figure 7.6(b), which is comparable to the trend with increasing pulse separation shown in Figure 7.5(b). Over this velocity range, the cross-correlation amplitudes [Figure 7.6(c)] maintain fairly steady average values of 0.5, 0.6 and 0.9 for the 20 MHz, 5 MHz and 3.5 MHz transducers, respectively. All three data sets exhibit a drop in cross-correlation amplitude over the range $0.5 \leq |V/V_{max}| < 1$ (lighter grey shading), as well as decreases in absolute and percentage resolution [Figures 7.6(a) and 7.6(b)]. These changes are explained by the loss of correlation associated with an increasing proportion of absorbers moving out of the acoustic focal beam during the time between the two laser pulses; the de-correlation is also exacerbated by the wheel motion, which becomes increasingly irregular with increasing velocity. Beyond $|V_{max}|$ there is minimal correlation and the measured velocities bear little association with the known values, and therefore the relationship of measurement resolution with measured or known velocity is no longer valid.

Both Figures 7.5 and 7.6 illustrate the competing effects of the increase of time shift and the loss of correlation on resolution. The measurement resolution firstly improves as the time shift becomes increasingly larger compared to the time sampling interval and then, for longer pulse separations, as the absorbers are swept out of the transducer field-of-view, the influence of the loss of correlation begins to dominate and the resolution becomes poorer. The de-correlation effect appears to most notably degrade measurement resolution for pulse separations T greater than about 0.5 T_{max} (Figure 7.5) and for velocities V' greater than about 0.5 $|V_{max}|$ (Figure 7.6); below these thresholds the resolution appears to follow the theoretical inverse trend due to the finite sampling interval. For measurement of a particular velocity, the resolution can therefore be optimized by selecting the pulse separation such that T is as large as possible but still below the 0.5 T_{max} threshold; this will ensure that the sampling interval effect and the

correlation effect are both minimized.

In general, the resolution for all measurements made below $|V_{max}|$ is expected to scale inversely with transducer frequency. This is because a low detector frequency results in a broad cross-correlation peak and hence a greater uncertainty in the location of the maximum. This behaviour is demonstrated in Figure 7.6 by the absolute and percentage resolution values for the 5 MHz and 20 MHz transducers, and it is also apparent that the poorest absolute resolution data is that acquired with the 3.5 MHz transducer.

7.4 Measurement scalability

In this study, pulsed photoacoustic Doppler velocity measurements were limited to the range 0.15 - 1.5 m/s due to experimental limitations as outlined in Section 5.1.1. However, a key feature of the technique is its scalability, enabling measurement of much lower velocities by appropriate choice of the time separation between the laser pulses.

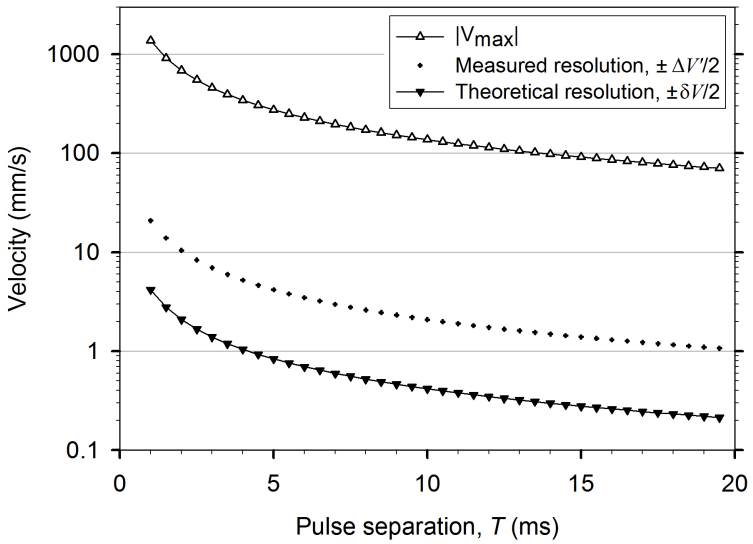

Figure 7.7: Scaling of theoretical resolution $\pm\delta V/2$, measured resolution $\pm\Delta V'/2$ (assuming $T < 0.5\ T_{max}$) and maximum measurable velocity V_{max} with increasing pulse separation T. The values are calculated based on the 5 MHz transducer (w = 0.97 mm) with $\theta = 45°$, and a sampling interval δt_s = 4 ns.

Theoretical values for maximum measurable velocity $|V_{\max}|$ and minimum detectable velocity (resolution) $\pm\delta V/2$ can be calculated for any pulse separation T using Equation 7.1 and Equation 7.5, respectively. Figure 7.7 shows these data plotted for the 5 MHz transducer ($w = 0:97$ mm, $\theta = 45°$, $\delta t_s = 4$ ns) over a range 1.0 ms $\leq T \leq$ 19.5 ms and illustrates how the range of measurable velocities scales with increasing pulse separation. A long pulse separation improves measurement resolution by reducing the influence of the finite temporal sampling interval δt_s. For example, a maximum velocity of nearly 0.7 m/s is measurable using a pulse separation of 2 ms, which also gives a resolution of ±2 mm/s. Increasing the pulse separation to 8 ms would reduce $|V_{\max}|$ by a factor of 4 to 0.17 m/s, but the resolution would improve correspondingly, allowing measurement of velocities down to ±0.5 mm/s. From the graph and the equations, it is evident that the ratio between $|V_{\max}|$ and $\pm\delta V/2$ remains constant for all pulse separations.

In practice, as seen in Figure 7.5 and Figure 7.6, the minimum detectable velocity $\pm\Delta V'/2$ obtained experimentally is worse than the theoretical limit $\pm\delta V/2$ by at least a factor of five. This discrepancy is chiefly a result of de-correlation caused by absorbers moving out of the transducer focal beam; however, for pulse separations below 0.5 $T_{\max}$ the de-correlation effect is sufficiently small such that the measurement resolution values still follow the theoretical inverse trend defined by the finite sampling interval. To reflect the discrepancy between the theoretical and experimental resolution values, and provide a realistic indication of the practically achievable resolution, values of $5 \times \delta V/2$ are also plotted in Figure 7.7 to represent the measured values $\pm\Delta V'/2$. These reflect the variation of the resolution with pulse separation that can be expected to be achieved in practice using the 5 MHz transducer. These values suggest that pulse separations of $T \geq 20$ ms are required to attain a measurement resolution of ±1 mm/s. However, adjustment of other experimental factors (for example, increasing the detector bandwidth) could improve the measurement resolution values $\pm\Delta V'/2$ and push them closer to the theoretical limit $\pm\delta V/2$.

7.5 Spatial resolution

The spatial resolution of the velocity measurements can be defined in lateral and axial directions relative to the axis of the transducer receive beam. The lateral spatial resolution is defined by the FWHM beam width of the transducer (w in Figure 7.2), whereas the axial spatial resolution is determined by the length of the range gate (D in Figure 4.1). The effect of the axial spatial resolution on the accuracy and resolution of the velocity measurements was investigated by sequentially reducing the range gate ap-

plied to FastFrame data sets (25 waveform pairs), which is equivalent to progressively increasing the axial resolution. This is the resolution that would be achieved in the case where absorbers are distributed along the transducer axis, even though the wheel phantom used in this study was confined to a single depth.

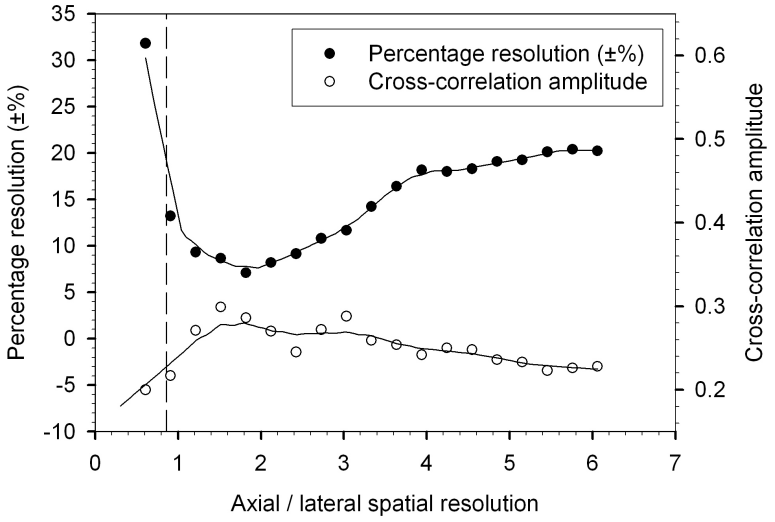

Figure 7.8: Variation of velocity resolution and cross-correlation amplitude with the ratio of axial to lateral spatial resolution. Acquisition with the 5 MHz transducer defines the beam width (lateral spatial resolution) to be 0.97 mm, and the length of the range gate (axial resolution) was varied from 6.0 to 0.6 mm. The data points are derived from one measurement, which is plotted in Figure 7.1(b), for which the velocity was $V = -0.68$ m/s (0.86 $V_{\max}$). Correlation is lost for axial: lateral spatial resolution ratios to the left of the dashed line at 0.86.

Figure 7.8 shows the results for one FastFrame data set of 25 waveform pairs obtained using the 5 MHz transducer with the wheel phantom moving at a velocity of 0.86 $V_{\max}$. The percentage velocity resolution and cross-correlation amplitude were computed for different range gates. The results were then plotted as a function of the ratio of the axial resolution (defined by the range gate) to the lateral resolution (defined by the FWHM beam width). As the range gate is reduced relative to the beam width the velocity resolution initially improves and there is a corresponding increase in the cross-correlation amplitude. This behaviour is due to rejection of the un-correlated data existing in the extremities of the range gate where there is no PA signal; the proportion of correlated data within the range gate is thereby increased. However, as the range gate is reduced further, the two spatial resolution values become comparable (range gate: transducer beam width $\rightarrow 1$) and the velocity resolution and cross-correlation amplitude deteriorate; this is due to over-restriction of the range

gate leading to rejection of correlated parts of the signals arising from absorbers lying in the extremities of the transducer beam profile (i.e. regions just outside the FWHM beam width), but which are nonetheless still sensitive to PA signals. When the range gate is smaller than the transducer beam width it becomes the limiting factor for $|V_{max}|$. In this example, the phantom is moving at a velocity of 0.86 V_{max}, which means that the absorbers traverse 86% of the transducer beam width in the interval between the two illumination pulses. Therefore, once the range gate becomes less than 86% of the transducer beam width (dashed line in Figure 7.8) there is no correlation between the waveform pairs. This gives rise to a dramatic increase in fractional error and an associated increase in percentage velocity resolution.

7.6 Summary

Several conclusions in relation to the maximum measurable velocity, accuracy and resolution can be drawn.

Firstly, the maximum velocity $|V_{max}|$ is defined by the time taken for the absorbers to traverse the transducer focal beam. When that time is less than the pulse separation, complete de-correlation occurs and accurate velocity estimates can no longer be obtained. For measurements made at velocities below the upper limit, a high level of quantitative accuracy ($< 1\%$) has been demonstrated. The velocity resolution is at best less than 4% of the measured value, but may be improved by increasing the transducer bandwidth and/or centre frequency. This is evidenced in Figure 7.6 where the mean absolute and percentage resolution values obtained using the 5 MHz transducer (bandwidth 2.25 MHz) are 2-3 times poorer that the respective values acquired using the 20 MHz transducer (13 MHz bandwidth).

Under the ideal conditions presented by the disc phantom in this study, the movement of the absorbers is unidirectional and the degrading effect of de-correlation on measurement resolution can be minimised using pulse separations $T < 0.5\ T_{max}$.Whilst the lateral spatial resolution of the velocity measurements is determined by the transducer beam width, the axial spatial resolution depends on the length of the range gate. Figure 7.8 suggests that the velocity resolution may be optimised using a range gate slightly larger than the transducer beam width.

Within a blood vessel, non-uniform movement of RBCs may cause correlation to be lost more rapidly than in the ideal case, necessitating shorter pulse separations and a lowering of the 0.5 T_{max} threshold. However, the following chapter presents studies of absorbers flowing in tubes, which reveal additional challenges relating to the range of flow velocities, coupled with the limited penetration of light into the tube.

8

Results: fluid phantoms

Having successfully demonstrated the principle of pulsed photoacoustic flowmetry using a wheel phantom (Chapter 7), the method was applied to more tissue-realistic fluid phantoms. These comprised suspensions of absorbers flowing within optically transparent tubes, as described in Section 5.1.2, and thus no longer presented the simple situation of two-dimensional, bulk absorber motion as in the wheel phantom.

8.1 Carbon microspheres and different illumination schemes

The initial velocity measurements were made with the carbon microspheres, and using the setup with two lasers [Figure 5.1(b), page 68], since these were the experimental components available at the time. The findings made under these conditions led to further investigations and refinement of the experiments, the results of which are described in this section and in the subsequent sections of this chapter.

The results in Figure 8.1 show velocity measurements made with the carbon microspheres, and using the Ultra and Minilite lasers with various time separations between the pulses. For a pulse separation of $T = 1$ ms [Figure 8.1(a)] the measured values gen-

erally agree well with the known velocities up to about 75 mm/s, which is the $|V_{\max}|$ value observed for this data set. This value is denoted $|V_{\max}|_{\text{obs}}$ and is the experimental equivalent of $|V_{\max}|$; it can therefore be defined analogously to Equation 7.1, using a de-correlation distance d_{D} that can be considered as an effective transducer beam width:

$$|V_{\max}|_{\text{obs}} = \frac{d_{\text{D}}}{T\,|\sin\theta|} \tag{8.1}$$

As T is increased, the $|V_{\max}|_{\text{obs}}$ values decrease inversely as expected, and the inverse relationship is plotted in Figure 8.1(e). However, at each pulse separation, the $|V_{\max}|_{\text{obs}}$ values are significantly smaller than predicted by $|V_{\max}|$, with de-correlation occurring over a distance d_{D} that is five times smaller than the transducer focal beam width w.

It is possible that premature de-correlation could arise from laser timing jitter. To exclude this possibility, the microsphere-filled tube was manually shifted as described in sub-section 5.1.3 and Section 6.1, thus eliminating T. Time shift measurements t_s' are shown in Figure 8.2(a) and (b) for experiments where each laser was used separately: in (a) the Ultra laser generated both the first and the second PA signals in each pulse pair, in between which the tube was manually shifted on a translation stage; likewise for the data in Figure 8.2(b) where the Minilite was used instead of the Ultra. It is evident from Figure 8.2(a) and (b) that manually shifting the tube, rather than flowing the microspheres through it, gives excellent correlation for time shifts up to values corresponding to or even exceeding $\left|t_{s,\max}\right|$ (see discussion on page 102) calculated from the transducer focal beam width w (Equation 7.3, page 101). The observed maximum accurately measured time shift is denoted $\left|t_{s,\max}\right|_{\text{obs}}$and defined analogously to $|V_{\max}|_{\text{obs}}$ using the de-correlation distance d_{D} in place of w (see Equations 7.3 and 8.1):

$$\left|t_{s,\max}\right|_{\text{obs}} = \frac{d_{\text{D}}}{c\,|\tan\theta|} \tag{8.2}$$

Figure 8.2(c) shows results for the case where the first and second photoacoustic signals were generated using the Ultra and Minilite respectively. Again there are instances of accurate measurements up to $\left|t_{s,\max}\right|_{\text{obs}} \approx \left|t_{s,\max}\right|$, but the majority of time shift measurements demonstrate poor accuracy, even where the known time shift values are much smaller than $\left|t_{s,\max}\right|$. In other words, there is poor correlation even in cases where the absorbers have not moved entirely out of the transducer focal beam by the time the second laser pulse is emitted. This premature de-correlation may result from misalignment of the two laser beams or discrepancies in their energy profiles; the latter is a likely cause given that the beams are coupled into separate multi-modal fibres. Different illumination profiles will result in differences in the photoacoustic signals since their shapes depend on the spatial distribution of absorbed energy. In

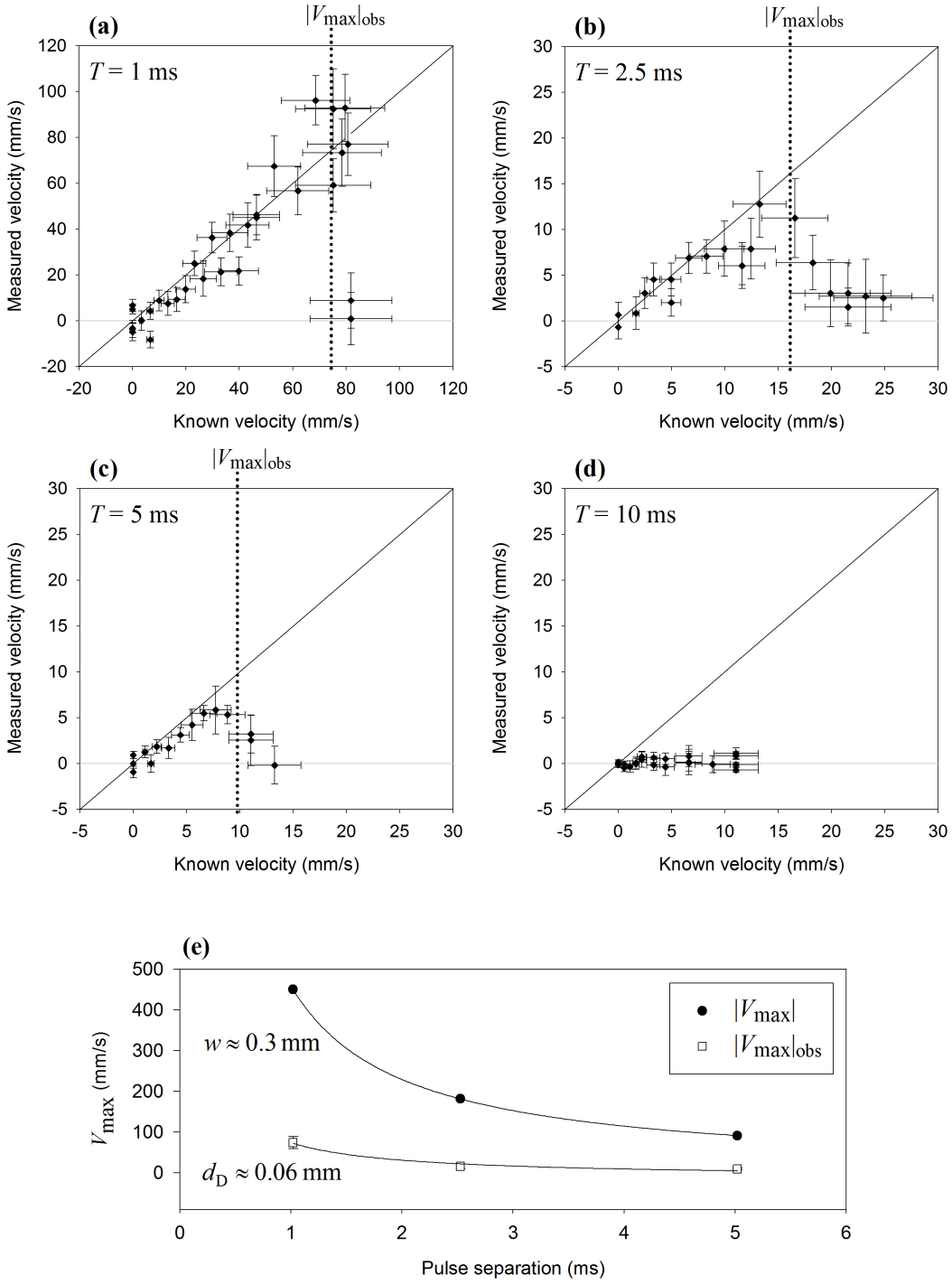

Figure 8.1: Velocity measurements acquired using the Ultra and Minilite lasers and the 30 MHz focussed transducer with the 22 μm spheres flowing in the 800 μm tube at various speeds set using the syringe pump. Measurements for pulse separations T =1, 2.5, 5 and 10 ms are shown in (a), (b), (c) and (d) respectively. $|V_{max}|_{obs}$ values derived from (a), (b) and (c) are shown in (e) as a function of pulse separation T and compared with calculated values of $|V_{max}|$ (Equation 7.1). The resulting de-correlation distance d_D is five times smaller than the transducer focal beam width w.

such cases, the correlation or de-correlation of two successive PA signals is not purely due to the movement of the underlying distribution of absorbers and therefore the measured time shift may not reflect the absorber motion. Note however that Figure 8.2(c) demonstrates that there are still instances of good correlation when using two lasers, otherwise it would not have been possible to obtain measurements as accurate as those in Figure 8.1. Nonetheless, it is desirable to eliminate the potential for different illumination profiles to reduce measurement accuracy.

A single high-repetition-rate laser can overcome the problem of poor correlation arising from two different laser illumination profiles. Figure 8.3 shows results for the 22 μm spheres flowing in the 800 μm tube as before (Figure 8.1), but now using the FQ laser pulsing at 1 kHz (see Section 5.2) instead of triggering the Ultra and Minilite lasers alternately. A repetition rate of 1 kHz provided $T = 1$ ms allowing direct comparison with Figure 8.1(a). From Figure 8.3(a) it is difficult to see any improvement in the results: the measurement resolution (vertical error bars) is very poor, possibly due to the lower beam energy giving rise to a smaller SNR. Better data quality is obtained by taking the mean of five measurements at each velocity and propagating the y-axis errors as shown in Figure 8.3(b). Here the measurement resolution takes a mean value of 5.5 mm/s for velocities up to 55 mm/s, and it is only beyond $|V_{\max}| = 66$ mm/s that the error bars become disproportionately large. Figure 8.4 compares the results in Figure 8.1(a) and Figure 8.3 for velocities below 55 mm/s: it is evident that use of a single laser rather than two separate lasers improves the measurement accuracy and, to a lesser extent, the measurement resolution.

Figure 8.5 shows measurements at four different pulse separations. The data was acquired using the FQ laser and the 30 MHz focussed transducer with the 22 μm spheres flowing in the 800 μm tube at various speeds set using the syringe pump. A repetition rate of 2 kHz enabled any multiple of $T = 0.5$ ms to be investigated from a single acquisition by correlating appropriately spaced signal pairs within the pulse train. Despite the improvement in accuracy and resolution resulting from the use of a single laser instead of two, there is still a premature loss of correlation: Figure 8.5(e) shows that, as in Figure 8.1(e), the distance d_{D} over which de-correlation occurs is much smaller than the transducer focal beam width w leading to an observed maximum measurable velocity, $|V_{\max}|_{\mathrm{obs}}$, that is considerably smaller than the calculated $|V_{\max}|$.

Figure 8.6 compares the discrepancies between $|V_{\max}|_{\mathrm{obs}}$ and $|V_{\max}|$ for the wheel phantom and for the three sizes of carbon microspheres. For the data acquired with

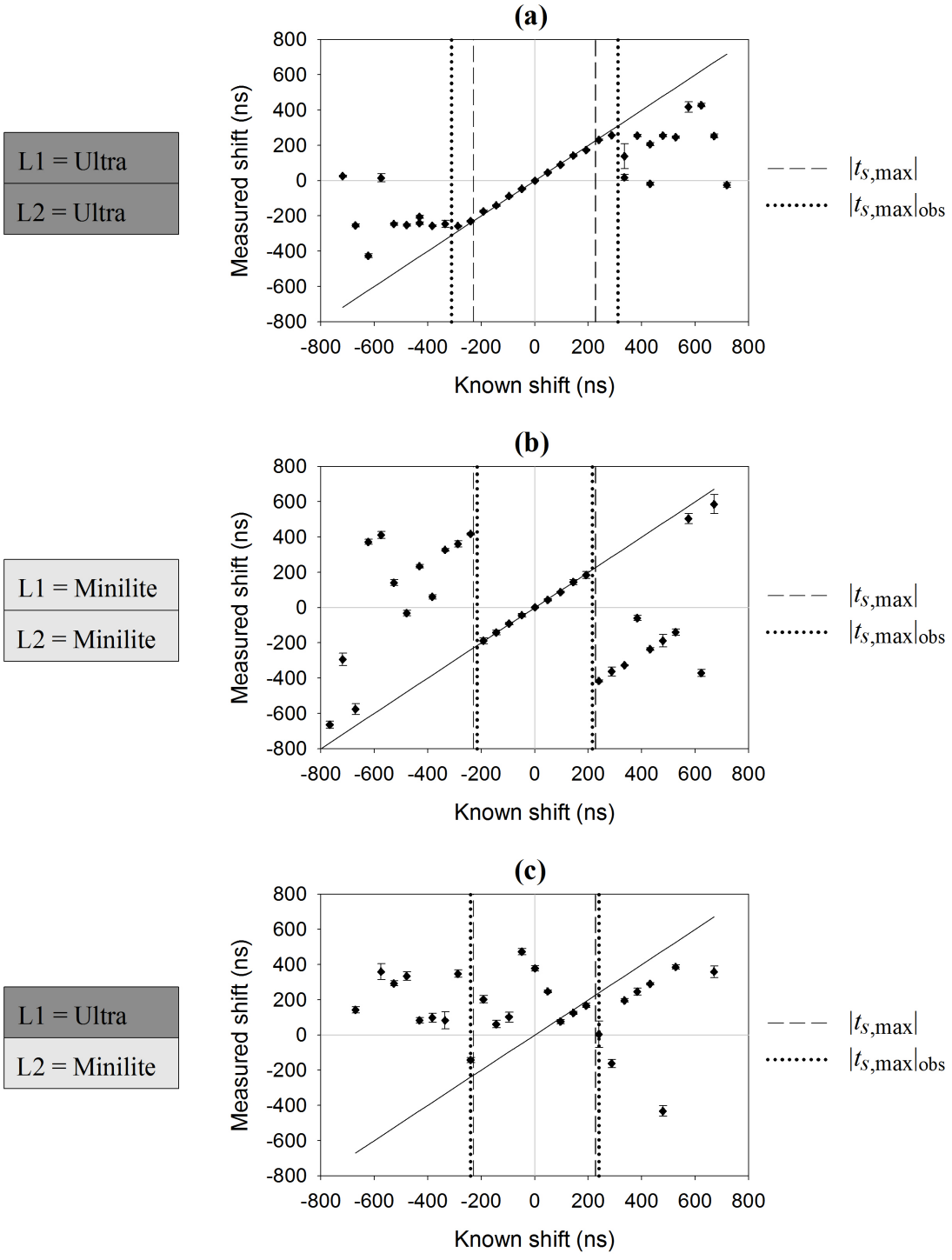

Figure 8.2: De-correlation caused by discrepancies between the Ultra and Minilite laser beams. The measured time shifts resulted from manual shifting of the 6 μm carbon microspheres in the 800 μm tube, and signal acquisition with the 30 MHz focussed transducer. L1 and L2 refer to the lasers used to illuminate the tube before and after the shift respectively. In (a) the Ultra laser was used for both illuminations, and in (b) only the Minilite was used. In (c) the Ultra was used for the first illumination and the Minilite for the second.

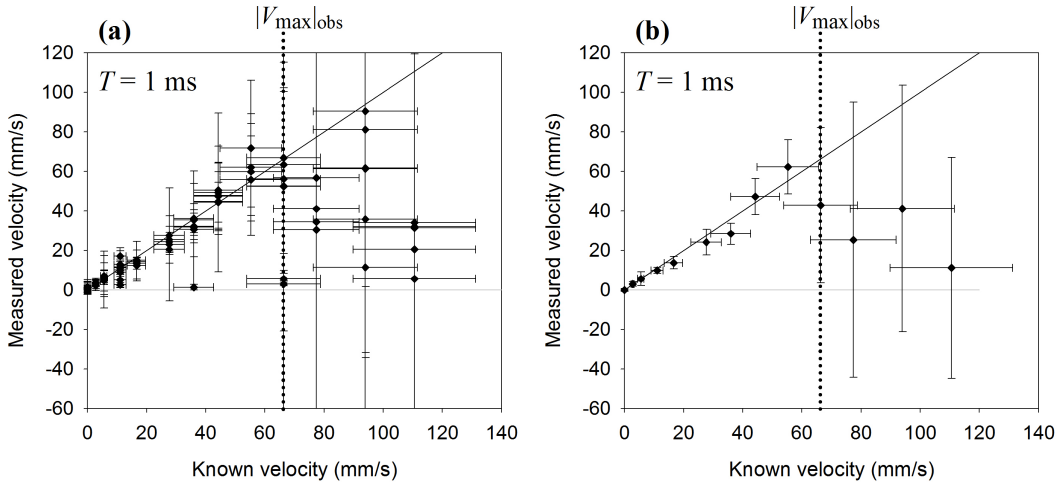

Figure 8.3: Velocity measurements acquired using the FQ laser and the 30 MHz focussed transducer. The data is for the 22 μm spheres flowing at various speeds in the 800 μm tube. (a) Raw data. Five measurements were made at each velocity. (b) Mean values of the data in (a) with propagation of the vertical error bars.

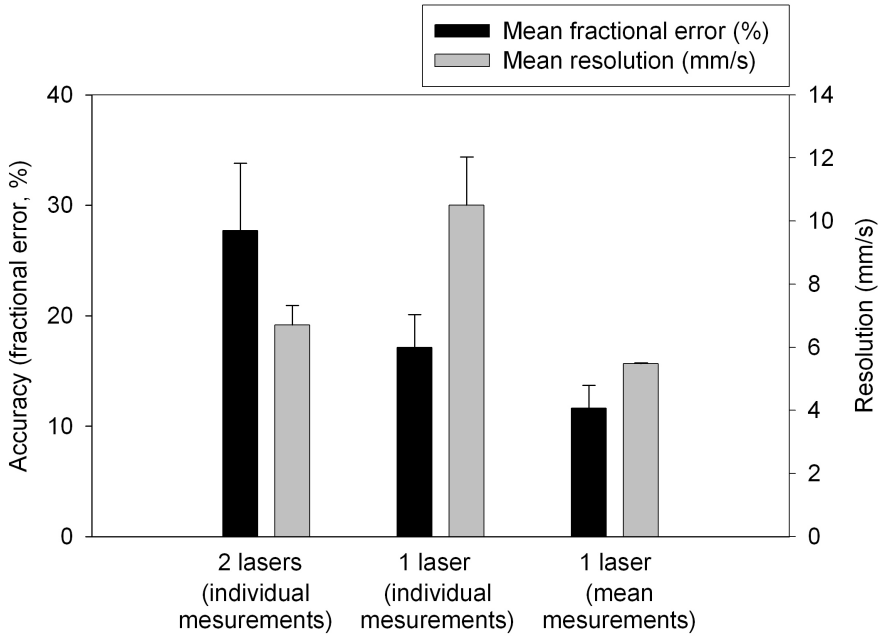

Figure 8.4: Accuracy (fractional error) and resolution of velocity measurements made with the two lasers (Ultra and Minilite) and with the single FQ laser. Mean values for the fractional error and measurement resolution were calculated for the 22 μm spheres flowing in the 800 μm tube at speeds up to 55 mm/s. The bars and errors correspond to the mean and standard error for the data shown in Figure 8.1(a) [bar labelled "2 lasers (individual measurements)"], Figure 8.3(a) ["1 laser (individual measurements)"] and Figure 8.3(b) ["1 laser (mean measurements)"].

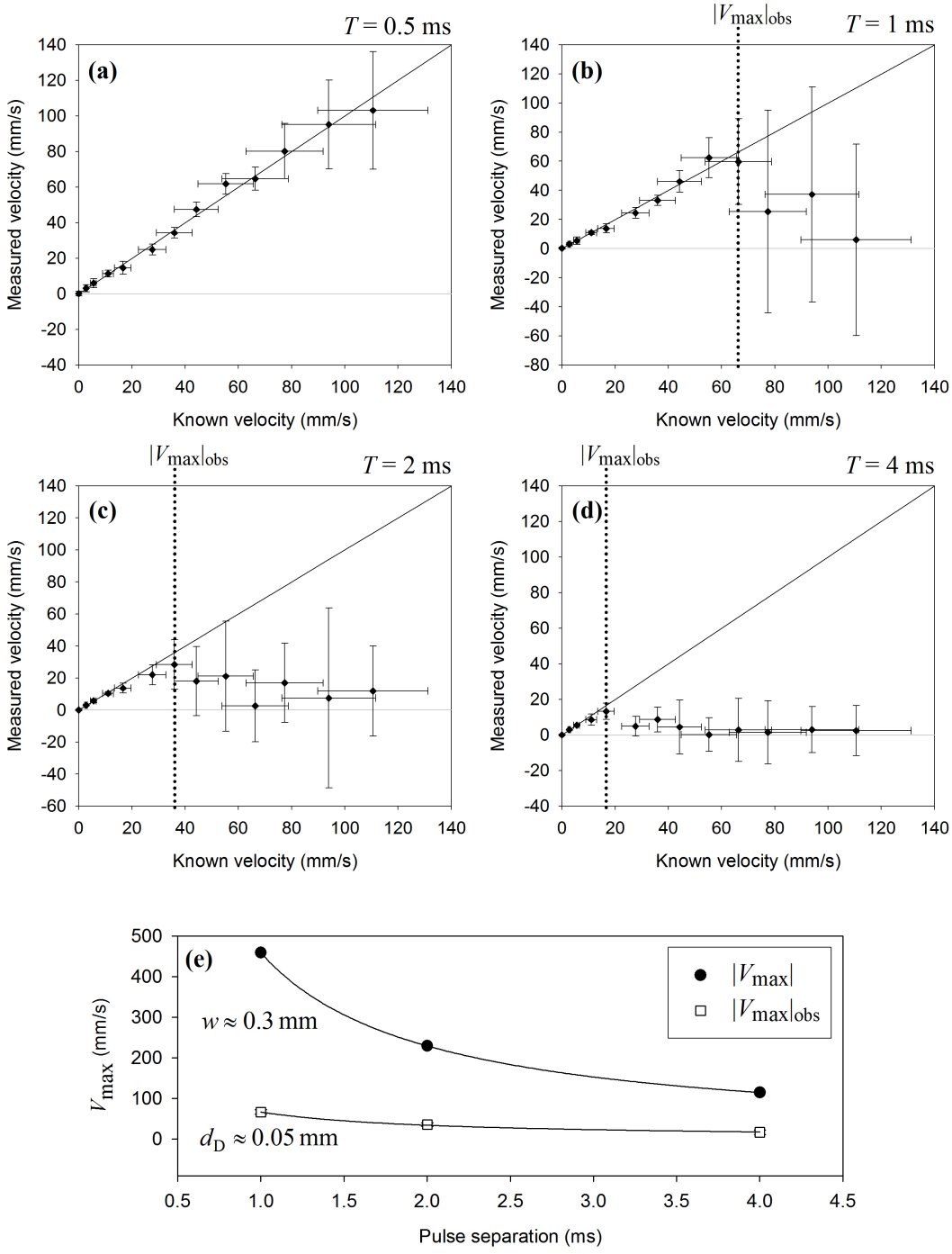

Figure 8.5: Velocity measurements acquired using the FQ laser and the 30 MHz focussed transducer with the 22 μm spheres flowing in the 800 μm tube at various speeds set using the syringe pump. Measurements for pulse separations T =0.5, 1, 2 and 4 ms are shown in (a), (b), (c) and (d) respectively. $|V_{\max}|$ values derived from (b), (c) and (d) are shown in (e) as a function of pulse separation T. The resulting de-correlation distance d_{D} is six times smaller than the transducer focal beam width w.

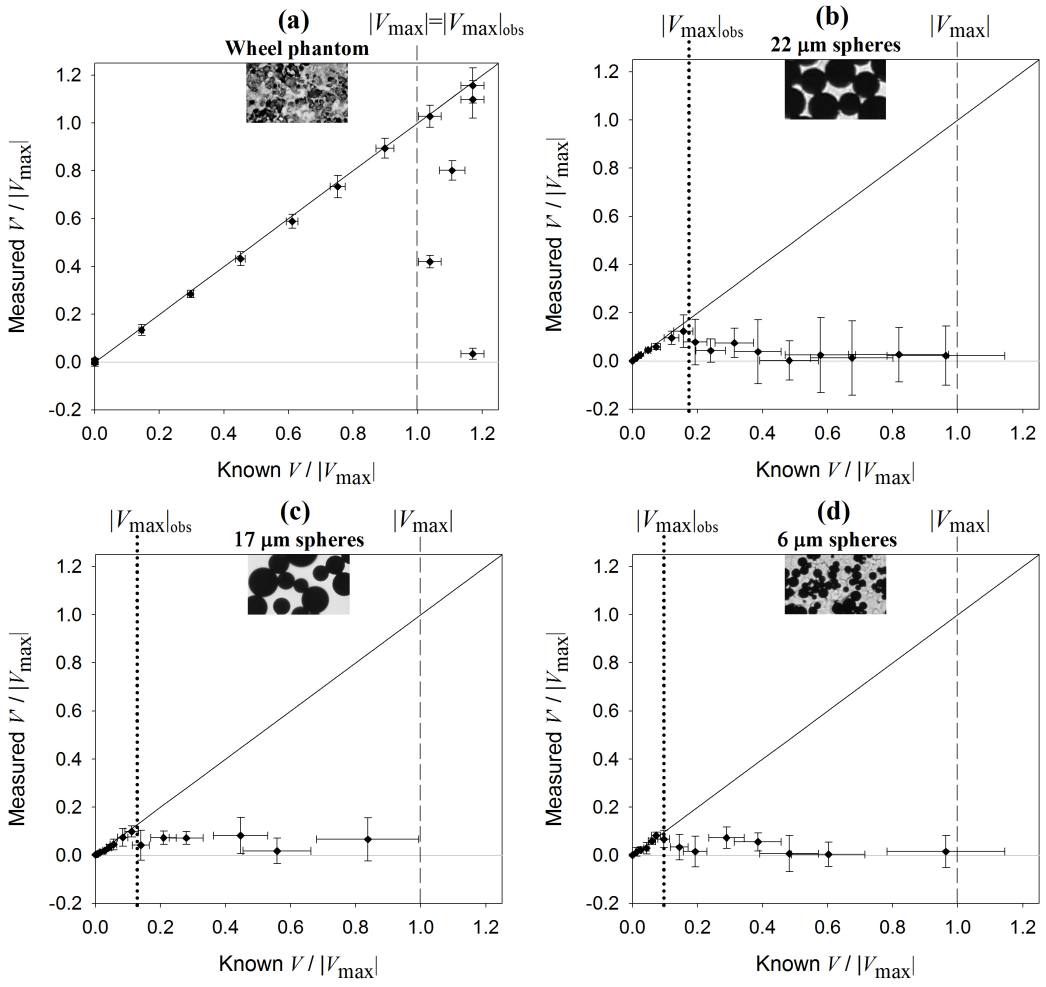

Figure 8.6: Comparison of observed and calculated maximum measurable velocities, $|V_{max}|_{obs}$ and $|V_{max}|$, for the wheel phantom (a) and three different sizes of microspheres, 22 μm, 17 μm and 6 μm in (b), (c) and (d) respectively, each in suspensions flowing in the 800 μm tube. The data for the wheel phantom is also shown in Figure 7.1, page 98, and was acquired using two different lasers (the Ultra and Minilite) and the 20 MHz planar transducer. The data for the flowing microsphere phantoms was acquired using a single laser (the FQ laser) and the 30 MHz focussed transducer.

the wheel phantom [Figure 8.6 (a)], there is a direct agreement between $|V_{\max}|_{\text{obs}}$ and $|V_{\max}|$ even though these results were acquired with the two separate lasers. The data for the three fluid phantoms were acquired using a single laser, and $|V_{\max}|_{\text{obs}}$ is less than $|V_{\max}|$ by factors of ~ 6, ~ 8 and ~ 10 for the 22 μm, 17 μm and 6 μm spheres as shown in (b), (c) and (d) respectively. It is difficult to draw any conclusion from the variation of $|V_{\max}|_{\text{obs}}$ with the microsphere diameter, since the concentration of these suspensions were also different (see Figure 5.2, page 70). However, the clear difference in $|V_{\max}|_{\text{obs}}$ values between the wheel phantom (two lasers) and the fluid phantoms (one laser) suggests that, whilst different spatial distributions of absorbed energy may lead to instances of poor correlation [Figure 8.2], a discrepancy in the illumination profiles is not the cause for the loss of correlation observed in the flowing phantoms.

The following sections in this chapter present further velocity measurements made with fluid phantoms using different tube diameters and various suspensions of absorbers, including red blood cells (RBCs). The FQ laser did not provide sufficient pulse energy at suitable wavelengths to generate sufficient SNR in RBCs. All the experiments with RBCs, and also subsequent experiments with microspheres, therefore employed a twin laser system: the "PIV laser" (see Section 5.2). This produced pulse pairs from two in-built lasers in a manner similar to the separate Ultra and Minilite lasers. However, unlike the Ultra and Minilite, the two lasers in the PIV system were co-aligned and matched in energy and so the two light pulses were, in theory, near-identical in terms of their spatial and temporal distributions. In practice, however, the beam alignment was not perfect, and the effect of this on the correlation is discussed on page 123 and in Section 10.2.

8.2 Blood velocity measurements

8.2.1 Heterogeneity: absorber compartmentalisation and concentration

The cross-correlation method relies on tracking a unique photoacoustic "signature" (see page 65), and therefore requires spatial heterogeneity of the absorbing medium. This requirement is satisfied in the case of the microspheres, since the absorber is compartmentalised in spherical structures, and, under normal circumstances, blood also provides spatial heterogeneity since haemoglobin (the dominant absorber) is contained within red blood cells (RBCs). However, it is possible for RBCs to undergo haemolysis whereby the cell membranes rupture and the haemoglobin leaks out into the surroundings, thus producing an essentially homogeneous absorbing medium. One cause of haemolysis is the movement of excessive fluid into the cell, which results

from an imbalance of ion concentrations on either side of the cell membrane. Suspension of RBCs in phosphate buffered saline (PBS) preserves this ion balance enabling the RBCs to remain intact, but immersion of RBCs in distilled water will result in haemolysis as fluid rushes down the osmotic gradient into the cell. Figure 8.7 illustrates these two conditions, and the velocity measurements made in both cases. The photographs show that for RBCs suspended in PBS (a) the cell structures are clearly visible, but after suspension in distilled water (b) only faint remnants of the red blood cell membranes are discernible, and thus there is a clear difference in heterogeneity. As expected therefore, it is difficult to track the motion of (haemolysed) RBCs in distilled water and the results in (b) show that the measurements average to zero for all velocities. However, for the RBCs in PBS (a), there is good measurement accuracy for $V < 5$ mm/s, and for $V > 5$ mm/s the measured velocity continues to increase with increasing known velocity, which suggests that there is some degree of correlation between signals even when the RBCs are moving relatively rapidly. Note also that haemolysed and suspended RBCs give similar photoacoustic signal amplitudes using an excitation wavelength of 532 nm, but it has been shown [86] that suspended RBCs produce a significantly larger photoacoustic signal than haemolysed RBCs when excited with a wavelength of 1064 nm.

In addition to the absorber compartmentalisation, it is possible that heterogeneity, and therefore the ability to track photoacoustic signatures, is also affected by the number of absorbing "packets" per unit volume. This may explain why initial attempts to measure velocity for whole blood were unsuccessful, and yet good velocity accuracy was obtained using reduced concentrations of red blood cells, for which the results are presented in this section. The dilutions were prepared by suspending the RBCs in phosphate buffered saline (PBS), rather than distilled water, in order to preserve the cell structure; care was also taken to use cells that had not disintegrated due to old age. RBC concentration is typically expressed as the fractional volume or haematocrit (Ht), which takes a normal physiological value of ~ 0.45, and therefore each suspension concentration is described in terms of Ht = 0.45. For example, a fractional volume of 0.225 would be 50% Ht.

8.2.2 Initial observations: effect of concentration and tube diameter

Figure 8.8 shows illustrative velocity measurements for three different RBC concentrations flowing in tubes of two different diameters. From Figure 8.8(a), which is for RBC suspensions flowing in a tube of diameter 390 μm, it is immediately apparent that the measured velocities under-read the "known" (average) flow velocities, and that the ac-

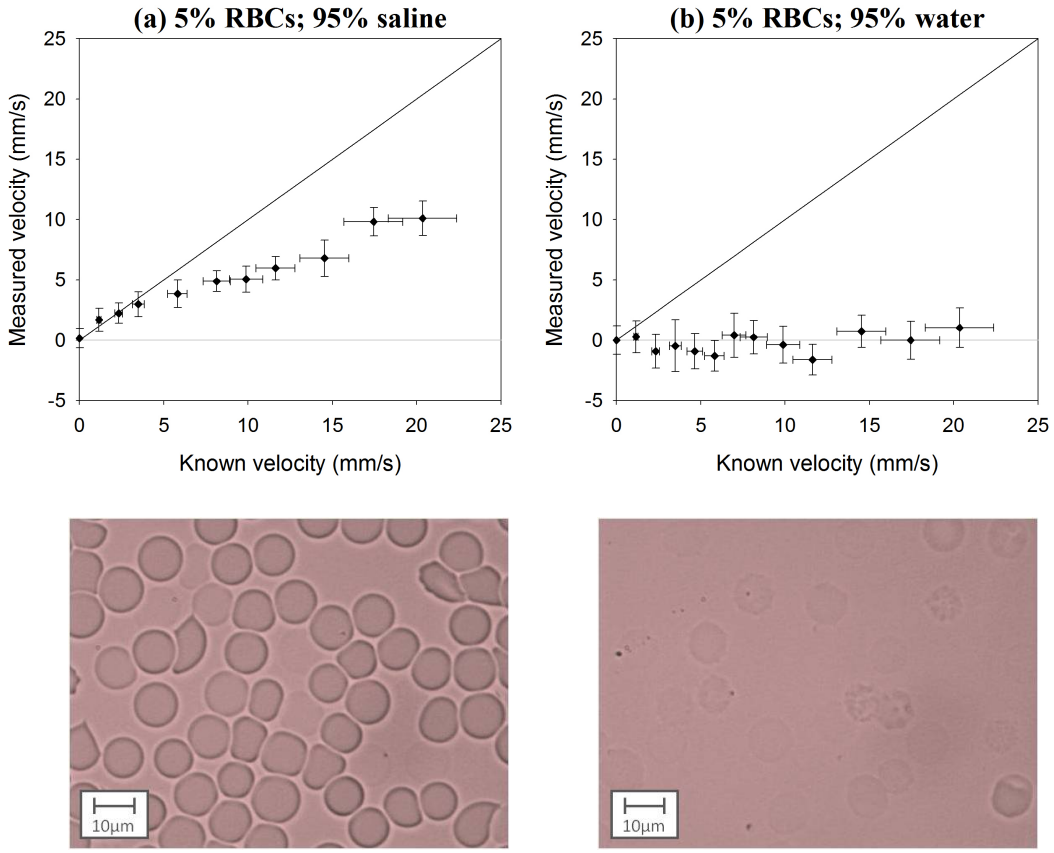

Figure 8.7: The effect of red blood cell lysis on the suspension heterogeneity and, consequently, the accuracy of the time-correlation velocity measurement method. Velocity measurements were made for a suspension of intact red blood cells (5%) in phosphate buffered saline (a) and for haemolysed red blood cells (5%) in distilled water (b). The measurements were acquired using the PIV laser with $T = 0.5$ ms and the 30 MHz focussed transducer, followed by a 10-100 MHz Butterworth filter (order 2). Microscopy images of the red blood cells are shown below the graphs.

curacy of the velocity measurements becomes poorer as the concentration is increased from 2% Ht to 6% Ht to 16% Ht. The accuracy deteriorates further for flow in a wider tube, as illustrated by the data in plots Figure 8.8(b) where the same RBC suspensions were flowed through a tube of diameter 800 μm. For the 2% Ht and 6% Ht dilutions, there is an increase of measured velocity with known velocity, but for the 16% Ht dilution the measured values remain virtually constant across the velocity range. In addition, for the 2% Ht and 16% Ht dilutions there is a zero velocity offset.

The effect of the absorber concentration and the tube diameter are investigated further in the following two sections. The zero velocity offset may be related to spatial misalignment of the two beams emitted from the twin laser system, which is discussed further in Section 10.2.

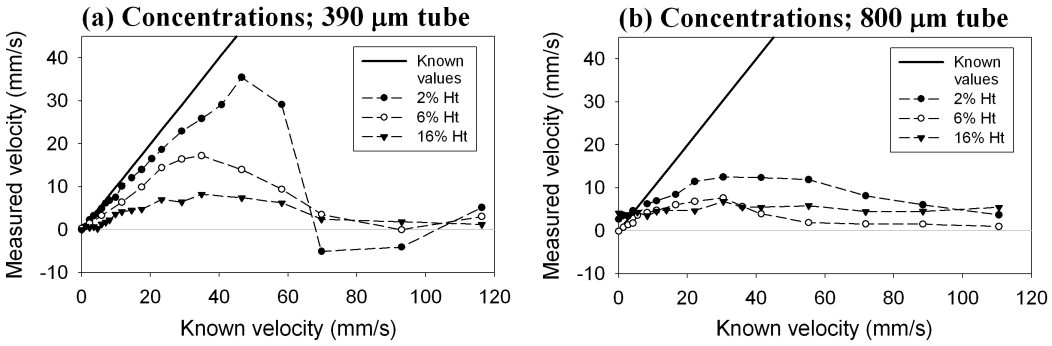

Figure 8.8: The effect of RBC concentration on the accuracy of velocity measurements made in tubes with diameters of 390 μm (a) and 800 μm (b). The measurements were acquired using the PIV laser with T = 0.5 ms and the 30 MHz focussed transducer, followed by a 10-100 MHz Butterworth filter (order 2). Error bars have been omitted for clarity.

8.3 Effect of absorber concentration

8.3.1 Concentration of red blood cells

Figure 8.8 demonstrated the improvement in velocity measurement accuracy with reduced RBC concentration of suspensions flowing in tubes of 390 μm and 800 μm. Figure 8.9 compares the accuracy and resolution of results acquired under the same experimental conditions, but for a wider range of RBC concentrations. The quality of each data set was assessed using the mean fractional error and the mean resolution calculated for known velocities $|V| < 50$ mm/s, and these mean values are plotted in (a) and (b) respectively for the different RBC concentrations. From Figure 8.9 (a) it is clear that higher RBC concentrations are associated with greater fractional error (poorer velocity accuracy); there is also a dependence on tube diameter, with poorer accuracy

obtained for the larger diameter tube at each of the RBC concentrations investigated. In (b) there is little difference in resolution values for the two different tube diameters, both showing an improvement of resolution with increasing concentration. However, this apparent improvement should be considered together with the deterioration in velocity accuracy shown in (a): for high concentrations, the measurements are consistently close to zero, and therefore the resolution appears to be high even though there is insensitivity to changes in flow velocity.

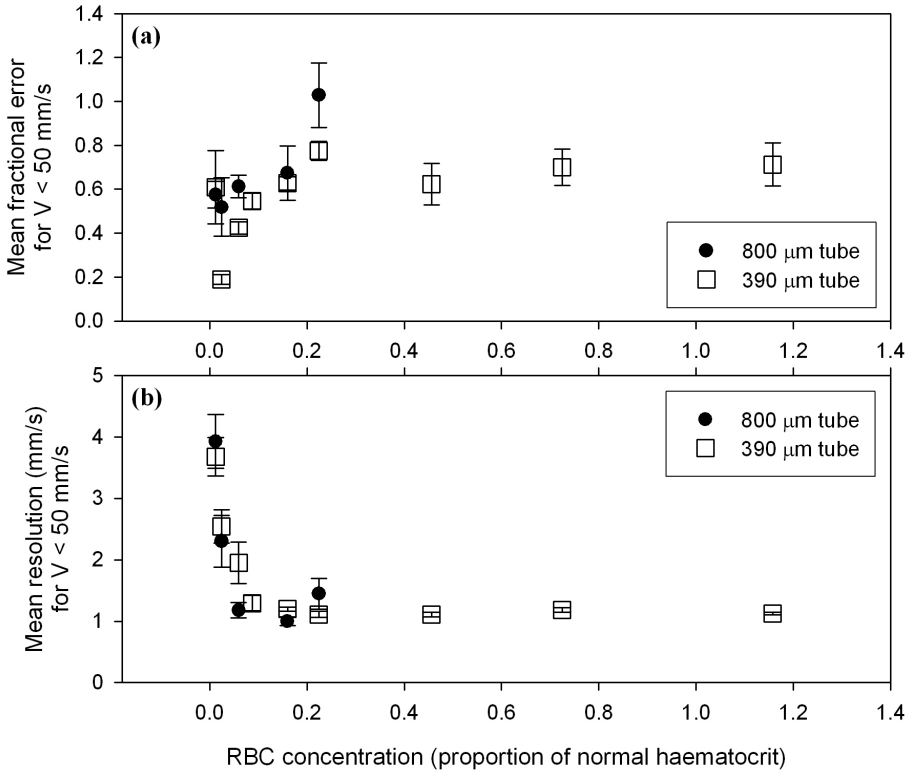

Figure 8.9: Comparison of accuracy (a) and resolution (b) for RBCs of concentrations ranging from 1% to 116% of a physiologically normal haematocrit (Ht = 0.45), and flowing in tubes of 800 μm and 390 μm diameters under the same experimental conditions described in Fig. 8.8. Mean values for the fractional error and measurement resolution were calculated for known velocities $|V| < 50$ mm/s, and the vertical error bars represent the standard errors on these mean values.

8.3.2 Concentration of red polystyrene microspheres

The effect of absorber concentration was also investigated using suspensions of red polystyrene spheres, 3 μm in diameter [see Figure 5.2 (f), page 70]. Figure 8.10 shows velocity measurements made using RBCs (a) and the red spheres (b) in suspensions of PBS and distilled water respectively, made to volume concentrations of approximately 5% and 10% respectively. These concentrations give rise to similar numbers of

particles per unit volume, as demonstrated by the bar graph in Figure 5.2. The experimental conditions were otherwise identical, allowing direct comparison between the two absorbers. It is evident from Figure 8.10 (c) and (d) that both the absorbers give very similar values for accuracy and resolution at each known velocity, and therefore it seems that their differences in size and shape, and possibly a small difference in concentration, do not affect the ability to track a unique photoacoustic signature. The red polystyrene spheres therefore serve as a realistic RBC-simulating phantom.

The plots in Figure 8.11 show velocity measurements made for four different concentrations of red spheres ranging from 5% to 80%. The percentages used to denote the red sphere volume concentrations are roughly equivalent to RBC numbers relative to the RBCs per unit volume for a normal haematocrit (Ht = 0.45). For the 5% concentration of spheres, there is good measurement accuracy for known velocities up to about 40 mm/s. The measurement accuracy across the velocity range deteriorates with increasing concentration, until for the 80% concentration the velocity measurements appear to be consistently zero. These measurements are enlarged in Figure 8.12 (a) from which it is evident that for velocities $V < 10$ mm/s there is in fact a fairly regular increase in the velocity measurements with increasing known velocity. This is made more obvious in Figure 8.12 (c) where the zero offset ($V' \approx 3$ mm/s for $V = 0$ mm/s) is subtracted from each of the data points; possible reasons for this zero offset are discussed further in Section 10.2. The results in (b) and the zero-corrected data in (d) are of additional interest: here the accuracy of measurements made for velocities $V > 4$ mm/s is improved by adding one drop of TWEEN®20 surfactant (P1379, Sigma-Aldrich) to 2.5 ml of the 80% red sphere suspension. Before adding TWEEN®20 the tube appeared to be stained even when empty, whereas the surfactant removed the staining; therefore the most likely explanation for the improvement in velocity measurements accuracy is a reduction in the numbers of spheres adhering to the tube walls. Spheres clinging to the tube walls and remaining stationary would restrict the penetration of light into the tube and also reduce the average velocity of the absorbers.

The plot in Figure 8.13 (a) compares the mean velocity resolution of velocity measurements made for red spheres of concentrations ranging from 5% to 80% and moving at known velocities $|V| < 50$ mm/s. The individual velocity measurements are shown in Figure 8.11 for a selection of these concentrations. The arrow in Figure 8.13 (a) indicates the result for the 80% suspension after addition of TWEEN®20. The lowest concentrations give results with the best accuracy for all velocities up to 50 mm/s. However, as in Figure 8.9, these measurements have the poorest velocity resolution and this is because for high flow velocities the measurements demonstrate a greater range of velocity values. An interesting observation is the change in accuracy of the

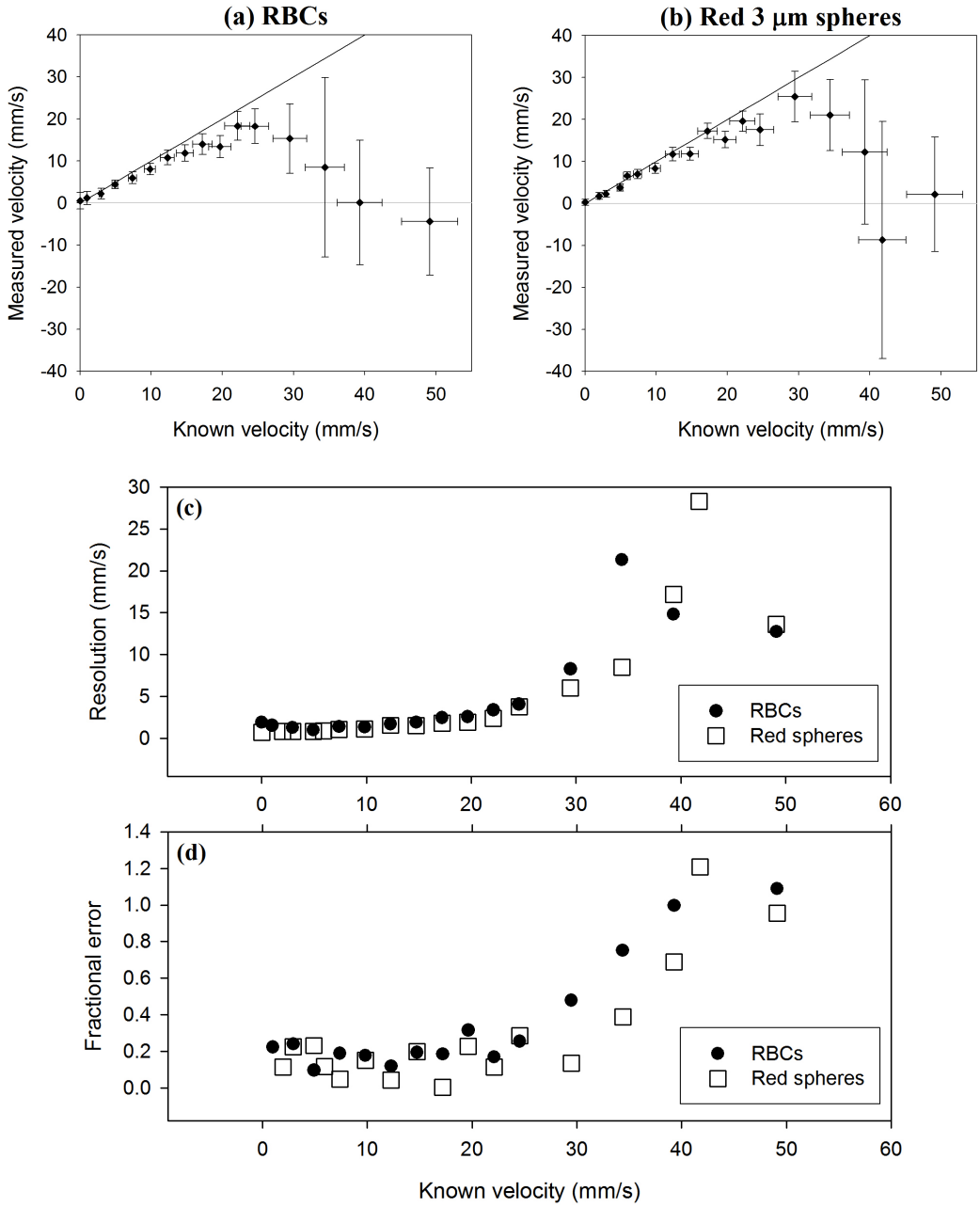

Figure 8.10: Comparison of velocity measurements made for red blood cells (a) and 3 μm red microspheres (b) both in suspensions with particle concentrations approximately equivalent to 5% Ht and flowing in a 600 μm tube. The measurement resolution and accuracy (fractional error) values are shown in (c) and (d). The measurements were acquired using the PIV laser with T = 0.5 ms and the 80 MHz focussed transducer, followed by a 10-100 MHz Butterworth filter (order 2).

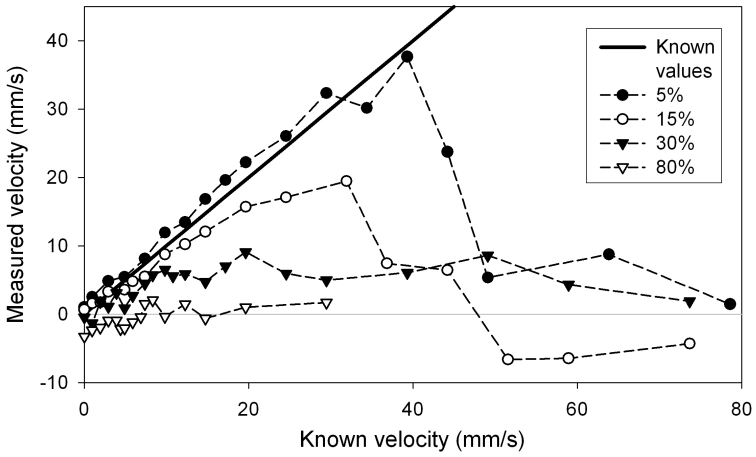

Figure 8.11: Comparison of velocity measurements made for suspensions of 3 μm red spheres in distilled water in concentrations of 5%, 15%, 30% and 80%, and flowing in a 600 μm tube. The measurements were acquired using the PIV laser with $T = 0.5$ ms and the 80 MHz focussed transducer. Error bars have been omitted for clarity.

measurement at $V = 0$ mm/s, which is shown in Figure 8.13 (b). There is a small, positive zero offset of about 1 mm/s for concentrations below 20%, but for higher red sphere concentrations the offset is negative and becomes increasingly negative with increasing concentration. The reason for this is unclear; however, the accuracy, not only of the zero velocity but also of all measurements of $|V| < 50$ mm/s, deteriorates with increasing concentration. This is shown by the mean fractional error values in (c) and (d) which were calculated for the measurements of $|V| < 50$ mm/s both before (c) and after (d) correcting for the zero offset.

The velocity measurements for various different absorber concentrations lead to two conclusions. The first is that lower concentrations of absorbers enable better measurement accuracy over a wider range of velocities: the velocity under-reading becomes progressively worse for increasing concentration, so that for the highest concentrations the measurements are consistently close to zero and therefore insensitive to changes in flow velocity. This leads to the second conclusion which concerns the velocity resolution: the lower concentrations demonstrate poorer measurement resolution and this is because at the higher velocities there is a greater distribution of measurement values. In other words, the range of measurements appears to scale with the velocity, and this may suggest that there is a greater range of velocities present in the tube. The idea of variable absorber velocity, and in particular the presence of a laminar flow profile is discussed in detail in Chapter 9. The following sub-section describes how the *concentration* of the absorbers may vary within the tube.

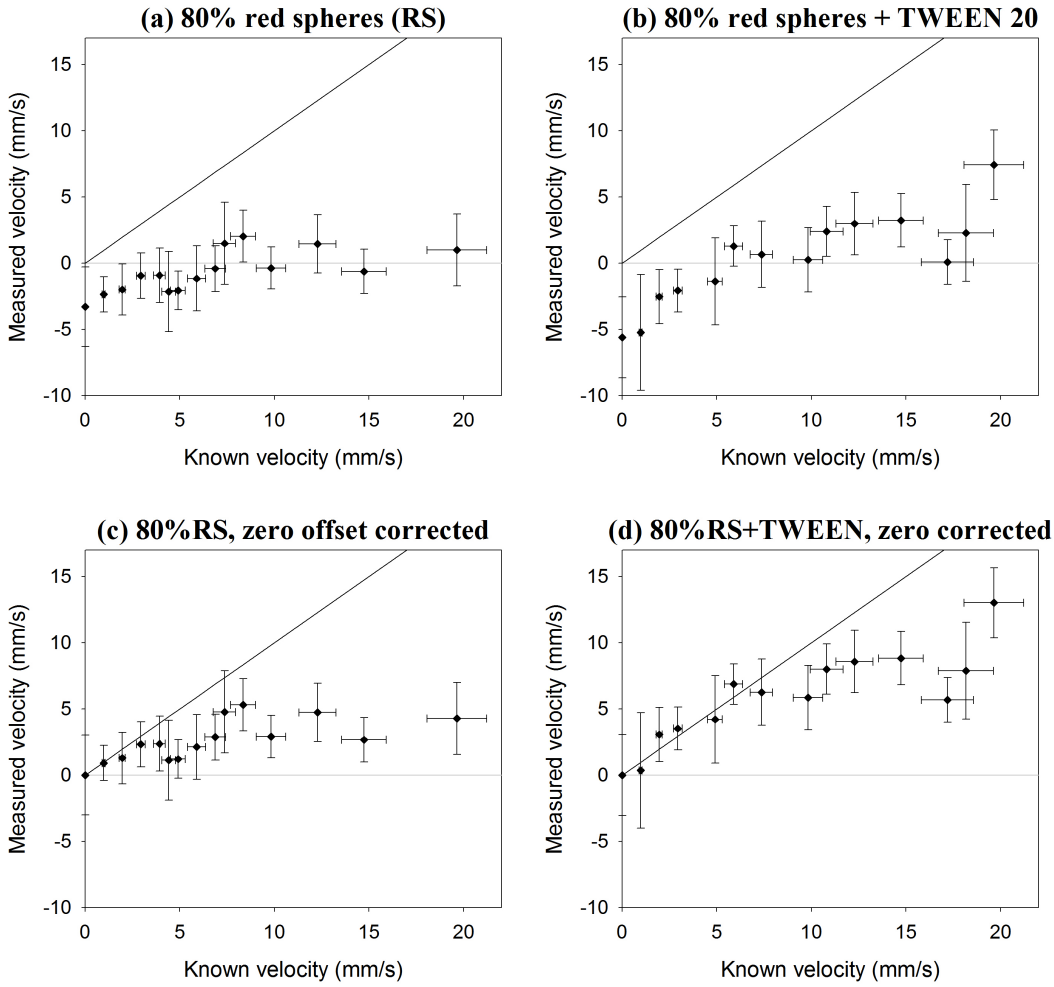

Figure 8.12: Comparison of velocity measurements made for an 80% suspension of 3 μm red spheres in distilled water before (a) and after (b) adding TWEEN®20. Both data sets have a zero velocity offset which is subtracted in (c) and (d).

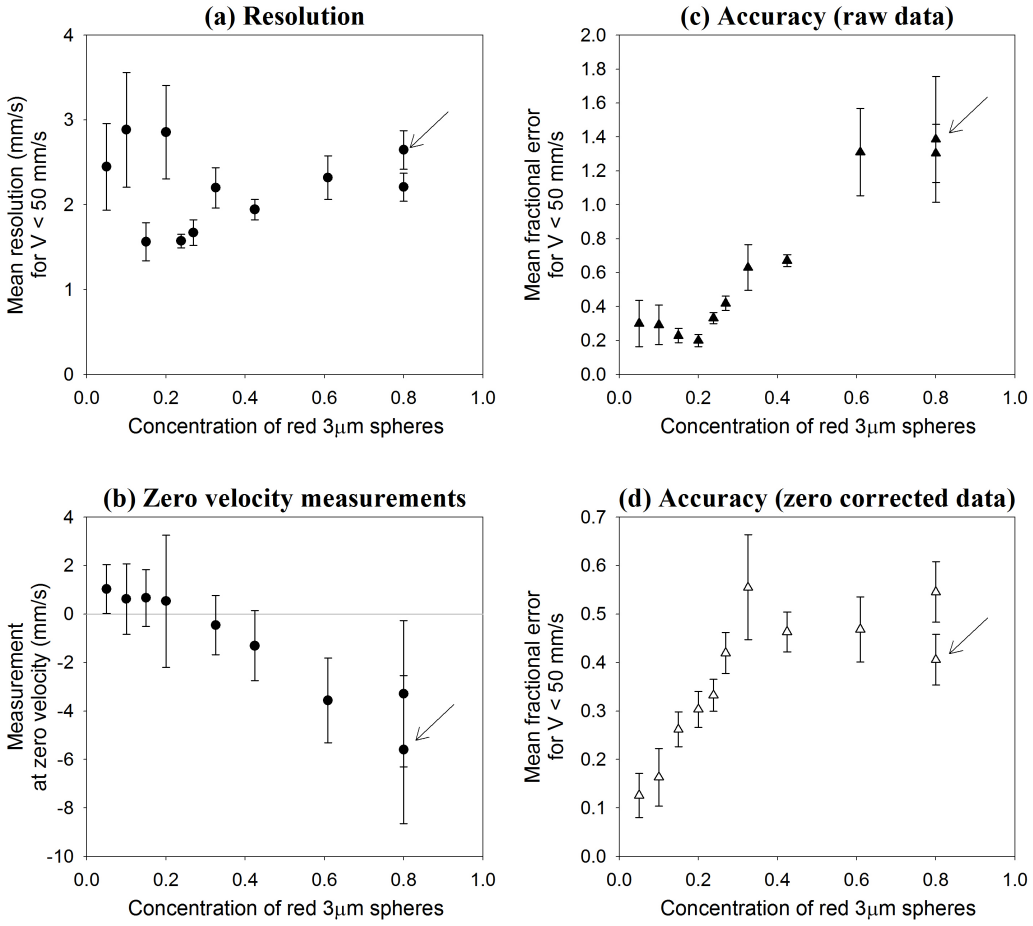

Figure 8.13: Comparison of resolution (a), zero velocity measurements (b) and accuracy (c) for 3 μm red spheres suspended in distilled water in concentrations ranging from 5% to 80%. The accuracy (fractional error) after correcting for the zero velocity offsets is shown in (d). Mean values for the measurement resolution and fractional error were calculated for known velocities $|V| < 50$ mm/s. The arrows indicate the values corresponding to the 80% suspension to which TWEEN®20 was added.

8.3.3 Variation of absorber concentration within the tube

The beneficial effect of TWEEN®20 highlights the importance of the absorber distribution within the tubes to the overall velocity measurements. It is possible that uneven distribution of particles within the tubes or adherence of particles to the cell walls create an inconsistent flow pattern. Density matching (see sub-section 5.1.2) ensured that the microspheres did not all sink to the bottom, but this was not the case for the RBC dilutions, where cells were seen settling at the bottom of the tube. This effect is illustrated by the schematic in Figure 8.14 and also by the experimental data in Figure 8.15. The velocity measurements plotted as data points in Figure 8.15 were made repeatedly over a period of 45 minutes for a 16% Ht suspension of RBCs flowing at a rate of 12 ml/hr (28 mm/s) in a 390 μm diameter tube. Over this period, the RBCs gradually settle to the bottom of the syringe so that there is a concentration gradient from the bottom to the top of the syringe. This becomes evident after about 35 minutes when the velocity measurements increase in value (i.e. the accuracy improves) as the lower concentration of fluid at the top of syringe flows into the tube. The sudden drop in accuracy at the end of the measurement period coincides with the emptying of the syringe and therefore the sudden influx into the tube of a high concentration of settled cells. In practice, the syringe is changed, refilled or shaken to avoid cell settling and therefore the slow sedimentation of RBCs is unlikely to have any bearing on individual velocity measurements, which take only a few seconds to acquire. However, the example serves as an additional illustration of the effect of changing concentration on measurement accuracy.

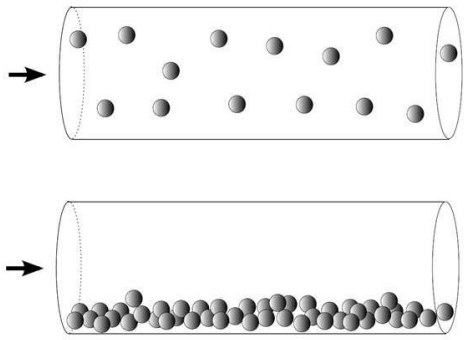

Figure 8.14: Illustration of possible flow patterns of the microsphere and blood suspensions.The absorbers (microspheres or red blood cells) may either be evenly distributed across the tube axis (top) or they may settle at the lower surface of the tube (bottom) [50].

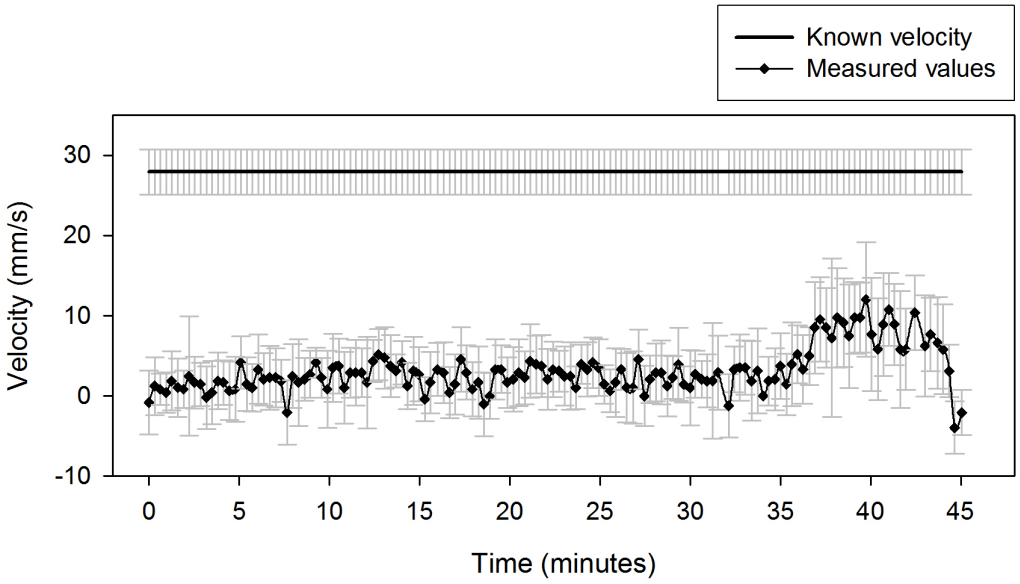

Figure 8.15: Illustration of changes in measurement accuracy over a period of 45 minutes. Sedimentation of the RBCs results in a reduction in the concentration of fluid towards the end of the measurement period. The RBCs were flowing at an average velocity of $V = 28 \pm 3$ mm/s in a 390 μm diameter tube and suspended in phosphate buffered saline with a nominal concentration of 16% of a physiologically normal haematocrit. The measurements were acquired using the PIV laser with $T = 0.5$ ms and the 30 MHz focussed transducer, followed by a 10-100 MHz Butterworth filter (order 2). Each data point represents an individual V' value calculated from the mean cross-correlation of 12 waveform pairs, and the error bars represent $\Delta V'$ (see Equation 6.4, page 93).

8.3.4 "Manual shifting": tubes of different microsphere concentrations

To further investigate the effect of absorber concentration, two suspensions were prepared: one contained a high concentration of the 22 μm carbon microspheres, the other a much lower concentration, both embedded in Norland 61 Optical Adhesive. The adhesive suspensions were injected into 10 cm lengths of THV tubing (583 μm diameter) and cured with UV light so that the microspheres were fixed permanently in the tubes. The difference in concentration was obvious, as can be seen from the photographs in Figure 8.16. The tube containing a low concentration of spheres was inserted into the experimental setup. It was illuminated with the PIV laser, and then shifted on a translation stage, followed by a second illumination; thus time shift measurements were made according to the "manual shifting" protocol (see sub-section 5.1.3 and Section 6.1). The same procedure was carried out for the tube containing a high concentration of microspheres.

Figure 8.17 shows the time shift measurements for the two concentrations of microspheres. The measured shifts for the low concentration sample corresponded exactly with the known values, with loss of correlation occurring at a shift corresponding to the known beam width of the transducer. The measured time shifts for the high density sample were also accurate up to a time shift $\left|t_{s,\max}\right|_{\text{obs}}$ that even exceeds $\left|t_{s,\max}\right|$. This is surprising considering the trend of decreasing accuracy with increasing concentration shown previously [for example, in Figure 8.9 (b) and Figure 8.13 (c) and (d)]. It could be argued that imperfections on the *outside* of the tube generated unique features (a "signature") that could be tracked in the manually shifting method; however, the signal amplitude was negligible for the empty tube, which suggests that the PA signals were generated predominantly, if not only, from the absorbers within the tube. Thus it seems possible to make accurate velocity measurements by manually shifting a seemingly homogeneous absorber, suggesting that the heterogeneity itself is not a limitation; rather, the difficulty in accurately measuring time shifts arises when high concentrations of absorbers are *flowing*. Reasons for this are discussed in Sections 8.5 and 9.1.

The following section examines the effect of different tube diameters, which was the second variable that was identified in Section 8.2.

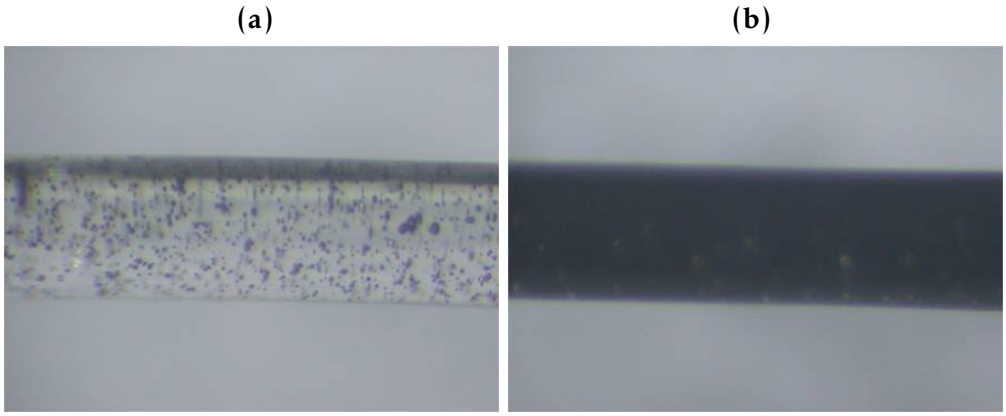

Figure 8.16: Lengths of tubing (583 μm diameter) with 22 μm spheres fixed inside using optical adhesive. (a) Low concentration of spheres; (b) high concentration of spheres.

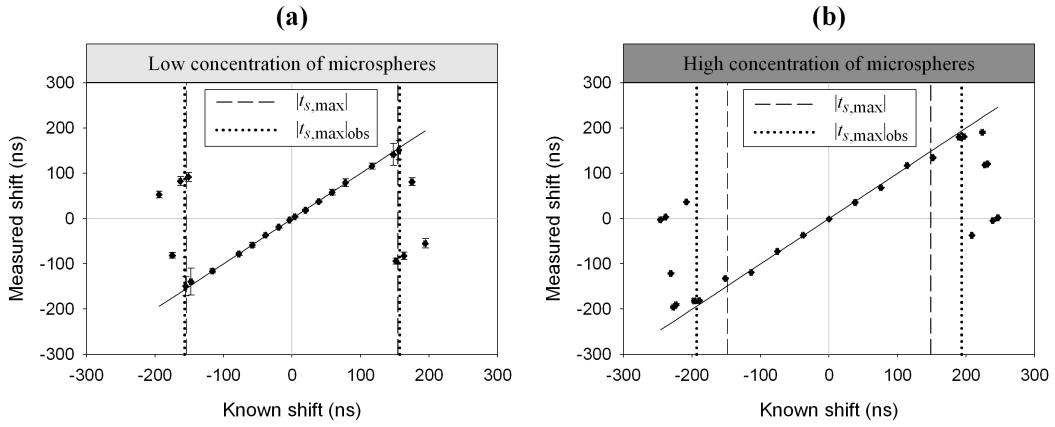

Figure 8.17: Time shifts measured by manually shifting 22 μm spheres fixed with optical adhesive in the 593 μm tube. Measurements were made using the 30 MHz focussed transducer, and illumination was with Laser 1 of the PIV laser.

8.4 Effect of tube diameter

Figure 8.9(b), page 124, shows poorer accuracy of velocity measurements obtained with various RBC concentrations, and using an 800 μm tube compared to a 390 μm tube. Further investigations into the effect of tube diameter were made using a suspension of the 3 μm red polystyrene spheres at the concentration in which they were originally supplied [see bar graph in Figure 5.2], with addition of TWEEN®20. The same suspension was used in each of the tubes, enabling the effect of tube diameter to be assessed independently of the concentration.

Figure 8.18(a) shows velocity measurements acquired using the 25 MHz PVDF transducer (see Table 5.3, page 85) for three different tubes with diameters of 250μm, 600 μm and 800 μm. To provide a cross-check, and to assess the effect of different transducers, photoacoustic signals were also acquired simultaneously using the 80 MHz PVDF transducer and the corresponding velocity measurements are shown in Figure 8.18(b). The effect of different transducers on the accuracy and resolution of fluid velocity measurements is discussed further in sub-section 10.1, but here it is interesting to note that both the 25 MHz and the 80 MHz transducers show similar measurement accuracy, and that in both cases this deteriorates as the tube diameter is increased. However, even for the largest tubes (1.4 mm diameter) the Reynolds numbers (Equation 2.1, page 43) were still well below the threshold at which laminar flow becomes turbulent, as discussed further in Section 8.5.

The mean resolution and mean fractional error were also calculated for measurements made over the velocity range $|V| < 50$ mm/s, and these values are plotted in Figure 8.19 (a) and (b) respectively for all the tube diameters (see Table 5.1) ranging from 167 μm to 1400 μm. As the tube diameter is increased the resolution of the measurements acquired with the 25 MHz transducer improve due to the improved SNR; however, there is also a reduction in measurement accuracy. The fractional error values associated with measurements acquired using the 80 MHz transducer are closely similar to those for the 25 MHz transducer, but the corresponding resolution values remain virtually consistent across the range of tube diameters.

The results in Figures 8.18 and 8.19 lead to conclusions similar to those drawn at the end of sub-section 8.3.2 for the different absorber concentrations. As with low concentrations, it appears that narrow tubes enable better measurement accuracy over a wider range of velocities. The results for narrower tubes also demonstrate poorer resolution due to larger distributions in the measured velocities. The change in resolution was only apparent for the 25 MHz transducer, but not for the 80 MHz transducer,

which could be due either to the difference in detector bandwidths or to the narrower focal beam width for the 80 MHz transducer. The latter explanation points to the existence of a range of flow velocities within the tubes, and this is discussed further in sub-section 8.5 and in more detail in Chapter 9.

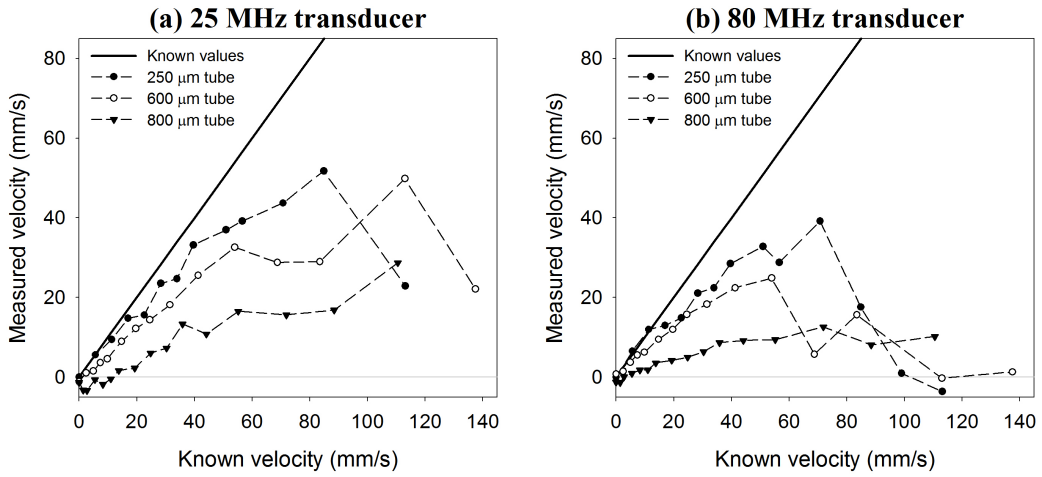

Figure 8.18: Comparison of the accuracy of the velocity measurements made for 3 μm red spheres flowing in tube diameters of 250 μm, 600 μm and 800 μm. The measurements were acquired using two focussed transducers with centre frequencies of 25 MHz (a) and 80 MHz (b).

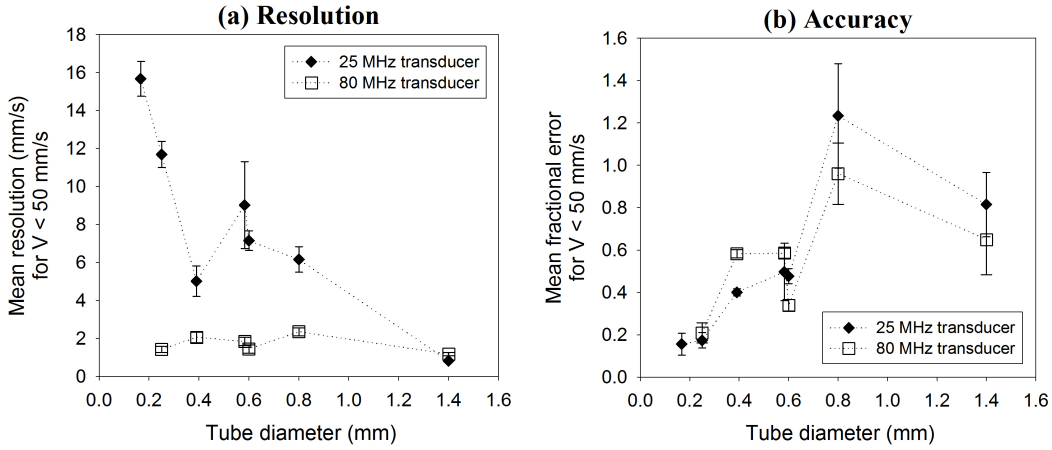

Figure 8.19: Comparison of the resolution (a) and accuracy (b) of velocity measurements made for 3 μm red spheres flowing in tube diameters ranging from 167 μm to 1400 μm. Selected results showing measurements made for V = 0 mm/s to 140 mm/s are given in Figure 8.18. Mean values for the measurement resolution and fractional error were calculated for known velocities $|V| < 50$ mm/s.

8.5 Summary of results: plug vs. non-plug flow

The foregoing results have demonstrated two flow types: the rotating wheel phantom and manual shifting of the absorber-filled tubes (either with absorbers glued in the tube, or suspended in a fluid within the tube) both simulate plug "flow", whereas absorbers moving through the tube under the influence of the syringe pump demonstrate non-plug flow.

Figure 8.20 shows clearly that the distance d_D over which de-correlation occurs, and therefore also $|V_{max}|_{obs}$ (Equation 8.1, page 113), is much reduced in the experiments where absorbers are flowing through the tube (grey bars) compared to the manual shifting experiments (black and white bars). Working from the top of the figure, it is evident that manual shifting of static particles (the wheel phantom and the 22 μm spheres fixed in tube, shown by black bars) results in a d_D value corresponding to the transducer beam width w, as expected. Manual shifting of particles that are theoretically stationary, but freely suspended within the tube, results in d_D that is approximately 60% - 70% less than w for the carbon microsphere phantoms, as shown by the white bar for the 22 μm spheres. This loss of correlation is likely to be due to random motion of the particles within the fluid in the time between acquiring successive signals. There is a much greater reduction in d_D for 22 μm spheres *flowing* through the tube, with a de-correlation distance $\sim 15\%$ of w, as shown by the grey bar. The concentration of these spheres, in terms of the number of spheres per unit volume, is likely to be approximately three orders of magnitude less than that for whole blood (see Figure 5.2, page 70). Therefore red blood cells in a suspension only 2% of the normal RBC haematocrit (Ht) will still be more concentrated than the suspension of 22 μm carbon spheres. It was established in Section 8.3 that the accuracy of velocity measurements deteriorates with increasing concentration, and therefore it is not surprising that de-correlation occurs over a shorter distance ($d_D \approx 2.1\%w$) for the 2% Ht RBCs than for the carbon spheres ($d_D \approx 15\%w$). However, there is also a dependence on tube diameter, as shown in Section 8.4, with narrower tubes enabling more accurate velocity measurements. Therefore, d_D for 2% Ht RBCs flowing in an 800 μm tube is shorter than for the same concentration of RBCs flowing in a 390μm tube ($d_D \approx 7\%w$). The final grey bar in Figure 8.20 plots $d_D \approx 2.2\%w$ for a higher concentration of RBCs also flowing in a 390 μm tube. This illustrates the effect of concentration directly, by comparison with the 2% Ht RBCs; whilst the concentration of the 22 μm carbon spheres is certainly less than the 2% Ht RBCs (both flowing in an 800 μm tube), the difference in absorber type introduces additional, potentially, confounding variables such as absorber colour, shape and size. Finally, it is surprising that it was possible to measure time shifts using the manual shifting method with whole blood (100% Ht), as shown

by the white bar in Figure 8.20, where $d_D \approx 45\%w$; this suggests that the commonly cited "heterogeneity problem" is not significant. In contrast, for a RBC concentration of 60% Ht (not shown in Figure 8.20) flowing in the 390 μm tube, the maximum accurately measured velocity was for $V \approx 3$ mm/s, which gives $d_D \approx 0.3\%w$. This apparent anomaly of greater measurement accuracy for both low and high concentrations when manually shifted compared to when flowing is explained by the flow profile within the tube, as described below.

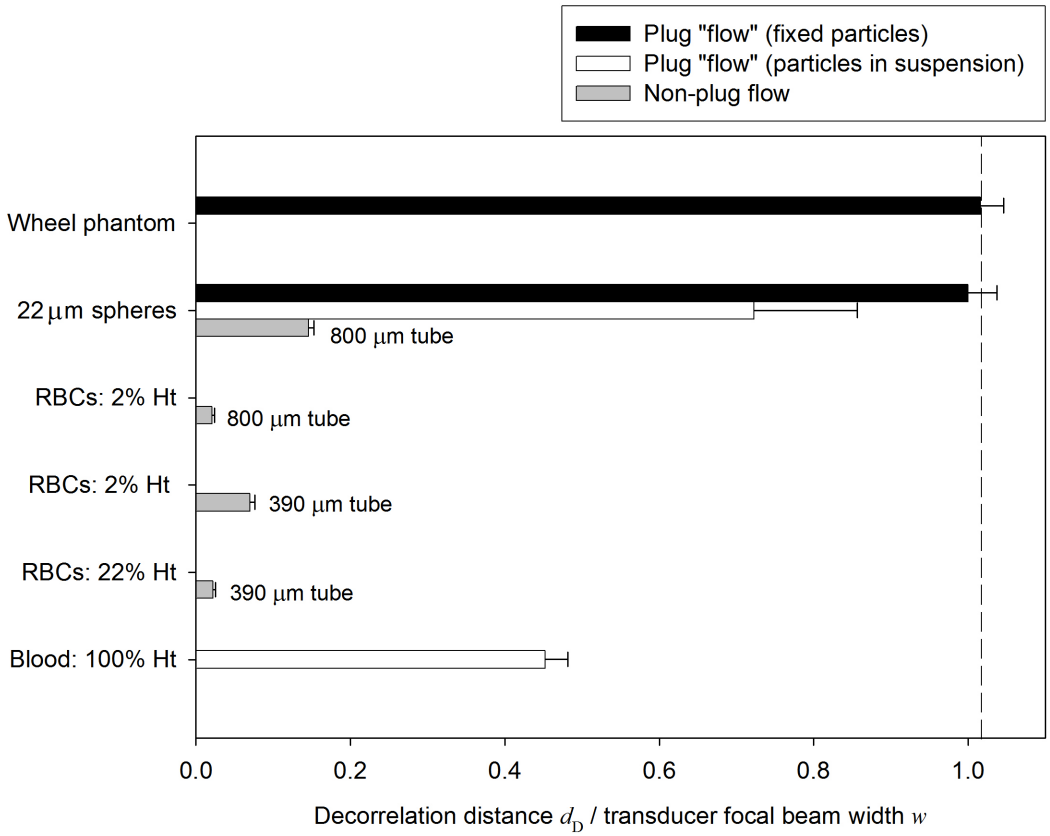

Figure 8.20: Minimum distances moved by the absorbers leading to de-correlation. For the flowing phantoms, d_D was estimated by the largest velocity measurement with a fractional error < 0.5.

The key conclusion from the results summarised in Figure 8.20 is that for the flowing phantoms $|V_{max}|_{obs} << |V_{max}|$ (i.e. $d_D << w$), whereas for the manually shifting results $|V_{max}|_{obs} \approx |V_{max}|$, even for high concentrations of absorbers. This suggests that the nature of flow within the tube leads to loss of correlation. Figure 8.21 illustrates three possible flow patterns: plug flow, laminar flow and turbulent flow. Both the wheel phantom and the manually shifting experiments simulate the ideal case of plug flow. However, when the particles are flowing through the tube, the flow in the tube is more

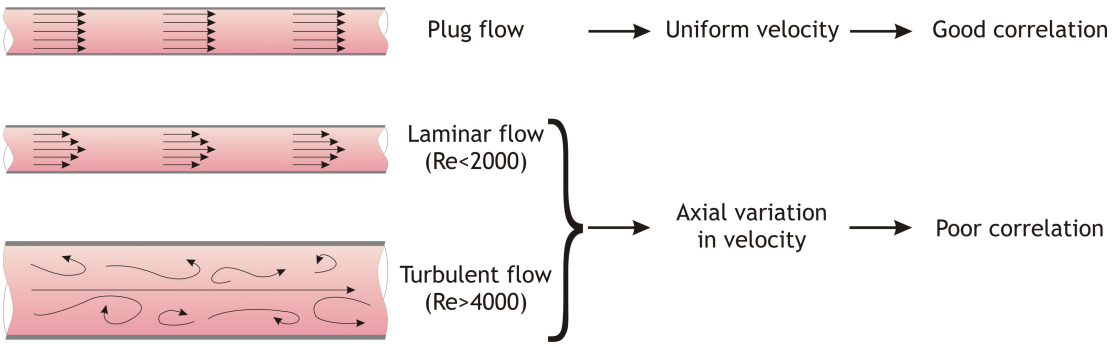

Figure 8.21: Illustration how non-plug flow leads to poor correlation.

likely to be laminar, or even turbulent, where the Reynolds number Re defines the condition for turbulence. Re is a dimensionless number given, as in Equation 2.1, by

$$\mathrm{Re} = \frac{DV\rho}{\mu} \tag{8.3}$$

where D is the tube diameter, V is the average flow velocity in the tube, ρ is the density of the flowing fluid and μ is the dynamic viscosity of the flowing fluid. If $\rho \approx 1$ gcm^{-3} and $\mu \approx 0.02$ gcm^{-1}s^{-1} for blood, then an average flow velocity $V = 50$ mm/s in a tube of diameter $D = 800$ μm gives a Reynolds Re ≈ 20. The microsphere suspensions are less viscous than blood, but in order to depart from laminar flow (Re > 2100) we would require $\mu_{microspheres} < 0.01\mu_{blood}$, which is very improbable. Moreover, although Re scales with tube diameter and flow velocity, all the experiments used $D < 1.5$ mm and $|V| < 200$ mm/s which are insufficiently large to push Re beyond the laminar flow regime, and it is even more unlikely that these conditions would give rise to turbulence. However, the flow within the tubes is likely to be further complicated by the presence of the particles. The Reynolds criteria are for a single phase fluid, whereas for both the microsphere phantoms and blood dilutions we effectively have two-phase solid-liquid suspensions. There are cases where the particle size and concentration influence the critical Reynolds number at which turbulence develops [77]. In addition, it is possible that the non-spherical shape of the RBCs leads to premature de-correlation: as the cells tumble and rotate they will present a different absorption cross-section, and therefore generate a different photoacoustic signal. However, tumbling occurs over a time given by the inverse of the shear rate ($\dot{\gamma} = \delta V/\delta D$) that is several milliseconds, and therefore is unlikely to affect the photoacoustically measured velocities, where the time T between laser illuminations is typically a fraction of a millisecond. Thus it is reasonable to conclude that the tumbling of RBCs has a negligible effect, and this is supported by Figure 8.10 where the results from non-spherical RBCs and spherical red spheres are remarkably similar.

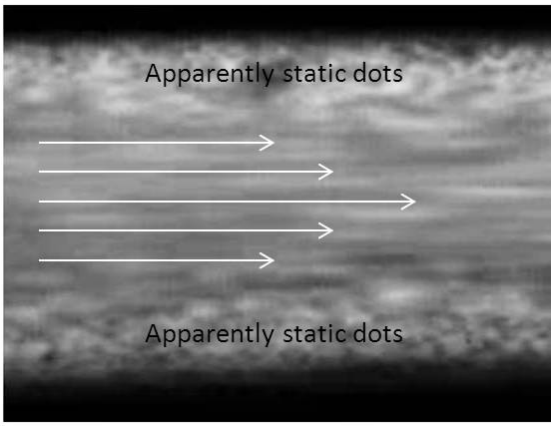

Figure 8.22: Capture from a video recording of blood cells (100% normal haematocrit) flowing through the 583 μm diameter tube. A layer of slow-moving cells is evident at the wall boundaries, with faster-moving cells in the centre of the tube, which may imply laminar flow.

In order to verify the nature of flow within the tubes in the context of the above speculations, several video recordings were captured using a camera attached to a confocal microscope (Neuroinflammation Unit, Wakefield Street). A drop of fluoroscein was added to each suspension so that the absorbers (microspheres or red blood cells) were observed as shadows against a fluorescent background. Figure 8.14 shows an image from a video recording of blood cells with a concentration equivalent to the normal haematocrit (40-50%). The apparently static dots compared to the central bright streaks indicate that the velocity of blood cells at the tube boundaries was much reduced compared to the faster velocity in the tube centre, and this implies laminar flow. In the following section, the flow is therefore assumed to be laminar and various simulations are performed in order to explain the experimental results in Sections 8.2 to 8.4, namely the dependence of velocity accuracy on absorber concentration and on tube diameter.

9

Analysis: laminar flow and light absorption

The results for the wheel phantom described in Chapter 7 show that, in the simple case where all absorbers move with a single velocity, the measurements are accurate up to a maximum measurable velocity $|V_{\max}|$, which corresponds to movement of absorbers a distance $d_{\mathrm{D}}/\sin\theta$ in the time T. The value of d_{D} is equivalent to the transducer beam width w, and therefore for speeds greater than $|V_{\max}|_{\mathrm{obs}}$, correlation is lost due to absorbers moving out of the focal beam between the two laser pulses. The results for the fluid phantoms show the same equivalence between d_{D} and w in the experiments where the tube is manually shifted. However, this plug-flow simulation does not represent the true laminar flow profile: when the absorbers are flowing, d_{D} is much reduced compared to w, and the measurements consistently under-read the known average flow velocity values. Moreover, the under-reading is worse for greater absorber concentrations (when flowing) and larger tube diameters.

In order to understand the trends observed for flowing absorbers, and form a plausible explanation, it is necessary to consider the range of flow velocities present within

the tube due to laminar flow, and how these translate to the time shift measurements. Section 9.1 describes the mathematical and experimental challenges in evaluating the laminar flow profile, and thus provides a basis for the new signal processing method introduced in Section 9.2.

9.1 Simulations

To evaluate the flow profile within the tubes, and provide an explanation for the deteriorating accuracy with increasing concentration and tube diameter, it is necessary to consider the spatial information associated with the photoacoustic signals. The schematic in Figure 4.1 illustrates waveform segments $p_1(t)$ and $p_2(t)$ that appear at a time F/c from the start of the photoacoustic signal, where F is the depth of the blood vessel (at the transducer focus) and c is the speed of sound in the medium. Thus there is a correspondence between the time axis of the signal and the distance from the transducer. In the same manner, the photoacoustic signal arising from the absorbers in the tube can be dissected to reveal information about the flow at different points within the tube, and this is analogous to "range gating" used to localise signals in Doppler ultrasound.

This section considers the velocities that would be measured for different small segments of the waveforms $p_1(t)$ and $p_2(t)$, assuming that there is a laminar flow profile. Sub-section 9.1.1 describes calculations of the average velocity across the entire tube radius, and for small parts of the tube. Sub-section 9.1.2 then illustrates how small segments of the photoacoustic signals can be associated with small parts of the tube, and thus different velocities calculated for each signal segment to obtain a measured velocity profile. The following three sub-sections then assess how this measured velocity profile is altered under different experimental conditions: first, by absorbers moving out of the transducer focal beam (sub-section 9.1.3); second, by different transducer angles (sub-section 9.1.4), and finally, by a non-uniform distribution in absorbed light energy across the tube radius (sub-section 9.1.5). This last sub-section is important in explaining the observed effects of absorber concentration and tube diameter.

9.1.1 Calculation of average velocity

It was established in Section 8.5 that the flow profile in the tubes is laminar: based on the tube diameters and flow velocities it would be very surprising if any turbulence were generated. Fluid in laminar flow can be considered as a series of circular layers (laminae), each moving at a velocity determined only by the radial distance from the centre of the tube. Taking a two-dimensional vertical cross-section through the tube,

the velocities form a parabola, as illustrated in Figure 9.1. The fluid moves fastest in the centre of the tube and, assuming a no-slip condition, it is stationary at the tube walls.

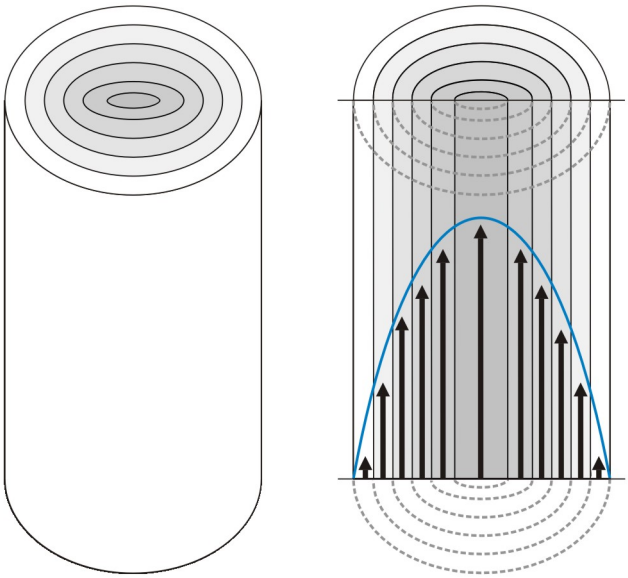

Figure 9.1: Illustration of laminar flow in a cylindrical tube. On the left a tube is shown with imaginary layers (laminae) of fluid; a cross-section through the tube is shown on the right. Each lamina moves at a different speed as indicated by the arrows; the parabolic velocity profile is traced with a solid blue line.

For a Newtonian fluid flowing in a tube of radius R, the laminar velocity profile $v(r)$ can be derived [81, 108] from the Navier-Stokes equations to give:

$$v(r) = \hat{v}\left(1 - \frac{r^2}{R^2}\right). \tag{9.1}$$

At a distance $r = 0$ from the central axis the velocity is maximum, and denoted $\hat{v}$:

$$\hat{v} = \frac{\Delta P R^2}{4\mu L}, \tag{9.2}$$

where μ is the dynamic fluid viscosity (Pa.s) and ΔP is the pressure difference (Pa) between the start and the end of a tube of length L.
The flow rate Q (volume per unit time) is the integral of $v(r)$, which gives Hagen-

Poiseuille's law (Equation 9.5):

$$Q = \hat{v} \int_0^{2\pi} \int_0^R \left(1 - \frac{r^2}{R^2}\right) r\,dr\,d\theta \tag{9.3}$$

$$= 2\pi\hat{v} \int_0^R r\left(1 - \frac{r^2}{R^2}\right) dr \tag{9.4}$$

$$= \hat{v}\frac{\pi R^2}{2} = \frac{\pi R^4 \Delta P}{8\mu L}. \tag{9.5}$$

Thus, by comparing Equations 9.2 and 9.5, the average flow velocity $\bar{v}$ across the tube (cross-sectional area A) is half the maximum velocity $\hat{v}$:

$$\bar{v} = \frac{Q}{A} = \frac{Q}{\pi R^2} \tag{9.6}$$

$$= \frac{\hat{v}}{2}. \tag{9.7}$$

Note that $\bar{v}$ is the value denoted by the "known" velocity V with which the photoacoustically measured velocity V' is compared in the fluid phantom experiments (see Equation 5.6).

To calculate the velocity within a particular "range gate", it is necessary to consider the average flow velocity in small sections of the tube. Figure 9.2 shows three examples where flow in particular regions of the tube are highlighted. In Figure 9.2 (i) the highlighted region corresponds to radial distances $|r| \leq a$; the average velocity $\delta\bar{v}$ is therefore calculated by substituting R with a in Equation 9.4 (in the upper integral limit only) to give a flow rate $\delta Q = Q_a$, and then using $\delta A = A_a = \pi a^2$ in Equation 9.6. In Figure 9.2 (ii) a small segment is highlighted where $a \leq r \leq b$. Calculation of δQ in this segment entails subtraction of flow rates in the larger and smaller volumes: $\delta Q = Q_b - Q_a$. Subsequent division by the appropriate cross-sectional area ($\delta A = A_b - A_a$) gives the average velocity $\delta\bar{v}$, which applies to the small segment highlighted, as well as to the entire circular layer (lamina) where $a \leq r \leq b$. A similar calculation is required for the case in Figure 9.2 (iii), using addition instead of subtraction: $\delta\bar{v} = (Q_b + Q_a)/(A_b + A_a)$. In general therefore, the average velocity $\delta\bar{v}$ in a region bounded by $r = a$ and $r = b$ is calculated as follows:

$$\begin{aligned}
\delta\bar{v} &= \frac{\delta Q}{\delta A} \\
&= \frac{\frac{b}{|b|}Q_b - \frac{a}{|a|}Q_a}{\frac{b}{|b|}A_b - \frac{a}{|a|}A_a} \\
&= \hat{v}\left[1 - \frac{\frac{b}{|b|}b^4 - \frac{a}{|a|}a^4}{2R^2\left(\frac{b}{|b|}b^2 - \frac{a}{|a|}a^2\right)}\right].
\end{aligned} \tag{9.8}$$

Figure 9.3 shows values for the average velocity of fluid moving in a tube of radius $R = 0.4$ mm. The average velocity $\bar{v} = 50$mm/s for the entire profile is shown in Figure 9.3 (a). The illustrations in Figure 9.3 (b), (c) and (d) correspond to those in Figure 9.2 (i), (ii) and (iii) respectively, with $|a| = R/3$ and $|b| = R/2$. However, an important simplification is the reduction from three to two dimensions: the three-dimensional problem is mathematically complex and beyond the scope of this section. Note also that in each of these examples $\delta\bar{v} > \bar{v}$; however, sections near the edges of the velocity profile would lead to $\delta\bar{v} < \bar{v}$. The distance (in mm) shown on the left-hand y axes is the distance that the absorbers move in the time $T = 1.0$ ms between consecutive laser pulses, and this is numerically equivalent to the absorber flow speed (in m/s), which is shown on the right-hand y axes.

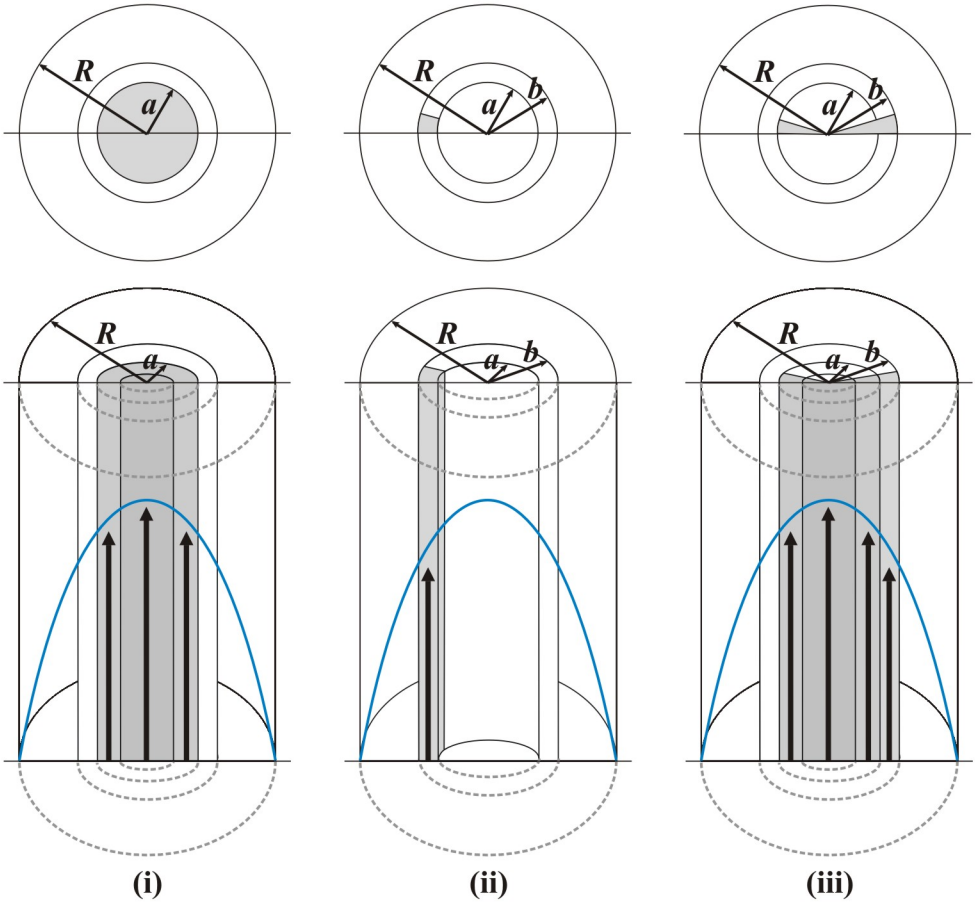

Figure 9.2: Illustrative sections of the laminar velocity profile in a tube of radius R. The average velocity of the entire profiles is $\bar{v}$ (Eq. 9.7). The text describes the calculation of average velocities $\delta\bar{v}$ over small sections of the tube where the radius $|r| \leq a$ (i), $a \leq r \leq b$ for $a, b < 0$ (ii) and for $a < 0, b > 0$ (iii). Two-dimensional aerial viewpoints are shown above each diagram to highlight the shaded sections. See also Fig. 9.3.

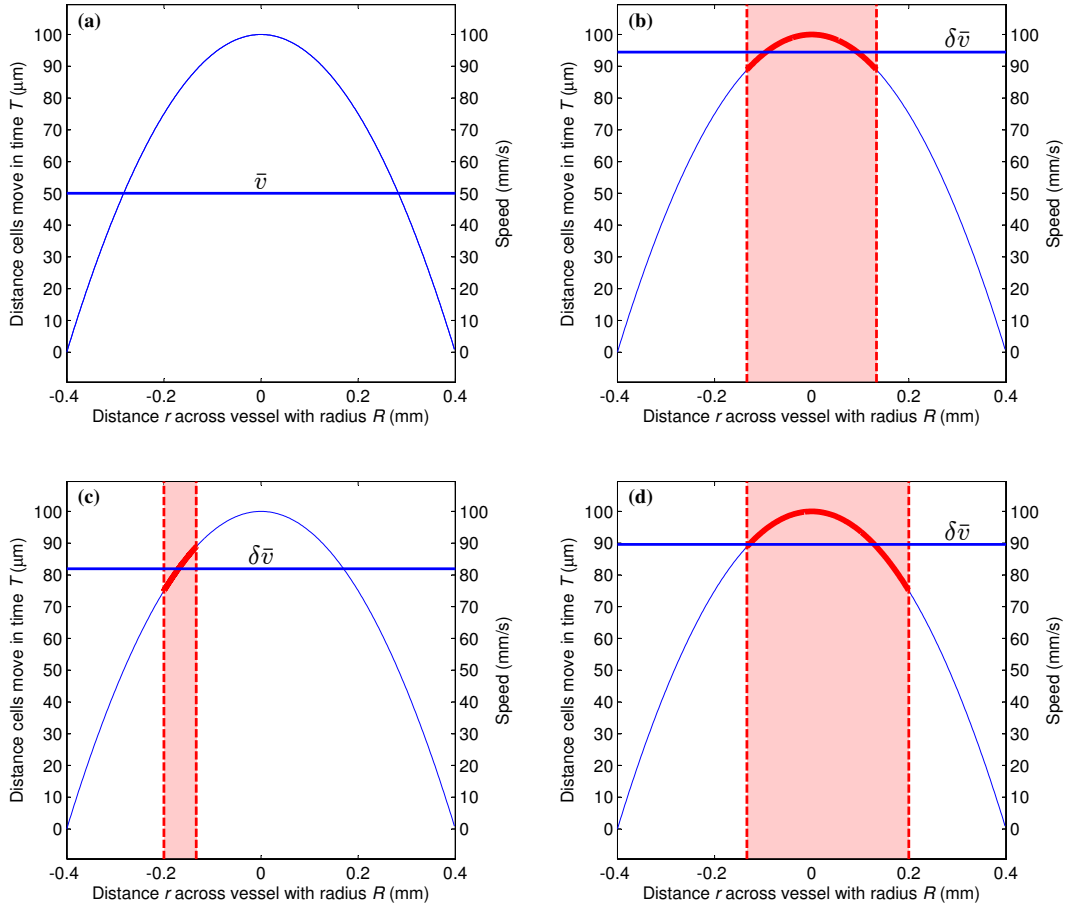

Figure 9.3: Calculation of the average velocity from the laminar velocity profile in a tube of radius $R = 0.4$mm. (a) shows the average velocity $\bar{v} = 50$ mm/s of the entire velocity profile. (b) shows the average velocity $\delta\bar{v} = 94$ mm/s in the part of the tube where the radius $-R/3 \leq r \leq R/3$, as also illustrated in Fig. 9.2 (i). (c) shows $\delta\bar{v} = 82$ mm/s for the section of the tube where $-R/3 \leq r \leq -R/2$ [see also Fig. 9.2 (ii)]. (d) shows $\delta\bar{v} = 90$ mm/s for $-R/3 \leq r \leq R/2$ [see Fig. 9.2 (iii)]. The left-hand y-axes show the distance moved by absorbers in the time $T = 1.0$ ms between two laser excitation pulses.

9.1.2 Measurement of flow velocity via time shifts

Figure 9.4 illustrates a section of a blood vessel within the focal region (grey shading) of a transducer (see also Figure 4.1, page 64). Photoacoustic signals are generated from the moving red blood cells when illuminated with laser pulses, and the time shift t_s between photoacoustic signals is used to calculate the red blood cell velocity V' (Equation 4.3, page 65). Figure 9.5 (a) is a graphical representation of this blood vessel section (subsequently referred to as a "tube"), together with the shaded region corresponding to the transducer focus beam. The illustrated time shift is for idealised plug flow where all the absorbers are moving at the average ("known") velocity $V = \bar{v}$; as a result, the measured velocity V' corresponds exactly to the known velocity ($V = V'$). Figure 9.5 (b) and (c) show laminar flow, and the projection of the flow profile in the direction of the transducer time axis. An estimate of the measured velocity at particular times along the transducer axis (i.e. for different range gates) is found by evaluating $\delta\bar{v}$ (Equation 9.8) for values of $v(r)$ between the two vertical dashed lines. Absorbers near the centre of the tube are moving faster than the average velocity, and so evaluation of the time shift for the part of the signal arising from absorbers in this region [Figure 9.5 (b)] gives a measured velocity ($\delta\bar{v}$) that overestimates the average velocity. Conversely, the part of the signal corresponding to the absorbers near the edge of the tube undergoes a smaller time shift, and the measured velocity *under*estimates the average velocity.

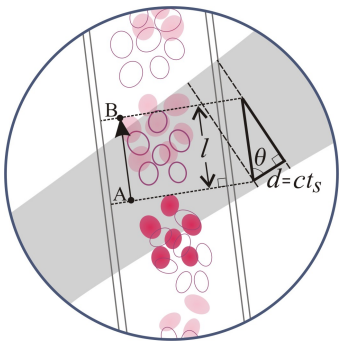

Figure 9.4: Schematic showing clusters of red blood cells (RBCs) moving along a blood vessel. See also Figure 4.1. The RBCs are illuminated by a pair of laser pulses separated by a time T, during which the cells move a distance l from A to B, producing a time shift t_s between the photoacoustic signals generated. The signals are acquired using an ultrasound transducer at an angle θ to the direction of flow, as indicated by the grey shading.

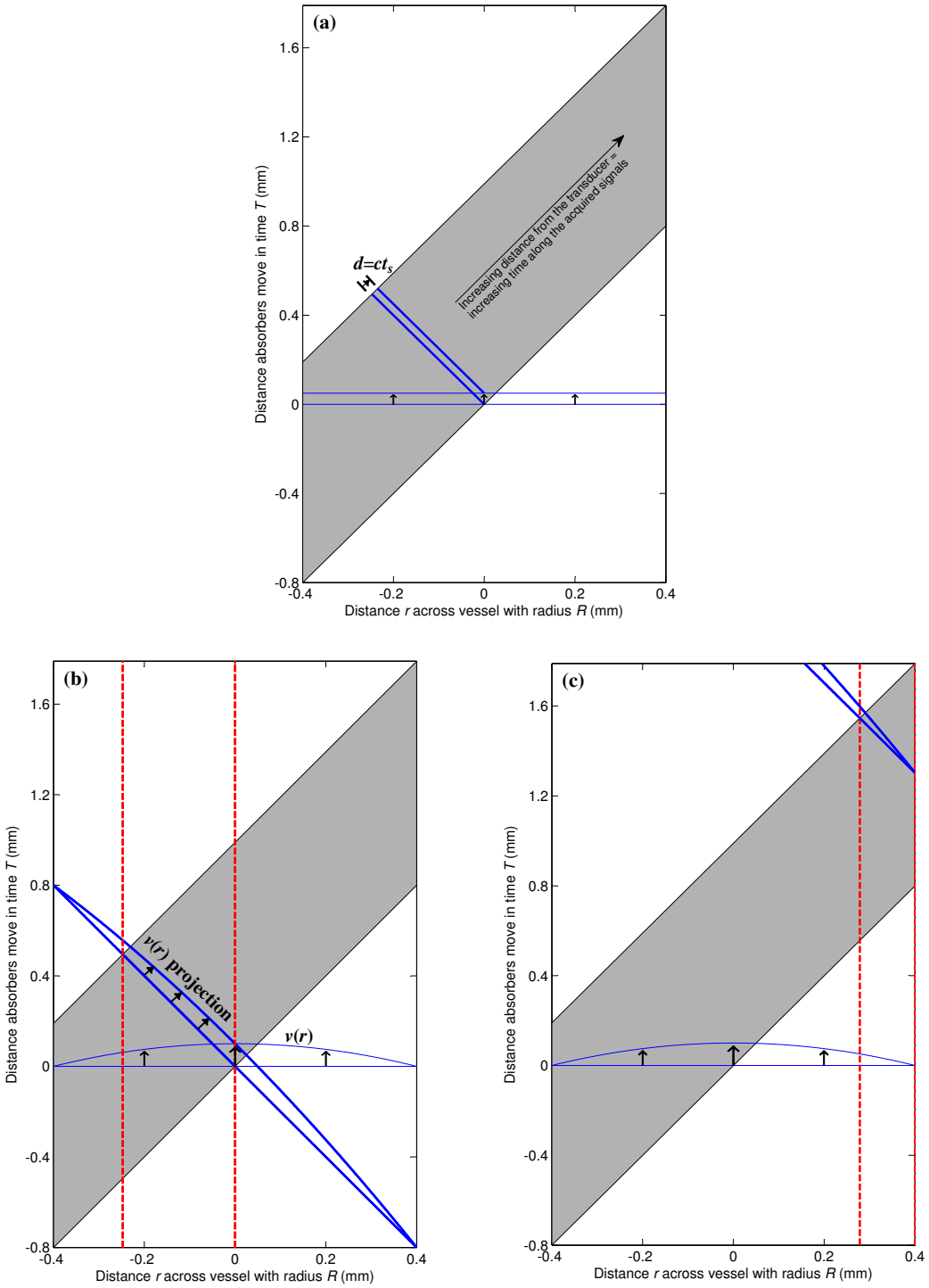

Figure 9.5: Measurements of time shifts at different parts of the photoacoustically-acquired signals. Idealised plug flow is shown in (a) and laminar flow in (b) and (c) for two different range gates. The shaded region represents the transducer focus beam (width 0.35 mm) oriented at an angle of 45° to the direction of flow in a tube of radius R = 0.4 mm. In (a) the measured time shift t_s is exactly equivalent to the known velocity (50 mm/s). In (b) and (c) the measured velocity ($\delta\bar{v}_{approx}$) between the vertical dashed lines is 81 mm/s and 26 mm/s respectively. The y-axis corresponds to the distance (mm) that the absorbers move in the time T = 1.0 ms between consecutive laser pulses.

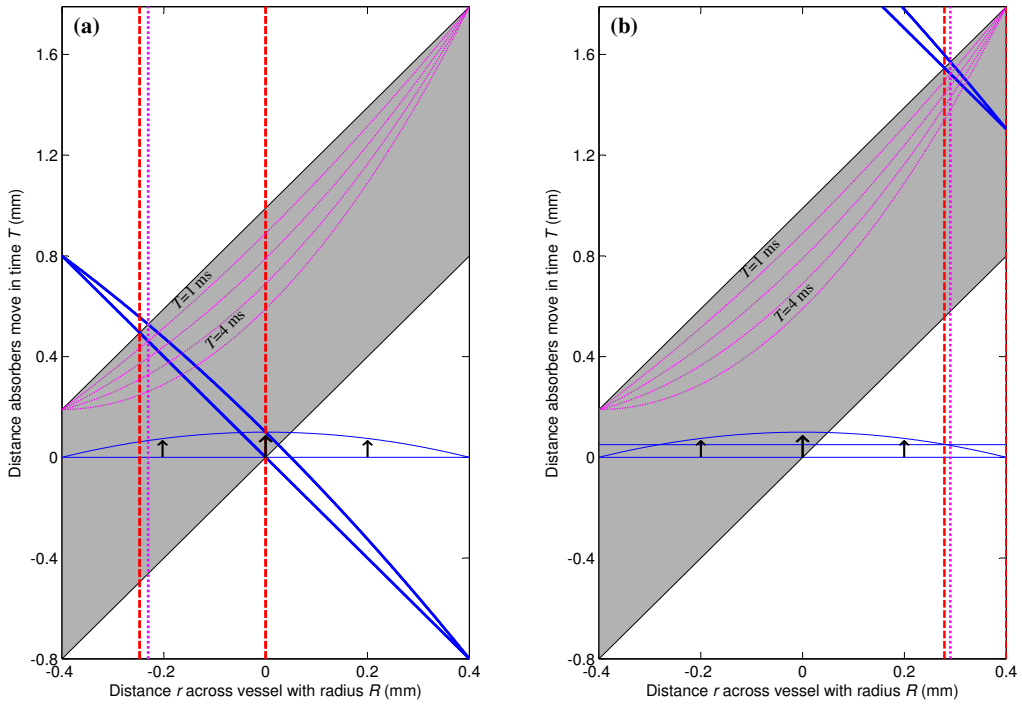

Figure 9.6: Narrowing of the detected range of velocities due to movement of absorbers out of the transducer focal region in the time T between successive laser pulses. The mean velocity $\delta\bar{v}$ was calculated for T = 1.0 ms and for r values between the vertical dotted line on the left, and the vertical dashed line on the right, giving 86 mm/s at the transducer time point shown in (a) and 22 mm/s for the time point shown in (b). The corresponding mean velocities in Fig. 9.5 (b) and Fig. 9.5 (c) were calculated for the larger range of r values between the two vertical dashed lines. The y-axis corresponds to the distance (in mm) that the absorbers move in the time T = 1.0 ms between consecutive laser pulses, which is numerically equivalent to the absorber flow speed (in m/s).

9.1.3 The Vmax effect

In practice, a certain proportion of the absorbers will move out of the transducer focal region in the time T between successive laser pulses: this is the effect that gives rise to $|V_{\max}|$ (Section 7.1). The curved, dotted lines in Figure 9.6 (a) and (b) mark the $|V_{\max}|$ boundaries calculated for T = 1.0, 2.0, 3.0 and 4.0 ms: any absorbers lying beyond the relevant boundary at the time of the first illumination will have moved out of the transducer focal region (shaded) by the time of the second illumination. Therefore the velocity of these absorbers cannot be measured using the cross-correlation of the two photoacoustic waveforms. This results in sampling of a slightly narrower range of velocities, as indicated by the vertical dotted line, as opposed to the vertical dashed line, on the left hand side of the velocity range (T = 1.0 ms). In Figure 9.6 (a) the rejected velocities are further from the tube centre, and so the measured velocity ($\delta\bar{v}$) is slightly larger than the previously calculated value [Figure 9.5 (b)]. In Figure 9.6 (b) the rejected velocities are *closer* to the tube centre, and so the measured velocity ($\delta\bar{v}$) is slightly *smaller* than the previously calculated value [Figure 9.5 (c)].

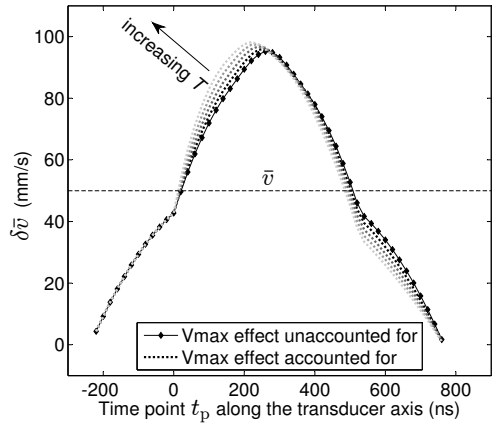

Figure 9.7: Illustration of the $|V_{\max}|$ effect. Values of $\delta\bar{v}$ calculated for the conditions in Fig. 9.5 at a range of time points t_P stepped by 20 ns along the transducer axis (note that the tube only occupies the entire transducer focal beam width for time points greater than 0 ns and less than 540 ns). Data points are shown for the case where the $|V_{\max}|$ effect is ignored (Fig. 9.5) and the dotted lines represent the case where the $|V_{\max}|$ effect is taken into account with values of T = 1.0, 2.0, 2.0 and 4.0 ms (Fig. 9.6).

Figure 9.7 shows the values of $\delta\bar{v}$ calculated at a range of time points along the transducer axis; these form the velocity profile that would be mapped out experimentally by advancing the range gate along the measured PA signal, and calculating the cross-correlation for each waveform segment. Examples are shown for the case where the

$|V_{\max}|$ effect is ignored (see also Figure 9.5) and also for the cases where the $|V_{\max}|$ effect is taken into account (see also Figure 9.6). Time points less than 0 ns and greater than 540 ns correspond to those where the relevant tube segments only occupy part of the transducer focal beam width; even between these time points the profiles do not match the expected parabolic velocity profile and this is because the measurements are made at a projection angle θ. As T is increased from 1.0 ms to 4.0 ms, the $|V_{\max}|$ effect becomes more significant, resulting in greater overestimation of velocities to the left of the tube centre and greater underestimation of velocities to the right of the tube centre. However, the overall velocity measurement V' is some kind of average of the individual time shifts along the time axis of the signals (which corresponds to the distance from the transducer). Therefore it is possible that the velocity *over*estimation arising from loss of slower-moving absorbers from the transducer focal region is balanced to some extent by the velocity *under*estimation due to the loss of faster-moving absorbers in other parts along the transducer focus beam. In any case, it is assumed that the $|V_{\max}|$ effect is unlikely to have a significant effect on the overall velocity measurement.

9.1.4 Effect of transducer angle

Figure 9.8 illustrates two different transducer orientations: in (a) the transducer is at an angle $\theta = 20°$ to the direction of flow, and in (b), $\theta = 70°$. For $\theta = 20°$, the profile of $\delta\bar{v}$ values [Figure 9.8 (b)] is affected by the varying extent to which the tube occupies the transducer beam width ($t_{\mathrm{P}} < 0$ ns and $t_{\mathrm{P}} > 933$ ns), and the maximum value for $\delta\bar{v}_{t_{\mathrm{P}}}$ ($t_{\mathrm{P}} = 473$ ns) under-reads $\hat{v} = 100$ mm/s by $\sim 8.5\%$. In contrast, the profile of $\delta\bar{v}$ values for $\theta = 70°$ [Figure 9.8 (d)] is virtually parabolic (i.e. it closely resembles the laminar velocity profile) and the maximum value for $\delta\bar{v}$ ($t_{\mathrm{P}} = 239$ ns) under-reads $\hat{v} = 100$ mm/s by only $\sim 1\%$. In summary therefore, a larger angle θ enables more accurate representation of the laminar velocity profile, since a narrower range of velocities is sampled at each time point t_{P}. In practice large angles improve the signal-to-noise ratio (SNR), since the strongest component of the photoacoustic signal is perpendicular to the tube axis due to the nature of acoustic propagation from a cylindrical source. However, large angles also lead to poor velocity resolution due to the measurement of very small time shifts (see Equation 6.4, page 93). Therefore, as a compromise, all the phantom experiments used $\theta \approx 45°$, which is a trade-off between high SNR and high velocity resolution. There is also a trade-off involving the transducer beam dimensions, with a small beam width giving greater measurement accuracy, but a lower maximum measurable velocity.

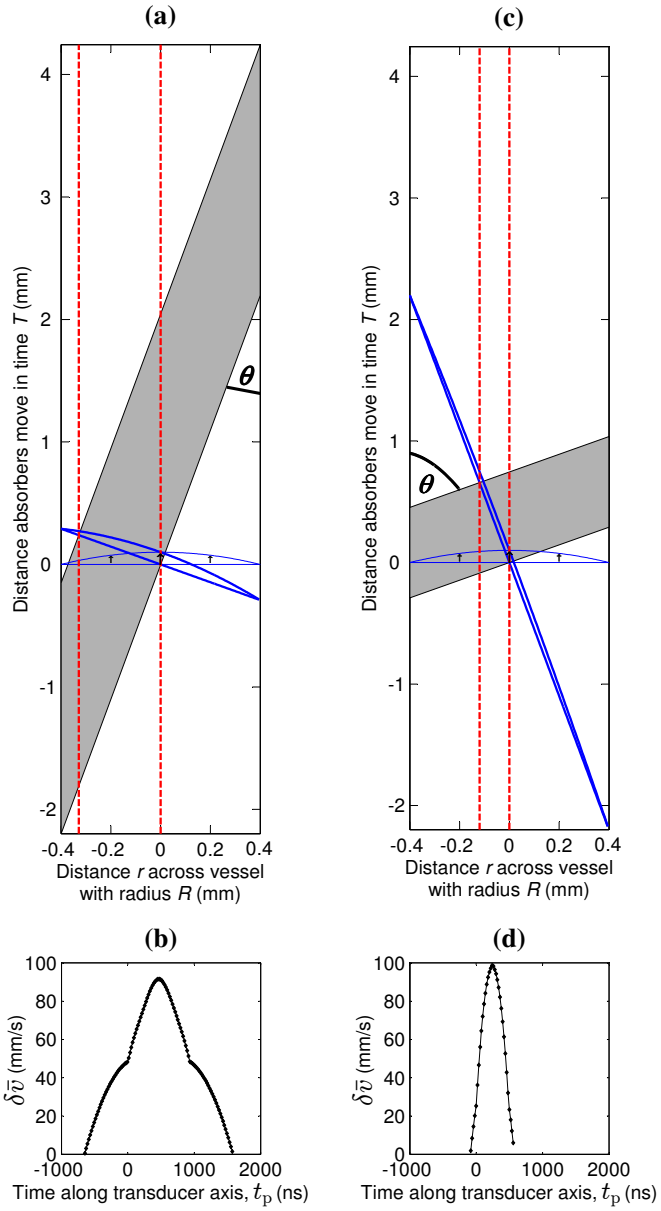

Figure 9.8: Time shift measurement at a particular time point along the transducer axis with the transducer in two different orientations: $\theta = 20°$ (a) and $\theta = 70°$ (c). The values for $\delta\bar{v}_{t_P}$ for different time points t_P along the length of the transducer axis are shown in (b) and (d) respectively for the two different orientations. The calculations are made for laminar flow ($\bar{v} = 50$ mm/s) in a tube with a radius of 0.4 mm. The transducer focal beam width is 0.35 mm.

9.1.5 Effects of tube radius and light absorption

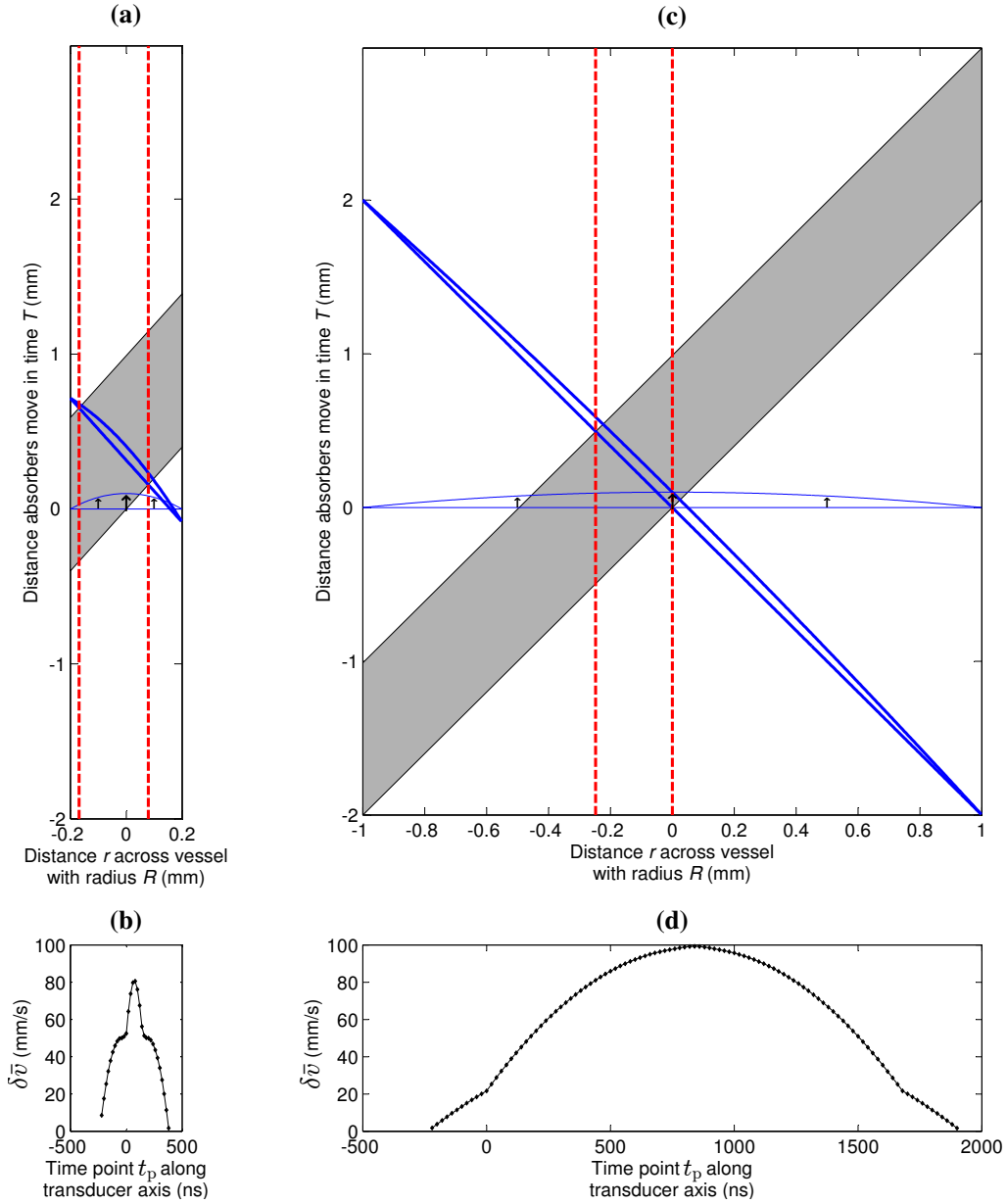

Figure 9.9: Time shift measurement for laminar flow ($\bar{v}$ = 50 mm/s) in tubes with diameters of 0.4 mm (a,b) and 2.0 mm (c,d). The transducer focal beam width is 0.35 mm and is oriented at an angle $\theta = 45°$ to the direction of flow. The illustrations in (a) and (c) show measurement of the time shift at one particular point along the transducer time axis; values of $\delta\bar{v}$ for different time points t_p along the length of the transducer axis are shown in (b) and (d) respectively for the two different tube diameters.

Figure 9.9 (a) and (c) illustrate laminar flow in tubes with diameters of 0.4 mm and 2.0 mm respectively, and also show a time shift measurement at a particular point along the transducer time axis. In the wider tube [Figure 9.9 (c)], the time shift meas-

urement entails sampling a smaller range of velocities than for the narrower tube [Figure 9.9 (a)] where the transducer focal beam cuts across the entire tube radius and therefore includes the full range of velocity values (0 mm/s to $\hat{v}$ mm/s). Time shift (and therefore velocity) measurements at multiple time points are plotted as $\delta\bar{v}$ values in Figure 9.9 (b) and (d) for the 0.4 mm and 2.0 mm tubes respectively. By comparison with Figure 9.8 (b) and (d), it is evident that increasing the tube radius has a similar effect to increasing the angle θ: whilst the narrower tube produces an un-parabolic $\delta\bar{v}$ profile and a maximum velocity that under-reads $\hat{v}$ = 100 mm/s, the profile of $\delta\bar{v}$ values for the wider tube more closely resembles the parabolic laminar velocity profile and the maximum value for $\delta\bar{v}$ is approximately equal to $\hat{v}$. The implication is that wider tubes (or, equivalently, narrower transducer beam widths) should enable more accurate velocity measurements. In contrast, the experimental data (Section 8.4) demonstrate poorer velocity accuracy obtained from larger diameter tubes (using a consistent transducer beam width). A likely explanation for the experimental results is the attenuation of light by absorbers close to the edge of the tube.

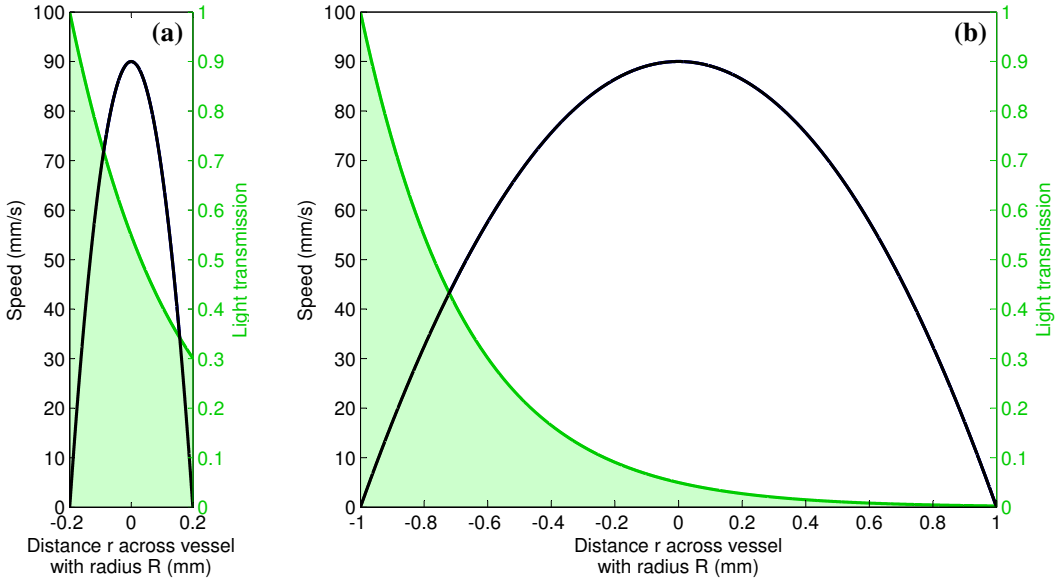

Figure 9.10: The effect of light absorption on the measured laminar flow profiles in tubes with diameters of 0.4 mm (a) and 2.0 mm (b). The green shaded region shows the exponential decay of light intensity (Eq. 9.9) due to absorption (coefficient $\mu_a = 3\ \text{mm}^{-1}$). The maximum intensity of light is absorbed at the lowest velocity part of the laminar velocity profile, which is shown for $\bar{v}$ = 45 mm/s (solid line).

The green shading in Figure 9.10 shows the exponential decay in the intensity of light as it passes through a 0.2 mm (a) and a 1.0 mm (b) radius tube. The decay is

calculated using the Beer-Lambert law with an absorption coefficient $\mu_a = 3$ mm^{-1}:

$$A = A_0 \exp(-\mu_a d) = A_0 10^{-\frac{\mu_a}{\ln(10)} d}. \tag{9.9}$$

A is the intensity of light after it has passed a distance d mm through a medium with an absorption coefficient μ_a mm^{-1}, and it is commonly compared to the original intensity A_0 using the optical density (OD):

$$\text{OD} = \log_{10}\left(\frac{A}{A_0}\right). \tag{9.10}$$

It is evident from Figure 9.10 that whilst ~55% of the light is transmitted to the centre of the 0.2 mm tube (an attenuation of 0.3 OD), only ~5% of the light reaches the centre of the 1.0 mm tube (an attenuation of 1.3 OD). As a result, the photoacoustic signal, which is generated as a consequence of light absorption and has a magnitude proportional to the light intensity, will arise predominantly from the absorbers in the first few hundred microns from the tube edge. Thus, for a laminar velocity profile, the greatest contribution to the photoacoustic signal will be from the slowest moving absorbers, and this will tend the photoacoustically-measured velocity to under-read the true average flow velocity ($\bar{v} = \hat{v}/2$).

It is not straightforward to quantitatively simulate the under-reading due to light attenuation. However, one approach is to consider the effect of signal amplitude on the cross-correlation function: the relative amplitudes of the lobes in the cross-correlation function are directly related to the amplitudes of the corresponding parts of the signals. The time shift measurement t_s is derived from the position of the maximum amplitude cross-correlation lobe (see Figure 6.3, page 93) and therefore t_s is biased towards the time shift associated with the largest amplitude parts of the underlying signals. Hence the time shift will be weighted towards the shift associated with signal segments arising from absorbers close to the first edge of the tube (i.e. early time points in the signals), where the light intensity, and consequently the photoacoustic signal amplitude, is greatest.

At a wavelength of 532 nm, human blood has an absorption coefficient of $\mu_a \approx 25$ mm^{-1} (see Figure 5.8). Therefore, according to the Beer-Lambert law (Equation 9.9), the intensity A of light that penetrates through to the centre of an $R = 0.4$ mm radius tube will be only ~0.0045% of the original intensity A_0. In other words, the light will be attenuated by 4.3 optical densities (OD) across the radius R, and the consequentially low SNR would make photoacoustic measurement of the maximum velocity ($\hat{v} = 2 \times \bar{v}$) virtually impossible. Moreover, the transport of light in blood is not limited to absorption: the light is also strongly forward scattered, and the reduced scattering coefficient

(μ_s'), as well as the absorption coefficient, increases with increasing haematocrit [83]. The overall light attenuation due to both absorption and scattering would result in a bias towards the low velocities at the edge of the tube, giving velocity measurements with values $V' << \bar{v}$, which would agree with the experimental data (for example, Figure 8.8). However, analysis of only a small segment of the time signals could avoid the bias due to averaging over the entire attenuation-weighted signals: provided that a non-negligible intensity of light penetrates to the depth F_0 of interest, it should be possible to make accurate velocity measurements over a small range of depths around F_0, by time-gating around the corresponding time point $t_0 = F_0/c$ (for sound speed c). In fact, a depth range could be chosen such that the mean velocity in the corresponding small region of the tube represents the average velocity across the entire tube radius. A simple consideration of two-dimensional slices parallel to the tube walls suggests that a depth range in the centre of the tube would entail averaging over the entire laminar flow profile. However, in practice the transducer is never perpendicular to the tube (velocity measurements would not be possible in this orientation), and an analysis of the velocities in the tube sections corresponding to a particular range gate is a complicated three-dimensional problem, as mentioned on page 144. It is certainly not possible to predict the velocities of small three-dimensional segments from Equation 9.8, but the analyses in the foregoing sub-sections serve as a useful illustration of the effects of transducer beam width (the $|V_{\max}|$ effect), transducer angle and tube diameter.

The extent of absorption, and its effect on the photoacoustically measured velocities, could be elucidated by comparing velocity measurements made using a range of different wavelengths of light; in the absence of such measurements it is difficult to draw any definite conclusions. However, further insight into the flow speed of the absorbers (red blood cells) at different distances r across the tube radius could be obtained in a manner similar to the calculations of $\delta\bar{v}$ at specific time points t_P, by evaluating time shifts for small segments along the time axis of the photoacoustic signals. This process is termed "waveform segmentation" and is discussed in the following section.

9.2 Waveform segmentation

The previous section identified that laminar flow gives rise to velocities ranging from zero at the tube walls to $\hat{v}$ in the tube centre. The known velocity V in the experiments is the average flow velocity $\bar{v} = \hat{v}/2$. However, it seems likely that different time segments of the photoacoustic signals undergo different time shifts according to the range of flow velocities in the corresponding segments of the tube. This is analogous to the calculation of $\delta\bar{v}$ at specific time points t_{P}, as described in the previous section.

9.2.1 Segmentation method

Figure 9.11 illustrates the process by which a time shift between small time segments of the photoacoustic signals can be evaluated. Figure 9.11 (a) shows a pair of waveforms (1.25 μs long) extracted from a FastFrame record obtained with a red blood cell (RBC) suspension flowing at an average velocity of $V = \bar{v} = 58 \pm 6$ mm/s in a 390 μm tube, with $T = 0.5$ ms and using the 30 MHz focussed transducer. The discrete unbiased cross-correlation function (Equation 4.7, page 66) was evaluated for this waveform pair, as well as for each of the 25 pairs in the FastFrame record. The mean $C(t)$ of all the cross-correlation functions is illustrated in Figure 9.11 (b), and an expanded view of the 100 points centred on the central peak lobe of $C(t)$ is shown in Figure 9.11 (c). The lower three plots, (d), (e) and (f), in Figure 9.11 repeat the information shown in (a) to (c), but for a small time segment (62.5 ns) of the waveform pairs. For the waveform segments, the peak of the mean cross-correlation function $C_s(t)$ [Figure 9.11 (f)] occurs at a horizontal position that coincides almost exactly with the "known" (average) time shift ($t_s \approx 14$ ns), whereas the peak value of $C(t)$ [Figure 9.11 (c)] corresponds to a time shift measurement of approximately zero, and thus greatly under-reads the known value. This suggests that time shift calculated from the entire waveform is somehow biased towards the slower velocities in the laminar profile, whereas by analysing only a small waveform segment, the average velocity can be more accurately quantified.

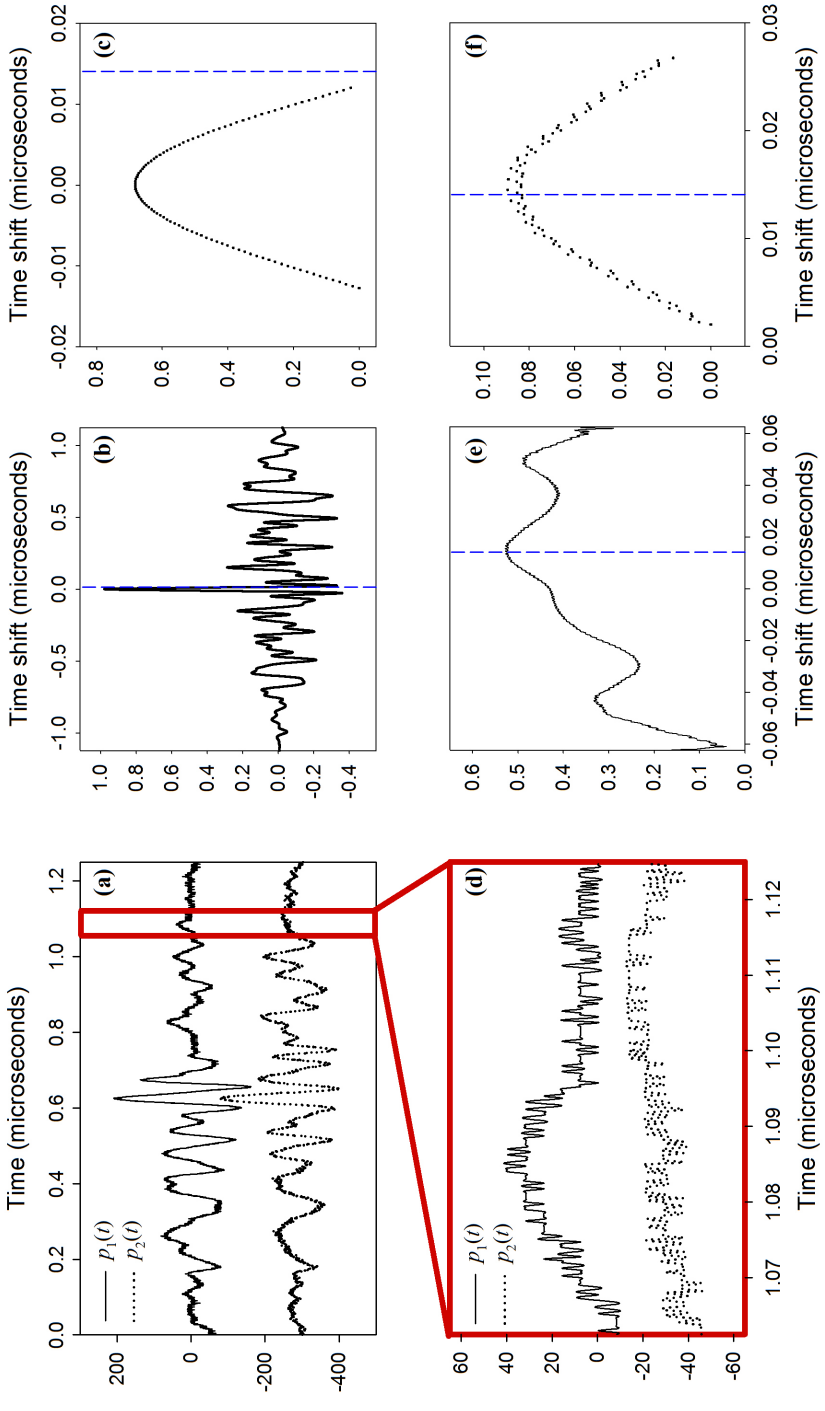

Figure 9.11: Illustration of the signal segmentation process. (a) One of 25 (5000-point) PA waveform pairs ($p_1(t)$, $p_2(t)$) acquired using the 30 MHz transducer ($\theta = 45°$) following double pulse illumination (PIV laser, $T = 0.5$ ms) of a RBC suspension (27% of a normal haematocrit) flowing in a $2R = 390$ μm tube. The mean $C(t)$ of all 25 cross-correlation functions is shown in (b) and an enlargement of 100 points (sampling interval 0.25 ns) centred on the peak in (c). The dashed vertical line marks the known time shift (14 ns). A 250-point segment of $p_1(t)$, $p_2(t)$ is enlarged in (d), and the corresponding mean cross-correlation function $C_s(t)$, and 100 points around the peak are shown in (e) and (f).

The signals shown in Figure 9.11 (a) were acquired with the 30 MHz focussed transducer, and using an oscilloscope bandwidth of 250 MHz, which warrants rejection of frequencies at least above 250 MHz. Figure 9.12 (a) shows the signal segments in Figure 9.11 (d) after the data was passed through a low-pass 250 MHz Butterworth filter (order 10). The resulting mean cross-correlation function $C_s(t)'$ [Figure 9.12 (b)] is free from high-frequency noise, which eases the problem of finding an appropriate fit to the peak lobe: Figure 9.12 (c) shows the peak lobe with a ten-point Interpolant. Subsequent analysis will therefore entail removal of high frequency noise (using a low-pass 250 MHz order 10 Butterworth filter) followed by an analysis of the cross-correlation peak lobe via an Interpolant fit.

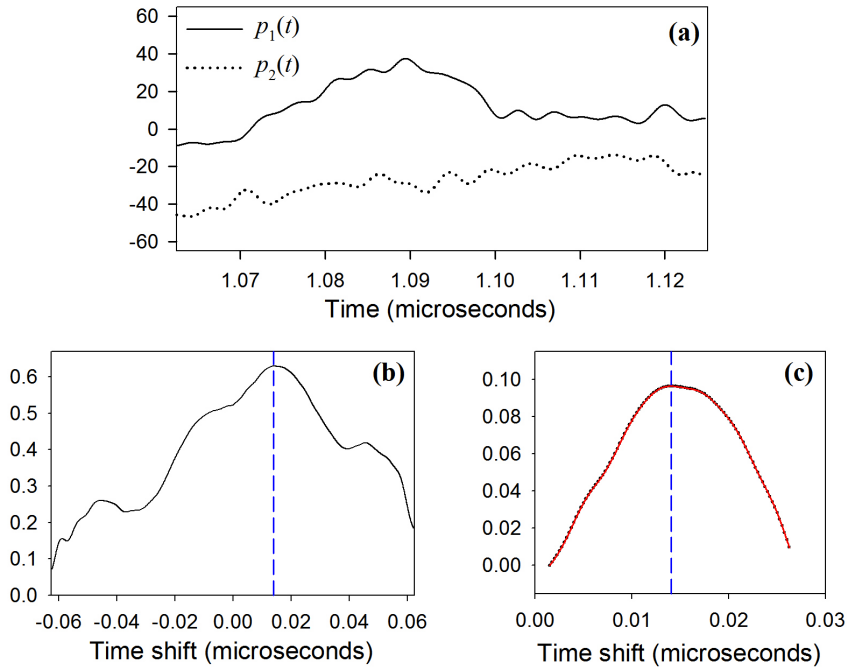

Figure 9.12: Fitting to the peak lobe of the mean cross-correlation function $C_s(t)'$ calculated for the data shown in Fig. 9.11, after filtering with a low-pass 250 MHz Butterworth filter (order 10). The filtered waveform segments are shown in (a) and mean cross-correlation function in (b). A ten-point Interpolant fit to the cross-correlation peak lobe is shown in (c), and the dashed vertical line marks the known time shift (14 ns).

9.2.2 Calculation of velocity resolution

Section 6.3 described a method for calculating a time shift resolution $\Delta t_s'$ (and therefore a velocity resolution $\Delta V'$) based on the error bars associated with the cross-correlation peak lobe. These y axis error bars reflect the variation in amplitude of the underlying 25 normalised cross-correlation functions, and this variation in turn points to vari-

ability in the location of the cross-correlation peak amongst the 25 functions, since each function is normalised to its maximum value. Therefore it is logical to conclude that the resulting $\Delta t_s'$ (Equation 6.3, page 91) reflects the variation in the time shift measured for the individual waveform pairs and thus provides a good estimate of the uncertainty in the time shift measurement. Even so, further investigation reveals that in fact the above method – subsequently referred to as the "Peak analysis method" – is *not* always the most representative way to estimate $\Delta t_s'$, for reasons discussed below. An alternative, more straightforward method – the "Standard deviation method" – is introduced on page 164.

Essentially, the "Peak analysis method" entails calculating a resolution for a single measurement obtained from 25 cross-correlation functions, as described in Section 6.3, and then propagating many such resolution values in order to arrive at a single resolution associated with the mean of multiple measurements. The "Standard deviation method" does not analyse the cross-correlation peak to find the resolution from 25 waveform pairs, but simply takes the time shift value, and then calculates a resolution from the standard deviation of multiple measurements, the mean of which is the final measurement value, as in the "Peak analysis method".

There are two disadvantages of the "Peak analysis method" and these are discussed in the following two sub-sections. The first limitation is one of subjectivity, since the individual resolution values vary according to the selected number of points in the cross-correlation peak lobes. The second disadvantage arises when there is considerable variation in the 25 individual cross-correlation functions, leading to very large error bars in the individual measurements even though the spread of multiple measurements is small; this is particularly true for cross-correlations calculated for waveform segments. However, for the entire waveforms, where the spread of individual time shift values is similar to that of multiple measurements (in other words, simply averaging over the 25 cross-correlation functions is sufficient), the "Peak analysis" and "Standard deviation" methods give comparable resolution values.

Peak analysis method: variability with extent of cross-correlation peak lobe

Figure 9.13 illustrates that, using the "Peak analysis method", the calculated resolution value $\Delta t_s'$, and therefore the velocity resolution $\pm\Delta V'/2$, depends on the chosen extent of the cross-correlation peak lobe, which in the preceding examples [Figure 9.11(c),(f) and Figure 9.12(c)] comprised $m = 100$ data points centred on the peak. The cross-correlation function $C(t)'$ in Figure 9.13 (1a) is the mean of 25 cross-correlation functions for waveform pairs acquired under the same conditions as in Figure 9.11 but for the RBC suspension moving at an average velocity of $V = \bar{v} = 35 \pm 3$ mm/s. The $m = 175$

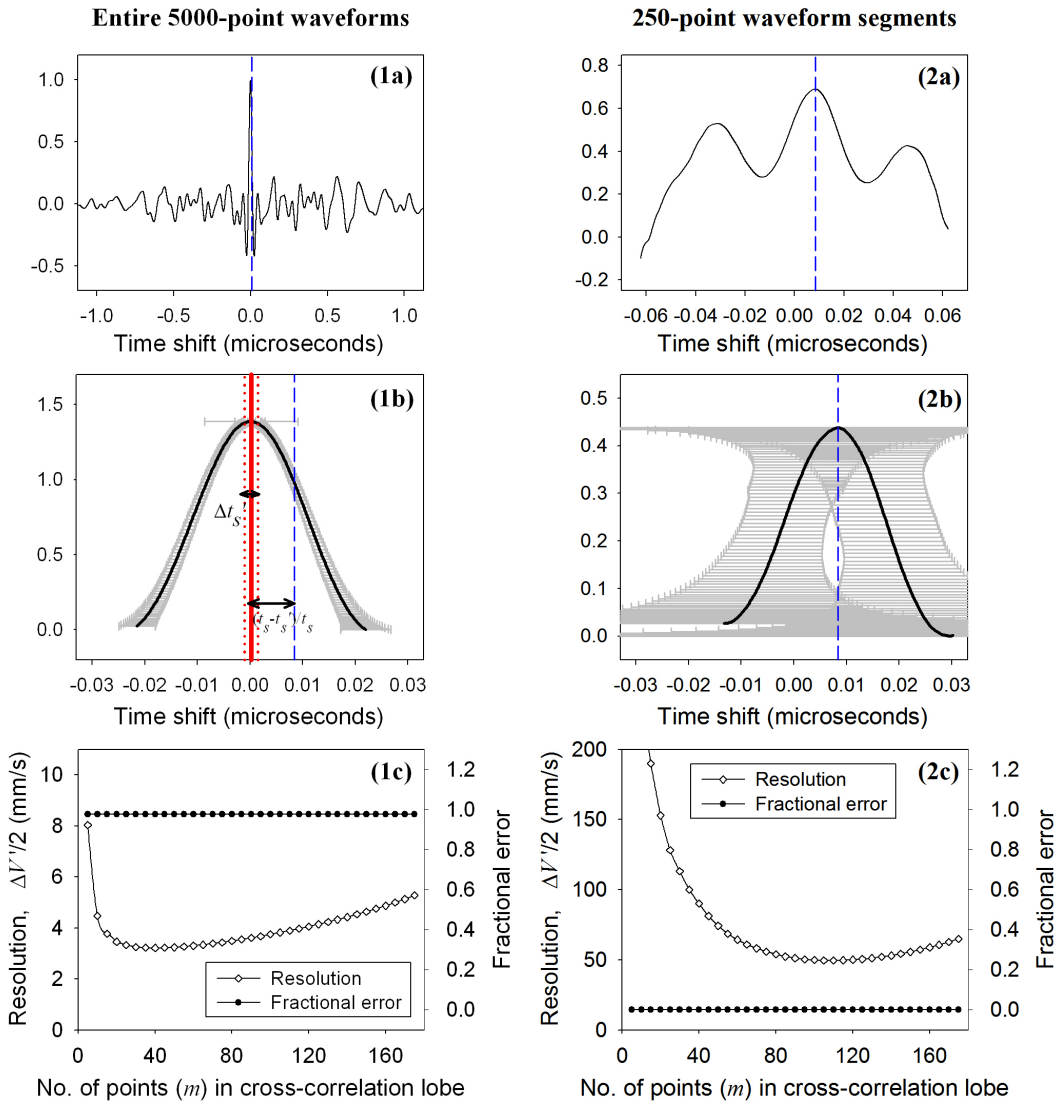

Figure 9.13: Variation in the velocity resolution $\pm\Delta V'/2$ with the number of data points in the cross-correlation peak lobe. (1a) Mean cross-correlation function for a series of 25 (5000-point) waveform pairs acquired under the same conditions described in Fig. 9.11 but for RBCs moving at an average velocity of $V = \bar{v} = 35 \pm 3$ mm/s. The $m = 175$ data points centred on the cross-correlation peak are shown in (1b) with the propagated time shift (x axis) errors calculated as described in the text, giving a weighted mean time shift resolution $\Delta t_s' \approx 1.3$ ns, as shown by the dotted vertical lines. The dashed vertical lines in (1a) and (1b) mark the known time shift ($t_s \approx 8.4$ ns), and the solid vertical line in (1b) shows the measured time shift ($t_s' \approx 0.2$ ns). The resolution values $\pm\Delta V'/2$ derived from $\Delta t_s'$ are plotted in (1c), together with fractional errors in the time shift position of the cross-correlation peak, for values of m ranging from 5 to 175. The data in (1a)-(1c) are repeated in (2a)-(2c) but for a 250-point segment of the waveforms.

data points centred on the cross-correlation peak are shown in (1b), together with the time shift (x axis) error bars δt_i (Equation 6.2, page 91). The weighted mean of these time shift errors is used to calculate a resolution $\Delta t_s' \approx 1.3$ ns ($\pm\Delta V'/2 \approx 5.3$ mm/s), and the position of the peak ($t_s' \approx 0.2$ ns) gives a fractional error $(t_s - t_s')/t_s \approx 100\%$ in the velocity measurement V' relative to the "known" value V. Values for the resolution $\pm\Delta V'/2$ and fractional error $(V - V')/V = (t_s - t_s')/t_s$ are plotted in Figure 9.13 (1c) for m ranging from 5 to 175 data points. The same data are plotted in Figure 9.13 (2c) but for 250-point segments extracted from the 25 waveform pairs evaluated in Figure 9.13 (1a)-(1c). The mean $C_s(t)'$ of the 25 segment cross-correlation functions is shown in Figure 9.13 (2a) and the $m = 175$ data points centred on the cross-correlation peak are shown in (2b), together with the x axis error bars, calculated in the same way as described above for (1b).

As m is reduced from 175 to 40 points, the resolution calculated for the entire waveforms [Figure 9.13 (1c)] improves due to exclusion of the larger δt_i values at the edges of the lobe [Figure 9.13 (1b)]; for $20 \leq m \leq 40$ there is little change in the measured velocity resolution, but for $m < 20$, the resolution rapidly deteriorates due to the large δt_i values at the cross-correlation peak. This trend of $\pm\Delta V'/2$ with respect to m, and in particular the negligible variation in $\pm\Delta V'/2$ for $20 \leq m \leq 40$, is fairly consistent under different experimental conditions, and therefore all the experiments in the preceding sections (Section 8.1 to 8.4) used $m = 20$; whilst this number of data points may not always have resulted in the best value for $\pm\Delta V'/2$, it provided a consistent means for estimating $\pm\Delta V'/2$ values that were within $\sim 5\%$ of the optimum. For short and potentially noisy segments of the waveforms, it is inappropriate to choose a fixed number of data points (m) for the cross-correlation peak lobe, since there is considerable variation of $\pm\Delta V'/2$ with m. There is a factor of ~ 10 difference between the resolution calculated at $m = 5$ and the optimum value at $m = 110$ [Figure 9.13 (2c)], whereas for the entire waveforms [Figure 9.14 (1c)], the poorest resolution at $m = 5$ is larger than the optimum value of $\pm\Delta V'/2 \approx 3.2$ mm/s (at $m = 40$) by a factor of ~ 1.5. Although the variation in $\pm\Delta V'/2$ in Figure 9.13 (2c) is less than 10% for $80 \leq m \leq 120$, this feature is not consistent under different experimental conditions. Note however that, in both (1c) and (2c), the fractional error, which is derived from the error in the position of the peak relative to the known time shift (dashed vertical line), remains consistent regardless of m (provided an Interpolant fit is used), since the m points are always chosen to be centred on the cross-correlation peak. The selection of m therefore influences the calculated resolution $\Delta t_s'$, but not the measured time shift t_s'. However, subsequent calculations will avoid this subjectivity by using an alternative method – the "Standard deviation method" – for estimating $\pm\Delta V'/2$ that makes the resolution,

as well as the accuracy, independent of the m data points in the cross-correlation peak lobe.

Comparison of "Peak analysis" and "Standard deviation" methods

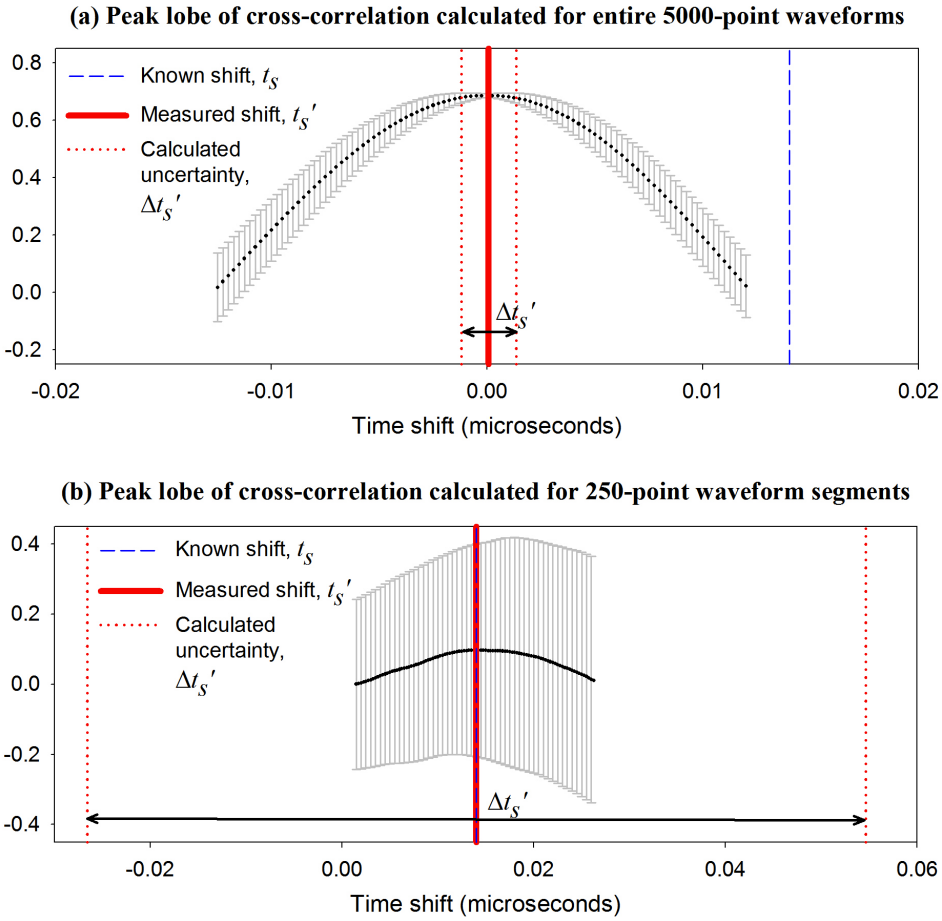

Figure 9.14: Uncertainties associated with peak lobes of the cross-correlation functions calculated from the entire 5000-point waveforms (a) and from the 250-point waveform segments (b). The data is that shown in Fig. 9.11 (a) after filtering with a low-pass 250 MHz Butterworth filter (order 10). The y axis error bars represent the standard deviations in the amplitudes at each point, and the dotted vertical lines mark the resolution calculated from these error bars (see Section 6.3). The solid vertical line shows the position of the maximum amplitude value, which gives $t_s' \approx 1$ ns in (a) and $t_s' = \approx 14$ ns in (b); the dashed vertical line in each plot marks the known time shift ($t_s = 14$ ns).

Figure 9.14 shows the peak lobes of the mean cross-correlation functions calculated for the data described in Figure 9.11 (a) after filtering with a low-pass 250 MHz Butterworth filter (order 10). The peak lobe in Figure 9.14 (a) is for the mean cross-correlation function $C(t)'$ calculated from the entire 5000-point filtered waveforms, whilst the peak in (b) corresponds to the mean cross-correlation function $C_s(t)'$ cal-

culated from the 250-point waveform segments shown in Figure 9.12 (a). The y axis error bars correspond to the standard deviations of the amplitudes of the 25 cross-correlation functions used to calculate the mean (see Section 6.3). The weighted mean time shift error $\Delta t_s'$ is calculated using an Interpolant fit and Equation 6.3 (page 91) and indicated by the dotted vertical lines on either side of the peak (solid vertical line). From Figure 9.14 (a) the calculated $\Delta t_s'$ value (1.26 ns) for $C(t)'$ appears to be a representative estimate of the uncertainty in the time shift measurement (t_s' = 0.08 ns). However, in Figure 9.14 (b), the calculated $\Delta t_s'$ value (40.6 ns) is nearly three times larger than the time shift measurement itself (which is approximately equal to the known time shift: $t_s' \approx t_s$ = 14.0 ns). Whilst this large resolution reflects the large y axis error bars, it over-estimates the variability in repeated measurements of t_s' (each derived from the mean of 25 cross-correlation functions), and this is illustrated in Figure 9.15.

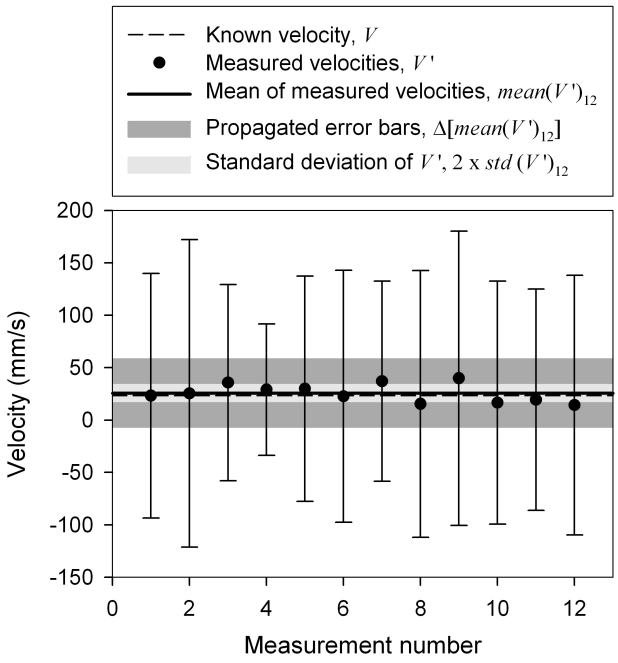

Figure 9.15: A typical distribution of velocity measurements V' for absorbers moving at a "known" average velocity $V = \bar{v} = 23 \pm 2$ mm/s, marked by a dashed horizontal line. Each data point V_n' was derived from the mean of 25 cross-correlation functions calculated for 250-point segments of 5000-point waveforms, and the length of the vertical error bars are equal to $\Delta V_n'$ (Equation 6.4, page 93). The mean of the twelve V_n' [$mean(V')_{12} \approx 26$ mm/s] is marked with a solid horizontal line. The total height of the dark grey shading is the propagated resolution $\Delta[mean(V')_N]$ (Equation 9.11, the "Peak analysis method") and the total height of the light grey shading is equal to twice the standard deviation (i.e. $2 \times std(V')_{12}$, the "Standard deviation method").

The data points in Figure 9.15 show twelve nominally identical velocity measurements (V') made under the experimental conditions described in Figure 9.11, but with

the RBC suspension moving at an average velocity of $V = \bar{v} = 23 \pm 2$ mm/s, which is marked by the dashed horizontal line. Each value of V' was derived from the mean of 25 cross-correlation functions calculated for 250-point waveform segments, which were extracted from the 5000-point waveforms at the time point shown in the example in Figure 9.15 (b). The mean of the twelve measurements ($mean(V')_{12}$) is 26 mm/s, and this is marked with a solid horizontal line in Figure 9.15. According to the "Peak analysis method", the resolution $\Delta[mean(V')_N]$ associated with this mean velocity is calculated by propagating the error bars $\Delta V'_n$ of the N individual measurements V'_n:

$$\Delta[mean(V')_N] = \frac{\sqrt{\sum_{n=1}^{N} (\Delta V'_n)^2}}{N}. \tag{9.11}$$

The propagated error $\pm\Delta[mean(V')_N]/2 \approx 33$ mm/s is shown in Figure 9.15 by the dark grey shading. It is clear that this overestimates the variation in V'_n since the upper limit $\{mean(V')_{12} + \Delta[mean(V')_{12}]/2\}$ is larger than the maximum value for V'_n by a factor of ~ 1.5. A more representative measure for the variability in V'_n is the sample standard deviation, denoted $std(V')_N$, which is shown in Figure 9.15 by the light grey shading ($\pm std(V')_{12} \approx 9$ mm/s): this is the resolution calculated according to the "Standard deviation method". The subsequent results in this section present mean values $mean(V')_N$ of N individual measurements V'_n (each calculated from the mean of 25 cross-correlation functions), with y axis error bars representing the resolution $\pm std(V')_N$.

The error bars for the velocities calculated from waveform segments are much larger than those for velocities calculated from the entire waveform, and this is due to the reduced SNR in the segments. In other words, more averaging is required for the segments, whereas for the entire waveforms, averaging over the 25 cross-correlation functions (the "Peak analysis" method) is sufficient. The following sub-section describes another consequence of the limited SNR for the segments: the occurrence of "extreme" velocity measurements, which, unless they are excluded, will further degrade the measurement resolution.

9.2.3 Exclusion of extreme velocity measurements

It is inevitable that velocity measurements derived from a short segment of the waveform pairs will demonstrate greater variability than measurements calculated from the entire waveforms. This is because the correlation of short signal segments is more susceptible to corruption by small irregularities in absorber motion (for example, non-linear motion of absorbers, or the appearance of new absorbers in the region of interest in the time T between two laser illuminations), giving rise to cross-correlation peaks at extreme time shift positions.

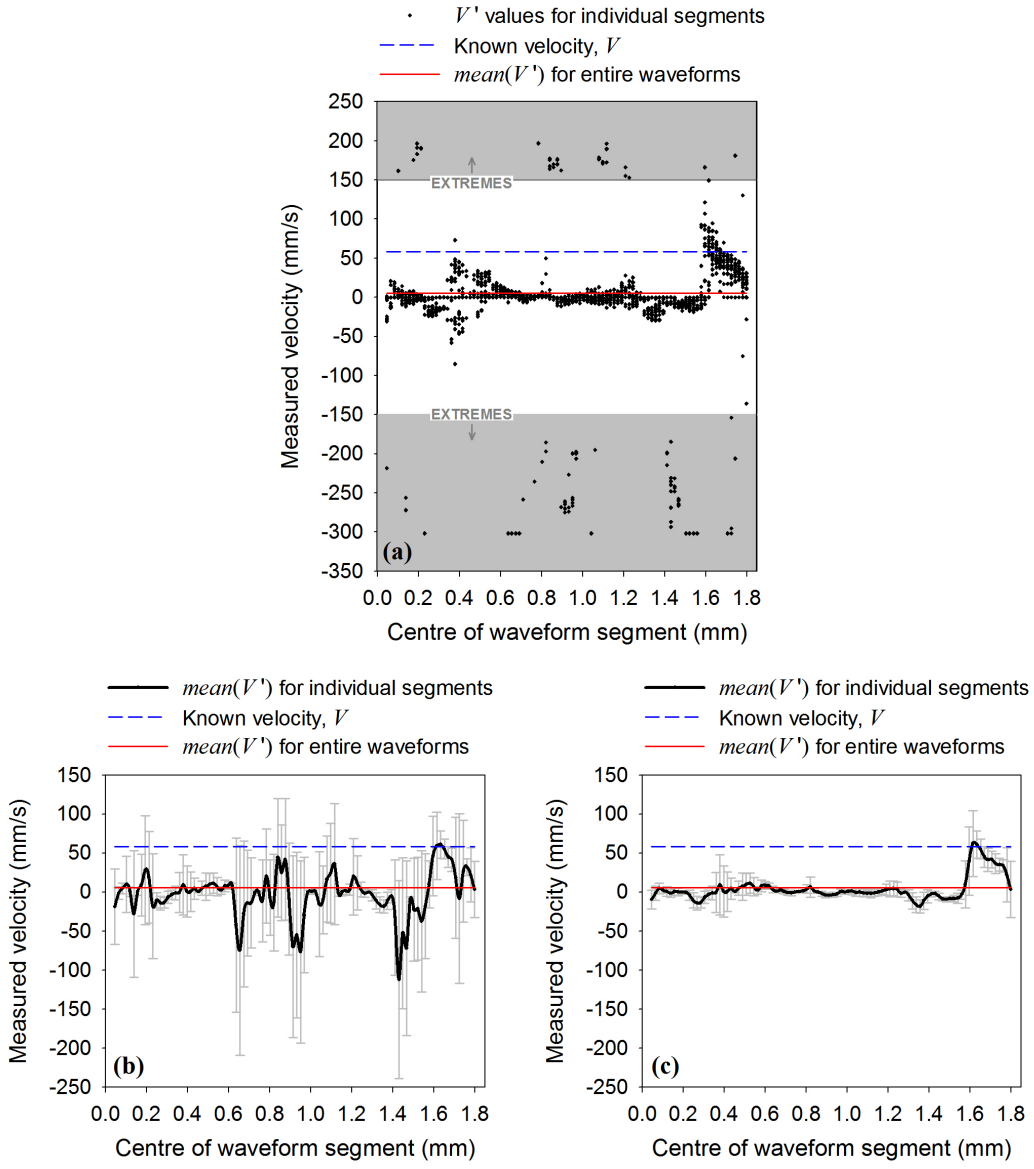

Figure 9.16: Velocity measurements V'_n ($n = 1 \ldots 20$) calculated for 250-point waveform segments (a); the lower two plots show mean velocity measurements $mean(V')_N$ where extreme values ($|V'_n| > 150$ mm/s) are included and excluded in (b) and (c) respectively. The values $mean(V')_N$ are the mean of N velocity measurements acquired under the experimental conditions described in Figure 9.11, where the RBC suspension was moving in a 390 μm diameter tube at a "known" average velocity of $V = \bar{v} = 58 \pm 6$ mm/s, which is marked by the dashed horizontal lines. $mean(V')_N$ for the entire 5000-point waveforms is marked with a solid horizontal line, whilst the black curve plots $mean(V')_N$ for 250-point waveform segments stepped by 50 points along the signal lengths. The centre of each waveform segment is shown on the x axis, where the time along the signal length is converted to distance using a sound speed of $c = 1476$ m/s.

Figure 9.16 (a) shows $N = 20$ measurements V'_n ($n = 1 \ldots 20$) made under the experimental conditions described in Figure 9.11. Each V'_n was calculated from $C_s(t)'$ (the mean of 25 cross-correlations of the 250-point (62.5 μs) waveform segments), for segments extracted at different time points (centred on t_P, analogous to the t_P used in the simulations: see page 149) stepped by 50 points (62.5 μs) along the signal lengths. The centre of each waveform segment is shown on the x axis, where the time along the signal length is converted to distance using a sound speed of $c = 1476$ m/s. The majority of the measurements take values $|V'_n| < 150$ mm/s: values $|V'_n| > 150$ mm/s are therefore denoted "extreme" values. The "known" average velocity of the RBC suspension ($V = \bar{v} = 58 \pm 6$ mm/s) is marked by the dashed horizontal line, and the mean velocity $mean(V')_{20}$, where each V'_n was calculated from $C(t)'$ (the mean of 25 cross-correlations of the entire 5000-point (1.25 μs) waveforms), is marked with a solid horizontal line.

The black curve in Figure 9.16 (b) shows the mean velocity values $mean(V')_{20}$ (denoted as the "measured velocity" on the y axis) of the $N = 20$ measurements V'_n ($n = 1 \ldots 20$) shown in Figure 9.16 (a) for different 250-point segments. The error bars equate to $\pm std(V')_{20}$ for the corresponding values of $mean(V')_{20}$. The "extreme" values ($|V'_n| > 150$ mm/s) result in considerable fluctuation in the mean measured velocity $mean(V')_{20}$ for segments at different time points, and large error bars. If however, values of $|V'_n| > 150$ mm/s are excluded from the calculation of the mean velocity, then the resulting values $mean(V')_N$ produce a much smoother profile along the signal length, as shown in Figure 9.16 (c). Note that these measurements are referred to as $mean(V')_N$, rather than $mean(V')_{20}$ as for Figure 9.16 (b), since the number of points N used to calculate the mean will vary according to the number of extreme values ($|V'_n| > 150$ mm/s) at the relevant time point. In subsequent calculations of $mean(V')_N$, the extreme values will be excluded and, where relevant, the remaining number N of $|V'_n| \leq 150$ mm/s will be quoted.

9.2.4 Velocity profiles for different RBC concentrations

Figure 9.17 shows values of $mean(V')_N \pm std(V')_N$, calculated for $|V'_n| \leq 150$ mm/s [i.e. excluding "extreme" values, as in Figure 9.16 (c)], for four different RBC concentrations (3%, 6%, 27% and 131% of a physiologically normal haematocrit), and for six different "known" velocities ($V = 0$, 6, 12, 23, 35 and 58 mm/s). The physiologically normal haematocrit, Ht, is taken to be 0.45 (i.e. RBCs comprising 45% of the total blood volume). For the plots labelled (a) (i.e. the left column of plots), the V'_n underlying $mean(V')_N$ were derived from $C(t)'$ (the mean cross-correlation of the entire 5000-point signals). In the middle column plots, labelled (b), the underlying V'_n were derived from $C_s(t)'$ calculated for 250-point waveform segments centred at a time

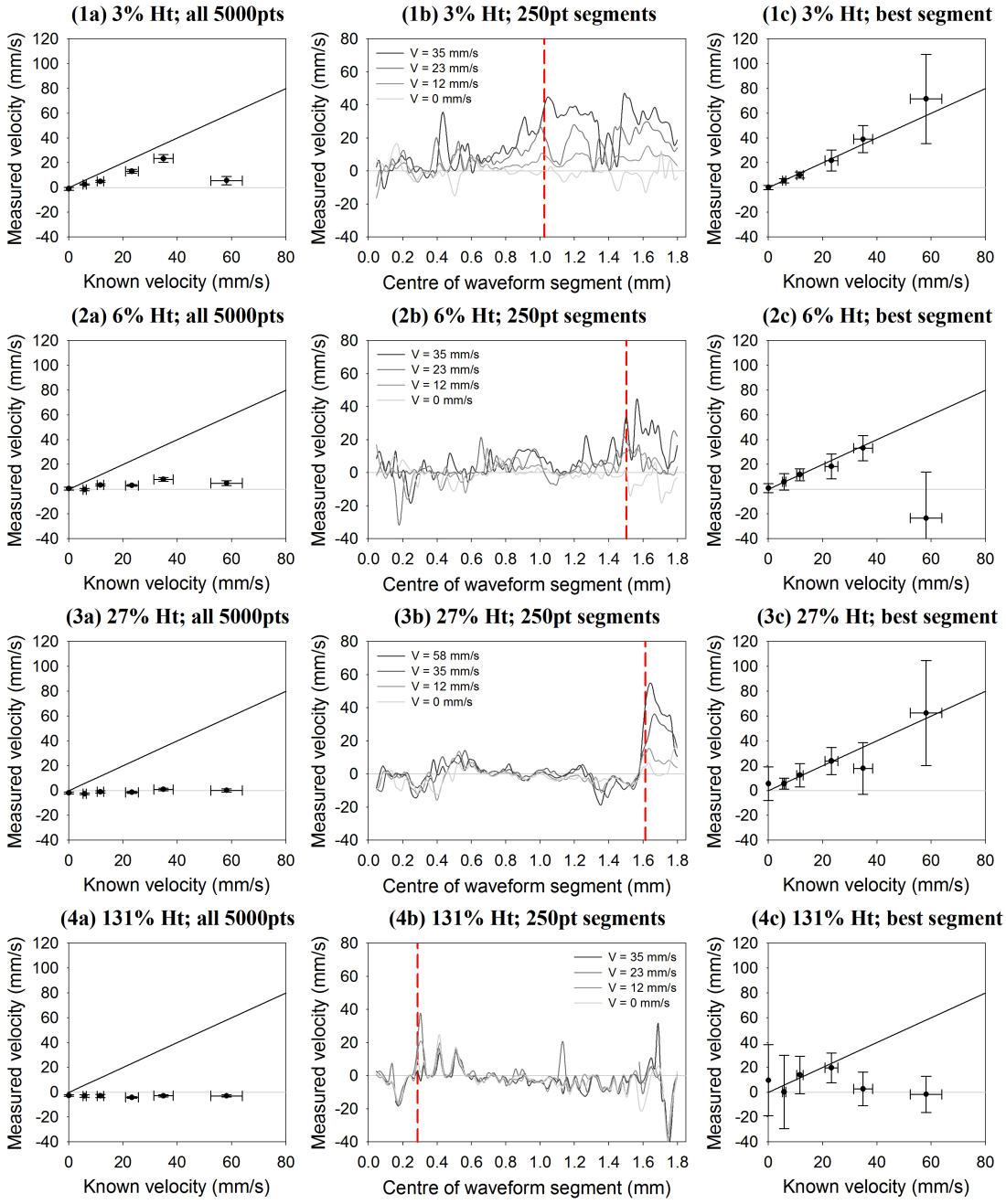

Figure 9.17: Velocity measurements made at "known" average velocities V = 0, 6, 12, 23, 35 and 58 mm/s for four different red blood cell (RBC) concentrations, 3%, 6%, 27% and 131% of a physiologically normal haematocrit (Ht), shown in rows 1-4 respectively. In each plot, the measured velocity (y axis) is the mean value $mean(V')_N$ calculated for N individual velocity measurements V_n' (each using 25 cross-correlation functions) acquired using the 30 MHz transducer ($\theta = 45°$) following double pulse illumination (PIV laser, T = 0.5 ms) of the RBC suspension flowing in a $2R$ = 390 μm tube. For the $mean(V')_N$ values plotted in the left column of plots (a), the cross-correlations $C(t)'$ were performed for the entire 5000-point signals, whereas for the middle (b) and right (c) columns of plots, the cross-correlations $C_s(t)'$ were performed for 250-point waveform segments; plots (b) show $mean(V')_N$ values at the time point indicated by the dashed vertical lines in plots (c). Further details are given in the text (page 169).

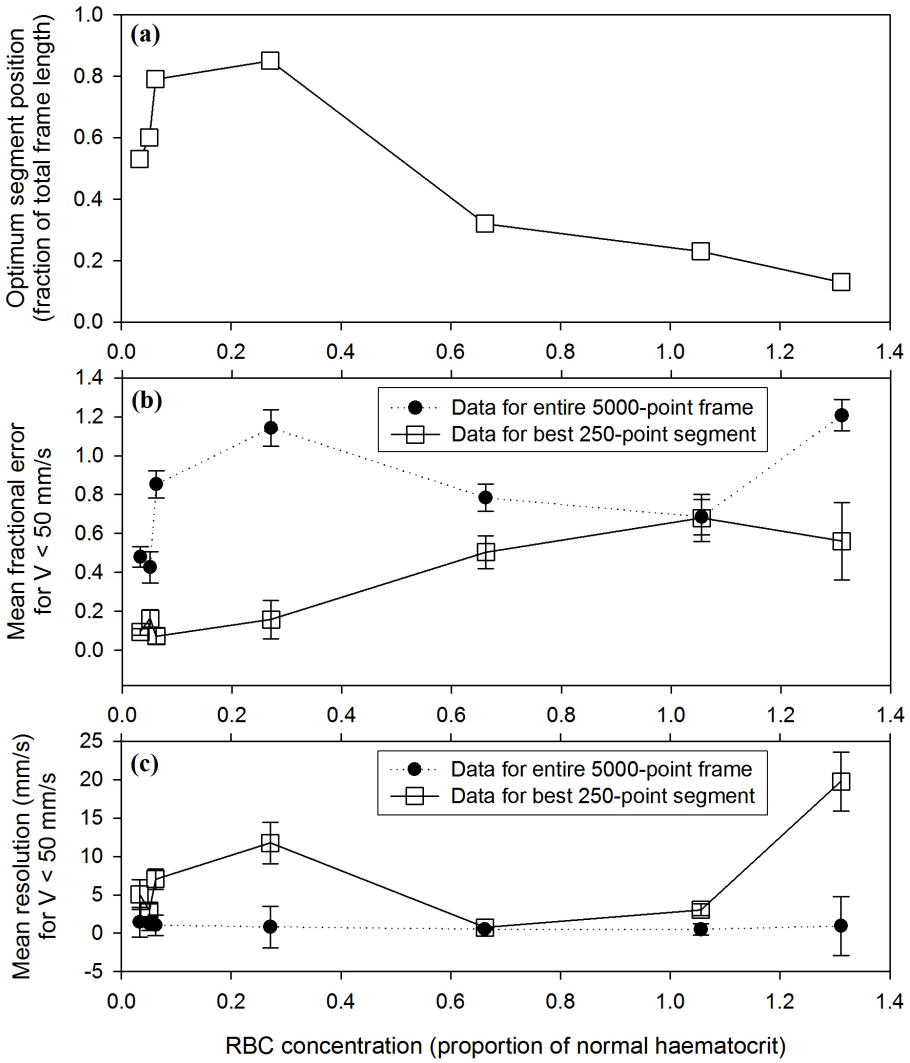

Figure 9.18: Comparison of the position of the "best" segment (a), the accuracy (b), and the resolution (c) for red blood cell (RBC) concentrations ranging from 3% to 131% of a physiologically normal haematocrit (Ht). The accuracies in (b) are the fractional errors (relative to V) of measurements $mean(V')_N$ made for known velocities $V < 50$ mm/s. The solid circles plot the average fractional error in the cases where the $(V')_N$ underlying $mean(V')_N$ were calculated for the entire 5000-point waveforms, whilst the underlying $(V')_N$ for the unfilled squares were calculated for the best 250-point segment. The resolution in (c) is the average $std(V')_N$ associated with measurements $mean(V')_N$ in (b). The error bars in (b) and (c) represent the standard error on the average fractional error and resolution values respectively.

point t_P; this central time point was stepped by 50 points along the signal lengths, resulting in profiles of $mean(V')_N$ values as a function of the segment position (directly proportional to t_P); examples are plotted for four different velocities. The number of measurements used in the calculation of $mean(V')_N$ varied according to the number of extreme measurements ($|V'_n| > 150$ mm/s) rejected at each of the corresponding time points (96 time points in total). The right column plots (c) show the $mean(V')_N$ values for all six velocities, calculated for the segments at the time point indicated by the dashed vertical line in the corresponding plot (b), where $N = 19$, 20, 20 and 13 for the 3%, 6%, 27% and 131% concentrations respectively. These same N values were used to calculate $mean(V')_N$ for the entire waveforms (left column of (a) plots) to enable a direct comparison in accuracy and resolution. The "best" segments for the (c) plots were selected to give the optimum accuracy. This entailed calculating the absolute fractional error in $mean(V')_N$ (i.e. $|[V - mean(V')_N]/V|$) for each of the six velocities V at each of the 96 segment time points, and then averaging across the six velocities (since the optimum accuracy varies for different velocities) in order to associate each time point with a single mean accuracy. The "best" segment was that with the minimum mean fractional error.

The middle column of plots (b) in Figure 9.17 show that the profiles of $mean(V')_N$ values vary according to the RBC concentration. Consider, for example, the profiles plotted for $V = 35$ mm/s. For the lowest concentration (3% of a physiologically normal haematocrit, Ht), $mean(V')_N \approx 40$ mm/s over a range of time points corresponding to ~ 1.0 mm to ~ 1.3 mm, and thus there is a comparatively broad peak that extends over a range roughly equivalent to the tube diameter ($2R/\sin\theta \approx 0.55$ mm). This may suggest that there is a relatively even penetration of light across the tube. As the RBC concentration is increased (and the absorption coefficient proportionally), the largest values for $mean(V')_N$ are limited to a smaller range of time points, giving the appearance of narrower peaks. This may relate to the stronger, and therefore more localised, light absorption, which would limit the distance range over which photoacoustic signals are generated from the RBCs, and therefore the distance over which velocities $mean(V')_N \approx V$ are measured. A noteworthy feature is the main peak in the 27% Ht case (3b) which, for each velocity, takes a parabolic-like shape reminiscent of the laminar velocity profile [see page 142, and also Figure 9.20 (3b)]. It is also interesting to note the time points of the "best" segments, which increase from concentrations 3% Ht to 27% Ht, but for 131% Ht, the optimum segment appears at a much earlier time point; a similar trend is shown in Figure 9.18 (c) where the position of the optimum segment is plotted for RBC concentrations 5% Ht, 66% Ht and 106% Ht in addition to the four concentrations shown in Figure 9.17. The trend of increasing optimum

segment time point with increasing concentration may again be related to the extent of light penetration: if the photoacoustic signal only arises from the nearer part of the tube (for high concentrations of absorbers), then the contribution from absorbers moving at the average flow velocity would appear later in the signal than for the case where light penetrates throughout the tube (low concentrations of absorbers) to the slower-moving absorbers at the further side. However, it is difficult to draw any definite conclusions since different experiments did not always maintain precisely the same transducer position and/or the same chosen delay time for the start of the signal frame: it is possible that such adjustments account for the earlier appearance of the optimum segment for the highest RBC concentrations.

The relationship of the accuracy of the $mean(V')_N$ measurements with the RBC concentration is illustrated in Figure 9.18 (b). In the case where the V'_n underlying the $mean(V')_N$ are calculated for the entire 5000-point frames, the $mean(V')_N$ values average to approximately zero (fractional error approximately 1.0) for all concentrations greater than about 5% Ht. When the underlying V'_n are calculated for 250-point waveform segments, there is a more gradual decline in accuracy with increasing concentration, with fractional errors remaining less than 20% for concentrations $\leq 27\%$. This is also evident from Figure 9.17, for example by comparing the plots in (3a) and (3c). The mean resolution (for $V < 50$ mm/s) also deteriorates as the concentration is increased from 3% to 27% Ht, which is shown by the unfilled square data points in Figure 9.18 (c). For the higher concentrations, there is an apparent improvement in resolution before the poorest resolution is reached for 131% Ht, but the corresponding accuracy of the measurements for these concentrations is poor. For the same reason, the high resolution for the entire-frame data [solid circle data points in in Figure 9.18 (a)] is also of marginal interest.

Choice of segment length

The foregoing discussion relates to waveform segments 250 points long, which was considered to be the most appropriate length for reasons supported by Figure 9.19. Here the data are processed as in the middle column of plots in Figure 9.17, but for different segment lengths. In Figure 9.19 (1a)-(1f), the RBC concentration is 3% Ht, whilst in (2a)-(2f) it is 27% Ht, but in both cases the known average velocity is $V = 35 \pm 4$ mm/s, as shown by the dashed horizontal lines. The solid horizontal lines mark the mean velocity $mean(V')_N$, where each V'_n was calculated from $C(t)'$ (the mean of 25 cross-correlations of the entire 5000-point waveforms).

A longer segment (larger M) effectively averages over $mean(V')_N$ values calculated for a shorter segment (smaller M) and, as a result, the profiles of $mean(V')_N$

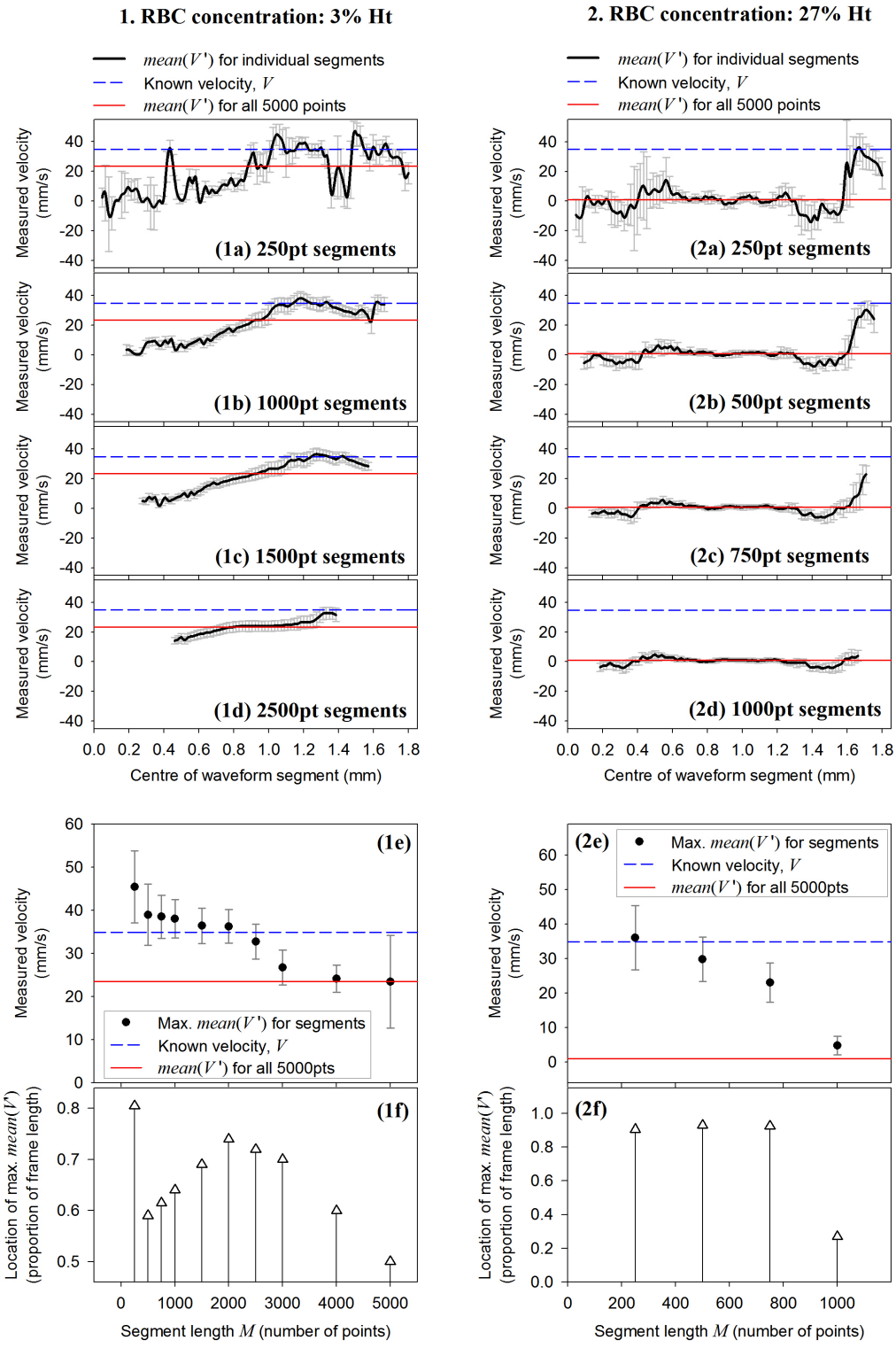

Figure 9.19: Calculation of $mean(V')_N$ values for different waveform segment lengths. Examples of $mean(V')_N$ derived from M-point waveform segments are shown by the black curves in (1a)-(1d) and (2a)-(2d), and compared with $mean(V')_N$ calculated from the entire 5000-point signals (solid horizontal lines) and the known velocity $V = 35 \pm 4$ mm/s (dashed horizontal lines). The plots on the left show results for a RBC concentration of 3% Ht, and on the right for 27% Ht. Plots (1e) and (2e) show the maximum values of $mean(V')_N$ measured for different segment lengths, and the time points at which these maxima occur are plotted in (1f) and (2f).

take on a smoother appearance with a reduced variation of velocities along the signal length. This is evident from plots (1e) and (2e), which show that, as M is increased, the maximum value for $mean(V')_N$ corresponding to the segments (shown by circle data points) moves away from the known velocity V and approaches the $mean(V')_N$ calculated for the entire 5000-point waveforms (solid horizontal line). The positions along the signal length of these maximum $mean(V')_N$ values are shown in (1f) and (2f). In (2e), which is the 27% Ht example, the data points reach the solid line sooner ($M = 1000$) than in (1e) for the 3% Ht example ($M = 4000$) due to the fact that in the former case the main (laminar-like) peak is narrower. In general, it would be desirable to make M as small as possible in order to accurately assess the change in velocities along the signal length. However, a value of $M = 250$ was found to be the minimum practial number of points since for shorter segment lengths the low SNR produces a large number of "extreme" values ($|V'_n| > 150$ mm/s). Subsequent segmentation analyses will therefore continue to use a segment length of $M = 250$.

9.2.5 Velocity profiles for different absorbers

Figure 9.20 shows plots similar to those in Figure 9.17 but here the rows correspond to results from four different absorbers: RBCs, red polystyrene spheres (3 μm), blue polystyrene spheres (3 μm) and black polystyrene spheres (6 μm) in rows 1-4 respectively. Optical microscopy images of each of these phantoms are given in Figure 5.2 (e)-(g), page 70. In each case the concentration of absorbers was made equivalent to $\sim 5\%$ Ht.

In both Figures 9.17 and 9.20, it can be difficult to identify a laminar-like shape within the profiles of $mean(V')_N$ values. The inset in Figure 9.20 (3b) maps out the laminar-like profiles more clearly using parabolic fits to the data points and taking the centre of the peak to be equivalent to the tube axis. However, it is still unclear why the maximum velocity of the peaks correspond to the average flow velocities, and not the maximum flow velocities, which would be twice this value (see Equation 9.7, page 143).

The profiles of $mean(V')_N$ values as functions of ct_P are strikingly similar for the RBCs and red spheres, as shown in Figure 9.20 (1b) and (2b) respectively. For the blue spheres [Figure 9.20 (3b)], the "best" segment (dashed line) appears at a broader peak than for the cases in (1b) and (2b), whilst for the black spheres [Figure 9.20 (4b)] the magnitude of $mean(V')_N$ is more consistent across the entire frame, resulting in very few distinct peaks. It seems likely that these observations are related to the respective absorption coefficients, with $\mu_a(RBCs) \approx \mu_a(redspheres) > \mu_a(bluespheres) > \mu_a(blackspheres)$ as shown in Figure 5.8, page 78. Lower light attenuation would produce a more uniform light distribution and therefore a more consistent signal amp-

litude along the photoacoustic signal length; a low signal amplitude is associated with an inaccurate velocity measurement due to liability of the cross-correlation to be corrupted by noise. However, it is curious that for the black spheres [Figure 9.20 (4b)] accurate velocity measurements are obtained over a distance that extends beyond that which would be expected from the tube diameter ($2R/\sin\theta \approx 0.55$ mm). Moreover, the accuracy of $mean(V')_N$ values obtained for the "best" segment [Figure 9.20 (4c)] is closely similar to that for the $mean(V')_N$ values corresponding to cross-correlation $C(t)'$ of the entire waveforms [Figure 9.20 (4a)], whereas in each of the other cases, and in all other experiments, the segmented data produced significantly improved accuracy. This is also illustrated in Figure 9.21 (a), where the mean fractional error across all $mean(V')_N$ values measured for $V < 50$ mm/s is plotted for each of the suspensions and for the two cases shown in the left and right columns of plots in Figure 9.20.

Figure 9.21 (b) gives an alternative measure for the accuracy of each data set by plotting the range of velocities over which accurate velocity measurements are made. Here, the observed maximum measurable velocity $|V_{\max}|_{\text{obs}}$ is taken to be the largest velocity for which the fractional error is less than 50%. Low light penetration would produce a large fractional error in the measurements of large average velocities since the measured velocity arises from the slower-moving absorbers close to the near edge of the tube: this slower velocity becomes a smaller proportion of the average flow speed, as the flow speed increases. Figure 9.21 (b) shows that the measurement range increases from the RBCs to the red spheres, and to the blue spheres, and finally the black spheres, which supports the above hypothesis since the absorption coefficients increase in the reverse order. However, the uncertainties in these ranges (shown by the error bars) are also relatively large. As for the mean fractional error [Figure 9.21 (b)], is apparent that for the black spheres the measurement range is similar for the entire 5000-point frames and for the 250-point segments, whereas for the other three suspensions evaluation of the waveform segments yields a significantly improved (larger) measurement range. This is again related to the uniformity of the $mean(V')_N$ values across the entire frame for the black spheres [Figure 9.20 (4b)].

Figure 9.21 (c) compares the resolution values of the same data sets, from which it is clear, as in Figure 9.18, that poor accuracy is often associated with an artificially high resolution simply because all the velocity measurements average to zero. The mean resolution values for the segments, shown by grey bars in Figure 9.21 (c), are comparable for each of the suspensions; even though the RBCs give a slightly worse mean resolution, the variation (standard deviation, represented by the error bar) in the individual resolution measurements is also large in this case.

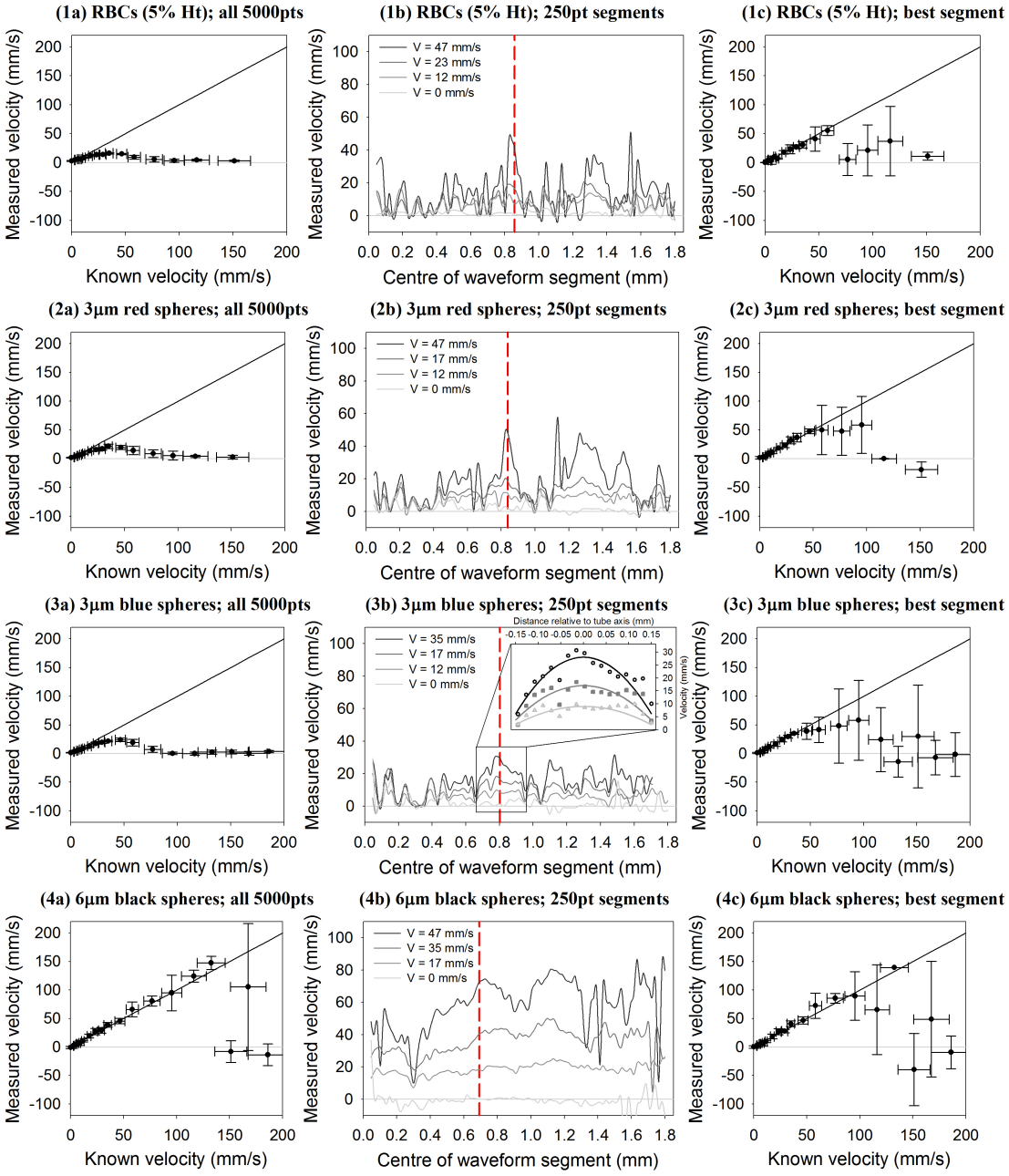

Figure 9.20: Velocity measurements made at "known" average velocities ranging from $V = 0$ mm/s to 186 mm/s for four different absorbers, RBCs, red polystyrene spheres (3 μm), blue polystyrene spheres (3 μm) and black polystyrene spheres (6 μm), as shown in rows 1-4 respectively. In each plot, the measured velocity (y axis) is the mean value $mean(V')_N$ calculated for N individual velocity measurements V_n' (each using 25 cross-correlation functions) acquired using the 30 MHz transducer ($\theta = 45°$) following double pulse illumination (PIV laser, $T = 0.5$ ms) of the suspension flowing in a $2R = 390$ μm tube. For the $mean(V')_N$ values plotted in the left column of plots (a), the cross-correlations $C(t)'$ were performed for the entire 5000-point signals, whereas for the middle (b) and right (c) columns of plots, the cross-correlations $C_s(t)'$ were performed for 250-point waveform segments; the right column of plots show $mean(V')_N$ values at the time point indicated by the dashed vertical lines in the middle column of plots. Further details are given in the text (page 169). The inset in (3b) shows parabolic fits to the velocity profiles.

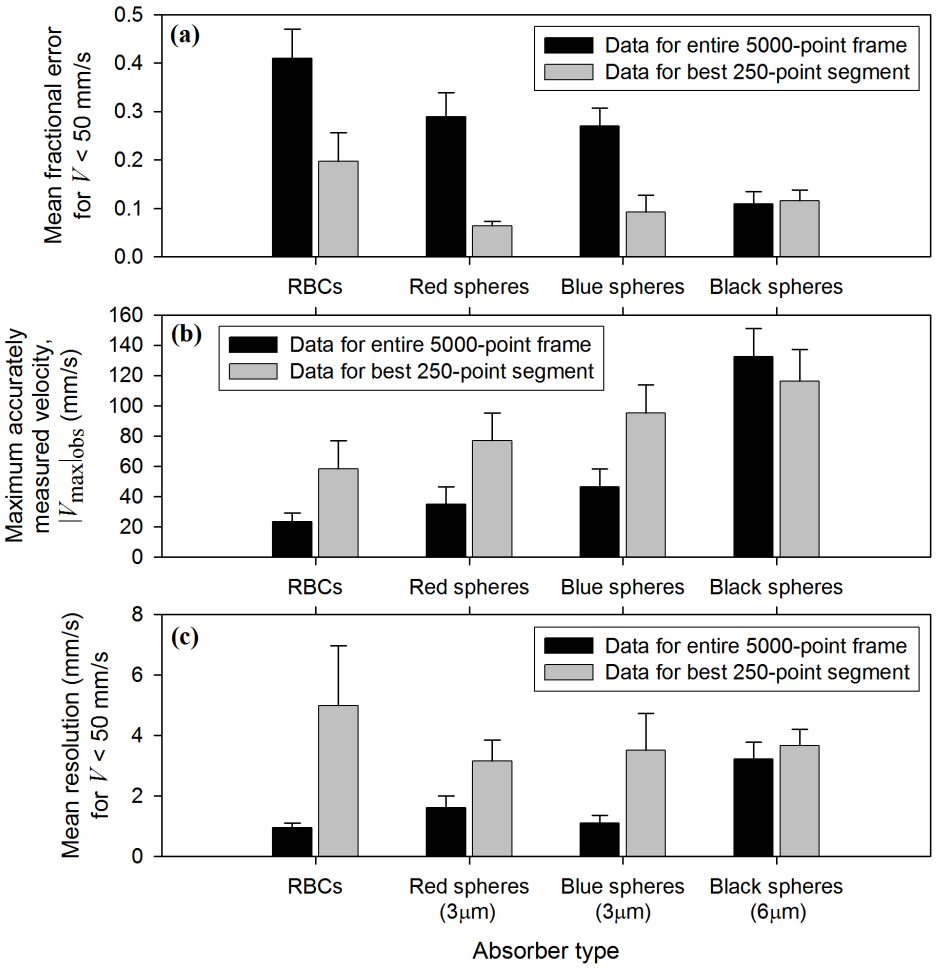

Figure 9.21: Comparison of the accuracy (a), measurement range (b), and resolution (c) of $mean(V')_N$ values plotted in the left and right columns of Fig. 9.20. The accuracies in (a) are the fractional errors (relative to V) of $mean(V')_N$ measurements made for known velocities $V < 50$ mm/s, in cases where the $(V')_N$ underlying $mean(V')_N$ were calculated for the entire 5000-point waveforms (black bars), and in cases where the underlying $(V')_N$ were calculated for the best 250-point segment (grey bars). The $|V_{\max}|_{\text{obs}}$ values plotted in (b) correspond to the largest velocity in each data set for which the fractional error is less than 50%, and the resolution in (c) is the average $std(V')_N$ associated with measurements $mean(V')_N$ in (a). The error bars in (a)-(c) represent the standard error associated with the mean value (the solid bar).

9.3 Summary

Section 9.1 described calculations of velocities within particular "range gates". These assume that the time axes of the photoacoustic signals can be associated with distance, and therefore by advancing the range gate along the measured waveforms, a velocity profile across the tube can be obtained. The measured velocity profile does not correspond exactly with the parabolic laminar profile, and this is due to the orientation of the transducer with respect to the flow direction, and the finite transducer focal beam width. It is unclear how the profile of velocities or time shifts translates to a single time shift measurement for the entire waveform, but it is likely that the measurement is dominated by those parts of the signal with the greatest amplitude. Therefore, in cases where light is attenuated across the tube, the largest signal amplitude will arise from the slower-moving absorbers at the first edge. This leads to under-reading of the average velocity, but the velocities corresponding to small waveform segments remain accurate since they are not dominated by other, large amplitude parts of the signal.

In Section 9.2 "range gating" was applied to experimentally acquired photoacoustic signals in order to obtain velocity profiles. This novel method of analysis, termed "waveform segmentation", entailed calculating the cross-correlation of short segments of the photoacoustic waveforms, but the correspondence of these time segments with distances across the tube still needs to be verified. In the process of developing the method, an alternative calculation for velocity resolution was defined: this involves taking the standard deviation of repeated measurements, as described in sub-section 9.2.2. Analysis of short waveform segments can give rise to extreme velocity values, which are anomalous and are therefore excluded, as illustrated in sub-section 9.2.3.

The segmentation method was applied to data acquired for different concentrations of flowing RBCs, and for different colours of microspheres, and almost invariably resulted in improved velocity measurement accuracy compared to results for the entire waveforms. The velocity resolution was poorer for the segment data rather than that calculated for the whole signals, but this could be improved by taking more repeated measurements. The velocity measurements along the signal lengths were more consistent for the lower absorber concentrations and for microspheres supposed to have a lower absorption coefficient, and this may relate to the extent to which light penetrates through the tube.

Segmentation enabled accurate velocity measurements even with RBCs in a suspension *more* concentrated than whole blood (116% Ht). The prospects for the success of the method in whole blood are therefore very promising, but further data is needed to verify this.

10

Experimental considerations

The instruments used to generate and acquire the photoacoustic signals from moving absorbers will inevitably affect the accuracy and resolution of the cross-correlation velocity measurements. Considerations relating to the detector bandwidth, the laser and transducer alignment, and the oscilloscope sampling interval are discussed respectively in sub-sections 10.1, 10.2 and 10.3.

10.1 Detector bandwidth

Sections 8.2.1 and 8.3.4 mentioned the challenge of tracking photoacoustic signals generated in relatively homogeneous suspensions of absorbers. From Section 8.2.1 it appears that it is difficult to make accurate velocity measurements from flowing haemolysed RBCs using a 30 MHz focussed transducer; however, Section 8.3.4 presented accurate time shift measurements made by manually shifting a very dense, apparently homogeneous, suspension of microspheres, and acquiring signals with the same 30 MHz transducer.

The spatial heterogeneity must be defined relative to the detector bandwidth, and

it is difficult to quantitatively determine the scale on which the heterogeneity becomes insufficient to track unique photoacoustic "signatures". In any case, it seems likely that closely packed particles are responsible for high frequency components and subtle changes in the photoacoustic signals, which would be better detected using a broadband detector [55, 98], and therefore this section examines how the velocity measurements are affected by the detector bandwidth and the signal frequency content. This is of particular relevance to the acoustic resolution mode of photoacoustic Doppler, which is designed to penetrate several millimetres or centimetres into tissue. Ultrasound attenuation in tissue is frequency dependent, with a coefficient of approximately 0.54 dB cm^{-1} MHz^{-1}[31], and therefore the amplitude of signals at 30 MHz will be reduced by a factor of about 6.5 for every centimetre. Thus, at a penetration depth of about 5 mm it may be possible to acquire adequate SNR at 30 MHz, but detection of higher frequencies will be limited.

Velocity measurements made using different transducers are compared in sub-section 10.1.1, and the frequency contents of the signals are examined in sub-section 10.1.2 for different transducers and various absorbers. Sub-section 10.1.3 demonstrates the effect of post-filtering on velocity measurement accuracy and resolution, with examples shown for data acquired for different absorbers and for zero velocity measurements made for a range of absorber concentrations.

10.1.1 Velocity measurement accuracy and resolution

Figure 10.1 compares the mean accuracy and resolution of velocity measurements obtained for flowing carbon spheres (22 μm diameter) using four different focussed PZT transducers with centre frequencies of 5 MHz, 15 MHz, 20 MHz and 30 MHz [see Table 5.3(a)]. The 5 MHz transducer yields 100% fractional error and therefore appears to be unsuitable for making flow measurements at all. The 15 MHz transducer produces better accuracy, but the uncertainty on the mean value is very large, making it difficult to pass a definitive judgement; in fact, this transducer demonstrated excessive signal ringing when, as for the other transducers, it was terminated with 1 MΩ at the oscilloscope, and therefore a 50 Ω termination was used. In any case, the 20 MHz and 30 MHz transducers both give comparable accuracy, and the mean resolution is similar for all three of the 15 MHz, 20 MHz and 30 MHz transducers. These preliminary results suggest that there is not a significant difference between the accuracy and resolution for the transducers with centre frequencies greater than 5 MHz.

Figures 10.2 and 10.3 present a more detailed analysis of measurements made using different transducers. Figure 10.2 shows plots similar to those in Figures 9.20 and

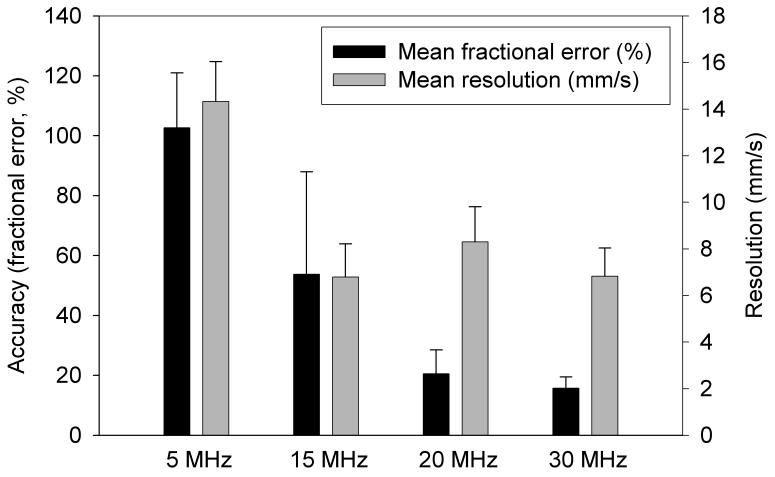

Figure 10.1: Comparison of the performance of the 5 MHz, 15 MHz, 20 MHz and 30 MHz transducers for measuring the velocity of flowing microspheres. Mean values for the accuracy (fractional error) and measurement resolution were calculated for the 22 μm spheres illuminated with the FQ laser (repetition rate 2 kHz) and flowing in the 800 μm tube at speeds up to 110 mm/s (all the velocities were less than $|V_{\max}|_{\text{obs}}$ and $|V_{\max}|$). The error bars are the standard errors of the mean values.

9.17 but here the rows correspond to results from focussed PZT transducers with four different centre frequencies: 5 MHz, 20 MHz, 30 MHz and 50 MHz in rows 1-4 respectively.

The profiles of $mean(V')_N$ values as functions of ct_{P} are messy, but in each of the plots in the middle column (b) there is a region where the $mean(V')_N$ values exhibit a roughly laminar-like peak that extends over a range of distances approximately equivalent to the tube diameter ($2R/\sin\theta \approx 0.55$ mm). The accuracy of the velocity measurements for the segments [right column, (c)] is better than for the whole frames [left column (a)], and both improve with increasing transducer centre frequency. This is also demonstrated in Figure 10.3(a) where mean fractional error values for all velocities $V < 50$ mm/s are plotted for the data in Figure 10.2, and also for additional data sets recorded for the 20 MHz and 30 MHz transducers, as well as for the 15 MHz PZT and 25 MHz PVDF transducers. Figure 10.3(b) shows that for each transducer the velocity resolution is worse for the segments than for the whole frames, but is relatively consistent across the different transducers.

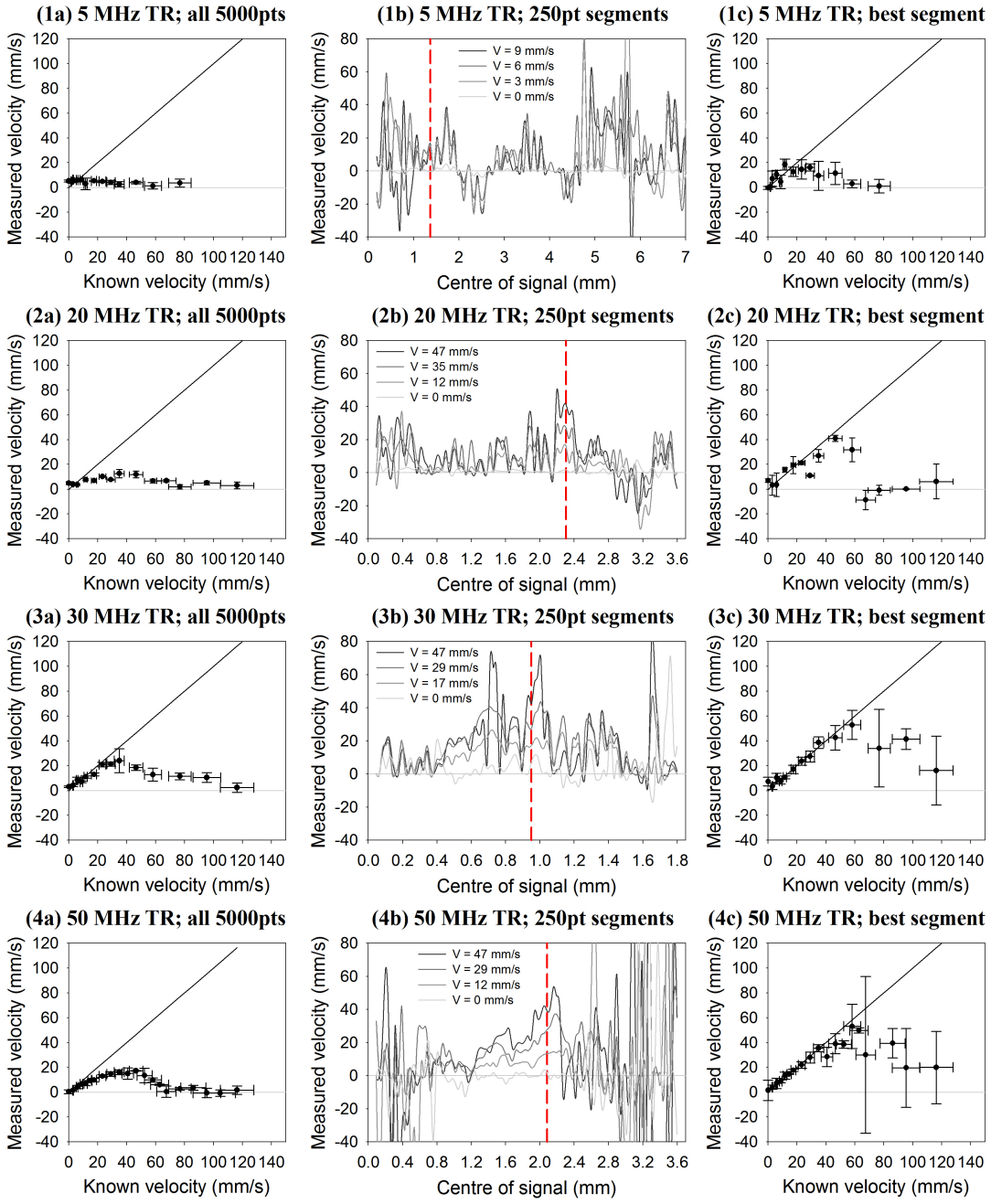

Figure 10.2: Velocity measurements made at "known" average velocities ranging from $V = 0$ mm/s to 116 mm/s for focussed PZT transducers with four different centre frequencies: 5 MHz, 20 MHz, 30 MHz and 50 MHz, as shown in rows 1-4 respectively. In each plot, the measured velocity (y axis) is the mean value $mean(V')_N$ calculated for N individual velocity measurements V'_n (each using 25 cross-correlation functions) acquired using the 30 MHz transducer ($\theta = 45°$) following double pulse illumination (PIV laser, $T = 0.5$ ms) of a RBC suspension (5% Ht) flowing in a $2R = 390$ μm tube. For the $mean(V')_N$ values plotted in the left column of plots (a), the cross-correlations $C(t)'$ were performed for the entire 5000-point signals, whereas for the middle (b) and right (c) columns of plots, the cross-correlations $C_s(t)'$ were performed for 250-point waveform segments; the right column of plots show $mean(V')_N$ values at the time point indicated by the dashed vertical lines in the middle column of plots. Further details are given in the text on page 169.

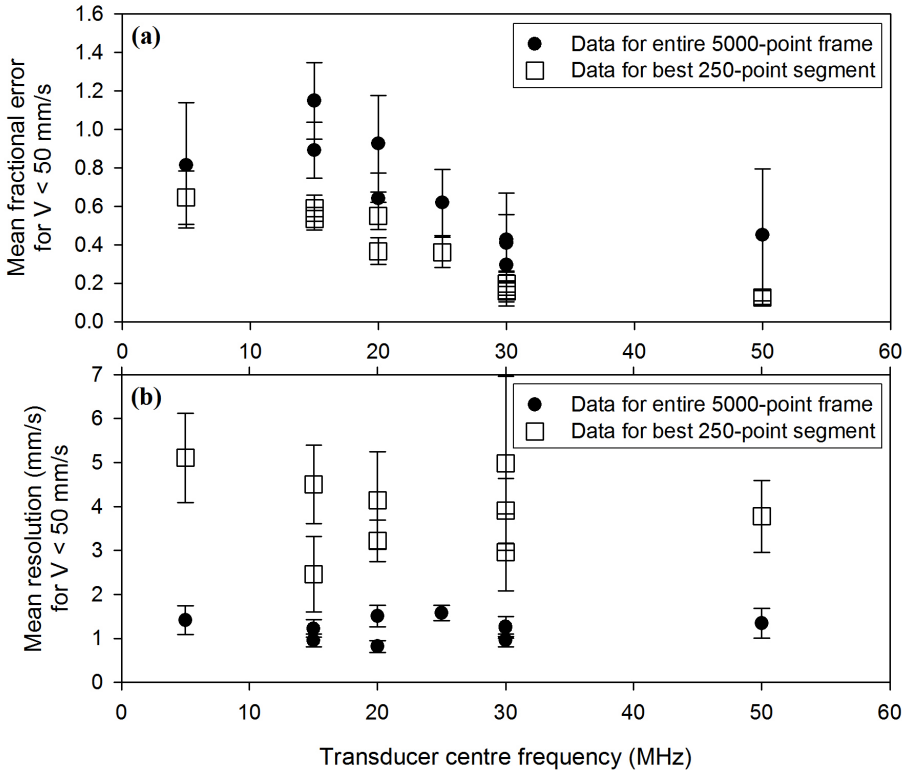

Figure 10.3: Comparison of the accuracy (a) and the resolution (b) of velocity measurements made using transducers with centre frequencies ranging from 5 MHz to 50 MHz (see Table 5.3). For each transducer the measurements were made for RBCs (5% Ht) flowing in a $2R = 390$ μm tube, and illuminated with the PIV laser ($T = 0.5$ ms). The accuracies in (a) are the fractional errors (relative to V) of measurements $mean(V')_N$ made for known velocities $V < 50$ mm/s. The solid circles plot the average fractional error in the cases where the $(V')_N$ underlying $mean(V')_N$ were calculated for the entire 5000-point waveforms, whilst the underlying $(V')_N$ for the unfilled squares were calculated for the best 250-point segment. The resolution in (b) is the average $std(V')_N$ associated with measurements $mean(V')_N$ in (a). The error bars in (a) and (b) represent the standard error on the average fractional error and resolution values respectively.

10.1.2 Observed frequency responses

Data for different transducers

Figure 10.4 illustrates typical signal waveforms and frequency responses, in columns (a) and (b) respectively, obtained using four different focussed transducers with centre frequencies of 5 MHz, 20 MHz, 30 MHz and 50 MHz; the data are the same as that used to obtain the measurements presented in Figure 10.2. For each transducer, the mean waveform and frequency spectra were calculated for over 2,500 waveforms acquired for RBCs (5% Ht) flowing at average velocities ranging from $V = 0$ mm/s to $V = 116$ mm/s, with $T = 0.5$ ms and $\theta = 45°$. Examples of individual waveforms (those with median amplitude) and their corresponding frequency spectra are also shown. The tube diameter of 390 μm corresponds to a time of approximately 0.37 μs (sound speed, $c \approx 1500$ m/s), but, from the left column of plots (a), each of the waveforms are longer by this time by at least a factor of two. This is probably due to the resonant nature of the transducer, which is particularly apparent for the 5 MHz transducer [note the different x axis scale in Figure 10.4(1a)]. The frequency content of the signals acquired with the 5 MHz transducer matches reasonably well with the frequency response specified in the manufacturer's data sheet, as shown in Figure 10.4(1b). However, for the signals acquired with the three other transducers [Figure 10.4(2b), (3b) and (4b)], the low frequency content dominates over the higher frequencies associated with the manufacturer-specified responses. This may be expected for the mean waveforms and corresponding frequency spectra, but the individual waveforms are also lacking in high frequency content. The mean frequency spectra in (2b) and (3b) both have peaks around 5 MHz, 7 MHz and 9 MHz; for comparison, note that 5.4 MHz corresponds to approximately half the tube diameter. For the 50 MHz transducer, there was considerable variability in the individual waveforms as shown by the two examples. For the second example in (4b) there is a large peak at about 37 MHz, but the absence of this peak in other waveforms, such as the first example, results in only a small peak at 37 MHz in the mean frequency spectrum. There are much larger peaks at about 1 MHz, 7 MHz, 11 MHz and 13 MHz. The general similarity between the spectra in (2b), (3b) and (4b), with very little relationship to the manufacturer-specified responses, suggests that the frequency content of the signals is not solely determined by the detector bandwidth, but rather by the nature of the absorber, which was the same in each case.

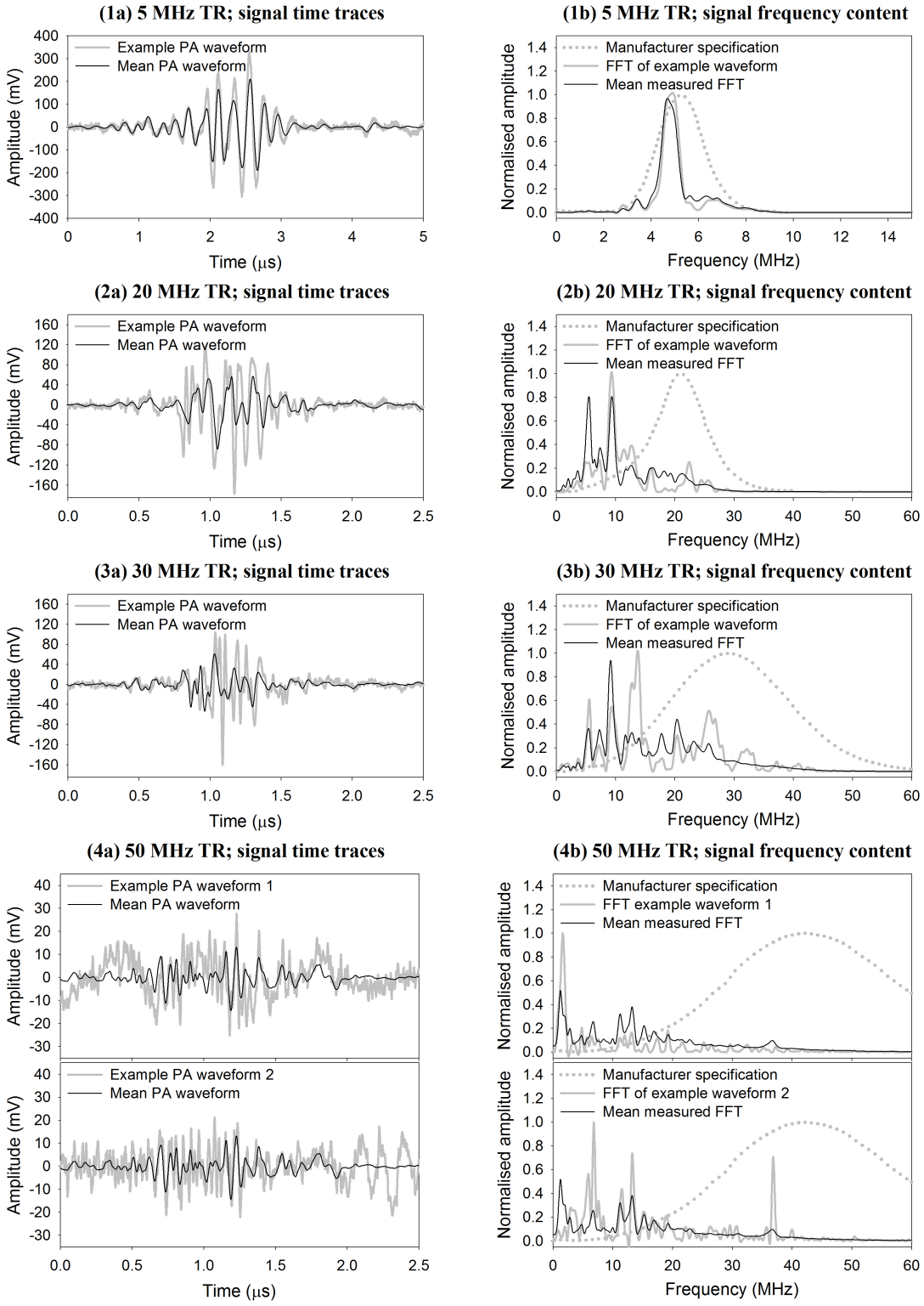

Figure 10.4: Signal waveforms (a) and frequency spectra (b) obtained using transducers with centre frequencies of 5 MHz, 20 MHz, 30 MHz and 50 MHz in rows 1-4 respectively. The mean waveforms and mean frequency spectra were calculated for over 2,500 waveforms acquired for RBCs (5% Ht) flowing in a 390 μm diameter tube at average velocities ranging from $V = 0$ mm/s to $V = 116$ mm/s, with $T = 0.5$ ms and $\theta = 45°$. The example waveforms shown in grey are those with the median amplitude. The dotted curves in plots (b) correspond to the frequency responses specified in the manufacturer's data sheets. FFT: Fast Fourier Transform (MATLAB).

Data for different absorbers

Figure 10.5 shows signal waveforms and frequency spectra in a similar manner to those in Figure 10.4. The data in Figure 10.5 are those shown in Figure 9.20, which were acquired using the 30 MHz focused transducer, and for absorbers flowing in a 390 μm diameter tube, and illuminated with the PIV laser (T = 0.5 ms). Results for 5% Ht RBCs, 3 μm red polystyrene spheres, 3 μm blue polystyrene spheres, and 6 μm black polystyrene spheres are shown in rows 1-4 respectively. The peak-to-peak amplitudes of the mean waveforms acquired for the RBCs and red spheres [Figure 10.5(1a) and (2a)] are larger than those for the blue spheres and black spheres [Figure 10.5(3a) and (4a)], which is due to the fact that, at a wavelength of 532 nm, the absorption coefficients of the RBCs and red spheres are greater than those for the other two absorbers (see Figure 5.8 and discussion on page 172). The shapes of the mean signals are however very similar for the four absorbers, each demonstrating two principal peaks separated by approximately 0.2 μs, which corresponds to approximately half the tube diameter ($\theta = 45°$, $c \approx 1500$ m/s). The mean frequency spectra for the RBCs (1b), red spheres (2b) and blue spheres (3b) are also very similar, each exhibiting a large peak around 11 MHz. The individual frequency spectra show instances of peaks at higher frequencies, for example around 18 MHz, but the inconsistency across the waveforms results in suppression of this peak in the mean spectrum. Th 11 MHz peak also appears in the mean frequency spectrum for the black spheres (4b) but there is a larger amplitude peak around 18 MHz, and in general the spectrum of frequencies is much broader than for the other three absorbers. The individual waveform example shows a significant peak around 30 MHz, which was not observed for the other absorbers. It is possible that this is again related to the relative absorption coefficients: greater light penetration (lower absorption) would enable sampling of a wider range of the laminar flow profile of velocities, and if this also produces a wider distribution of absorber spacings it could lead to the broader spectrum of frequencies observed for the black spheres.

The key point to note from Figures 10.4 and 10.5 is that the frequency spectra appear to be influenced more by the nature of the absorber – its colour, shape and size – than by the detector bandwidth.

10.1.3 Data post-filtering: application of Butterworth filters

The velocity measurements presented in Chapter 8 were typically acquired using the 250 MHz bandwidth setting on the oscilloscope, and then post-filtered once downloaded to the PC using a 10-100 MHz band-pass Butterworth filter (order 2). The

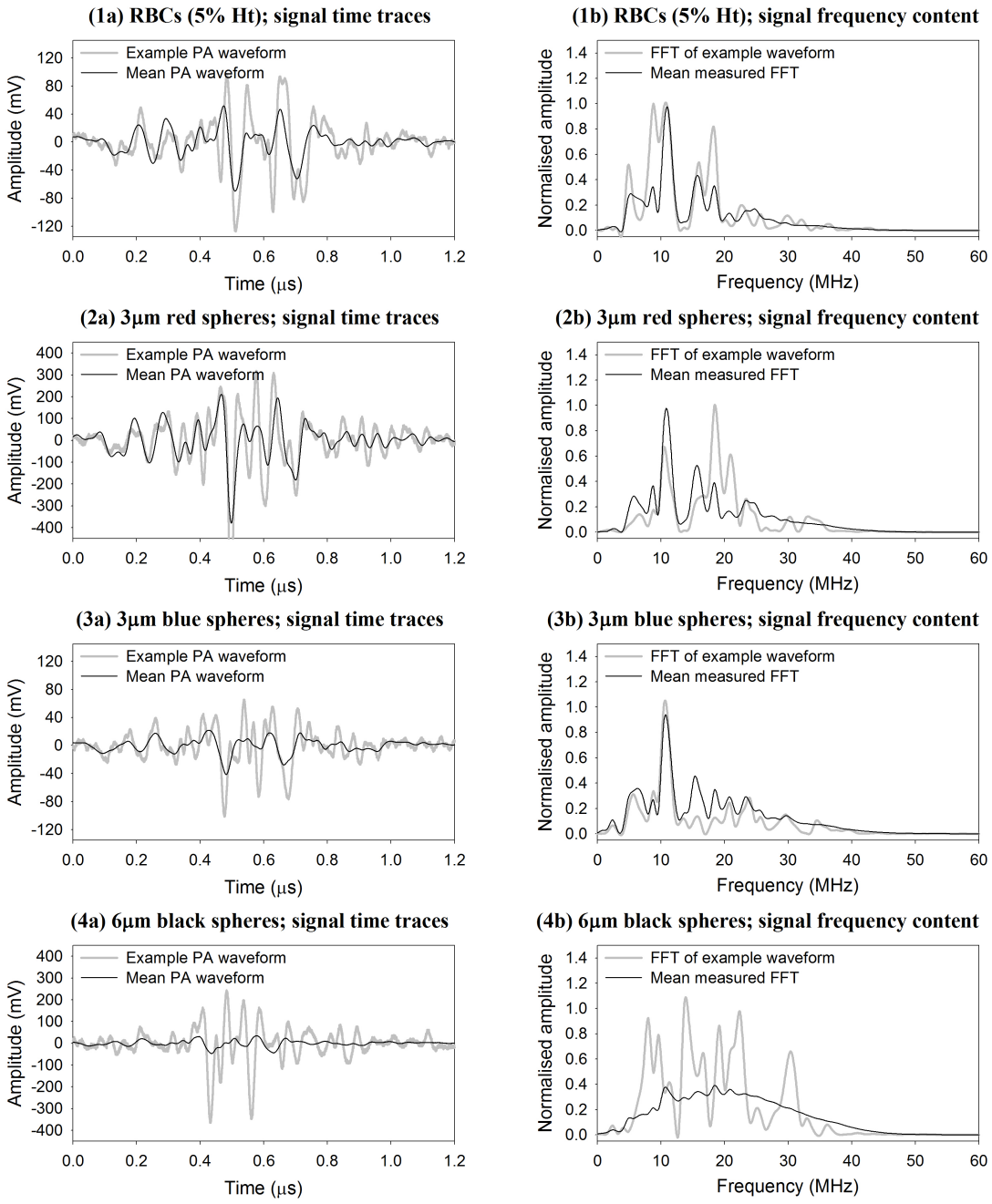

Figure 10.5: Signal waveforms (a) and frequency spectra (b) corresponding to the velocity measurements in Fig. 9.20, which were acquired for four different absorbers, RBCs, red polystyrene spheres (3 μm), blue polystyrene spheres (3 μm) and black polystyrene spheres (6 μm), as shown in rows 1-4 respectively. The waveforms and frequency spectra are the means of over 4,750 photoacoustic waveforms acquired with the 30 MHz focussed transducer. The example waveforms shown in grey are those with the median amplitude. FFT: Fast Fourier Transform (MATLAB).

reasons for choosing a Butterworth filter are outlined in Appendix B.2, and Figure 10.6 illustrates the effect of the 10-100 MHz bandwidth.

Figure 10.6 shows a typical data set acquired for the 3 μm red polystyrene spheres flowing in the 250 μm diameter tube, using the PIV laser (T = 0.5 ms) and the 80 MHz PVDF transducer. Figure 10.6(a) plots the velocity measurements before and after the 10-100 MHz filter was applied, and the corresponding frequency spectra are shown in Figure 10.6(b). The measurement accuracy is plotted as the fractional error at each velocity in (c) and the mean fractional error for all velocities $V < 50$ mm/s in (d), from which it is evident that 10-100 MHz filtering had very little effect on the measurement accuracy. However, from the plots of velocity resolution in (e) and (f) it is apparent that the mean resolution improved by approximately 35% after the 10-100 MHz filter was applied, and this was the reason why it was used.

The experimental post-filtering invariably employed a conventional (in other words, non-zero-phase) Butterworth filter, order 2. However, for the post-filtering presented in the rest of this section, the Butterworth filters are also order 2, but zero-phase. This eliminates the possibility that the time shift could be altered by a phase shift introduced by the filter, as described in Appendix B.2.

Demonstration of filtering individual waveforms: experimental data

Figure 10.7 demonstrates low-pass and high-pass filtering of a photoacoustic waveform pair $p_1(t)$ and $p_2(t)$, and the effect on the accuracy of the time shift measurement. The waveforms were acquired from RBCs (5% Ht) moving at an average flow velocity V = 35 mm/s (t_s = 8.35 ns) in a $2R$ = 390 μm tube, and illuminated with the PIV laser (T = 0.5 ms). The unfiltered waveform pair (1a) produces a cross-correlation function (1b) with a maximum amplitude at t_s' = 3.25 ns (1c), and thus under-reads the known time shift (t_s = 8.35 ns), which is marked with a dashed vertical line. Removal of the high frequencies causes further under-reading, as illustrated in the second row of plots: plot (2a) shows the waveform pair after filtering with a 5 MHz low-pass filter, and the inset shows the mean of the two frequency spectra overlaid on the filter amplitude response (the shading indicates the frequencies excluded by the filter). Compared to the plots in row 1, the cross-correlation function (2b) has a broader peak lobe (2c) that is maximal at t_s' = 1.75 ns. However, removal of the low frequencies improves the measurement accuracy compared to the unfiltered and low-pass filtered cases, as illustrated in the third row of plots: when filtered with a 30 MHz high-pass filter the waveform pair (3a) produces a high-frequency cross-correlation function (3b) with narrower peaks (3c), and the maximal peak occurs at t_s' = 8.25 ns, which agrees closely

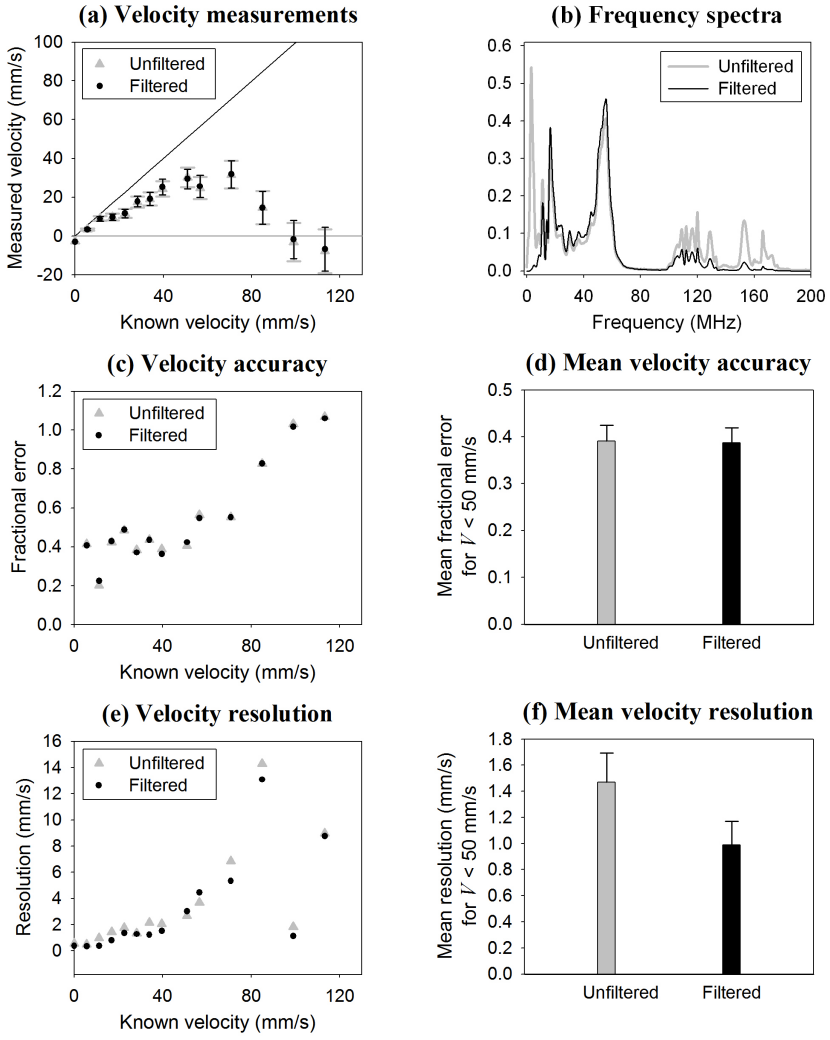

Figure 10.6: Comparison of velocity measurements before and after filtering the photoacoustic waveforms with a 10-100 MHz band-pass Butterworth filter (order 2). The data were acquired using the PIV laser (T = 0.5 ms) and the 80 MHz PVDF transducer, for the 3 μm red polystyrene spheres flowing in the 250 μm diameter tube. Velocity measurements for V = 0 mm/s to 113 mm/s are shown in (a): each data point is the mean of five velocity measurements, and the vertical error bars are the standard deviations; horizontal error bars are omitted for clarity. The mean frequency spectra of all the waveforms acquired across all velocities are shown in (b). The fractional error and resolution (vertical error bars) of each velocity measurement is plotted for each velocity in (c) and (e) respectively, and the mean values across the velocities are shown in (d) and (f).

with the known time shift. As expected therefore, low-pass filtering has a "blurring" effect: the high-frequency detail is lost, resulting in two waveforms that have largely similar low-frequency features and give rise to a broad cross-correlation peak that is maximal at a time shift close to zero. In contrast, high-pass filtering preserves, and enhances, the subtle differences between the two waveforms, and the cross-correlation peak more accurately represents the "known" time shift between them. Note however, that the "known" time shift is that corresponding to the average of the laminar profile of flow velocities, and it remains unclear whether the overall time shift between two waveforms should indeed represent this average (see Section 9.2).

Demonstration of filtering individual waveforms: simulated data

In order to better understand the translation of a laminar flow profile of velocities into a single measured time shift, cross-correlation functions were calculated for simulated signals. Figure 10.8 shows a very simple case for two signals $p_1(t)$ and $p_2(t)$, which are both 5000 points long, with a sampling interval of $\delta t_s = 0.25$ ns, as for the waveforms in Figure 10.7(a). The first signal $p_1(t)$ was generated in MATLAB from a normal distribution of random numbers with a mean of zero, and a standard deviation of 0.01. Note that $p_2(t)$ also has a mean amplitude of zero, but is translated down the y axis for clarity. This second signal $p_2(t)$ was populated from the end in 250-point segments $\mathbf{s}_{2,n}, n = 20, 19, \ldots, 1$. Segments $\mathbf{s}_{2,20}, \mathbf{s}_{2,19}, \mathbf{s}_{2,18}$ and $\mathbf{s}_{2,17}$ are identical to the corresponding segments $\mathbf{s}_{\mathbf{1},20}, \mathbf{s}_{\mathbf{1},19}, \mathbf{s}_{\mathbf{1},18}$ and $\mathbf{s}_{\mathbf{1},17}$ in the first signal. For $n = 16, 15, \ldots, 6$ the segments in $p_2(t)$ correspond to segments in $p_1(t)$ that appear at times 10 ns earlier, and then for $n = 5, 4, \ldots, 1$, the segments are again identical between the two signals. This profile of time shifts – measured by cross-correlating corresponding 250-point segments from each signal – is shown in Figure 10.8(1b), and is analogous to the profiles of $mean(V')_N$ shown in the middle columns of plots in Figures 9.17 and 9.20. The cross-correlation of $p_1(t)$ and $p_2(t)$ is shown in Figure 10.8(1c) for time shifts -0.02 μs to 0.02 μs. There are two distinct peaks at 0 ns and 10 ns, with relative amplitudes that correspond to the proportion of the signal lengths that are time-shifted by the relevant amounts: eleven of the segments are shifted by 10 ns, compared to nine with a zero time shift.

The inset in Figure 10.8(1a) shows the mean frequency spectrum of the two simulated signals, which is very broadband. Passing both signals through a 50 MHz low-pass filter produces the signals shown in (2a): the mean frequency spectrum [inset in (2a)] bears closer similarity to that in Figure 10.7(1a), and thus the signals in Figure 10.8(2a) are better than those in (1a) for simulating typical signals acquired using a detector with a limited bandwidth. As in Figure 10.7 the frequency spectra in the

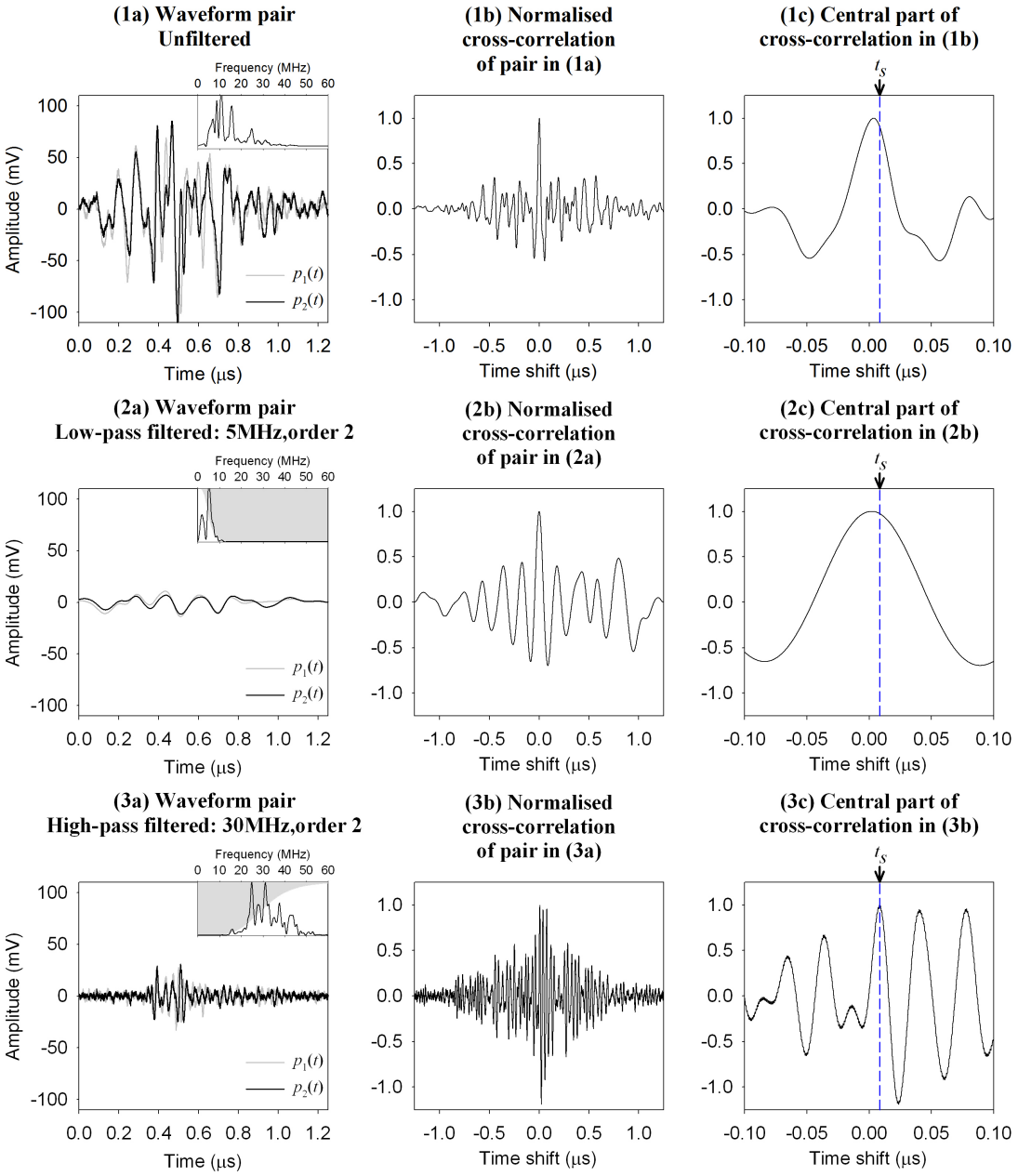

Figure 10.7: Demonstration of low-pass and high-pass filtering of a photoacoustic waveform pair, and the effect on the accuracy of the time shift measurement. The waveforms were acquired using the 30 MHz focussed transducer for RBCs (5% Ht) moving at an average flow velocity V = 35 mm/s (t_s = 8.35 ns) in a 390 μm tube, and illuminated with the PIV laser (T = 0.5 ms). The unfiltered waveform pair is shown in (1a), after low-pass filtering (5 MHz cut-off, order 2) in (2a) and after high-pass filtering (30 MHz cut-off, order 2) in (3a). The frequency spectra in the insets are normalised to the maximum amplitude and overlaid on shading which indicates the filter amplitude response. The cross-correlation functions of the relevant pairs are shown in the middle column of plots (b) and the central parts of the cross-correlation functions (time shifts -0.1 to 0.1 μs) are shown in the right column of plots (c). The measured time shifts are t_s' = 3.25 ns, 1.75 ns and 8.25, as found from the maximum peaks in (1c), (2c) and (3c) respectively.

insets are normalised to their maximum amplitudes, and overlaid on the filter amplitude response, with shading indicating the frequencies excluded by the filter. Figures 10.8(2b) shows the time shifts calculated by cross-correlating 250-point segments: the profile matches that in (1b) although there is some distribution of values around the nominal shifts of 0 ns and 10 ns. The cross-correlation of signals in (2a) is shown in (2c): the peak lobe is much broader than the peaks in (1c) and the maximum amplitude occurs at a time shift $t_s' = 5.75$ ns, which is approximately midway between the two time shifts present in the signals. When the signals in (2a) are passed through a 30 MHz high-pass filter (3a), the detail in the cross-correlation function is slightly restored: in (3c) the broad cross-correlation peak shows evidence of distinct peaks at 0 ns and 10 ns, and the maximal amplitude now occurs at $t_s' = 9.25$ ns, which is in close agreement with the 10 ns time shift measured for the unfiltered signals in row 1 (i.e. before "acquisition" with a band-limited "detector"). There is also a smaller distribution of time shifts around 10 ns measured for the 250-point segments $n = 6, 7, \ldots, 16$, as shown in (3b), and the remaining segments consistently give time shift measurements of 0 ns, as in (1b). However, when the signals are passed through a low-pass 5MHz filter (4a), only segments $n = 2, 4, 5, 17, 19$ and 20 produce time shift measurements close to 0 ns as expected: the measured time shifts for the remaining segments are inaccurate and the overall profile in (4b) bears no resemblance to those in (1b), (2b) and (3b). The cross-correlation peak lobe in (4c) is very broad with a maximum at $t_s' = 0$ ns, which shows again, as in Figure 10.7(2c), that low-pass filtering has the effect of removing high-frequency detail so that the signals become artificially similar and therefore with a time shift biased towards zero.

In the following sub-section, different low-pass and high-pass filters are applied to photoacoustic signals acquired from flowing absorbers, as in Figure 10.7. An analysis is made of the effect of filtering on the accuracy and resolution of measurements made for a range of velocities.

Filtering data acquired from different absorbers

The frequency spectra in the right column of Figure 10.5 are repeated in the insets of the plots in Figure 10.9, column (a), and the velocity measurements in these plots are those shown previously in Figure 9.20, column (a). The middle and right columns of plots in Figure 10.9 show velocity measurements after the photoacoustic data were passed through a low-pass 5 MHz filter and a high-pass 30 MHz filter respectively, and the insets show the corresponding mean frequency spectra. For the RBCs (1b), red spheres (2b) and blue spheres (3b), low-pass filtering removes the ability to make

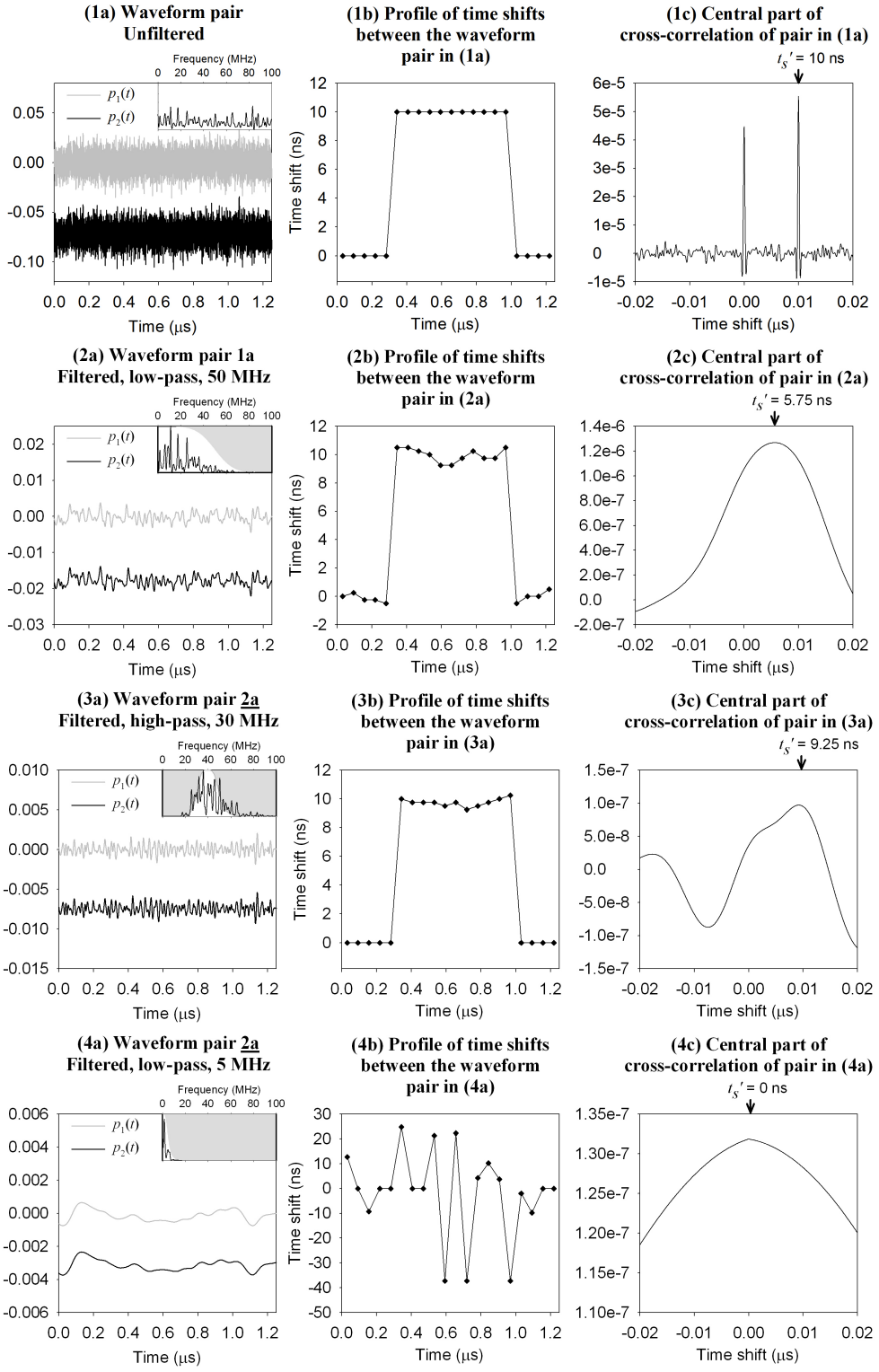

Figure 10.8: Demonstration of low-pass and high-pass filtering of simulated random signals, and the effect on the accuracy of time shift measurements t_s'. The signals $p_1(t)$ and $p_2(t)$ in (1a) were generated as described in the text. The cross-correlation of $p_1(t)$ and $p_2(t)$ is shown in (1c), and the time shift t_s' corresponding to the maximum amplitude is marked with an arrow. The plots in rows 2 show the same information as in row 1, but after applying a low-pass 50 MHz Butterworth filter to the signals in (1a) in order to simulate a typical transducer bandwidth. These "detector-acquired" signals were then post-filtered, either with a high-pass 30 MHz filter (row 3), or with a low-pass 5 MHz filter (row 4).

accurate velocity measurements. For the black spheres, the measurements increase with increasing velocity, but they under-read the "known" values by approximately 50%. In contrast, high-pass filtering improves the measurement accuracies for the RBCs (1c), red spheres (2c) and blue spheres (3c); for the black spheres (4c) there is little difference between the velocity measurements for unfiltered data and the high-pass filtered data until reaching very high velocities ($V > 95$ mm/s) where the velocity accuracy and resolution are poorer for the high-pass filtered data. This suggests that for the black spheres the broad frequency content plays an important role in producing high measurement accuracy and resolution.

Figure 10.10(a) and (b) plot the mean fractional error and mean resolution respectively across velocities $V < 50$ mm/s for each of the four absorbers in Figure 10.9 after the data were passed through various low-pass and high-pass filters. It is clear from Figure 10.10(a) that, for the RBCs, red spheres and blue spheres, the accuracy (fractional error) deteriorates after low-pass filtering, but improves after high-pass filtering compared to the velocity accuracy for the unfiltered data. However, high-pass filtering produces slightly poorer velocity resolution, as shown in Figure 10.10(b), and this is due to "resonance" resulting from a narrow bandwidth of high frequencies. The "resonance" effect results in multiple cross-correlation peaks of similar amplitudes [see Figure 10.7(3c)], and there is some variability in which of these peaks are maximal. The resolution for the black spheres remains relatively consistent for all the different filters, apart from the 5 MHz low-pass filter; this is because the frequency spectrum of the unfiltered data [Figure 10.5(4b)] is broad, and therefore the filters remove a smaller proportion of the data compared to the cases where the waveforms are dominated by a few principal frequencies [Figure 10.5(1b), (2b) and (3b)] . The accuracy too is relatively unaffected by filtering, apart from when the 5 MHz and 10 MHz low-pass filters are applied.

Filtering and segmentation

Figure 10.11(a) repeats the high-pass 30 MHz filtered data shown for the RBCs in Figure 10.9(1c). The photoacoustic waveforms were then analysed in 250-point segments as described in Section 9.2 to give the profile of $mean(V')_N$ values as shown in Figure 10.11(b); the velocity measurements in (c) are those calculated for the segment marked by the dashed vertical line in (b). Unlike for the unfiltered data (row 1 in Figure 9.20), the accuracies of velocity measurements for $V < 50$ mm/s are not significantly improved for the "best" segment [Figure 10.11(c)] compared to the measurements calculated for the entire frames [Figure 10.11(a)], and this is shown by the bar graph of

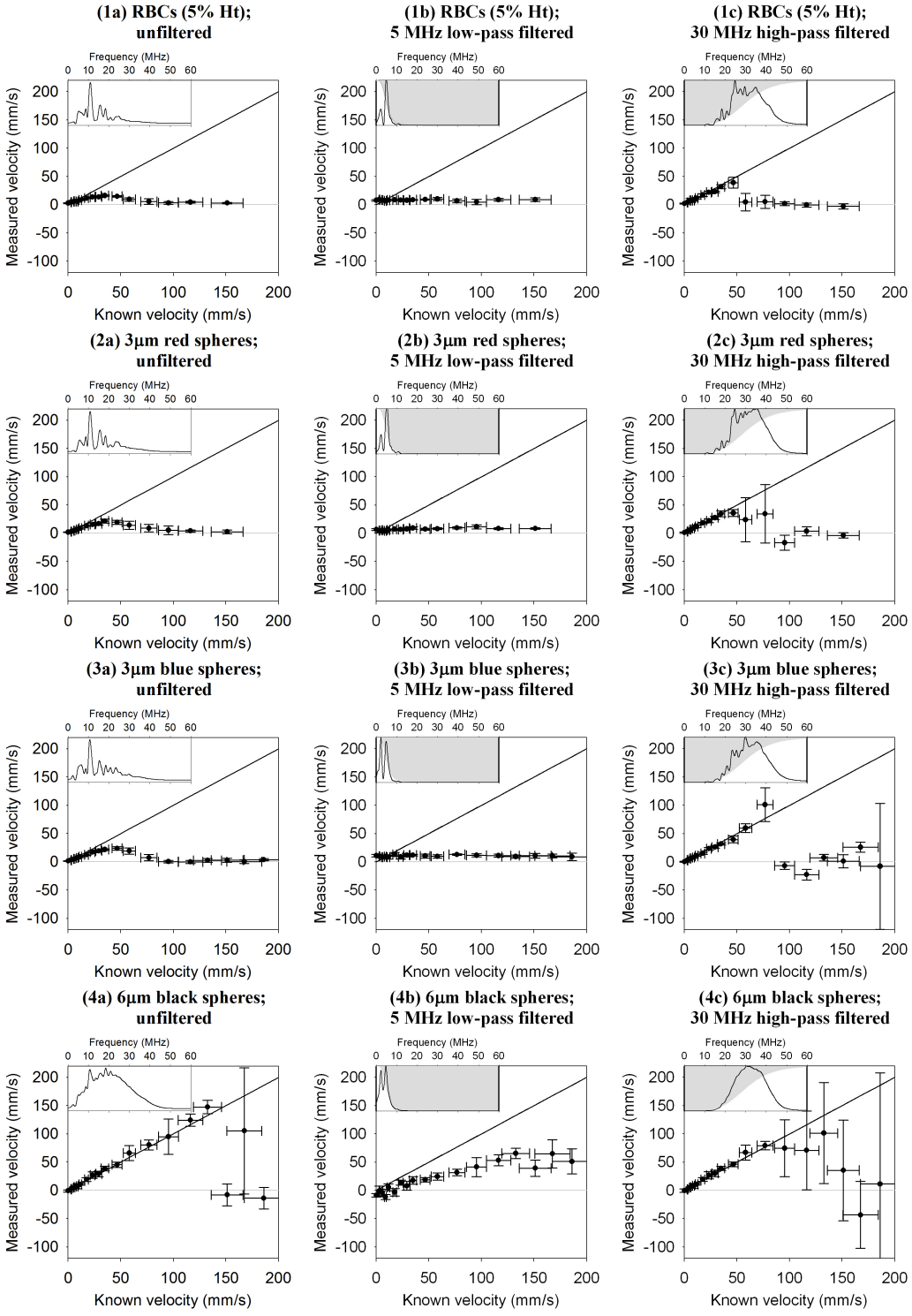

Figure 10.9: The effect of low-pass and high-pass filtering the photoacoustic data on velocity measurements made for four different absorbers, RBCs, red polystyrene spheres (3 μm), blue polystyrene spheres (3 μm) and black polystyrene spheres (6 μm), as shown in rows 1-4 respectively. The velocity measurements shown in column (a) are same as those in Figure 9.20, column (a), and the insets are the mean frequency spectra as shown in Fig. 10.5, column (b). The velocity measurements and frequency spectra in column (b) and (c) are those calculated after filtering the data with a low-pass filter 5 MHz and high-pass 30 MHz filter.

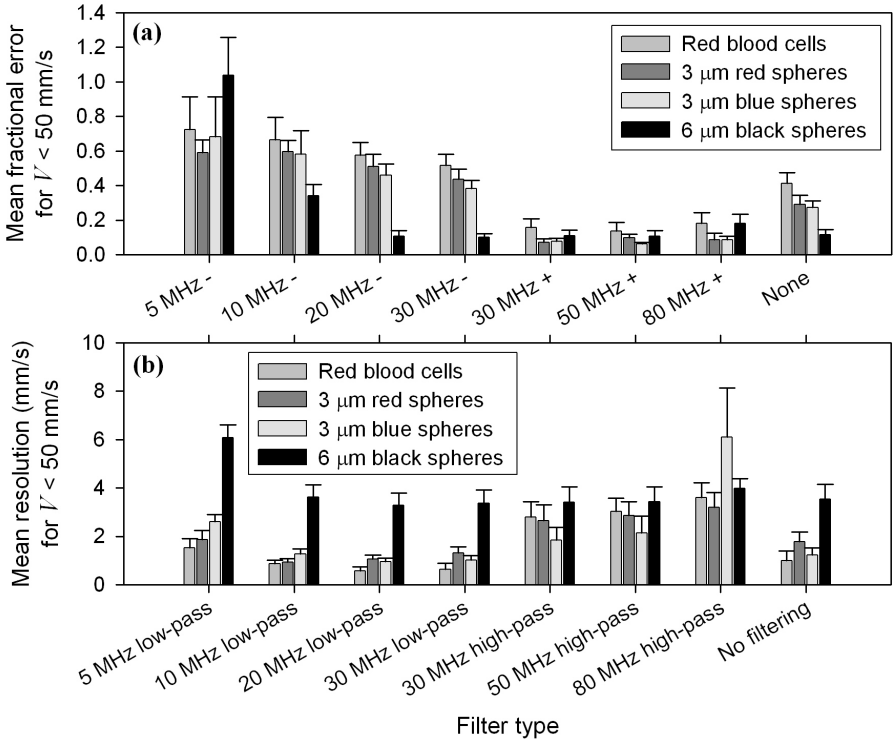

Figure 10.10: Comparison of the accuracy (a) and resolution (b) of velocity measurements made for the four absorbers in Fig.9.20, 10.5 and 10.9 after the data were filtered with various low-pass and high-pass filters as labelled for each group of bars.

mean fractional error in Figure 10.12(a). However, it is clear from Figure 10.11(c) that the accuracies of the velocity measurements for $V = 58$ mm/s and $V = 76$ mm/s are improved compared to the unfiltered data in (a), and therefore there is a greater measurement range after high-pass filtering. This is also shown in Figure 10.12(b) where $|V_{\max}|_{\text{obs}}$ is defined to be the highest velocity for which the fractional error is less than 0.5. This increase in measurement range is at the expense of a small deterioration in measurement resolution, but from Figure 10.11 the difference is not significant. The accuracy (a) and measurement range (b) for the high-pass filtered "whole frame" data is similar to that for the unfiltered "segmented" data, and yet the resolution is much improved for the former compared to the latter.

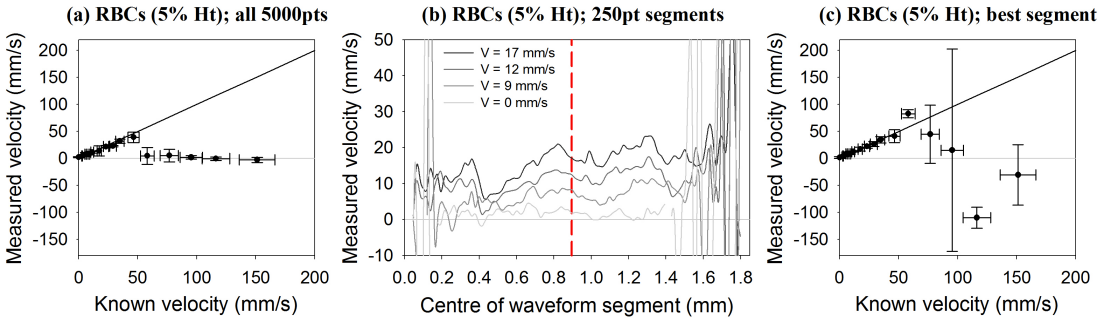

Figure 10.11: "Segmentation" of the data acquired for the RBCs (5% Ht) as in Fig. 9.20, row 1, but after the photoacoustic signals were filtered with a high-pass 30 MHz Butterworth filter.

In summary, it seems that high-pass filtering, particularly with a cut-off frequency around 30 MHz, can improve accuracy of photoacoustically measured velocities, and the accuracy of high velocities can be further improved by evaluating only a small waveform segment. Low-pass filtering always reduces measurement accuracy. High-pass filtering and segmentation both reduce velocity resolution, but the resolution could be improved by repeating more measurements. The effect of filtering also depends on the frequency content of the original data, as shown by the reduced effect of low-pass and high-pass filtering on the data for the black spheres that exhibit more broadband frequency spectra.

Effect of filtering on zero-offset

The association of lower concentrations with higher frequencies is in good agreement with the results in sub-section 10.1.3 where high-pass filtering improved velocity measurement accuracy: Section 8.3 showed that low concentrations also improve measurement accuracy compared to high concentrations. In particular, Figure 8.13(b) showed that the measurements demonstrated a zero velocity offset that increased with increas-

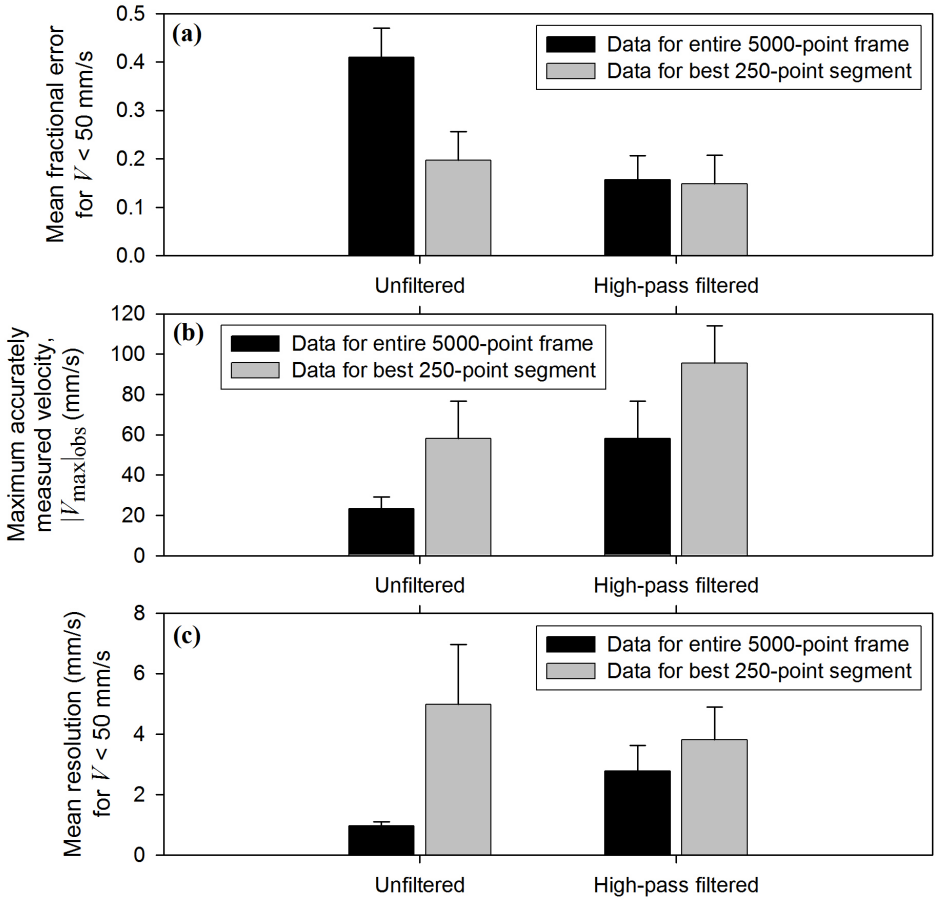

Figure 10.12: Comparison of the accuracy (a), measurement range (b), and resolution (c) of $mean(V')_N$ values plotted in the left and right columns of Fig. 9.20 (row 1) and Fig. 10.11. See also Fig. 9.21.

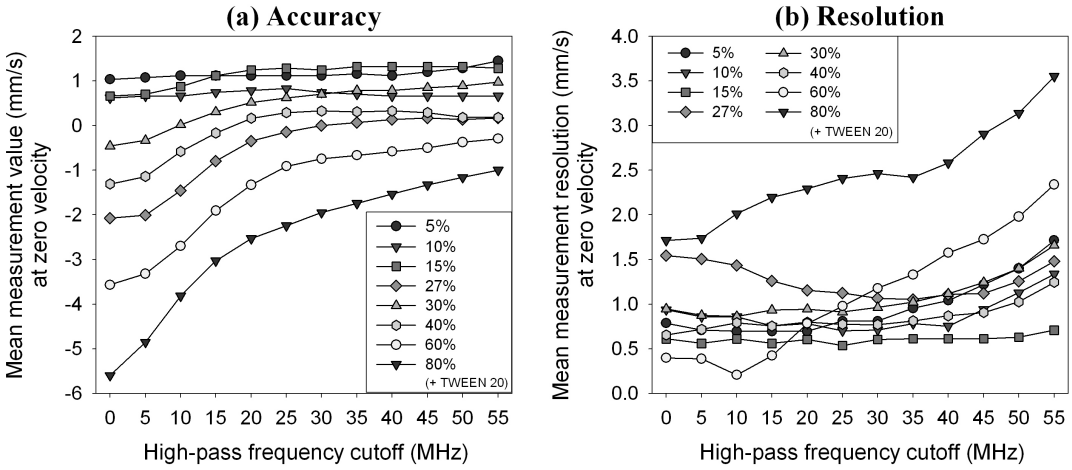

Figure 10.13: Demonstration of the effect of different high-pass filters on the accuracy and resolution of zero velocity measurements made for different concentrations of 3 μm red polystyrene spheres stationary ($V = 0$) in a tube of diameter 600 μm.

ing concentration of red spheres. Figure 10.13 demonstrates the effect of high-pass filtering the data acquired at zero velocity for these different concentrations. Figure 10.13(a) shows that as the high-pass filter cut-off frequency is increased the measurement error becomes smaller; in other words the measurements approach the true zero value. The measurement resolution values remain relatively consistent for the different filters, as shown in Figure 10.13(b), except for the two 80% concentrations where the resolution deteriorates with increasing cut-off frequency.

It is unclear why there is a zero velocity offset, and why it increases with increasing concentration; it is also not obvious why an increasing cut-off frequency reduces the measurement error. However, the following section presents some results that suggest that the laser and transducer alignments have important effects on measurement accuracy.

10.2 Laser and transducer alignment

Figure 10.14 illustrates two cases where the accuracies of the photoacoustically measured velocities were affected by the alignment of the laser and the transducer respectively.

Figure 10.14(a) demonstrates the effect of the alignment between the two beams used to generate the pairs of photoacoustic waveforms. The frequency doubling crystal was removed from the laser, and then replaced, which restored the wavelength to 532 nm as before, but disturbed the alignment between the two beams emerging from

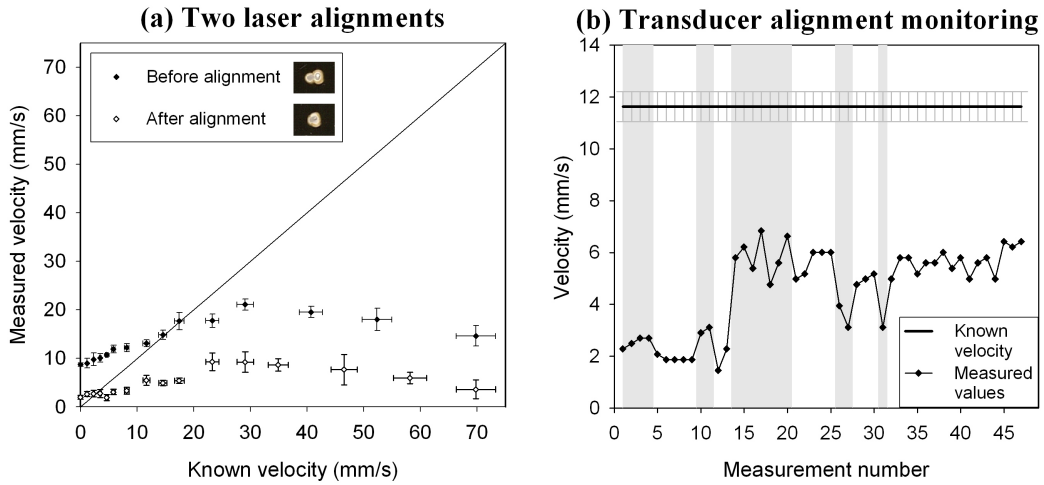

Figure 10.14: The effect of alignment of the laser (a) and the transducer (b) on the accuracy of photoacoustically measured velocities. (a) Measurements recorded before and after aligning the two lasers in the twin PIV system: the alignment is illustrated by the burn paper photographs in the plot legend. The two sets of velocity measurements were recorded in otherwise identical experimental conditions with RBCs (6% Ht) flowing in a 390 μm diameter tube and photoacoustic signals acquired using the 30 MHz focussed PZT transducer. (b) A series of 47 sequential measurements acquired using the 30 MHz focussed transducer in various different positions: a change in position is indicated by a change in the background shading. The data were recorded for RBCs (6% Ht) flowing with an average velocity $V = 11.6 \pm 0.6$ mm/s in a 390 μm diameter tube and illuminated with the PIV laser ($T = 0.5$ ms).

the two lasers in the system. This is evident from the top photograph of the burn paper in the legend, where two distinct spots are visible. Photoacoustic signals were then acquired using the 30 MHz focussed PZT transducer, with the (misaligned) beams separated by a time $T = 0.5$ ms, illuminating RBCs (6% Ht) flowing in a 390 μm diameter tube. The velocity measurements for $V < 10$ mm/s unusually *over*-read the "known" values, and there was a zero offset of approximately 9 mm/s, as shown by the solid data points in Figure 10.14(a). The two laser beams were then re-aligned as shown by the overlapping spots in the second burn paper photograph, and this reduced each velocity measurement by about 7 mm/s, including the zero velocity measurement, as shown by the unfilled data points.

Thus it seems that the laser beam alignment can have a significant effect on the velocity measurement accuracy, and this is due to the de-correlation effect of different spatial illumination profiles (see also 8.2). The laser alignment is relatively straightforward to correct; in fact some studies involve a deliberate spatial offset between two illumination beams in order to measure transverse flow [71]. However, it remains unclear why a zero velocity offset would be dependent on absorber concentration, as shown in Figures 8.13(b) and 10.13.

Figure 10.14(b) demonstrates the effect of transducer alignment on velocity measurement accuracy. The data were acquired using the 30 MHz PZT transducer for RBCs (6% Ht) flowing with an average velocity $V = 11.6 \pm 0.6$ mm/s in a 390 μm diameter tube and illuminated with the PIV laser ($T = 0.5$ ms). Measurements were made repeatedly, and the transducer position altered (on a translation stage) at regular intervals, as indicated by the changes in the background shading between measurement pairs (4, 5), (9, 10), (11, 12), (13, 14), (20, 21), (25, 26), (27, 28), (30, 31), and finally (31, 32). It is clear that changes in the measurement value are generally correlated with the changes in the transducer position; in particular, there was a large increase in the measurement value when the transducer was moved between measurements 13 and 14, even though the most accurate measurement (17) was still less than 60% of the "known" value.

Transducer misalignment will impact the measurement value, since there is a range of velocities within the tube, and it is possible for the transducer to focus on only a small section. In fact, precise scanning of the transducer across the tube would enable the velocity profile to be mapped in a manner analogous to the study carried out using time-correlation ultrasound [36].

The final section of this chapter relates to the oscilloscope sampling interval, and demonstrates that this is not such a stringent limitation as may be supposed.

10.3 Oscilloscope sampling interval

The oscilloscope imposes two potential limitations on the data captured from the transducers.

The first limitation is the oscilloscope bandwidth, which however was set to 250 MHz (options being 20 MHz, 250 MHz or "full") which is well above the highest frequencies detectable with any of the transducers.

The second limitation is the oscilloscope sampling interval δt_s, which in Equation 7.5, page 103, is proportional to the minimum measurable velocity, in other words, the velocity resolution. Sub-section 10.3.1 uses data recorded for "manually-shifted" microspheres to show that in fact it is possible to measure velocities smaller than those dictated by δt_s. An example for flowing RBCs is shown in sub-section 10.3.2.

10.3.1 Illustrations with data for "manually-shifted" microspheres

To investigate the effect of the oscilloscope sampling interval, an 800 μm diameter tube filled with 300 μm carbon spheres was illuminated with the FQ laser, and "manually shifted" as described in sub-section 5.1.3 and Section 6.1. This produced ideal "plug flow" where all the absorbers experience the same time shift (see Section 8.5).

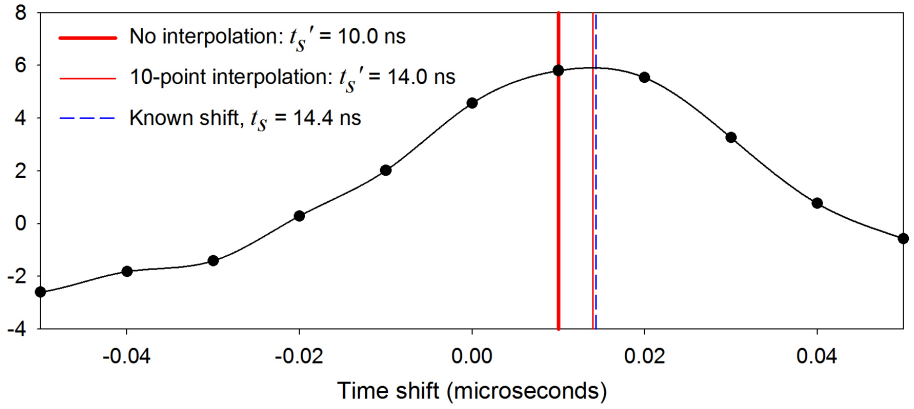

Figure 10.15: Illustration of the improvement in accuracy gained by interpolating the cross-correlation function. An 800 μm diameter tube filled with 300 μm carbon spheres was "manually shifted" and illuminated with the FQ laser. The data points correspond to the mean of two cross-correlation functions calculated for waveform pairs acquired using the 20 MHz focussed transducer and an oscilloscope sampling interval δt_s = 10 ns. Only the peak lobe is shown (data points from -50 ns to 50 ns) and the maximum amplitude corresponds to a time shift t_s' = 10.0 ns, as shown by the thick vertical line. The black curve is the ten-point interpolation of the data points, and has a maximum amplitude at t_s' = 14.0 ns, as shown by the thin vertical line. The dashed vertical line marks the known time shift (t_s = 14.4 ns).

The data points in Figure 10.15 plot the mean cross-correlation function (for time shifts from -50 ns to 50 ns) calculated for waveforms acquired using the 20 MHz PZT transducer and an oscilloscope sampling interval δt_s = 10 ns. The data point with the largest y value occurs at a time shift t_s' = 10.0 ns, and this is the closest point to the "known" time shift t_s = 14.4 ns. However, ten-point interpolation of the cross-correlation function, as shown by the black curve joining the points, enables an accurate measurement of t_s' = 14.0 ns, and thus it is possible to recover information lost due to oscilloscope under-sampling. Interpolation of the cross-correlation function will improve measurement precision, and this has also been shown using cross-correlation functions calculated from Doppler ultrasound signals [67].

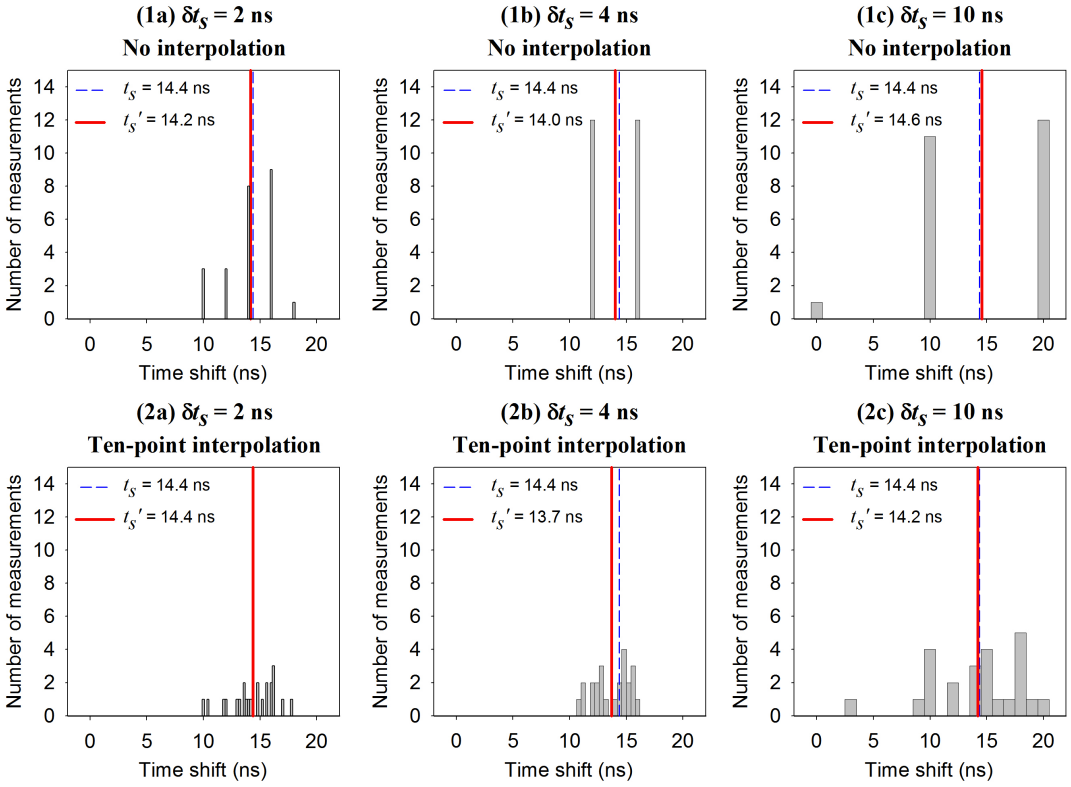

Figure 10.16: Distributions of time shifts derived from the maximum amplitudes of mean cross-correlation functions calculated for waveforms acquired with different sampling intervals, δt_s = 2 ns, 4 ns and 10 ns in columns (a), (b) and (c) respectively. The measurements in row 1 were made without interpolating the cross-correlation function, whereas in row 2 the time shifts were derived from a ten-point interpolation. Note that in both rows of plots, the widths of the bars correspond to the interpolated intervals of 0.2 ns, 0.4 ns and 1.0 ns respectively. The overall measured time shift t_s' is the mean of the 24 individual measurements. The known shift t_s = 14.4 ns was the result of "manually shifting" a tube filled with carbon spheres, as described in the text and in the caption to Fig. 10.15.

Figure 10.16 shows a second method for overcoming oscilloscope under-sampling, simply by taking the mean of repeated measurements. Each plot shows the distribution of 24 individual time shift measurements (such as that shown in Figure 10.15), and the mean overall measurement t_s' is marked by a solid vertical line compared to the dashed vertical line for the known time shift t_s = 14.4 ns. The data in the left column (a) was acquired using an oscilloscope sampling interval of δt_s = 2 ns, whereas δt_s = 4 ns in column (b) and δt_s = 10 ns in column (c). Row 1 shows that even without interpolating the cross-correlation functions, it is possible to arrive at mean time shift measurements that fall between the sampling points and accurately represent the known time shift. Row 2 shows that ten-point interpolation can further improve measurement accuracy (2a), or in some circumstances it may be detrimental (2b), or else it may bring about no change in the measurement error (2c).

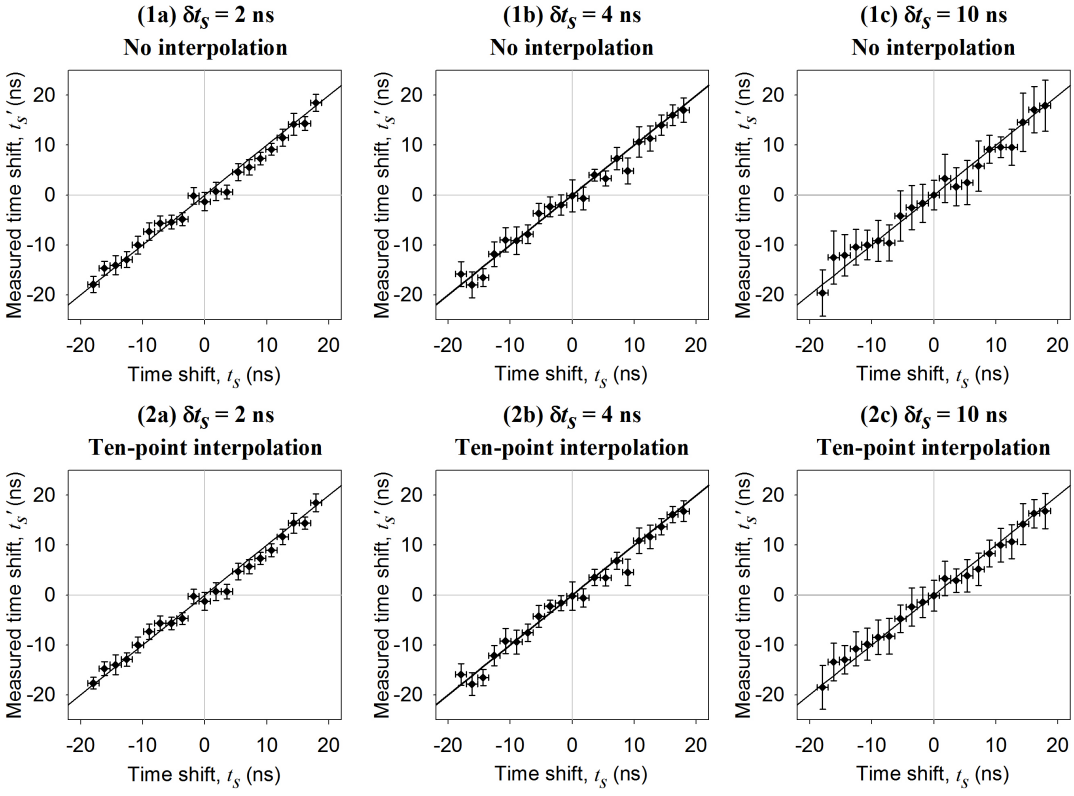

Figure 10.17: Time shift measurements t_s' made for t_s = −18 ns to +18 ns, and for sampling intervals, δt_s = 2 ns, 4 ns and 10 ns in columns (a), (b) and (c) respectively. The measurements in row 1 were made without interpolating the cross-correlation function, whereas in row 2 the time shifts were derived from a ten-point interpolation. The time shifts resulted from "manually shifting" a tube filled with carbon spheres, as described in the text and in the captions to Fig. 10.15 and Fig. 10.16. Each data point is the mean of 24 individual time shift measurements, and the vertical error bars are the standard deviations.

Figure 10.17 shows the same data as in Figure 10.16 but for a range of time shifts from $t_s = -18$ ns to +18 ns. The mean values are t_s' as in Figure 10.16 and the vertical error bars are the standard deviations of the distributions of 24 measurements. A cursory inspection reveals that there is deterioration in resolution with increasing sampling interval [moving from plots (a) to (b) to (c)] both without interpolation (row 1) and with interpolation (row 2). However, the accuracy of the measurements appears to be relatively unchanged with sampling interval and interpolation.

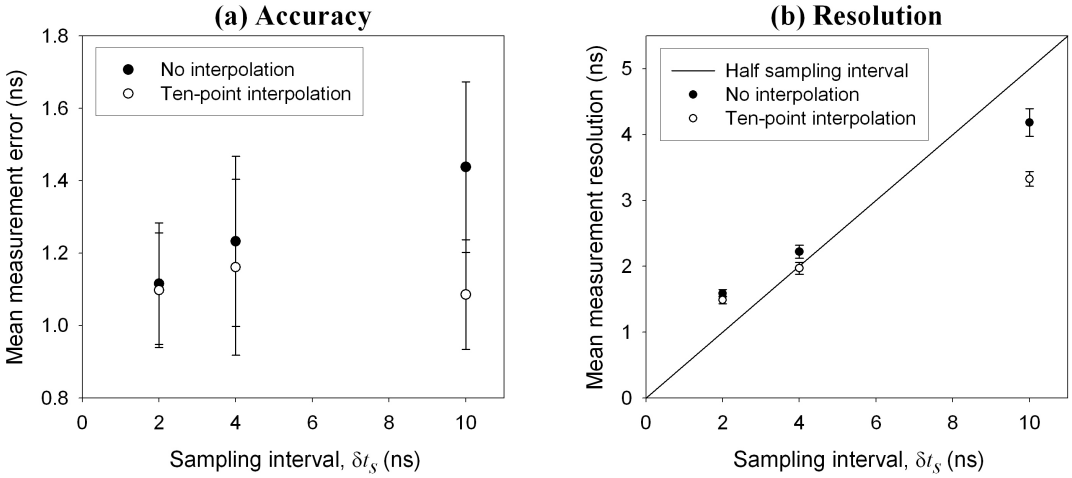

Figure 10.18: Mean accuracy (absolute measurement error) and resolution for the data shown in each of the six plots in Fig. 10.17. The vertical error bars are the standard errors on the mean values.

Figure 10.18 supports the initial impressions gained from Figure 10.17. In Figure 10.18(a) the solid data points represent the mean measurement error across the time shifts calculated for the cases where no interpolation was performed [Figure 10.17(1a), (1b) and (1c)]; they show a slight increase in measurement error as the sampling interval is increased, but there are large uncertainties (vertical error bars) on these mean values, and the unfilled data points show that when the cross-correlation functions are interpolated [Figure 10.17(2a), (2b) and (2c)] there is no significant difference in measurement accuracy for the different sampling intervals. However, Figure 10.18(b) shows that the mean velocity resolution becomes worse as the sampling interval is increased. The solid line plots the resolution based on $\pm\delta t_s/2$, and the solid data points (no interpolation of the cross-correlation function) are in rough agreement with this line. The unfilled data points show that measurement resolution can be improved by interpolation of the cross-correlation function, particularly for the larger sampling intervals.

In summary therefore, these data illustrate that the oscilloscope sampling interval has no discernible effect on velocity measurement accuracy, and the effect on velocity resolution can be reduced by interpolating the cross-correlation function and also by taking the mean of many repeated measurements.

10.3.2 Illustrations with data for flowing RBCs

Figure 10.19 shows data acquired for flowing RBCs using two different oscilloscope sampling intervals. Velocity measurements for the entire 5000-point waveforms are shown in column (a) for the cases where $\delta t_s = 0.25$ ns (1a) and $\delta t_s = 0.5$ ns (2a), and there appears to be no obvious difference in the measurement accuracies or resolution values. The middle column of plots (b) shows the $mean(V')_N$ values calculated for waveform segments as described in Section 9.2. In row 2 the segment length was 250 points, whereas in row 3 a 125-point segment length used so that the total time length of the segments were the same as those for the case where $\delta t_s = 0.25$ ns (row 1). The right column of plots (c) shows the $mean(V')_N$ values for the segments marked by the dashed vertical lines in plots (b). By comparing plots (1c) and (2c) it is evident that the accuracy and resolution of velocity measurements for $V < 50$ mm/s are similar for the two different sampling intervals. For higher velocities, the smaller sampling interval $\delta t_s = 0.25$ ns gives better velocity accuracy, but the measurement range for $\delta t_s = 0.5$ ns is improved by analysing shorter waveform segments (3c).

This brief analysis suggests that, as for the "manual shifting" data in the previous sub-section, the oscilloscope sampling interval is not a stringent limitation to the accuracy and resolution of velocity measurements made for flowing absorbers. However, additional data acquired using a greater range of sampling intervals would be needed to verify this further.

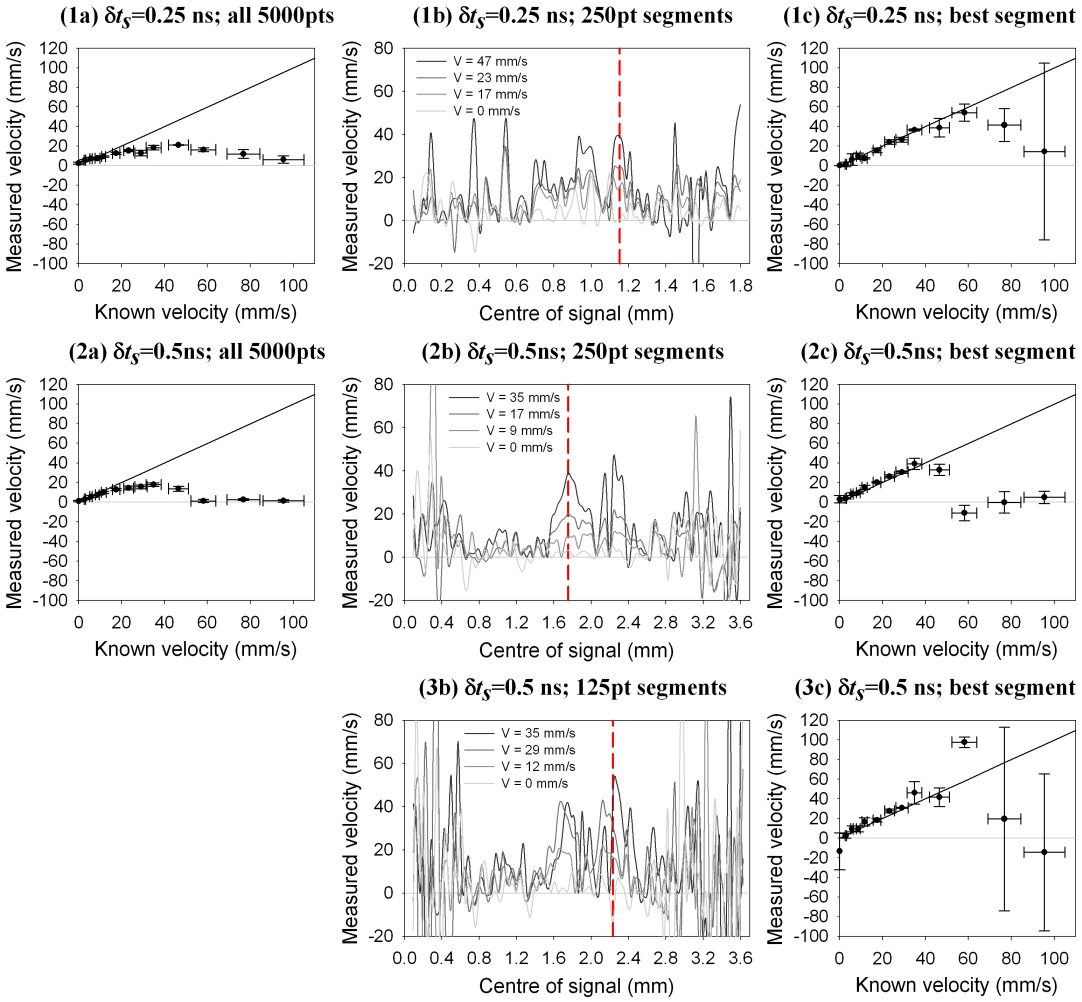

Figure 10.19: Velocity measurements made at "known" average velocities ranging from $V = 0$ mm/s to 95 mm/s for RBCs (5% Ht) flowing under the conditions described in Figure 9.20, but acquired using two different oscilloscope sampling intervals. The data in row 1 was acquired with an oscilloscope sampling interval $\delta t_s = 0.25$ ns, whereas in row 2, $\delta t_s = 0.5$ ns. The "segmentation" in row 3 is also for the data in row 2, but using a shorter segment length of 125 points compared to 250 points.

Part IV

Conclusions

11

Conclusions

This thesis has described the experimental validation of a new flow-measuring method involving pulsed photoacoustic Doppler and time-domain cross-correlation. After rigorous analysis of the accuracy and resolution of the velocity measurements, a number of conclusions can be drawn. In particular, it is important to identify the technical and methodological challenges that need to be addressed in order to apply the flowmetry technique *in vivo*.

11.1 Summary of findings

The studies have demonstrated that the velocity of a random distribution of micron-scale absorbers can be accurately estimated from time shift measurements obtained by cross-correlation signal processing of photoacoustic waveforms. Results were demonstrated in tissue phantoms in which the absorber size and distribution were comparable to those of red blood cells.

11.1.1 Two phantom types

In initial studies using a wheel phantom (Chapter 7), velocities up to 1.4 m/s were accurately measured with a resolution of ±0.008 m/s using a laser pulse separation of 1.5 ms. Although photoacoustic Doppler flowmetry is targeted at measuring the much lower flow velocities encountered in the microvasculature (< 50 mm/s), the technique is scalable as described in Section 7.4: increasing the pulse separation to 15 ms would, theoretically, allow velocities up to a maximum of 140 mm/s to be measured with a resolution of ±0.8 mm/s, with further increases in resolution possible by interpolating between the data sampling points, and by taking repeated measurements.

The maximum velocity $|V_{\max}|$ is defined by the time taken for the absorbers to traverse the transducer focal beam. This upper limit is a function of the pulse separation T and transducer beam width w – a predictable and well known result from time correlation ultrasound flowmetry [52]. For the wheel phantom, de-correlation occurs over a distance d_{D} approximately equivalent to w, and this is also true for absorbers fixed inside a tube, which is manually shifted (see Figures 8.2 and 8.17). Thus, for the simple cases of absorbers moving together in a consistent, uniform manner the photoacoustic flowmetry technique provides accurate and high resolution measurements over the velocity range expected.

Velocity measurements were also made for fluid phantoms (Chapter 8) comprising a suspension of microspheres or red blood cells (RBCs) flowing in a tube. The velocity resolution values were comparable to those obtained for the wheel phantom and manual shifting experiments, but the accuracy varied with absorber type, absorber concentration and tube diameter. In particular, the measurements consistently underestimated the known average flow velocities, and the under-reading became worse with increasing concentration and increasing diameter. This is likely to be a result of limited light penetration in combination with laminar flow.

11.1.2 Laminar flow

The wheel phantom and manual shifting experiments demonstrate plug flow, whereas non-plug flow results in a range of axial speeds. Simple theory suggest that the flow is laminar, and this is supported by microscopic observations where blood cells at the tube boundaries appeared to move with a much slower speed than those at the centre (Figure 8.22). The absorbers settle in the tube over time (Figure 8.15), but this does not occur over the time-scale of routine measurements. Dyed polystyrene spheres may also adhere to the tube walls, but this is prevented using TWEEN®20 surfactant.

The presence of laminar flow, in combination with limited light penetration into

the tube, serves as an explanation for the measurement under-reading, as described in Section 9.1. With narrow tubes, the light is able to penetrate throughout the tube generating photoacoustic signals from absorbers with the full range of laminar flow speeds; therefore the measured velocity is likely to represent the average flow velocity. However, with wider tubes or higher absorber concentrations, the light is absorbed principally by the slower-moving absorbers close to the tube walls; these absorbers therefore generate the largest photoacoustic signal and their velocities are likely to dominate the overall measured velocity.

11.1.3 Waveform segmentation

A "waveform segmentation" method was developed (Section 9.2) in order to address the problem of measurement under-reading. Analysis of small segments of the photoacoustic waveforms prevents large amplitude parts of the signal (possibility from the slow-moving absorbers close to the nearer tube wall) dominating the overall velocity measurement. The velocities calculated for each 250-point segment varied along the signal lengths; each data set exhibited a parabolic shape reminiscent of the laminar flow profile, but the correspondence between the location of this laminar-like peak in time and the spatial locations within the tube still needs to be verified. The laminar-like peak appeared to be broader for lower concentrations of absorbers, and also for the black polystyrene spheres, which are more weakly absorbing than the red and blue polystyrene spheres. This is to be expected since both low concentrations and low absorption coefficients enable greater light penetration. The "optimum" segment was chosen by minimizing the fractional error across all velocities, and this dramatically improved the measurement accuracy compared to the velocities calculated for the entire (5000-point) waveforms. For example, for a RBC concentration even greater than a physiologically normal haematocrit, a velocity of 23 mm/s was measured with a fractional error of approximately 15% for the best segment, whereas the same data yielded a fractional error of 100% when the velocity was calculated from the entire frame (see Figure 9.17).

11.1.4 Absorber heterogeneity

The ability to make accurate velocity measurements for a RBC concentration even greater than a physiologically normal haematocrit, either flowing or manually shifted, suggests that absorber heterogeneity is not such a fundamental limitation to the flowmetry technique as is commonly supposed. This is encouraging since ultrasound attenuation increases with increasing frequency (see page 178), and therefore a requirement for high frequency detectors would limit the penetration of acoustic resol-

ution flowmetry to depths comparable or only marginally greater than those achieved using the optical resolution mode (< 1 mm). It should be possible to detect frequencies below 20 MHz from depths of more than 5 mm. There is evidence that the accuracy and resolution of the velocity measurements can be improved by increasing the transducer bandwidth and/or centre frequency (Figures 10.1 and 10.3), but for centre frequencies greater than about 20 MHz the effect is limited. This implies that the absorbers themselves largely dictate the frequency content, and the ability to detect flow with bandwidths of just tens of MHz suggests that the heterogeneity is greater than that corresponding to the expected absorber spatial separations, which are equivalent to frequencies in the order of hundreds of MHz. However, the domination of low-frequency content is clearly detrimental to velocity accuracy, and this is evident from the beneficial effect of high-pass filtering, as described in sub-section 10.1.3. Figure 10.12 shows that 30 MHz high-pass filtering can reduce the mean fractional error from more than 40% to approximately 15%, and further reductions are obtained by applying waveform segmentation. However, the ability of high-pass filtering to produce a measurement close to the average flow velocity is not fully understood; the waveform segmentation method is considered to be the more valuable approach since it has the potential to map out flow velocity profiles.

11.1.5 Experimental considerations

Whilst the detector frequency response does not seem to present a fundamental limitation, the velocity measurement accuracy and resolution appears to be sensitive to the detector alignment. For example, altering the detector position may give rise to measurements with a zero velocity offset of up to 10 mm/s, as shown in Figure 10.14, and this may be related to detection of a limited part of the laminar velocity profile. In fact, the high sensitivity of the measurements to detector alignment could enable flow velocities to be measured with high spatial resolution.

Velocity inaccuracy may also arise from discrepancies in the spatial and temporal distributions of the two laser beams used to generate successive waveform pairs, which was demonstrated in Figure 8.2. In addition, it seems that increasing the concentration of red polystyrene spheres increases the zero velocity offset, but this offset is alleviated after high-pass filtering the data, with a greater improvement obtained using a filter with a higher frequency cut-off, as shown in Figure 10.13. There is yet no clear explanation for these two observations.

11.1.6 Summary

In summary, this work suggests that time correlation photoacoustic methods have potential for measuring blood flow in the microvasculature. Their distinguishing advantages are high spatial resolution, a high degree of scalability in terms of measurement resolution and upper limit of detection, the ability to use the type of Q-switched excitation lasers routinely used in biomedical photoacoustic imaging and the potential for use in acoustic as well as optical resolution photoacoustic sensing modes. Time correlation methods do not suffer from aliasing which can limit the maximum measurable velocity of other schemes, nor is there any need for calibration in order to obtain absolute velocity measurements.

The work in this thesis has shown that the measurement accuracy deteriorates with increasing RBC concentration and with increasing tube diameter, and this is most likely to be due to light absorption principally by slow-moving absorbers near the edge of the laminar profile. However, the accuracy can be recovered by analysing small segments of the photoacoustic signals, and also by high-pass filtering. Preliminary results have been obtained using a physiologically realistic concentration of RBCs, but further data is needed. Demonstrating the photoacoustic Doppler flowmetry technique with whole blood, and verifying the explanation relating to light absorption, will form the subject of future work as outlined in Section 12.1.

11.2 Publications arising from this work

- Initial results obtained with the wheel phantom were presented at an international conference (SPIE Photonics West 2010) as detailed in the proceedings [23].
- Further results with the wheel phantom, generated using a novel signal processing scheme, as well as preliminary fluid phantom studies were presented at the same conference the following year [24].
- A detailed analysis of the wheel phantom results, as a means for describing the principles of the technique, was published in the *Journal of the Acoustical Society of America* [25].
- An evaluation of preliminary fluid phantom results acquired for different absorber concentrations and in different tube diameters was presented at SPIE Photonics West 2013 [26].

12

Outlook

12.1 Suggestions for further work

12.1.1 Velocity measurements with whole blood

First and foremost, more measurements should be made using whole blood flowing in a tube; the data would be analysed using the "segmentation" method, and also by high-pass filtering. This would provide conclusive evidence for the ability to measure the flow of whole blood in the "acoustic resolution" photoacoustic mode. In addition, further measurements at reduced blood concentrations and/or measurements with different levels of RBC aggregation [55, 93, 94], and using the "manually shifting" method, would add further weight to the evidence that the commonly cited "heterogeneity" limitation (see pages 59, 121 and 132) is not as stringent as many suppose.

An interesting avenue for investigation would be the potential for a sufficiently narrow laser line width to create 3D speckle in a scattering medium. The speckle pattern would change with movement of the scatterers, and result in fluctuations in the absorbed light distribution. This effect could therefore enhance the spatial heterogeneity of the photoacoustic signals.

12.1.2 Laminar flow and light absorption

The second priority would be to evaluate the compromise between adequate light penetration and sufficient SNR. The SNR is proportional to light absorption, but excessive light attenuation will bias the velocity measurements towards the slower velocities near the edge of the tube. For a particular suspension, the absorption coefficient, and therefore the light penetration, varies with wavelength. The optimum wavelength(s) for the photoacoustic measurements should be determined using two wavelength-tunable (OPO) laser systems, or if possible a single OPO system, which would be programmed in order to produce pairs of light pulses.

In addition, a method should be developed for automated extraction of the most appropriate signal segment and the cutoff for "extreme" values (see sub-section 9.2.3). If possible, it would also be helpful to simulate the translation of the laminar profile of flow velocities to measured time shifts, although it would be challenging to realise this in three dimensions as discussed in Section 9.1. Possible RBCs flow patterns, and how these may vary with haematocrit and aggregation, should also be investigated (see refs. [66, 93, 94]).

12.1.3 Signal bandwidth

The bandwidth of the photoacoustic signals could be measured using a hydrophone; by measuring the bandwidths of signals arising from different absorber concentrations, it would be possible to associate differing degrees of heterogeneity with corresponding frequency bandwidths. It would also be helpful to assess in more detail the effect of transducer bandwidth on the accuracy of the velocity measurements in order to determine the detectors required for *in vivo* flowmetry. The minimum SNR for accurate velocity measurements, together with the bandwidth of the detector, will elucidate the maximum possible penetration depths in tissue (see page 178).

12.1.4 Investigation of experimental limitations

Further experiments are required to investigate the limitations described in Chapter 10. The effect of laser alignment and discrepancies in the spatial and temporal beam profiles could be investigated by comparing velocity measurements both with and without a TEM 00 aperture in the PIV laser system. The effect of transducer alignment should also be further evaluated since this will be important for making measurements *in vivo*. The limitation on measurement resolution imposed by under-sampling is of interest, but not of fundamental importance since it has already been shown that interpolation and repeated measurements can overcome this restriction.

12.2 *In vivo* measurements of blood velocity

The ultimate goal is to measure blood velocity in living tissue; this would be a novel accomplishment, since no other research group has succeeded in making such measurements in the so-called "acoustic resolution" mode, which has the potential to penetrate several centimetres into tissue.

12.2.1 Preliminary *in vivo* investigations

Phantom studies could entail velocity measurements made through a tissue-realistic light-scattering medium (such as Intralipid). These would identify the maximum penetration depth of the technique and therefore the ideal anatomical location (for example, a vessel in a mouse tail) in which to first demonstrate the method *in vivo*. In the first instance, the *in vivo* flow velocity could be varied temporally, (for example by performing a tail cuff occlusion), in order to validate changes in the flow measurements.

12.2.2 Spatial variation in flow

In this work, emphasis has been placed on demonstrating the underlying measurement principles using a single ultrasound receiver. In practice however, the technique would be extended from single to multiple point measurements in order to capture spatial variation in flow. This would require development of a computer-controlled scanning system, which would be guided using *a priori* anatomical information obtained from the photoacoustic imaging scanner. The ultrasound transducer could be scanned across the animal's body; alternatively, an array of ultrasound transducers could be implemented, and operated in a similar fashion to a conventional combined B-mode/Doppler ultrasound scanner. Thus, an anatomical photoacoustic image of the vasculature would be acquired in the usual way. The velocity could then be obtained at a specific user defined spatial point by synthesising an appropriate receive beam using the detector array. Since θ is available from the anatomical image and the receive beam direction, absolute velocity measurements can be made. Alternatively, the use of multi-dimensional cross correlation could be employed to obtain parametric images relating to flow in a manner analogous to conventional colour flow ultrasound imaging [39]. Each flow measurement would be associated with the position along the vessel in order to produce an image in which the vessels are encoded with blood flow information.

12.2.3 Measurement validation

The *in vivo* velocity measurements should be validated using alternative methods such as Doppler ultrasound for flow in large vessels, and optical techniques (for example, particle image velocimetry, PIV) for flow in small, but superficial, vessels. A method could be developed to allow ultrasound and photoacoustic blood velocity measurements to be made simultaneously and compared. Experiments and numerical simulations would be used to identify the most suitable ultrasound detector in terms of its focal width and frequency response; a means could then be developed for employing it in conjunction with the existing photoacoustic imaging scanner.

12.2.4 Application to tumour blood flow

Ultimately, the technique would be applied to studies of tumours implanted in mice. Mouse models are used extensively to study the pathophysiology of a wide variety of tumours and their response to treatment to aid the development and refinement of new cancer therapies. The initial goal would be to obtain a map of the blood flow in the tumour vessels. Attempts would then be made to monitor changes in the blood flow over a period of tumour growth followed by treatment with anti-cancer drugs (Vascular Disrupting Agents).

Finally, in the very long term, it is envisaged that the flowmetry technique could be incorporated in existing clinical photoacoustic scanners that are used for human cancer imaging. This PhD project is therefore a small contribution to a field that has the potential to significantly impact healthcare technology.

Part V

Appendices

A

Transducer characterisation

A.1 Calculation of FWHM beam width

Table A.1 lists the part numbers, focal lengths and element diameters for each of the transducers used variously to detect photoacoustic signals generated in the light-absorbing phantoms. All the PZT transducers were manufactured by Panametrics, Olympus NDT Inc., Waltham, Massachusetts, USA; the 25 MHz and 80 MHz PVDF transducers were made respectively by Precision Acoustics Ltd., Dorchester, UK, and by Krautkramer Foertser Co. Ltd., Tokyo, Japan.

For focussed transducers, the -6 dB (FWHM) pulse-echo beam diameter BD(−6dB) at the focus can be calculated [82] from the transducer centre frequency f, the focal length F, and the element diameter D:

$$\mathrm{BD}(-6\mathrm{dB}) = 1.02\frac{Fc}{fD}. \tag{A.1}$$

For planar transducers, Equation A.2 [82] is used with a normalized focal length $S_F = 1$:

$$\mathrm{BD}(-6\mathrm{dB}) = 0.2568\, D\, S_F. \tag{A.2}$$

The values in the final column of Table A.1 were all calculated using Equation A.1 with a sound speed c = 1476 m/s, except for V316 for which Equation A.2 was used.

(a) PZT transducers

Centre frequency (MHz)	Part number	Focus	Focal length		Element diameter		FWHM beam width (µm)
			(inches)	(mm)	(inches)	(mm)	
3.5	V383	Cylindrical	1.26	**32**	**0.375**	9.525	1417
5	A307S	Spherical	**2.5**	63.5	**1.0**	25.4	738
15	V319	Spherical	**0.75**	19.1	**0.5**	12.7	148
20	V316	Planar			**0.125**	3.175	815
20	V317	Spherical	**0.75**	19.1	**0.25**	6.35	221
30	V375	Spherical	**0.75**	19.1	**0.25**	6.35	148
50	V3337	Spherical	**2.0**	50.8	**0.25**	6.35	236

(b) PVDF transducers

Centre frequency (MHz)	Part number	Focus	Focal length		Element diameter		FWHM beam width (µm)
			(inches)	(mm)	(inches)	(mm)	
25	PA150	Spherical	0.94	**24**	0.375	**7**	202
80	80-3, -P-12.5R, H158835	Spherical	0.47	**12**	0.118	**3**	74

Table A.1: Part numbers, focal lengths and element diameters for the transducers listed in Table 5.3; a bold font indicates the units in which each parameter was specified by the manufacturer. The beam widths are calculated using Equations A.1 and A.2.

A.2 Mapping transducer beam profiles

The FWHM beam widths were also measured directly from the transducer beam profiles, which were mapped out using a Fabry-Perot (FP) sensor [114]. For the 5 MHz transducer, a 40 μm wedged sensor was used (PM40LP5LP6B10-P7), whereas a 20 μm wedged sensor (PM20LP5LP6B5-P51) was used for the transducers with higher centre frequencies. In each case, the transducer was mounted perpendicularly above the sensor on a vertical translation stage. The transducer was operated in transmission mode and, after pre-tuning the sensor, an image was acquired as shown in Figure A.1(a), which is a screen shot of the LabVIEW interface. In (a), the acoustic pressure is displayed as an intensity-scaled pixel over an area with x values ranging from -2.44 mm to 1.15 mm and y values (labelled as "z" in the figure) ranging from 2.21 mm to 3.26 mm. The same data is displayed in (b) as a 3D surface. A slightly enlarged ver-

sion of (a) is repeated in (c), and from (c) x and y profiles are extracted: the lateral (x) profile is shown in (d) and the vertical (y) profile is plotted in (e). Gaussian fits to the data points are shown by the red curves, from which FWHM values were calculated, and the lateral and vertical profiles were exported to text files for further analysis in MATLAB. The derivative of (d) is shown in (f) but this was not used for subsequent analysis.

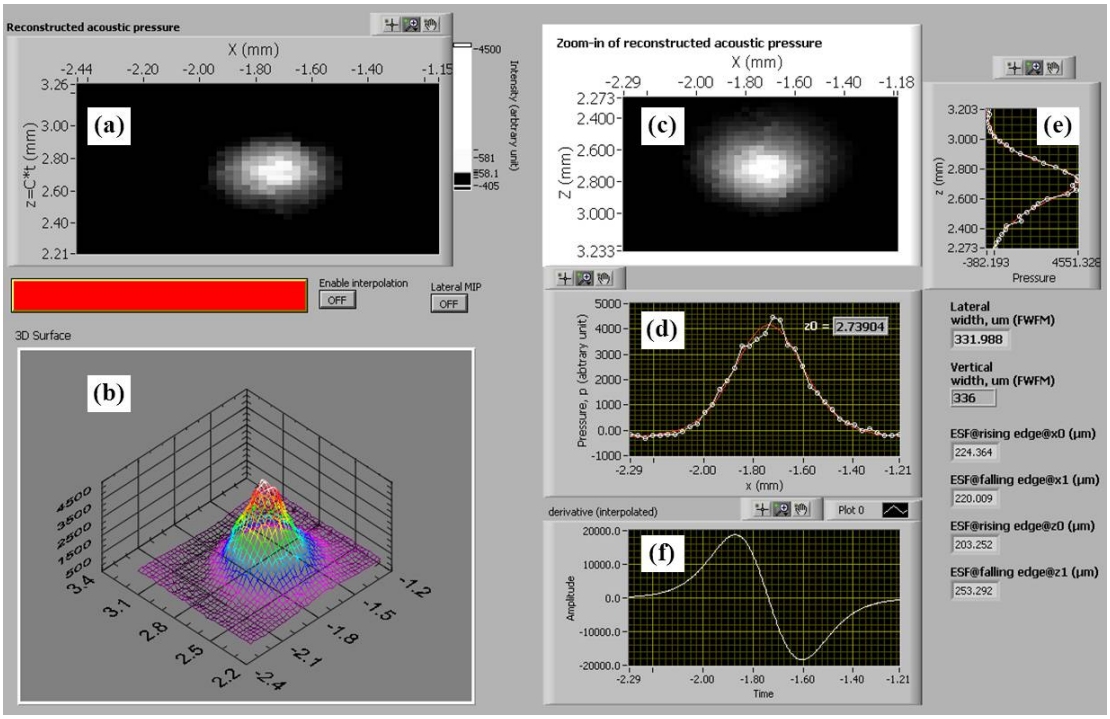

Figure A.1: LabVIEW interface developed by Edward Zhang for visualising images acquired from the Fabry-Perot detector. (a) Reconstructed image of the acoustic pressure received from the 30 MHz focussed transducer at a distance of 21.0 mm from the transducer face. (b) 3D representation of the acoustic pressure shown in 2D in (a). A slight enlargement of (a) is shown in (c), and the vertical and lateral profiles are shown in (d) and (e) respectively, with the derivative of (d) in (f).

The image acquisition process was repeated for the transducer in a number of vertical positions, which were converted to distances from the transducer face using the time of ultrasound signal arrival at the sensor. The profiles were then processed in MATLAB to produce colour maps, such as those in Figure A.2, which illustrate the lateral and vertical profiles in (a) and (b) respectively, using intensity-scaled pixels to represent the normalized pressure amplitude for distances between 17.5 mm and 26.9 mm from the transducer face. The peak amplitude is plotted at $y = 0$ and the points where the pressure amplitude falls to half the maximum value are traced with white lines, which delineate the FWHM. The FWHM values are plotted for the lateral and

vertical profiles in Figure A.3, and the data points are fitted with parabolas to determine the minimum FWHM values and the distances from the transducer face at which these minima occur. Figure A.3(a) shows separate fittings for the lateral and vertical profiles, but two minima are in close agreement (325.52 μm at a distance of 21.67 mm for the lateral profiles, and 323.29 μm at 21.96 mm for the vertical profiles). A single fit to both sets of data points is given in Figure A.3(b), where the FWHM is 324.56 μm at 21.82 mm.

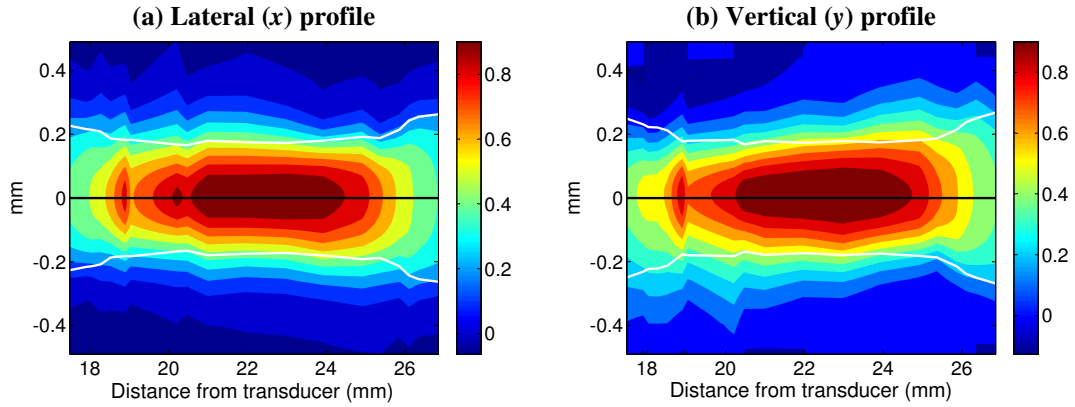

Figure A.2: Colour maps representing the lateral and vertical beam profiles, in (a) and (b) respectively, for the 30 MHz focussed transducer. The black horizontal line at $y = 0$ marks the profile peaks, and the white lines mark the points where the pressure amplitude falls to half the maximum value.

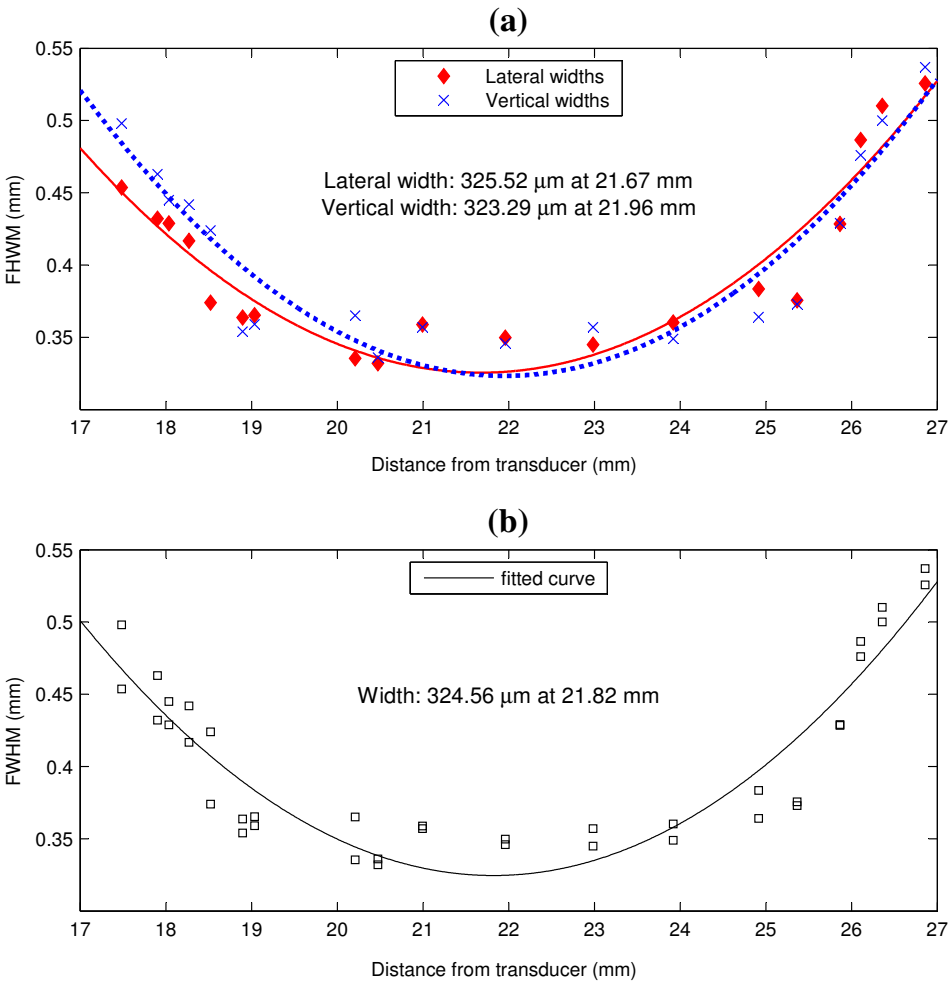

Figure A.3: FHWM values calculated from the lateral and vertical beam profiles of the 30 MHz transducer for distances between 17.5 mm and 26.9 mm from the transducer face. Two parabolic functions are fitted separately to the lateral and vertical data points in (a), and a fit to the combined data points is shown in (b).

A.3 Effective beam widths observed from Vmax values

Figure A.4 shows the lateral and vertical beam profiles for the 30 MHz transducer at a distance of 21.96 mm, which corresponds approximately to the location of the minima of the parabolas calculated in Figure A.3. The FWHM values for both profiles in Figure A.4 are approximately 0.35 mm. However, the maximum photoacoustically measured velocity, $|V_{\max}|$, corresponds to an "observed" width of $d \approx 0.53$ mm. This effective beam width can be determined from the "manual shifting" experiments (for example, see Figure 8.2), or by fitting to $|V_{\max}|$ values observed for data sets recorded using different laser pulse separations T (see Figures 7.3, 8.1 and 8.5).

Table A.2 compares the calculated FWHM values (also shown in Table A.1), the scanned beam widths w, and the observed widths d, for the 5 MHz focussed, 20 MHz planar, 20 MHz focussed and 30 MHz focussed transducers. The 3.5 MHz transducer was not scanned, but the observed beam width was found from the $|V_{\max}|$ values for data sets recorded with the wheel phantom and various different laser pulse separations T (as in Figure 7.3 for the 5 MHz transducer). This would vary according to the orientation of the cylindrical focus with respect to the direction of motion, but it is still unsurprising that the recorded value (≈ 2 mm) is much larger than the calculated beam width (≈ 1.4 mm), which only describes the narrowest part of the cylindrical focus.

The uncertainties for the experimental values, w and d, in Table A.2 are large – several tens of microns – as is evident from the scatter of data points in Figure A.3. The observed values are particularly variable since any slight deviation from the transducer focus would increase the effective beam width. However, the ball-park figures listed in the last column of Table A.2 serve to illustrate the general trends observed.

In general, the values calculated from the pulse-echo equations (A.1 and A.2) underestimate the scanned and observed beam widths, and the observed value d is also generally larger than the scanned FWHM w. The 20 MHz planar transducer is a notable exception, and should be re-scanned to verify the value obtained for w. For the 5 MHz transducer, d and w are closely similar, as also shown by Figure 7.3. However, for the 20 MHz and 30 MHz transducers the effective beam widths d, calculated from "manual shifting" experiments, are typically much larger than w, suggesting that there is still correlation once the absorbers have moved out of the immediate field-of-view defined by the FWHM . For the 30 MHz transducer, the observed beam width corresponds to approximately -14.8 dB (Figure A.4), rather than -6 dB for the FWHM. However, this -14.8 dB cannot be applied as a rule: even with repeated beam profile scans and photoacoustically determined $|V_{\max}|$ measurements, it is unlikely that an effective beam width d could be defined as the profile width at a specific drop in pres-

sure amplitude for all transducers in general. Moreover, whilst this is of interest for the ideal case of "plug" flow (in other words, the wheel phantom and "manual shifting" experiments), it is evident from Chapter 8 that for the fluid phantoms the transducer beam width is not a fundamental limitation of the maximum measurable velocities; rather, the accuracy is limited by the effect of light absorption and laminar flow.

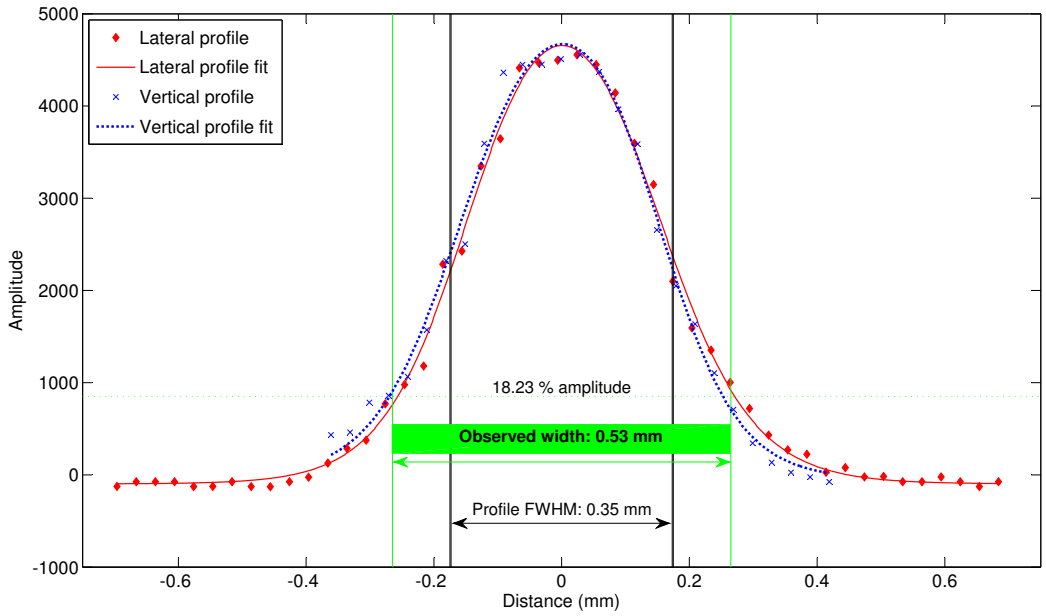

Figure A.4: Beam profile in the lateral and vertical directions at a distance of 21.96 mm from the face of the 30 MHz transducer. The lateral and vertical profile both have FWHM (-6 dB) values of approximately 0.35 mm. The effective beam width observed from the maximum photoacoustically measured velocities is approximately 0.53 mm, which corresponds to the width at approximately 18% (-14.8 dB) of the maximum amplitude.

Centre frequency (MHz)	Part number	Focus	FWHM beam width (µm)		
			Calculated	Scanned, *w*	Observed, *d*
3.5	V383	Cylindrical	1417		2022
5	A307S	Spherical	738	970	1129
20	V316	Planar	815	2420	1280
20	V317	Spherical	221	330	600
30	V375	Spherical	148	350	530

Table A.2: Comparison of the calculated FWHM values (also shown in Table A.1), the scanned beam widths w, and the observed widths d) for the 5 MHz focussed, 20 MHz planar, 20 MHz focussed and 30 MHz focussed transducers. Calculated and observed values are also given for the 3.5 MHz transducer, although the beam profile of this transducer was not scanned.

B

Filters

B.1 Filtering effect of amplifiers

An investigation was made into the effect of three different amplifiers (see Table 5.4) on the measured photoacoustic signals, which are illustrated in Figure B.1. The signal waveforms and their frequency spectra are shown for the 25 MHz focussed PVDF transducer in columns (a) and (b) respectively, for the 30 MHz focussed PZT transducer in columns (c) and (d), and for the 50 MHz focussed PZT transducer in columns (e) and (f). For the results in row 1, the transducers were used in conjunction with the 35 MHz amplifier, in row 2, the 45 MHz amplifier, and in row 3, the 100 MHz amplifier. In each case, the mean waveform and frequency response were calculated for over 350 waveforms acquired for the 6 μm black polystyrene spheres [see Figure 5.2(e)] flowing at average velocities ranging from $V = 0$ mm/s to $V = 55$ mm/s, with $T = 0.5$ ms and $\theta = 45°$. The tube diameter of 600 μm corresponds to a time of approximately 0.57 μs, which is in reasonable agreement with the lengths of the signals in columns (a), (c) and (e).

It is thought that the transducers are designed to be terminated by an impedance of 1 MΩ, but it appears that the differing amplifier input impedance values had little effect on the resulting signals. The more significant difference between the amplifiers is the gain, which, as expected, resulted in smaller signal amplitudes with the 100 MHz amplifier (40 dB gain) than the other two amplifiers (both approximately 60 dB gain). The small signal amplitude obtained for the 30 MHz transducer with the 35 MHz amplifier [Figure B.1 (1c)] is an anomalous results, possibly due to misalignment of the transducer. The frequency spectrum of these data [Figure B.1 (1d)] also demonstrates a higher proportion of low frequency content than for the spectra obtained for this transducer with the other two amplifiers [Figure B.1 (2d) and (3d)]. In general, however, there is very little difference between the frequency spectra obtained using different amplifiers, which is clear by comparing (1b) with (2b) and (3b), and also (1f) with (2f) and (3f). The greater difference is between the 25 MHz PVDF transducer and the two PZT transducers, which can be seen by comparing, for example, (2b) with (2d) and (2f): the signals obtained using 25 MHz transducer are limited mainly to frequencies below 20 MHz, whereas the data obtained with the 30 MHz and 50 MHz transducers both have broad frequency contents up to around 60 MHz, with peak frequencies around 20 MHz.

All the fluid phantom experiments used the 45 MHz amplifier (60 dB gain, 50 Ω input impedance), with the exception of the initial experiments with the carbon microspheres for which sufficient SNR was obtained without any amplification. This choice of amplifier was made in view of the uncertainty regarding the effect of the input impedance, the large gain, and also the apparently negligible benefit of using a more broadband (100 MHz) amplifier.

On page 182 a similarity was observed between the frequency content of the signals obtained using the 20 MHz, 30 MHz and 50 MHz PZT transducers for RBCs flowing in a 390 μm tube. These signals were acquired with the 45 MHz amplifier, and yet the frequency spectra in Figure 10.4(3b) and (4b) are very different from those in Figure B.1(2d) and (2f), which were acquired using the same detectors and amplifier, but for the 6 μm black polystyrene spheres flowing in 600 μm tube: the black spheres yield more broadband frequency spectra than those for the RBCs flowing in a 390 μm diameter tube. This highlights that the frequency spectra appear to be influenced more by the nature of the absorber than by the detector/amplifier combination. The signals from different absorbers were compared further in sub-section 10.1.2.

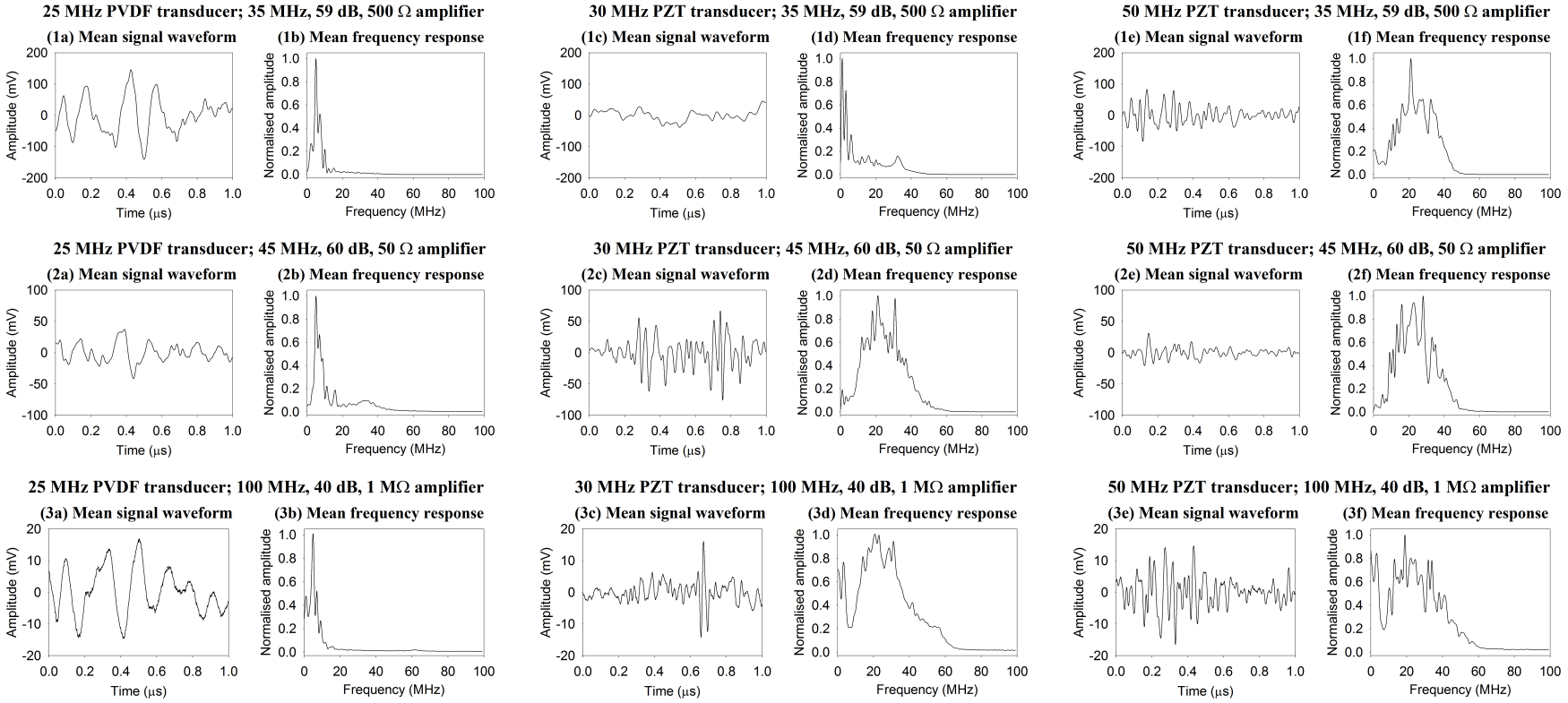

Figure B.1: Signal waveforms and frequency spectra obtained using the 25 MHz PVDF transducer [columns (a) and (b)], the 30 MHz PZT transducer [columns (c) and (d)], and the 50 MHz PZT transducer [columns (e) and (f)], each used with three different amplifiers, their bandwidths being 35 MHz, 45 MHz and 100 MHz (see Table 5.4), which correspond to the data in rows 1, 2 and 3 respectively. The mean waveforms and mean frequency spectra were calculated for over 350 waveforms acquired for the 6 μm black polystyrene spheres flowing in a 600 μm tube at average velocities ranging from $V = 0$ mm/s to $V = 55$ mm/s, with $T = 0.5$ ms and $\theta = 45°$.

B.2 Filters for signal processing

Figure B.2 shows the magnitude and phase responses, in columns (a) and (b) respectively, for five different filter designs: (1) Bessel, (2) Butterworth, (3) Chebyshev Type I, (4) Chebyshev Type II, and (5) Elliptic.

For post-filtering of the photoacoustic signals (see sub-section 10.1.3), a Butterworth filter was chosen due to its smooth magnitude response at all frequencies and its maximal flatness, with the ideal response of unity in the passband and zero in the stopband. Bessel filters are similar to Butterworth – in fact, for order 1 both filters are identical – but Butterworth filters have a steeper roll-off. Chebyshev Type I filters have an even sharper roll-off than Butterworth filters, and whilst the magnitude also decreases monotonically in the stopband, there is an equiripple response in the passband. Chebyshev Type II filters do not roll off as fast at Type I filters, but they are free of passband ripple; instead they have an equiripple response in the stopband. Elliptic filters have equiripples in both the passband and the stopband (note, however, that order 1 is identical to Chebyshev Type I, order 1), but these filters provide the sharpest roll-off characteristics, which accounts for their widespread use [1, 2].

It is evident from the right column of plots (b) in Figure B.2 that the phase response for each of the five filters varies with frequency. A zero-phase filter F_{zp} can be created by applying the conventional filter F_{c} to a M–length signal $\mathbf{p}_m$ ($m = 1, 2, \ldots, M$), reversing the filtered signal, then reapplying the conventional filter, and finally reversing the signal again:

$$\mathbf{p}'_m = F_{\text{c}}(\mathbf{p}_m) \tag{B.1}$$

$$\mathbf{p}''_n = F_{\text{c}}(\mathbf{p}'_{M-m+1}) \tag{B.2}$$

$$F_{\text{zp}}(\mathbf{p}_m) = \mathbf{p}''_{M-n+1}. \tag{B.3}$$

Figure B.3 shows the magnitude and phase responses, in (a) and (b) respectively, of zero-phase Butterworth filters. The shapes of the magnitude responses are similar to those in Figure B.2(2a), but, as expected, the phase change is zero degrees for all frequencies.

In Figure B.4, conventional and zero-phase Butterworth filters (order 2) are applied to the same simulated signal in order to demonstrate the phase shift introduced by conventional filtering, and the absence of this phase shift for zero-phase filtering. The original signal is a noisy ECG waveform generated in MATLAB, and is plotted in grey in (a) with the frequency spectrum also in grey in (b). After conventional filtering with a low-pass Butterworth filter, the filtered signal, shown by the darker grey solid curve in (a), is shifted by about 45 ns to the right of the unfiltered waveform.

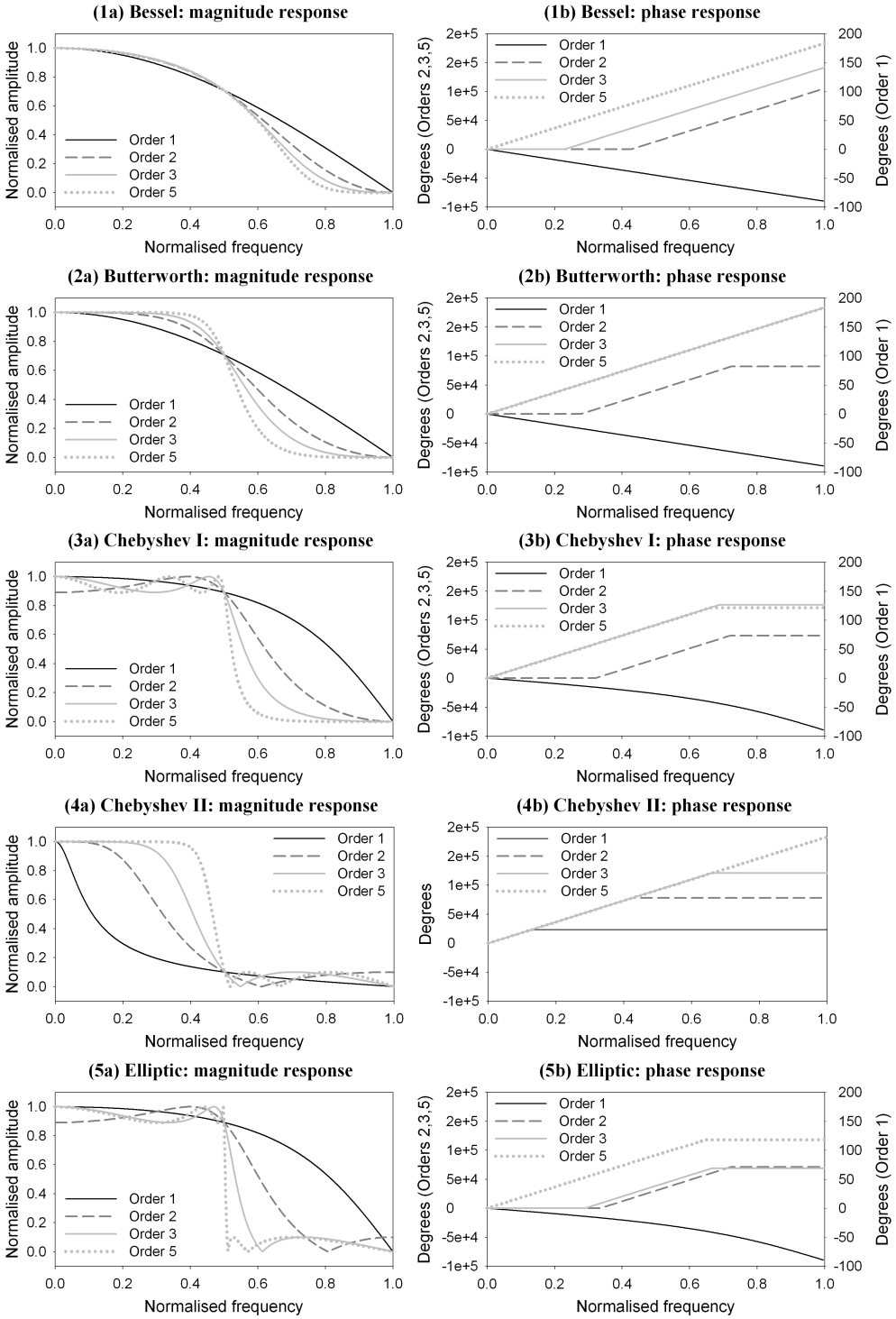

Figure B.2: Magnitude (a) and phase (b) responses of five different low-pass filter designs, showing filter orders 1, 2, 3 and 5. (1) Bessel filters with normalized frequency cut-off 0.5; (2) Butterworth filters with normalized frequency cut-off 0.5; (3) Chebyshev Type I filters with normalized passband edge frequency 0.5 and 1 dB of peak-to-peak ripple in the passband; (4) Chebyshev Type II filters with normalized stopband edge frequency 0.5 and stopband ripple 20 dB down from the peak passband value; (5) Elliptic filters with normalized passband edge frequency 0.5, 1 dB of ripple in the passband, and a stopband 20 dB down from the peak value in the passband. The plots were generated by applying each filter to a signal impulse.

After zero-phase filtering, there is no time shift, and the filtered signal, shown by the dashed curve in (a), is in phase with the original unfiltered waveform. Both the conventional and zero-phase filters remove the high-frequency noise from the signal, as shown by the frequency spectra in (b). However, the zero-phase filter (dashed line) offers a slightly sharper cut-off, even though both filters are order 2. This is also evident by comparing Figure B.2(2a) with Figure B.3(a); in fact, whilst for the conventional filters the specified cut-off values correspond to the half-power, or -3 dB, frequencies, for the zero-phase filters the cut-off values appear at the quarter-power, or -6 dB, frequencies.

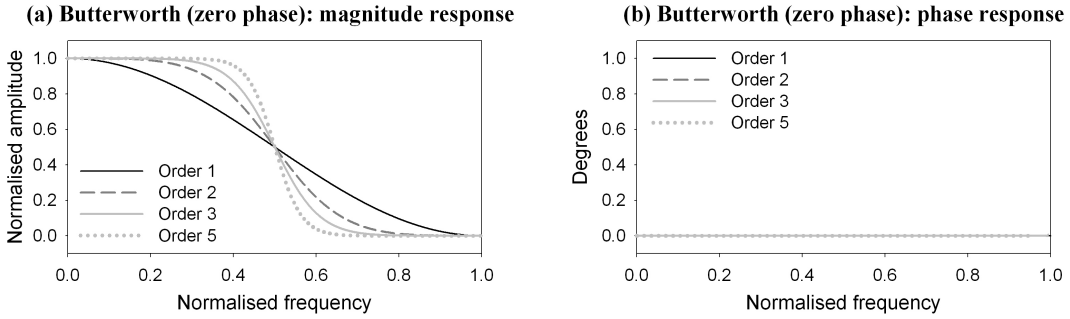

Figure B.3: Magnitude (a) and phase (b) responses of zero-phase low-pass Butterworth filters (normalized frequency cut-off 0.5), showing filter orders 1, 2, 3 and 5. The plots were generated by "double filtering" a signal impulse.

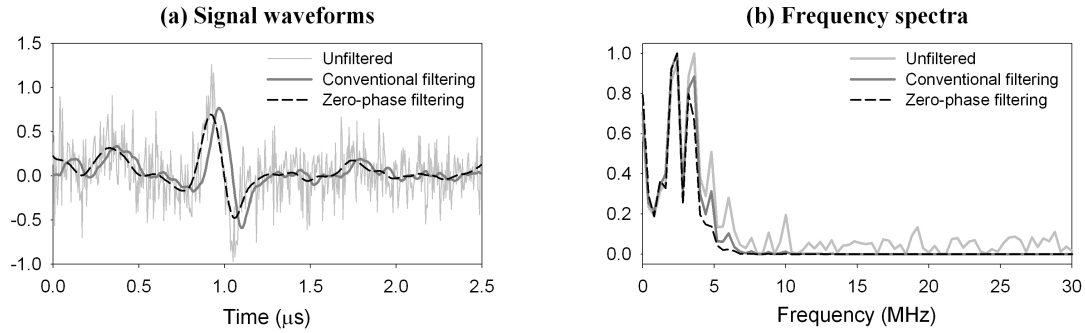

Figure B.4: Illustration of the time shift introduced by conventional filtering, and the absence of this time shift for zero-phase filtering. A noisy ECG waveform (500 points at intervals of 5 ns) was generated in MATLAB and then passed through an order 2 low-pass Butterworth filter (5 MHz cut-off, equivalent to a normalized cut-off of 0.05). The dark grey signal (a) and frequency spectrum (b) correspond to the conventionally filtered signal ("filter" function) and the dashed lines correspond to those for the zero-phase signal ("filtfilt" function). The MATLAB "filtfilt" function gives very similar – but not always identical – results to the "double filtering" described by Equations B.2 to B.3. Only the "double filtering" method was applied to the experimental data (Section 10.1).

Figure B.5 illustrates the effects of zero-phase and conventional high-pass filters (40 MHz cut-off) on the ability to make accurate time shift measurements by cross-correlating two photoacoustic waveforms. The example waveforms, $p_1(t)$ and $p_2(t)$, were acquired under the same conditions as those in Figure 10.7, namely from RBCs (5% Ht) moving at an average flow velocity $V = 35$ mm/s ($t_s = 8.35$ ns) in a $2R = 390$ μm tube, and illuminated with the PIV laser ($T = 0.5$ ms). Figure B.5(1a) shows the waveform pair after passing through a 40 MHz high-pass zero-phase filter, order 2, and the resulting mean frequency spectrum of the two waveforms is shown in the inset. The cross-correlation of these two waveforms is shown in (1b) and from the enlargement in (1c) it is evident that, whilst there is a clear peak at the known time shift ($t_s = 8.35$ ns), which is marked by a dashed vertical line, the maximum amplitude peak gives rise to a measured time shift $t_s' = -70.75$ ns. Figure B.5(2a) shows the same waveform pair after high-pass 40 MHz filtering, but here a conventional, rather than a zero-phase, filter is applied. The reduced sharpness of the filter roll-off is apparent by comparing the insets in (1a) and (2a) and also from the cross-correlation function in (1b) that has a greater proportion of high-frequency content than that in (2b). The maximum amplitude of the cross-correlation in (2b) appears at a time shift $t_s' = 7.25$ ns, which agrees closely with the known time shift, as shown in (2c). Application of a lower-order zero-phase filter (order 1 instead of order 2) generates very similar results to those in row 2, and these are shown in the third row of Figure B.5.

Thus it seems that the phase shift introduced by conventional filtering is of little significance since it applies equally to both waveforms, leaving the relative inherent time shift between the waveforms unchanged. Even so, the filtering in Section 10.1 used zero-phase Butterworth filters, which avoid any possible filter-induced time shifts. The more important effect is the difference in the sharpness of the filter cut-off between the conventional and zero-phase filters: for the same filter order, the zero-phase filter has a sharper cut-off and so has a more pronounced effect on the frequency content. The cut-off sharpness can be controlled using the filter order, but order 2 was used consistently in Section 10.1 so that the effect of different cut-off frequencies could be compared.

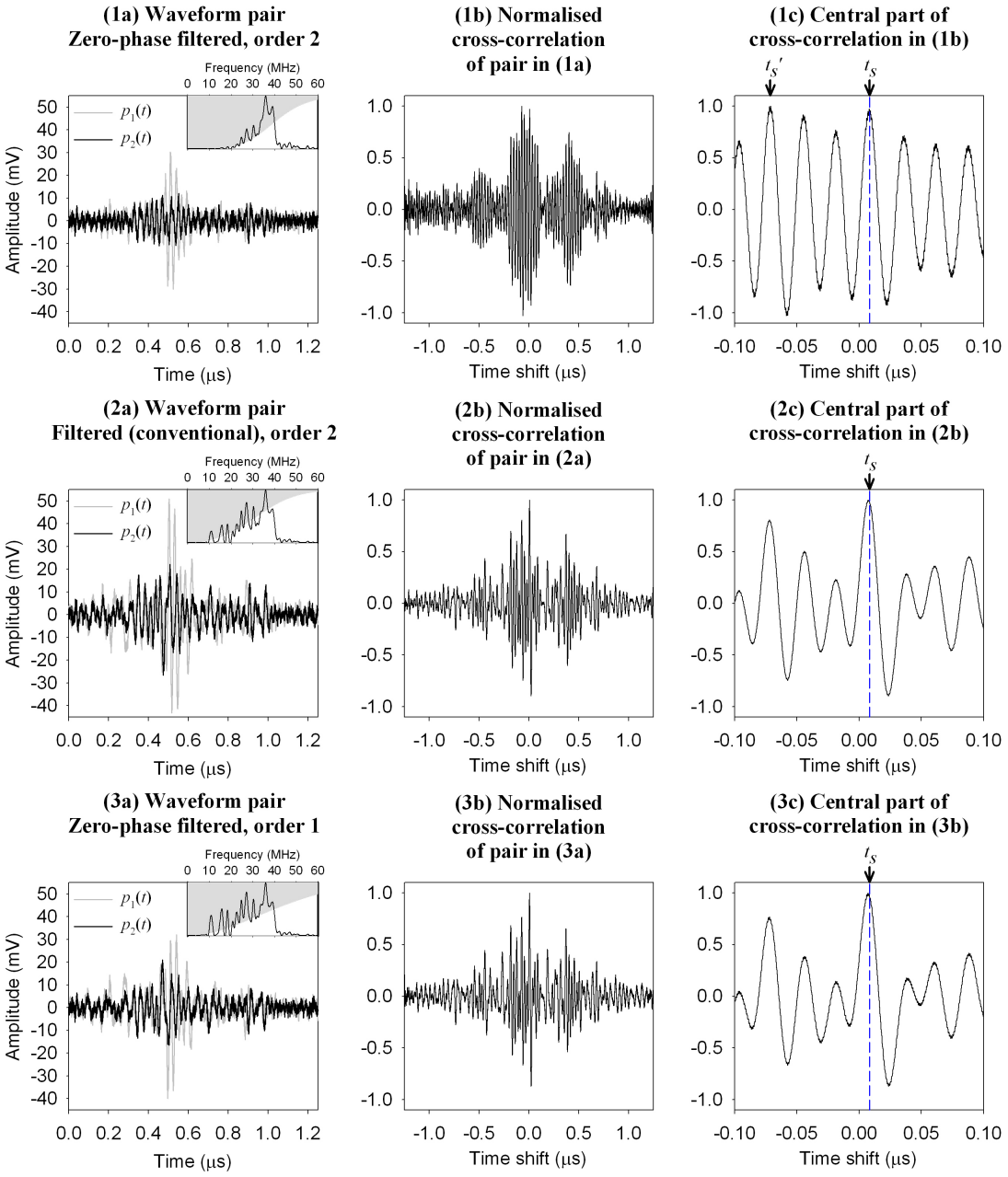

Figure B.5: Demonstration of zero-phase and conventional high-pass filtering of a photoacoustic waveform pair, and the effect on the accuracy of the time shift measurement. The waveforms were acquired from RBCs (5% Ht) moving at an average flow velocity V = 35 mm/s (t_s = 8.35 ns) in a 390 μm tube, and illuminated with the PIV laser (T = 0.5 ms). In row 1, the waveforms were passed through a zero-phase filter, order 2; in row 2 a conventional order 2 filter was applied, and in row 3 a zero-phase, order 1 filter. In each case the filters were high-pass with a cut-off frequency of 40 MHz. Column (a) shows the waveform pairs after filtering, and the insets show the frequency spectra. Column (b) shows the corresponding cross-correlation functions, and the central parts (time shifts -0.1 to 0.1 μs) are shown in the right column of plots (c). The measured time shifts are t_s' = −70.75 ns, 7.25 ns and 7.25, as found from the maximum peaks in (1c), (2c) and (3c) respectively.

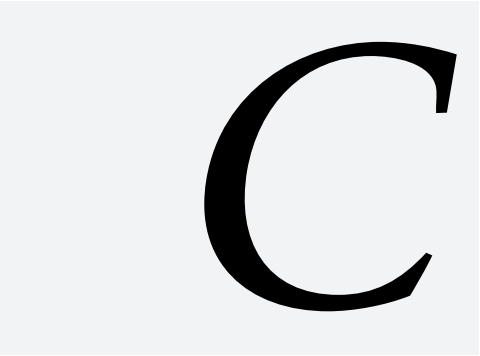

Statistics

In discussion of experimental data, it is important to distinguish terms such as *accuracy*, *precision*, *uncertainty* and *error*. Definitions appear in a variety of literature, for example refs. [5, 19, 49, 57, 63], but they are not always consistent. The following sub-sections describe the terms as they are used in this thesis.

C.1 Accuracy and error

Accuracy is a qualitative term describing the agreement between the measured and the true value. In practice the true value cannot be absolutely determined, and is replaced by an accepted reference value: determination of the "known values" in the experiments is described in Chapter 5. The error is the difference between the measured and the true value, and in this work a fractional error is used to quantify the accuracy (Equation 7.4, page 101).

C.2 Trueness and bias

Trueness is very similar to accuracy. It is a qualitative term describing the agreement between an average measured value and the true value. Trueness applies to the average value of many measurements, whereas accuracy applies to a single measurement. *Bias* is the difference between the average measurement and the true value, and can be used to quantify trueness. The fractional error defined in Equation 7.4 is more strictly a measure of *trueness*, but the term *accuracy* has been used to convey the same meaning.

C.3 Precision, repeatability and reproducibility

Precision is a qualitative term describing the agreement between independent measurements made under stipulated conditions. *Repeatability* refers to the precision in a case where all the experimental conditions are kept the same; *reproducibility* is the precision for measurements made using the same experimental method but under changed conditions, for example using different equipment and operators at a different location. Precision is normally expressed in terms of standard deviations. In Sections 6.3 and 9.2.2, standard deviation values are quoted as "uncertainties"; in fact, they essentially represent measurement precision.

C.4 Uncertainty and resolution

The terms "measurement uncertainty" and "measurement resolution" may both correctly describe the same experimental measure.

In general the uncertainty is defined as an interval $\pm\delta X$ around a measured value X_0 such that repetitions of this measurement will lie within the interval. The size of the interval is determined by various factors [3], including those due to random errors (fluctuations) and those due to the intrinsic instrument resolution [18, 46, 63].

Each individual time shift measurement, derived from the peak of the (mean) cross-correlation function, lies in an interval $\pm\Delta t_s'/2$ around the measured value t_s'. The size of $\pm\Delta t_s'/2$ is influenced by extrinsic factors such as jitter in laser pulse energy as well as the intrinsic instrument resolution (oscilloscope sampling interval δt_a). The value calculated for $\pm\Delta V'/2$ is therefore an "uncertainty" in the velocity measurement.

In accordance with common practice [64], the uncertainties $\pm\Delta V'/2$ are graphically represented (for examples, in Figures 7.1 and 8.10) by the lengths of the vertical error bars. Since each measurement can only be quoted as a value V' within the interval $V' \pm \Delta V'/2$, the error bars indicate the smallest difference that can be distinguished between two velocity values. By definition therefore [48], the error bars also represent

the velocity measurement resolution, with an associated time shift resolution $\pm\Delta t_s'/2$.

It is possible that the experimental uncertainties could be reduced by, for example, repeated measurements; however, this does not alter the fact that the calculated uncertainties represent the resolution of the system – the fundamental limit of values that can be distinguished using the flowmetry method – under the experimental conditions described. The fundamental resolution limit or minimum detectable velocity of the system is of particular importance and interest since photoacoustic Doppler flowmetry is targeted at measuring flow in microvasculature where the velocities are low (< 50 mm/s). Descriptions of other photoacoustic flowmetry methods [91, 113, 118] refer to a "minimum measurable velocity", but, since this is the smallest velocity interval that can be measured, the term "velocity resolution" is equally applicable and exact [5].

C.4.1 Standard deviation and standard error

The standard deviation s and the standard error $s_{\bar{x}}$ [13] are both measures of variability. The uncertainty, or resolution, $\pm\Delta V'/2$ is concerned with the variability of N individual time shift measurements. These N measurements are drawn from a hypothetical "population" of a very large number of time shift measurements made for a particular known velocity. The sample standard deviation is an estimate of the standard deviation for the whole population and can be defined for a sample of N data points $x_1, x_2, \ldots, x_N$ as follows:

$$s = \sqrt{\frac{1}{N-1}\sum_{i=1}^{N}(x_i - \bar{x})^2}. \tag{C.1}$$

In other words, it is a measure of average distance of the data points from the sample mean $\bar{x}$:

$$\bar{x} = \frac{1}{N}\sum_{i=1}^{N} x_i. \tag{C.2}$$

The sample mean $\bar{x}$ will vary from one sample to another, and this variability can be estimated using the standard error. The standard error of the mean depends on the standard deviation and the size of the sample:

$$s_{\bar{x}} = \frac{s}{\sqrt{N}} \tag{C.3}$$

In essence, the standard deviation describes how widely scattered the measurements are, whereas the standard error indicates the uncertainty in the estimate of the mean. For this reason, the standard deviation is used in calculating $\pm\Delta V'/2$ associated with mean values V', but when analysing entire data sets of such mean values the standard

error is used to estimate an uncertainty on overall mean measures such as the mean fractional error (see, for example, Figure 9.21).

C.4.2 Error propagation: propagation of uncertainties

Confusingly, the term "error" is often (incorrectly) used to mean "uncertainty"; in particular the phrase "error propagtion" is commonly understood to mean the propagation of uncertainties as in Equation 9.11. The standard rules for error propagation, as applied in this thesis, are described below in calculating the standard deviation σ_f of a function f of real, uncorrelated variables A, B with standard deviations σ_A, σ_B and precisely-known, real constants a, b.

$f = aA \pm bB$:

$$\sigma_f^2 = a^2\sigma_A^2 + b^2\sigma_B^2 \tag{C.4}$$

$f = aAB$ or $f = a\frac{A}{B}$:

$$\left(\frac{\sigma_f}{f}\right)^2 = \left(\frac{\sigma_A}{A}\right)^2 + \left(\frac{\sigma_B}{B}\right)^2 \tag{C.5}$$

$f = aA^{\pm b}$:

$$\frac{\sigma_f}{f} \approx b\frac{\sigma_A}{A} \tag{C.6}$$

In general, the standard deviation of a function $X = f(A, B, C, \ldots)$ is found from the partial derivatives with respect to each variable:

$$\sigma_X^2 = \left(\frac{\partial f}{\partial A}\sigma_A\right)^2 + \left(\frac{\partial f}{\partial B}\sigma_B\right)^2 + \left(\frac{\partial f}{\partial C}\sigma_C\right)^2 + \ldots \tag{C.7}$$

Bibliography

[1] LabVIEW Help page: IIR Filters. National Instruments LabVIEW 2010 SP1.

[2] MATLAB Help page: Analog Filter Design. *Signal Processing Toolbox*. The MathWorks, Inc. 1984-2012.

[3] Sources of uncertainty of measurement. In *Expression of the Uncertainty of Measurement in Calibration*. European co-operation for Accreditation, 1999, p. 20.

[4] Analysis of Sensory-Motor Control Performance. In *The Biomedical Engineering Handbook*, J. Bronzino, Ed., 2nd ed. CRC Press, 2000, ch. 149.4, p. 149:17.

[5] National Electrical Manufacturer's Association: Accuracy, Precision, Resolution and Uncertainty in Fire Protection Engineering. *Fire Protection Engineering 14* (2003).

[6] Webpage: Clinical trials. *National Cancer Institute*. www.cancer.gov/ clinicaltrials, Accessed on 31 August, 2011.

[7] Webpage: Hyperthermia in Cancer Treatment. *National Cancer Institute*. www.cancer.gov/cancertopics/factsheet/Therapy/hyperthermia, Accessed on 31 August, 2011.

[8] Webpage: Introduction to Cancer Therapy (Radiation Oncology). *Radiological Society of North America*. www.radiologyinfo.org/en/info.cfm?pg=intro_onco, Accessed on 31 August, 2011.

[9] Webpage: Observations of sections from healthy tissue. *University of Cambridge, Department of Pathology*. http://www.path.cam.ac.uk/partIB_pract/NHP1/, Accessed on 20 December, 2011.

[10] Webpage: Red blood cell count. *National Health Service (NHS)*. www.nhs.uk/conditions/Red-blood-count/Pages/Introduction.aspx, Accessed on 27 November, 2013.

[11] Webpage: Understanding the complete blood count. *Aplastic Anemia & MDS International Foundation*. www.aamds.org/node/72, Accessed on 27 November, 2013.

[12] Webpage: Tabulated Molar Extinction Coefficient for Hemoglobin in Water. *Compiled by Scott Prahl*. http://omlc.ogi.edu/spectra/hemoglobin/ summary.html, Accessed on 5 March, 2014.

[13] Altman, D. G., and Bland, J. M. Standard deviations and standard errors. *British Medical Journal 331*, 7521 (Oct. 2005), 903.

[14] Bain, B. J. Morphology of Blood Cells. In *Blood Cells: A Practical Guide*, 3rd ed. Wiley-Blackwell, 2002, pp. 52–154.

[15] Beard, P. Biomedical photoacoustic imaging. *Interface Focus 1*, 4 (Aug. 2011), 602–631.

[16] Beard, P. C. Flow velocity measurements. *UK Patent Application*, WO 03/039364 (2001).

[17] Bell, A. G. On the production and reproduction of sound by light. *American Journal of Science 20*, 118 (1880), 305–324.

[18] Bevington, P. R., and Robinson, D. K. Instrumental and statistical uncertainties. In *Data Reduction and Error Analysis for the Physical Sciences*, 3rd ed. McGraw-Hill, New York, 2003, ch. 3.1, pp. 36–39.

[19] Bevington, P. R., and Robinson, D. K. Uncertainties in measurements. In *Data Reduction and Error Analysis for the Physical Sciences*, 3rd ed. McGraw-Hill, New York, 2003, ch. 1.

[20] Bonnefous, O., and Pesque, P. Time domain formulation of pulse-Doppler ultrasound and blood velocity estimation by cross correlation. *Ultrasonic Imaging 85* (1986), 73–85.

[21] Brown, J. M., and Wilson, W. R. Exploiting tumour hypoxia in cancer treatment. *Nature reviews. Cancer 4*, 6 (June 2004), 437–47.

[22] Brunker, J. *Photoacoustic Doppler flowmetry using a cross-correlation cross correlation technique: Data processing methods and measurement limits*. Masters thesis, University College London, 2010.

[23] Brunker, J., and Beard, P. Pulsed photoacoustic Doppler flowmetry using a cross-correlation method. In *Proc. SPIE Int. Soc. Opt. Eng.* (Feb. 2010), A. A. Oraevsky and L. V. Wang, Eds., vol. 7564, pp. 756426–1 – 756426–8.

[24] Brunker, J., and Beard, P. Pulsed photoacoustic Doppler flow measurements in blood-mimicking phantoms. In *Proc. SPIE Int. Soc. Opt. Eng.* (Feb. 2011), A. A. Oraevsky and L. V. Wang, Eds., vol. 7899, pp. 78991K–1 – 78991K–10.

[25] Brunker, J., and Beard, P. Pulsed photoacoustic Doppler flowmetry using time-domain cross-correlation: accuracy, resolution and scalability. *Journal of the Acoustical Society of America 132*, 3 (2012), 1780–1791.

[26] Brunker, J., and Beard, P. Acoustic resolution photoacoustic Doppler velocity measurements in fluids using time-domain cross-correlation. In *Proc. SPIE Int. Soc. Opt. Eng.* (Mar. 2013), A. A. Oraevsky and L. V. Wang, Eds., vol. 8581, pp. 85811U–1 – 85811U–11.

[27] Cavalcanti Filho, J. L. G., de Souza Leão Lima, R., de Souza Machado Neto, L., Kayat Bittencourt, L., Domingues, R. C., and da Fonseca, L. M. B. PET/CT and vascular disease: current concepts. *European Journal of Radiology 80*, 1 (Oct. 2011), 60–67.

[28] Charm, S., and Kurland, G. *Blood Flow and Microcirculation*. Wiley, New York, 1974.

[29] Chen, S., Ling, T., Huang, S., Won Baac, H., and Guo, L. Photoacoustic correlation spectroscopy and its application to low-speed flow measurement. *Optics letters 35*, 8 (2010), 1200–1202.

[30] Chen, S.-L., Xie, Z., Carson, P. L., Wang, X., and Guo, L. J. In vivo flow speed measurement of capillaries by photoacoustic correlation spectroscopy. *Optics Letters 36*, 20 (Oct. 2011), 4017–9.

[31] Culjat, M. O., Goldenberg, D., Tewari, P., and Singh, R. S. A review of tissue substitutes for ultrasound imaging. *Ultrasound in Medicine and Biology 36*, 6 (June 2010), 861–873.

[32] Daly, S. M., and Leahy, M. J. "Go with the flow": A review of methods and advancements in blood flow imaging. *Journal of Biophotonics 6*, 3 (Mar. 2013), 217–55.

[33] Denekamp, J. Vascular attack as a therapeutic strategy for cancer. *Cancer and Metastasis Reviews 9*, 3 (Nov. 1990), 267–282.

[34] Denekamp, J., Hill, S. a., and Hobson, B. Vascular occlusion and tumour cell death. *European Journal of Cancer & Clinical Oncology 19*, 2 (Feb. 1983), 271–5.

[35] Diebold, G. J. Photoacoustic monopole radiation: waves from objects with symmetry in one, two and three dimensions. In *Photoacoustic Imaging and Spectroscopy*, L. V. Wang, Ed., 1st ed. CRC Press, New York, 2009, ch. 1, pp. 3–17.

[36] Embree, P. M., and Obrien, W. D. Volumetric blood flow via time-domain correlation: experimental verification. *IEEE Transactions on Ultrasonics Ferroelectrics and Frequency Control 37*, 3 (1990), 176–189.

[37] Evans, D. H., and McDicken, W. N. *Doppler Ultrasound: Physics, Instrumentation and Signal Processing*, 2nd ed. Wiley, Chichester, 2000.

[38] Evans, D. H., and McDicken, W. N. PW Systems - Difference between the CW and PW Doppler Shift frequency. In *Doppler Ultrasound: Physics, Instrumentation and Signal Processing*, 2nd ed. Wiley, Chichester, 2000, ch. 4.2.2.5, pp. 50–51.

[39] Evans, D. H., and McDicken, W. N. Velocity detecting systems. In *Doppler Ultrasound: Physics, Instrumentation and Signal Processing*, 2nd ed. Wiley, Chichester, 2000, ch. 4.2, p. 43.

[40] Fang, H., Maslov, K., and Wang, L. V. Photoacoustic doppler effect from flowing small light-absorbing particles. *Physical Review Letters 99*, 18 (2007), 184501.

[41] Fang, H., Maslov, K., and Wang, L. V. Photoacoustic Doppler flow measurement in optically scattering media. *Applied Physics Letters 91*, 26 (2007), 264103.

[42] Fang, H., and Wang, L. V. Photoacoustic Doppler effect and flow sensing. In *Photoacoustic imaging and spectroscopy*, L. V. Wang, Ed., 1st ed. CRC Press, New York, 2009, ch. 2, pp. 19–24.

[43] Feldmann, H. J., Molls, M., and Vaupel, P. Blood flow and oxygenation status of human tumors - Clinical investigations. *Strahlentherapie Und Onkologie 175*, 1 (1999), 1–9.

[44] Fens, M. H. a. M., Storm, G., and Schiffelers, R. M. Tumor vasculature as target for therapeutic intervention. *Expert Opinion on Investigational Drugs 19*, 11 (Nov. 2010), 1321–38.

[45] Folkman, J. Tumor angiogenesis: therapeutic implications. *The New England Journal of Medicine 285*, 21 (Dec. 1971), 1182–6.

[46] Fornasini, P. Uncertainty in direct measurements. In *The Uncertainty in Physical Measurements: An Introduction to Data Analysis in the Physics Laboratory*, 1st ed. Springer, 2008, ch. 4, pp. 45–49.

[47] Galanzha, E. I., Sarimollaoglu, M., Nedosekin, D. a., Keyrouz, S. G., Mehta, J. L., and Zharov, V. P. In vivo flow cytometry of circulating clots using negative photothermal and photoacoustic contrasts. *Cytometry Part A 79*, 10 (Oct. 2011), 814–24.

[48] Geddes, L. A., and Baker, L. E. Digital Systems. In *Principles of Applied Biomedical Instrumentation*, 3rd ed. Wiley, New York, 1989, p. 944.

[49] Guare, C. J. Error, Precision and Uncertainty. *Journal of Chemical Education 68*, 8 (1991), 649–652.

[50] Guazzelli, E. Particulate pipe flows. EUROMECH Fluid Mechanics Conference, www.mims.manchester.ac.uk/events/workshops/EFMC7/TALKS/guazzelli.pdf, 2008.

[51] Hein, I. A., and O'Brien, W. R. A real-time ultrasound time-domain correlation blood flowmeter. II. Performance and experimental verification. *IEEE Transactions on Ultrasonics, Ferroelectrics and Frequency Control 40*, 6 (Jan. 1993), 776–85.

[52] Hein, I. A., and O'Brien, W. R. Current time-domain methods for assessing tissue motion by analysis from reflected ultrasound echoes - a review. *IEEE Transactions on Ultrasonics, Ferroelectrics and Frequency Control 40*, 2 (Jan. 1993), 84–102.

[53] Hennessey, D., Martin, L. M., Atzberger, A., Lynch, T. H., Hollywood, D., and Marignol, L. Exposure to hypoxia following irradiation increases radioresistance in prostate cancer cells. *Urologic Oncology 31*, 7 (Oct. 2013), 1106–1116.

[54] Herrick, A. L., and Clark, S. Quantifying digital vascular disease in patients with primary Raynaud's phenomenon and systemic sclerosis. *Annals of the Rheumatic Diseases 57*, 2 (Feb. 1998), 70–78.

[55] Hysi, E., Saha, R. K., and Kolios, M. C. On the use of photoacoustics to detect red blood cell aggregation. *Biomedical Optics Express 3*, 9 (Sept. 2012), 2326–38.

[56] Isa, A. Y., Ward, T. H., West, C. M. L., Slevin, N. J., and Homer, J. J. Hypoxia in head and neck cancer. *The British Journal of Radiology 79*, 946 (Oct. 2006), 791–798.

[57] ISO5725-1:1995. Accuracy (trueness and precision) of measurement methods and results - Part 1: General principles and definitions.

[58] Jain, R. Understanding barriers to drug delivery: high resolution in vivo imaging is key. *Clinical Cancer Research 5*, 7 (1999), 1605–1606.

[59] Jain, R. K. Normalization of tumor vasculature: An emerging concept in anti-angiogenic therapy. *Science 307*, 5706 (2005), 58–62.

[60] Kasai, C., Harada, A., and Namekawa, K. Real-time blood-flow imaging system using ultrasonic Doppler techniques. *Systems and Computers in Japan 19*, 11 (Nov. 1988), 13–24.

[61] Kasai, C., Namekawa, K., Koyano, A., and Omoto, R. Real-time two-dimensional blood flow imaging using an autocorrelation technique. *IEEE Transactions on Sonics and Ultrasonics 32*, 3 (1985), 458–464.

[62] Keane, R. D., Adrian, R. J., and Zhang, Y. Super-resolution particle imaging velocimetry. *Measurement Science and Technology 6* (1995), 754–768.

[63] Kirkup, L. Dealing with uncertainties. In *Experimental Methods: An Introduction to the Analysis and Presentation of Data*. Jacaranda Wiley Ltd, Milton, 1994, ch. 4, p. 56.

[64] Kirkup, L. Error bars and line drawing. In *Experimental Methods: An Introduction to the Analysis and Presentation of Data*. Jacaranda Wiley Ltd, Milton, 1994, ch. 3.2.5, pp. 28–30.

[65] Koumoutsakos, P., Pivkin, I., and Milde, F. The Fluid Mechanics of Cancer and Its Therapy. *Annual Review of Fluid Mechanics 45*, 1 (Jan. 2013), 325–355.

[66] Krüger, T., Gross, M., Raabe, D., and Varnik, F. Crossover from tumbling to tank-treading-like motion in dense simulated suspensions of red blood cells. *Soft Matter 9*, 37 (2013), 9008–9015.

[67] Lai, X., and Torp, H. Interpolation methods for time-delay estimation using cross-correlation method for blood velocity measurement. *IEEE Transactions on Ultrasonics, Ferroelectrics and Frequency Control 46*, 2 (Jan. 1999), 277–90.

[68] Lankester, K. J., Maxwell, R. J., Pedley, R. B., Dearling, J. L., Qureshi, U. a., El-Emir, E., Hill, S. a., and Tozer, G. M. Combretastatin A-4-phosphate effectively increases tumor retention of the therapeutic antibody, 131I-A5B7, even at doses that are sub-optimal for vascular shut-down. *International Journal of Oncology 30*, 2 (Feb. 2007), 453–60.

[69] Laufer, J., Johnson, P., Zhang, E., Treeby, B., Cox, B., Pedley, B., and Beard, P. In vivo preclinical photoacoustic imaging of tumor vasculature development and therapy. *Journal of Biomedical Optics 17*, 5 (May 2012), 056016.

[70] Laufer, J., Zhang, E., and Beard, P. Evaluation of Absorbing Chromophores Used in Tissue Phantoms for Quantitative Photoacoustic Spectroscopy and Imaging. *IEEE Journal of Selected Topics in Quantum Electronics 16*, 3 (2010), 600–607.

[71] Liang, J., Zhou, Y., Maslov, K. I., and Wang, L. V. Cross-correlation-based transverse flow measurements using optical resolution photoacoustic microscopy with a digital micromirror device. *Journal of Biomedical Optics 18*, 9 (Sept. 2013), 96004.

[72] Liang, J., Zhou, Y., Winkler, A. W., Wang, L., Maslov, K. I., Li, C., and Wang, L. V. Random-access optical-resolution photoacoustic microscopy using a digital micromirror device. *Optics Letters 38*, 15 (Aug. 2013), 2683–6.

[73] Lighthill, J. Blood flow and arterial disease. In *Mathematical Biofluiddynamics*. Society for Industrial and Applied Mathematics, Philadelphia, 1975, ch. 13, pp. 253–267.

[74] Lighthill, J. The microcirculation. In *Mathematical Biofluiddynamics*. Society for Industrial and Applied Mathematics, Philadelphia, 1975, ch. 14, pp. 269–281.

[75] Lozhkin, K. Interactions with Matter. Radiation Chemistry. In *UCL lecture notes*. PHAS3892 Radiobiology, 2008.

[76] Markl, M., Frydrychowicz, A., Kozerke, S., Hope, M., and Wieben, O. 4D flow MRI. *Journal of Magnetic Resonance Imaging 36*, 5 (Nov. 2012), 1015–1036.

[77] Matas, J.-P., Morris, J. F., and Guazzelli, E. Influence of particles on the transition to turbulence in pipe flow. *Philosophical Transactions of the Royal Society of London. Series A, Mathematical, Physical, and Engineering Sciences 361*, 1806 (May 2003), 911–919.

[78] McHedlishvili, G., and Maeda, N. Blood flow structure related to red cell flow: determinant of blood fluidity in narrow microvessels. *The Japanese Journal of Physiology 51*, 1 (Feb. 2001), 19–30.

[79] McKeown, S., Cowen, R., and Williams, K. Bioreductive Drugs: from Concept to Clinic. *Clinical Oncology 19*, 6 (Aug. 2007), 427–442.

[80] McMillan, D. E. The effect of diabetes on blood flow properties. *Diabetes 32 Suppl 2*, June (May 1983), 56–63.

[81] Munson, B. R., Young, D. F., and Okiishi, T. H. Steady, laminar flow in circular tubes. In *Fundamentals of Fluid Mechanics*, 5th ed. John Wiley & Sons, 2006, ch. 6.9.3, pp. 327–329.

[82] Olympus. Ultrasonic Transducers Technical Notes. Tech. rep., 2006.

[83] Roggan, A., Friebel, M., DoÌˆrschel, K., Hahn, A., and MuÌˆller, G. Optical Properties of Circulating Human Blood in the Wavelength Range 400-2500 nm. *Journal of Biomedical Optics 4*, 1 (1999), 36–46.

[84] Rossow, M. J., Mantulin, W. W., and Gratton, E. Scanning laser image correlation for measurement of flow. *Journal of Biomedical Optics 15*, 2 (2010).

[85] Sagar, S., Klassen, G., Barclay, K., and Aldrich, J. Tumour blood flow: measurement and manipulation for therapeutic gain. *Cancer Treatment Reviews 19*, 4 (1993), 299–349.

[86] Saha, R. K., Karmakar, S., and Roy, M. Photoacoustic response of suspended and hemolyzed red blood cells. *Applied Physics Letters 103*, 4 (2013), 044101.

[87] Sarimollaoglu, M., Nedosekin, D. a., Simanovsky, Y., Galanzha, E. I., and Zharov, V. P. In vivo photoacoustic time-of-flight velocity measurement of single cells and nanoparticles. *Optics Letters 36*, 20 (Oct. 2011), 4086–8.

[88] Sheinfeld, A., and Eyal, A. Photoacoustic thermal diffusion flowmetry. *Biomedical Optics Express 3*, 4 (Apr. 2012), 800–13.

[89] Sheinfeld, A., and Eyal, A. Photoacoustic thermal diffusion flowmetry in tissue-mimicking phantoms. In *Proc. SPIE Int. Soc. Opt. Eng.* (Mar. 2013), A. A. Oraevsky and L. V. Wang, Eds., vol. 8581, pp. 85811O–1 – 85811O–6.

[90] Sheinfeld, A., Gilead, S., and Eyal, A. Photoacoustic Doppler measurement of flow using tone burst excitation. *Optics Express 18*, 5 (2010), 4212–4221.

[91] Sheinfeld, A., Gilead, S., and Eyal, A. Simultaneous spatial and spectral mapping of flow using photoacoustic Doppler measurement. *Journal of Biomedical Optics 15*, 6 (2010), 066010.

[92] Sheinfeld, A., Gilead, S., and Eyal, A. Time-resolved photoacoustic Doppler characterization of flow using pulsed excitation. In *Proc. SPIE Int. Soc. Opt. Eng.* (2010), A. A. Oraevsky and L. V. Wang, Eds., vol. 7564, pp. 75643N–1 – 75643N–6.

[93] Sherwood, J. M., Dusting, J., Kaliviotis, E., and Balabani, S. The effect of red blood cell aggregation on velocity and cell-depleted layer characteristics of blood in a bifurcating microchannel. *Biomicrofluidics 6*, 2 (June 2012), 024119–1 – 024119–18.

[94] Sherwood, J. M., Kaliviotis, E., Dusting, J., and Balabani, S. Hematocrit, viscosity and velocity distributions of aggregating and non-aggregating blood in a bifurcating microchannel. *Biomechanics and Modeling in Mechanobiology* (Nov. 2012), 1–15.

[95] Siemann, D. W. The unique characteristics of tumor vasculature and preclinical evidence for its selective disruption by Tumor-Vascular Disrupting Agents. *Cancer Treatment Reviews 37*, 1 (Feb. 2011), 63–74.

[96] Singh, V., Devgan, L., Bhat, S., and Milner, S. M. The pathogenesis of burn wound conversion. *Annals of Plastic Surgery 59*, 1 (July 2007), 109–115.

[97] Song, W., Liu, W., and Zhang, H. F. Laser-scanning Doppler photoacoustic microscopy based on temporal correlation. *Applied Physics Letters 102*, 20 (2013), 203501.

[98] Strohm, E., Berndl, E. S., and Kolios, M. Probing Red Blood Cell Morphology Using High-Frequency Photoacoustics. *Biophysical Journal 105*, 1 (July 2013), 59–67.

[99] Togawa, T., Tamura, T., and Oberg, P. A. Correlation methods for microvascular red blood cell velocity measurement. In *Biomedical Sensors and Instruments*, 2nd ed. CRC Press, 2011, ch. 3.2.7, pp. 119–122.

[100] Tozer, G. M., Ameer-Beg, S. M., Baker, J., Barber, P. R., Hill, S. a., Hodgkiss, R. J., Locke, R., Prise, V. E., Wilson, I., and Vojnovic, B. Intravital imaging of tumour vascular networks using multi-photon fluorescence microscopy. *Advanced Drug Delivery Reviews 57*, 1 (Jan. 2005), 135–52.

[101] Tozer, G. M., Kanthou, C., and Baguley, B. C. Disrupting tumour blood vessels. *Nature Reviews. Cancer 5*, 6 (June 2005), 423–35.

[102] Tozer, G. M., Kanthou, C., Parkins, C. S., and Hill, S. a. The biology of the combretastatins as tumour vascular targeting agents. *International Journal of Experimental Pathology 83*, 1 (Feb. 2002), 21–38.

[103] Vennemann, P., Lindken, R., and Westerweel, J. In vivo whole-field blood velocity measurement techniques. *Experiments in Fluids 42* (2007), 495–511.

[104] Wang, L., Maslov, K., and Wang, L. V. Single-cell label-free photoacoustic flowoxigraphy in vivo. *Proceedings of the National Academy of Sciences of the United States of America 110*, 15 (Apr. 2013), 5759–64.

[105] Wang, L., Xia, J., Yao, J., Maslov, K. I., and Wang, L. V. Ultrasonically Encoded Photoacoustic Flowgraphy in Biological Tissue. *Physical Review Letters 111*, 20 (Nov. 2013), 204301–1 – 204301–5.

[106] Wang, L., Yao, J., Maslov, K. I., Xing, W., and Wang, L. V. Ultrasound-heated photoacoustic flowmetry. *Journal of Biomedical Optics 18*, 11 (Nov. 2013), 117003.

[107] Wang, L. V. Prospects of photoacoustic tomography. *Medical Physics 35*, 12 (2008), 5758–5767.

[108] White, F. W. Laminar fully developed pipe flow. In *Fluid Mechanics*, 6th ed. McGraw-Hill, 2008, ch. 6.4, pp. 351–353.

[109] Wust, P., Hildebrandt, B., Sreenivasa, G., Rau, B., Gellermann, J., Riess, H., Felix, R., and Schlag, P. Hyperthermia in combined treatment of cancer. *The Lancet Oncology 3*, 8 (Aug. 2002), 487–497.

[110] Yao, J., Maslov, K., Shi, Y., Taber, L., and Wang, L. In vivo photoacoustic imaging of transverse blood flow by using Doppler broadening of bandwidth. *Optics Letters 35*, 9 (2010), 1419–1421.

[111] Yao, J., Maslov, K. I., Wang, L. V., Zhang, Y., and Xia, Y. Label-free oxygen-metabolic photoacoustic microscopy in vivo. *Journal of Biomedical Optics 16*, 7 (2011), 076003.

[112] Yao, J., and Wang, L. V. Photoacoustic microscopy. *Laser & Photonics Reviews 7*, 5 (Sept. 2013), 758–778.

[113] Yao, J. J., and Wang, L. H. V. Transverse flow imaging based on photoacoustic Doppler bandwidth broadening. *Journal of Biomedical Optics 15*, 2 (2010), 021304–1–021304–5.

[114] Zhang, E. Z., Laufer, J. G., Pedley, R. B., and Beard, P. C. In vivo high-resolution 3D photoacoustic imaging of superficial vascular anatomy. *Physics in Medicine and Biology 54*, 4 (Feb. 2009), 1035–46.

[115] Zhang, E. Z., Povazay, B., Laufer, J., Alex, A., Hofer, B., Pedley, B., Glittenberg, C., Treeby, B., Cox, B., Beard, P., and Drexler, W. Multimodal pho-

toacoustic and optical coherence tomography scanner using an all optical detection scheme for 3D morphological skin imaging. *Biomedical Optics Express 2*, 8 (Aug. 2011), 2202–15.

[116] Zhang, H. F., Maslov, K., Stoica, G., and Wang, L. V. Functional photoacoustic microscopy for high-resolution and noninvasive in vivo imaging. *Nature Biotechnology 24*, 7 (July 2006), 848–51.

[117] Zhang, H. F., Maslov, K., and Wang, L. V. In vivo imaging of subcutaneous structures using functional photoacoustic microscopy. *Nature Protocols 2*, 4 (Jan. 2007), 797–804.

[118] Zhou, Y., Liang, J., Maslov, K., and Wang, L. Calibration-free in vivo transverse blood flowmetry based on cross correlation of slow time profiles from photoacoustic microscopy. *Optics Letters 38*, 19 (2013), 3882–3885.